

Title	SPIV Flow Field Measurement around the Stern of a Self-propelled KVLCC2 Model Ship in Regular Head Waves
Author(s)	Mwangi, Benson Oyunge
Citation	大阪大学, 2021, 博士論文
Version Type	VoR
URL	https://doi.org/10.18910/85407
rights	
Note	

Osaka University Knowledge Archive : OUKA

<https://ir.library.osaka-u.ac.jp/>

Osaka University

Doctoral Dissertation

SPIV Flow Field Measurement around the Stern of a Self-
propelled KVLCC2 Model Ship in Regular Head Waves

Mwangi Benson Oyunge

June 2021

Department of Naval Architecture and Ocean Engineering
Division of Global Architecture
Graduate School of Engineering,
Osaka University

ACKNOWLEDGEMENTS

First and foremost, I would like to express my sincere gratitude to my advisor, Professor Yasuyuki Toda for giving me the opportunity to join his laboratory and Osaka University to pursue my Master's and Doctoral studies. His kindness, patience and unwavering support, and by sharing his top-notch knowledge and skills, made it possible for me to achieve the objectives of this research work. I am also very thankful to the committee of professors, Prof. Naoki Osawa and Prof. Hiroyoshi Suzuki for their valuable comments during my final doctoral thesis defense.

My sincere thanks also goes to Mitsubishi Corporation for granting me a scholarship for my upkeep during my doctoral studies. This made it easier for me to concentrate on my studies and research without any worry for my upkeep.

I would also like to extend my gratitude to the PIV group members (Mr. Endo Kazusa and Ms. Hina Matsuura) of Toda Laboratory for their enormous support during my experiments. I am especially very grateful to Ms. Hina Matsuura for her special contribution to the completion of this dissertation. The results of the SPIV measurement for the section upstream of the propeller during the ESDs effect study, is actually her work. To all members of Toda Laboratory, thank you very much for your support.

I am deeply indebted to my lovely wife, Rodah and our sons, Ethan and Austin for the love and joy they bring into my life, and their unceasing support during the entire period of my further studies. My sincere appreciation also goes to my parents, Mr. and Mrs. Mwangi and my brothers for their unwavering support and encouragement throughout my education.

To my friends especially in Kenya and Japan, thank you very much for your encouragement and support in the course of my further studies.

Above all, I reverently thank the Almighty God for His blessings thus far.

ABSTRACT

In order to curb the greenhouse gas (GHG) emissions from the shipping industry, the International Maritime Organization (IMO) introduced the Energy Efficiency Design Index (EEDI) for all new ships. For this reason, in order to achieve the requirements for the EEDI, there is need to investigate the propulsive performance for ships in waves. Therefore, in this study, the effect of the wave amplitude and energy saving devices (ESDs) on the self-propulsion factors, motions, thrust, torque and the flow field around the stern of a self-propelled model ship has been investigated in waves. Regarding the wave amplitude dependency study, the velocity distribution at the stern with various amplitude waves were analyzed and discussed with respect to the thrust fluctuation in waves. Concerning ESDs, most studies are conducted in calm water, and experiments on improving the propulsion performance by ESDs are rarely done in waves. Therefore, in this study, energy-saving rudders, which are known to be effective in calm water, were used. The two types of rudders that were used are; a normal rudder and rudders with a bulb and fins (RBFs) with an aim of recovering the lost energy or gaining extra thrust by utilizing the rotational flow after the propeller in waves. The fins for the RBFs were horizontal on both sides of the rudder with a zero angle of attack and a similar foil section but facing opposite directions in order to generate a forward force from the rotational flow behind the propeller. To understand the effect of the rudders on the self-propulsion factors, motions, thrust, torque and the flow field around the stern of the model ship, the results for with and without rudders were compared. From an investigation in calm water condition, an increase of propeller efficiency was observed. The study was done for a 3.2m KVLCC2 model tanker in fully loaded condition, appended with a propeller and rudders at a design Froude number of 0.142 in short and long waves. In this study, heave and pitch motions were free and surge was free by using a weak spring to compensate for

the unbalance of the steady force. So, the surge motion due to wave exciting force was measured as well as slow surge motion through a mass weak spring system. Time histories for heave and pitch motions, thrust, torque and effective wake were compared for various wave amplitudes and ESDs. From the results, the efficiency improvement was observed by RBF system in short waves and a decrease of efficiency was not observed for all wave ranges. The time averaged inflow velocity increased as the wave amplitude increased for long waves. So, the efficiency decreased as the wave amplitude increased for long waves. The velocity distribution and vortex behavior around the stern of the model ship were explained with respect to the wave amplitude and ESDs effect in waves. The velocity distribution was also discussed with respect to the thrust fluctuations. Regarding the ESDs, the results for with and without rudder were compared so as to understand the effect of the rudders on the flow field. It was observed that there is no substantial effect by the rudders especially on the flow field upstream of the propeller. However, there was a significant effect on the flow field downstream of the propeller. For the wave amplitude effect, the lower velocity part related to the longitudinal bilge vortices moved vertically relative to the propeller disk, and the high velocity area entered the propeller plane with respect to the effective inflow.

TABLE OF CONTENTS

ACKNOWLEDGEMENTS	I
ABSTRACT	II
LIST OF SYMBOLS	VI
LIST OF TABLES	IX
LIST OF FIGURES	X
CHAPTER 1: INTRODUCTION.....	1
1.1 Background	1
1.2 Objectives	2
1.3 Test Conditions	3
1.4 Literature Review	4
1.4.1 The effect of the wave amplitude	4
1.4.2 The effect of energy saving devices (ESDs)	7
CHAPTER 2: FACILITIES, EQUIPMENT AND EXPERIMENTS	20
2.1 Facilities and Equipment	20
2.1.1 Towing Tank	20
2.1.2 Some of the devices that were used in the experiments	21
2.1.3 The SPIV system	21
2.2 The Experiments that were conducted	22
2.2.1 Motions and Force Measurement Experiment	22
2.2.2 Ship Geometry and Particulars	23
2.2.3 Propeller Particulars	24
2.2.4 Coordinate System	26
2.2.5 SPIV Measurement Experiments	26
2.2.6 Measured Parameters	32
CHAPTER 3: MOTIONS AND FORCE MEASUREMENT RESULTS	34
3.1 Wave Amplitude Effect	34
3.1.1 Time histories	34
3.1.2 Thrust, torque and effective wake results	37
3.1.3 Motion results	50
3.1.4 Added Resistance results	57
3.2 ESDs Effect	59
3.2.1 Time histories	59

3.2.2	Force measurement results	59
3.2.3	Motions results	70
CHAPTER 4:	SPIV MEASUREMENT RESULTS	76
4.1	Wave Amplitude Effect.....	76
4.1.1	Velocity field result for calm water	76
4.1.2	Velocity field results for waves	77
4.2	ESDs Effect	90
4.2.1	Velocity field result for calm water	92
4.2.2	Velocity field results for waves	94
CHAPTER 5:	CONCLUSIONS AND FUTURE WORKS	138
5.1	CONCLUSIONS	138
5.2	FUTURE WORKS	140
REFERENCES	141
LIST OF PUBLICATIONS	151
CURRICULUM VITAE	152

LIST OF SYMBOLS

AP	After Perpendicular
CCD	Charge-Coupled Device
CFD	Computational Fluid Dynamics
DAVIS	Data Acquisition and Visualization Software
DOF	Degree of Freedom
EFD	Experimental Fluid Dynamics
EEDI	Energy Efficiency Design Index
ESDs	Energy Saving Devices
FP	Forward Perpendicular
Fr	Froude Number
IMO	International Maritime Organization
KVLCC2	KRISO Very Large Crude-oil Carrier 2
LCB	Longitudinal Center of Buoyancy
NR	Normal rudder
RBF-C	Rudder with a bulb and full port side fin and a cut starboard side fin
RBF-F	Rudder with a bulb and full fins on both the port and starboard sides
Rn	Reynolds Number

SPIV	Stereo-Particle Image Velocimetry
A	Wave Amplitude
B	Breadth over Waterline
D	Depth of Ship
J	Propeller advance coefficient
KG	Vertical Center of Gravity
K_{yy}	Radius of Gyration around y-axis
K_T	Thrust coefficient
K_Q	Torque coefficient
L/L _{PP}	Length between Perpendiculars
T	Ship draft
T	Propeller thrust
T_e	Encounter Wave Period
Q	Propeller torque
V_s	Ship Speed
Z	Heave
∇	Displaced Volume of Ship

θ	Pitch
$1-w$	Effective Wake
η_H	Hull efficiency
λ	Wavelength

LIST OF TABLES

Table 1-1 Test conditions.....	3
Table 2-1 KVLCC2 model Ship particulars.	24
Table 2-2 Measured parameters, their coordinates and devices used for measurement.	33
Table 3-1 Mean values for thrust, torque, effective wake and thrust deduction factor.	38
Table 3-2 The summary of forces and self-propulsion factors.	62

LIST OF FIGURES

Figure 2-1 Osaka University Towing Tank.	20
Figure 2-2 (a) Swing table, (b) Pitch free gimbal, heaving rod and light weight carriage.	21
Figure 2-3 The SPIV system.	22
Figure 2-4 Motions and force measurement experimental set up.	23
Figure 2-5 The KVLCC2 body plan and hull form in fully-loaded condition.	25
Figure 2-6 MOERI Propeller models.	25
Figure 2-7 The coordinate system.	26
Figure 2-8 The Osaka University SPIV system components.	28
Figure 2-9 The SPIV working principle.	30
Figure 2-10 The principle of cross-correlation of SPIV system.	30
Figure 2-11 The SPIV experiment set up.	31
Figure 2-12 SPIV phase synchronization for waves.	32
Figure 3-1 Time histories for wave elevation, X-force, heave, pitch and surge for $\lambda/L=1.1$, $A=3\text{cm}$ of a towed KVLCC2 model ship.	35
Figure 3-2 Time histories for wave elevation, X-force, heave, pitch and surge for $\lambda/L=1.1$, $A=3\text{cm}$ of a self-propelled KVLCC2 model ship.	36
Figure 3-3 Time histories for wave elevation, thrust and torque for $\lambda/L=1.1$, $A=3\text{cm}$ of a self-propelled KVLCC2 model ship.	37
Figure 3-4 Thrust time history for different wave amplitudes at $\lambda/L=1.1$	39
Figure 3-5 Torque time history for different wave amplitudes at $\lambda/L=1.1$	40
Figure 3-6 Effective wake time history for different wave amplitudes at $\lambda/L=1.1$	40
Figure 3-7 Comparison of thrust harmonic components.	41

Figure 3-8 Thrust time history for different wave amplitudes at $\lambda/L=1.6$.	42
Figure 3-9 Torque time history for different wave amplitudes at $\lambda/L=1.6$.	43
Figure 3-10 Effective wake time history for different wave amplitudes at $\lambda/L=1.6$.	43
Figure 3-11 Thrust time history for different wave amplitudes at $\lambda/L=2.0$.	44
Figure 3-12 Torque time history for different wave amplitudes at $\lambda/L=2.0$.	45
Figure 3-13 Effective wake time history for different wave amplitudes at $\lambda/L=2.0$.	45
Figure 3-14 Mean values for thrust.	46
Figure 3-15 1st harmonic values for thrust.	47
Figure 3-16 Mean values for torque.	48
Figure 3-17 1st harmonic values for torque.	48
Figure 3-18 Mean values for effective wake.	49
Figure 3-19 1st harmonic values for effective wake.	49
Figure 3-20 Heave motion time history at different wave amplitudes for $\lambda/L=1.1$.	50
Figure 3-21 Heave motion time history at different wave amplitudes for $\lambda/L=1.6$.	51
Figure 3-22 Heave motion time history at different wave amplitudes for $\lambda/L=2.0$.	51
Figure 3-23 1st harmonic amplitudes for Heave motion.	52
Figure 3-24 1st harmonic phases for Heave motion.	53
Figure 3-25 Pitch motion time history at different wave amplitudes for $\lambda/L=1.1$.	54
Figure 3-26 Pitch motion time history at different wave amplitudes for $\lambda/L=1.6$.	54
Figure 3-27 Pitch motion time history at different wave amplitudes for $\lambda/L=2.0$.	55
Figure 3-28 1 st Harmonic amplitudes for Pitch motion.	56
Figure 3-29 1 st Harmonic phases for Pitch motion.	56
Figure 3-30 Added resistance vs. square of wave amplitude, A^2 at different λ/L .	57

Figure 3-31 The added resistance coefficient vs. A/L at different λ/L .	58
Figure 3-32 The time histories for wave elevation, X-force, heave, pitch and surge motions for $\lambda/L=1.1$ of a self-propelled KVLCC2 model ship.	60
Figure 3-33 The time histories for thrust and torque for $\lambda/L=1.1$ of a self-propelled KVLCC2 model ship.	61
Figure 3-34 Thrust time histories for $\lambda/L=0.6$ for various rudders for one period.	64
Figure 3-35 Effective wake time histories for $\lambda/L=0.6$ for various rudders for one period.	65
Figure 3-36 Thrust time histories for $\lambda/L=1.1$ for various rudders for one period.	65
Figure 3-37 Effective wake time histories for $\lambda/L=1.1$ for various rudders for one period.	66
Figure 3-38 Thrust time histories for $\lambda/L=1.6$ for various rudders for one period.	66
Figure 3-39 Effective wake time histories for $\lambda/L=1.6$ for various rudders for one period.	67
Figure 3-40 Mean thrust values for various rudders at different wavelength conditions.	68
Figure 3-41 1 st harmonic thrust values for various rudders at different wavelength conditions.	68
Figure 3-42 Mean effective wake values for various rudders at different wavelength conditions.	69
Figure 3-43 1st harmonic effective wake values for various rudders at different wavelength conditions.	69
Figure 3-44 Time histories for heave, pitch and wave elevation at different stations for $\lambda/L=0.6$.	71
Figure 3-45 Time histories for heave, pitch and wave elevation at different stations for $\lambda/L=1.1$.	71
Figure 3-46 Time histories for heave, pitch and wave elevation at different stations for $\lambda/L=1.6$.	72

Figure 3-47 1 st harmonic RAOs for heave motion for various rudders.....	72
Figure 3-48 1st harmonic phases for heave motion for various rudders.....	73
Figure 3-49 1st harmonic RAOs for pitch motion for various rudders.....	73
Figure 3-50 1st harmonic phases for pitch motion for various rudders.....	74
Figure 4-1 Velocity distribution for calm water condition.	76
Figure 4-2 Phase-averaged velocity distribution at AP for $\lambda/L=1.1$, $A=0.75\text{cm}$; (a) 0° , (b) 90° (c) 180° and (d) 270°	78
Figure 4-3 Phase-averaged velocity distribution at AP for $\lambda/L=1.1$, $A=1.5\text{cm}$; (a) 0° , (b) 90° (c) 180° and (d) 270°	79
Figure 4-4 Phase-averaged velocity distribution at AP for $\lambda/L=1.1$, $A=3\text{cm}$; (a) 0° , (b) 90° (c) 180° and (d) 270°	80
Figure 4-5 Phase-averaged velocity distribution at AP for $\lambda/L=1.1$, $A=4.3\text{cm}$; (a) 0° , (b) 90° (c) 180° and (d) 270°	81
Figure 4-6 Thrust fluctuation and wave elevation for one period at $\lambda/L=1.1$, $A=3\text{cm}$	83
Figure 4-7 Thrust time history with its mean values for $\lambda/L=1.1$, at different wave amplitudes.	83
Figure 4-8 Phase-averaged velocity distribution at AP for $\lambda/L=1.6$, $A=1.5\text{cm}$; (a) 0° , (b) 90° (c) 180° and (d) 270°	85
Figure 4-9 Phase-averaged velocity distribution at AP for $\lambda/L=1.6$, $A=3.0\text{cm}$; (a) 0° , (b) 90° (c) 180° and (d) 270°	86
Figure 4-10 Phase-averaged velocity distribution at AP for $\lambda/L=1.6$, $A=4.3\text{cm}$; (a) 0° , (b) 90° (c) 180° and (d) 270°	87
Figure 4-11 Thrust fluctuation and wave elevation for one period at $\lambda/L=1.6$, $A=3\text{cm}$	89
Figure 4-12 Thrust time history for $\lambda/L=1.6$, at different wave amplitudes.	89

Figure 4-13 SPIV Measurement transverse planes.	91
Figure 4-14 The RBF-F system's port and starboard sides fins.	91
Figure 4-15 The RBF-F system and the normal rudder.	92
Figure 4-16 Phase averaged velocity distribution for calm water (a) without rudder, (b) normal rudder, (c) RBF-F system.	93
Figure 4-17 Wave elevation at various stations, motions, thrust and phases for SPIV measurement for $\lambda/L=0.6$	95
Figure 4-18 Wave elevation at various stations, motions, thrust and phases for SPIV measurement for $\lambda/L=1.1$	96
Figure 4-19 Wave elevation at various stations, motions, thrust and phases for SPIV measurement for $\lambda/L=1.6$	96
Figure 4-20 Phase averaged velocity distribution for (0°) for $\lambda/L=0.6$; (a) with normal rudder, no propeller, (b) normal rudder, (c) RBF-F system and (d)=(b)-(a).	98
Figure 4-21 Phase averaged velocity distribution for (90°) for $\lambda/L=0.6$; (a) with normal rudder, no propeller, (b) normal rudder, (c) RBF-F system and (d)=(b)-(a).	99
Figure 4-22 Phase averaged velocity distribution for (180°) for $\lambda/L=0.6$; (a) with normal rudder, no propeller, (b) normal rudder, (c) RBF-F system and (d)=(b)-(a).	100
Figure 4-23 Phase averaged velocity distribution for (270°) for $\lambda/L=0.6$; (a) with normal rudder, no propeller, (b) normal rudder, (c) RBF-F system and (d)=(b)-(a).	101
Figure 4-24 Phase averaged velocity distribution for (0°) for $\lambda/L=1.1$; (a) with normal rudder, no propeller, (b) normal rudder, (c) RBF-F system and (d)=(b)-(a).	103
Figure 4-25 Phase averaged velocity distribution for (60°) for $\lambda/L=1.1$; (a) with normal rudder, no propeller, (b) normal rudder, (c) RBF-F system and (d)=(b)-(a).	104

Figure 4-26 Phase averaged velocity distribution for (120°) for $\lambda/L=1.1$; (a) with normal rudder, no propeller, (b) normal rudder, (c) RBF-F system and (d)=(b)-(a).....	105
Figure 4-27 Phase averaged velocity distribution for (180°) for $\lambda/L=1.1$; (a) with normal rudder, no propeller, (b) normal rudder, (c) RBF-F system and (d)=(b)-(a).....	106
Figure 4-28 Phase averaged velocity distribution for (240°) for $\lambda/L=1.1$; (a) with normal rudder, no propeller, (b) normal rudder, (c) RBF-F system and (d)=(b)-(a).....	107
Figure 4-29 Phase averaged velocity distribution for (300°) for $\lambda/L=1.1$; (a) with normal rudder, no propeller, (b) normal rudder, (c) RBF-F system and (d)=(b)-(a).....	108
Figure 4-30 Phase averaged velocity distribution for (0°) for $\lambda/L=1.6$; (a) with normal rudder, no propeller, (b) normal rudder, (c) RBF-F system and (d)=(b)-(a).....	110
Figure 4-31 Phase averaged velocity distribution for (60°) for $\lambda/L=1.6$; (a) with normal rudder, no propeller, (b) normal rudder, (c) RBF-F system and (d)=(b)-(a).....	111
Figure 4-32 Phase averaged velocity distribution for (120°) for $\lambda/L=1.6$; (a) with normal rudder, no propeller, (b) normal rudder, (c) RBF-F system and (d)=(b)-(a).....	112
Figure 4-33 Phase averaged velocity distribution for (180°) for $\lambda/L=1.6$; (a) with normal rudder, no propeller, (b) normal rudder, (c) RBF-F system and (d)=(b)-(a).....	113
Figure 4-34 Phase averaged velocity distribution for (240°) for $\lambda/L=1.6$; (a) with normal rudder, no propeller, (b) normal rudder, (c) RBF-F system and (d)=(b)-(a).....	114
Figure 4-35 Phase averaged velocity distribution for (300°) for $\lambda/L=1.6$; (a) with normal rudder, no propeller, (b) normal rudder, (c) RBF-F system and (d)=(b)-(a).....	115
Figure 4-36 Phase averaged velocity distribution for (0°) for $\lambda/L=0.6$, for without rudder, normal rudder and RBF-F system.	118

Figure 4-37 Phase averaged velocity distribution for (90°) for $\lambda/L=0.6$, for without rudder, normal rudder and RBF-F system.	119
Figure 4-38 Phase averaged velocity distribution for (180°) for $\lambda/L=0.6$, for without rudder, normal rudder and RBF-F system.	120
Figure 4-39 Phase averaged velocity distribution for (270°) for $\lambda/L=0.6$, for without rudder, normal rudder and RBF-F system.	121
Figure 4-40 Phase averaged velocity distribution for (0°) for $\lambda/L=1.1$; (a)without rudder, (b) normal rudder and (c) RBF-F system.	124
Figure 4-41 Phase averaged velocity distribution for (60°) for $\lambda/L=1.1$; (a)without rudder, (b) normal rudder and (c) RBF-F system.	125
Figure 4-42 Phase averaged velocity distribution for (120°) for $\lambda/L=1.1$; (a)without rudder, (b) normal rudder and (c) RBF-F system.	126
Figure 4-43 Phase averaged velocity distribution for (180°) for $\lambda/L=1.1$; (a)without rudder, (b) normal rudder and (c) RBF-F system.	127
Figure 4-44 Phase averaged velocity distribution for (240°) for $\lambda/L=1.1$; (a)without rudder, (b) normal rudder and (c) RBF-F system.	128
Figure 4-45 Phase averaged velocity distribution for (300°) for $\lambda/L=1.1$; (a)without rudder, (b) normal rudder and (c) RBF-F system.	129
Figure 4-46 Phase averaged velocity distribution for (0°) for $\lambda/L=1.6$; (a)without rudder, (b) normal rudder and (c) RBF-F system.	132
Figure 4-47 Phase averaged velocity distribution for (60°) for $\lambda/L=1.6$; (a)without rudder, (b) normal rudder and (c) RBF-F system.	133

Figure 4-48 Phase averaged velocity distribution for (120°) for $\lambda/L=1.6$; (a)without rudder, (b) normal rudder and (c) RBF-F system. 134

Figure 4-49 Phase averaged velocity distribution for (180°) for $\lambda/L=1.6$; (a)without rudder, (b) normal rudder and (c) RBF-F system. 135

Figure 4-50 Phase averaged velocity distribution for (240°) for $\lambda/L=1.6$; (a)without rudder, (b) normal rudder and (c) RBF-F system. 136

Figure 4-51 Phase averaged velocity distribution for (300°) for $\lambda/L=1.6$; (a)without rudder, (b) normal rudder and (c) RBF-F system. 137

CHAPTER 1: INTRODUCTION

1.1 Background

In the recent times the world has experienced worse climatic changes as exhibited by deadly floods in some parts of the world, extreme weather conditions and rising in sea levels. These climatic changes are mostly as a result of global warming. Global warming is mainly caused by anthropogenic activities that result in releasing of huge amounts of greenhouse gas (GHG) emissions into the atmosphere. One of the industries that contribute to the GHG emissions is the shipping industry which is relied upon mostly to transport goods across the world by sea. For instance, the International Maritime Organization (IMO) estimates that the GHG emissions of total shipping increased by 9.6% from 977 million tonnes in 2012 to 1,076 million tonnes in 2018. For the same period, the shipping industry's share in the worldwide anthropogenic emissions increased from 2.76% in 2012 to 2.89% in 2018 (IMO, 2020). In order to curb the production of these GHG emissions from the shipping industry, the IMO has stipulated guidelines that regulate the amount of GHG emissions from ships. These are clearly outlined in the regulations of the IMO's Marine Environment Protection Committee (MEPC) that are geared towards improving the ships' energy efficiency. The two main measures under these regulations are the Energy Efficiency Design Index (EEDI) for new ships, and the Ship Energy Efficiency Management Plan (SEEMP) for both new and existing ships respectively.

In order to achieve the EEDI requirements, the propulsive performance including engine characteristics for ships in waves should be improved. Therefore, the topic of energy saving has become very important in the recent times, and various ESDs have been developed. However, most of these studies are conducted in calm water, and experiments on improving the propulsion performance by ESDs are rarely conducted in waves. Consequently, the fundamental

understanding of the hull-propeller-ESD interaction for ships in waves is insufficient because the viscous inflow velocity into the propeller plane in waves has not been done sufficiently. In order to understand the effect of ESDs on motions, forces and flow field around the stern of ships in waves, it is important to carry out studies for with and without ESDs in waves. This is why our research group which is called the Hull Form Design Sub-Area in the department of Naval Architecture and Ocean Engineering, Osaka University has conducted these kind of studies for KRISO Very Large Crude-oil Carrier2 (KVLCC2) and KRISO Container Ship (KCS) by Computational Fluid Dynamics (CFD) and Experimental Fluid Dynamics (EFD) methods for many years. For example, in one of our research group's previous studies, Tokgoz et al., (2015), CFD could predict well the thrust fluctuations for one wave amplitude but a nonlinear response was observed. Therefore, the relation between the thrust time history and the flow field were discussed, and it was noted that the vertical relative motion between the propeller disk and the bilge vortices were very important to explain the thrust fluctuations. So it seems that the wave amplitude has a lot of effect on the thrust fluctuation and averaged wake. Therefore, in this study, the effect of the wave amplitude on motions, forces and flow field was investigated first for a self-propelled KVLCC2 model tanker in regular head waves. Then energy-saving rudders were introduced so as to understand the hull-propeller-ESD interactions and their performance in waves.

1.2 Objectives

The main objective of this work was to investigate the effects of the wave amplitude and energy saving devices (ESDs) on the motions, forces and flow field around the stern of a self-propelled KVLCC2 model tanker in regular head waves by EFD method.

1.3 Test Conditions

The design Froude number, $Fr=0.142$ (0.795m/s) was used in these experiments. For the wave amplitude dependency study, three long wavelengths at various amplitudes were used whereas for the ESDs effect study the wave conditions were; one shorter wavelength ($\lambda/L=0.6$) and two longer wavelengths ($\lambda/L=1.1$ and 1.6) and an amplitude, A of 3cm. The summary of these conditions is as shown in Table 1-1. During the wave amplitude dependency study, the Reynolds number for the motions and force experiment was about $Rn=1.9141 \times 10^6$, and for the SPIV experiment it was about $Rn=2.2519 \times 10^6$.

Table 1-1 Test conditions.

Wave amplitude effect		
Test	λ/L	A(cm)
Motions and Force Measurement	1.1	0.75
		1.5
	1.6	3
	2	4 4.3
SPIV Measurement	1.1	0.75
		1.5
		3
		4.3
	1.6	1.5
		3 4.3
ESDs effect		
Test	λ/L	A(cm)
Motions and Force Measurement	0.6	3
	0.85	
	1.1	
	1.35	
	1.6	
SPIV Measurement	0.6	3
	1.1	
	1.6	

Whereas, during the ESDs effect study the Reynolds number was about $Rn=2.6847 \times 10^6$ for the motions and force measurement experiment, and about $Rn= 2.6159 \times 10^6$ and $Rn=2.8179 \times 10^6$ for the SPIV measurement experiments.

1.4 Literature Review

1.4.1 The effect of the wave amplitude

A resistance and self-propulsion experiment for a single screw high-speed container ship in regular and irregular waves was carried out by Nakamura et al., (1975). They studied the effects of propeller diameter and wave height on ship motions, forces and self-propulsion factors. The inflow velocity into the propeller disk, in regular head waves, was also measured using a ring-type wake meter so as to investigate the propeller performance. They concluded that the time averaged mean values of effective wake were larger in waves than in still water due to the effect of ship motions. They also added that the fluctuations of propeller thrust and torque were mainly caused by the fluctuation of axial inflow velocity into the propeller disk.

An experiment in regular waves with $\lambda/L=0.5$ and 1 in which a ship was towed both in heave and pitch free condition and motion fixed condition was conducted by Tsukada et al., (1997). They also run the ship with forced pitch motion in still water. They presented their results by showing the change of wake fraction and mean circulation in one encounter period. From this, they showed that the nominal wake increases in regular waves especially in longer waves where the ship vertical motions are large.

Ohashi et al., (2013) used CFD-SURF to do unsteady RANS simulations of flows around KVLCC2 tanker model ship with motions in regular waves. In their study, they observed that the vortices at the propeller plane in long waves were induced by the ship motions, and that the

increase of the time averaged nominal wake coefficient was as a result of the interaction between the waves and ship motions.

Sadat-Hosseini et al., (2013) studied motions and added resistance of KVLCC2 at $Fr=0.142$ and 0.25 with free and fixed surge in short and long waves using URANS, and validated their results against EFD data for $Fr=0.142$. In addition, they investigated the wake field and showed that waves have an influence on the wake field shape. They observed that the wake fields are compressed by higher velocity from the outer flow in both y and z directions when the ship stern is situated on the wave crest, and then they are extended when it is in the wave trough.

A study on the added resistance, motions and wake field at the propeller plane for KVLCC2 tanker model in fully-loaded and ballast conditions in head waves was conducted by Wu, (2013) using CFDSHIP-IOWA V4.5. He observed two types of vortices in the wake: the bilge vortex originating from the hull body and shedding into the propeller plane, and a low speed area vortex induced by vertical stern motion and shedding around the shaft. Furthermore, he pointed out that when the ship moves down there are counter-rotating vortices that occur above the shaft and the boundary layer becomes thicker in this region.

Kim, (2014) carried out a study on motions, added resistance and velocity field near the propeller plane for KVLCC2 model tanker under fully-loaded and ballast conditions at $Fr=0.142$ in regular head waves at one wave height. SPIV system was used to measure the velocity field near the propeller so as to investigate the effects of waves and ship motions on the propeller inflow distribution. He concluded that in long waves, the vertical ship motions are large and the relative gradient between the ship and waves is large. He also observed that the orbital motion has an effect

on the velocity distribution at the propeller plane, and that the low velocity region, due to bilge vortices, moves vertically relative to the propeller disk.

Wu et al., (2014) elaborately investigated the added resistance by using URANS for KVLCC2 tanker in ballast condition advancing at design $Fr=0.142$ in regular head waves, and validated their results against experimental data. In addition, they analyzed in detail the wake field and the periodic change of vortices including the bilge and dummy hub vortices. They showed that the bilge vortex moves relative to the ship stern motion, and the low speed area with a secondary vortex which is induced by the dummy hub movement. Moreover, they observed that the wake field becomes narrower or wider due to the higher or lower orbital velocity.

The flow field around a self-propelled KVLCC2 model tanker ship at design $Fr=0.142$ in regular head waves of $\lambda/L = 0.6, 1.1$ and 1.6 at a wave amplitude, $A=3\text{cm}$ was studied by Tokgoz et al., (2015) using CFD simulations and SPIV measurement. The experiments were done with 3DOF motion (free to heave, pitch and surge) and simulations done by CFDShip-Iowa V4.5 for 2DOF motion (free to heave and pitch but fixed surge motion). They analyzed the ship wake behavior in detail and its effect on the propeller performance, and observed a nonlinear response in thrust fluctuation especially in long waves. This was attributed to the movement of bilge vortices relative to the ship motions, and the pressure gradient between the inner and outer boundary layer.

Kim et al., (2017), numerically predicted the ship motions and added resistance at various ship speeds and wave steepnesses for KVLCC2 model ship in regular head waves using URANS and 3-D potential flow methods. They conducted the simulations in a wide range of wave conditions at various ship speeds (stationary, operating and design). In their investigation of the relationship between the added resistance and wave steepness, at the design ship speed especially

around the resonance period, they concluded that the added resistance is almost proportional to the square of the wave height.

Recently, Hossain et al., (2018) studied motions, added resistance and wake field for KRISO Container Ship (KCS) model in regular head waves using CFD and EFD methods. For CFD, the viscous flow simulations were done by CFDShip-Iowa V4.5 and for experiments the SPIV system was used for flow field measurement at the propeller plane. In one period, the bilge vortices were observed at the side or above the propeller dummy boss and that it never moves below it. This was attributed to the fine shape of KCS at the stern where the wide transom stern is almost like a T shape hence low mass at the stern compared to KVLCC2.

1.4.2 The effect of energy saving devices (ESDs)

The energy saving devices (ESDs) are categorized into three major classes. Those that are installed upstream of the propeller, those that are installed at the propeller station and those that are installed downstream of the propeller (Carlton, 2012). The main goal of using these ESDs is to improve the inflow into the propeller, and to recover the lost energy in the ship hull wake and the propeller slipstream.

The topic of ESDs has been studied by many researchers in order to improve the propulsion efficiency of the ships at sea. However, most of the studies have been done in calm water and rarely done in waves. Some of the previous studies on ESDs are highlighted in this sub-section as follows.

a) Air Lubrication systems

A resistance and self-propulsion experiment was conducted by Jang et al., (2014) for a 66K DWT bulk carrier in the Samsung Ship Model Basin (SSMB) with an air lubrication on the hull

bottom so as to estimate its energy saving. They measured the local frictional drag at various flow rates of the injected air and reported a net power saving of approximately 5-6%. The Mitsubishi Air Lubrication System (MALS) has been developed and designed with an aim of energy-saving in ships by reducing the frictional resistance of the ship (Kawakita et al., 2015). They utilized CFD-based technologies to measure the air bubble distribution around the hull as well as the frictional drag reduction effect and verified the results with actual ship tests. From their sea trial test results, obtained from a ship equipped with MALS, they reported an energy saving of about 10%.

b) Wake Equalizing Ducts, Pre-Swirl ducts and Stators

These are ESDs that are fitted upstream of the propeller so as to improve the flow into the propeller. Çelik (2007) numerically studied the effect of a wake equalizing duct (WED) on the propulsion performance of a chemical tanker using the Reynolds Averaged Navier-Stokes (RANS) method and reported a maximum gain of about 10% propulsive efficiency as well as an additional positive thrust with a suitable WED design. Mewis & Guiard (2011) have explained the developments of the Mewis Duct (MD), as a new ESD, and conducted tests at both model scale and full scale using both CFD and experiments. They obtained an 8% reduction on the required power with a mean of about 6.5% from over 35 tests. They also reported a significant reduction on vibration excitation by reducing the pressure pulses by about 80%. The Becker Twisted Fins (BTF) was used, as a new ESD, by Guiard et al., (2013) on ten 23-knot 7100 TEU container vessels. They conducted model tests for the optimized duct at a range of speeds and draughts, and reported a power saving of between 3.5% and 4.2%.

The working principles of ESDs including the Pre-Duct with inner Stator (PDS), Pre-Swirl Stator (PSS) and Hub Fins (HFs) have been investigated by Dang et al., (2012) using both PIV and

CFD. By comparing the kinetic energy in the wake for the selected cases with and without PDS and HFs, they were able to explain the effect of these ESDs in recovering the kinetic energy losses. They reported about 19% reduction on total kinetic energy in the wake by installing a PDS upstream of the propeller and a further 6% reduction by installing the HFs behind the propeller.

Kawakita et al., (2012) conducted a study on cavitation occurrence around the marine propellers that were equipped with reaction fins and stator fins as energy saving devices using CFD. They considered the hull, propeller, rudder and ESDs as one unit and compared the flow field and pressure distribution around the propeller with and without ESDs, and explained the effect of ESDs. A numerical and experimental study on conventional and unconventional pre-swirl duct for a VLCC (Very Large Crude-oil Carrier) was done by Shin et al., (2013) to establish and compare their effects on the propeller performance. They conducted cavitation test for the optimum configuration of the unconventional half circular duct which gave smoother blade surface and tip vortex cavitation as compared to the without duct condition. They also reported that the half circular duct homogenized the inflow into the propeller, and approximately 5.4% power saving was realized at various speed ranges.

The influence of the WED on the cavitation performance of the propeller has been analyzed by Martinas (2015). He concluded that there is no influence on the cavitation of the propeller from the WED. Kim et al., (2015) carried out a computational analysis for two energy saving devices on a low-speed, full 317K VLCC ship; wake adapted flow control fins with and without duct (WAFon-D and WAFon respectively), and compared the results with the without ESD condition. They validated the speed performances with model tests, and concluded that both ESDs improved the hull efficiency, η_H as well as the propulsive efficiency, η_D by enhancing both thrust deduction

fraction, t and effective wake fraction, w . They also reported that the WAFon reduced the delivered power by 3% whereas the WAFon-D reduced it by 6.1%.

A new method whose objective was to reduce the computational time and resources that are required for prediction of full scale wake from model scale with a pre-swirl stator (PSS) and a rudder was proposed by Park et al., (2015). Unlike the existing methods i.e. the ITTC 1978, ITTC 1999 and the full scale CFD computations, in which the inviscid wake component is calculated empirically, their new method accurately calculates it from the solution of the Euler equations which considers the wake improvement by ESD. They established that the PSS changed the cross flow and hence production of some thrust. Their proposed method also gave good quasi-propulsive efficiency value as compared to the existing methods. The hydrodynamic design of a pre-swirl stator (PSS), with a radially variable pitch, which was paired with a conventional propeller is described by Saettone et al., (2016). They investigated the designs and configurations for the propeller and stator in diverse operating conditions using the vortex-lattice method and CFD-based approach to describe the influence of the stator on the propeller. IHI Marine United Inc. (IHIMU) employed a Semicircular Duct in full scale ships and confirmed its energy-saving principles using both CFD and Particle Imaging Velocimetry (PIV) methods (Inukai et al., 2017).

Nowruzi & Najafi (2019) studied the effects of different pre-swirl ducts (Mewis duct, Becker twisted fins and unconventional half circular duct) on propulsion performance of series 60 ship. They compared the results for thrust and torque coefficients, hydrodynamic efficiency components as well as the wake and pressure distribution on the propeller with no pre-swirl duct condition. Among their conclusions, they found that the hub vortex was largest for without pre-swirl duct and smallest for with Mewis duct.

The effects of a fan-shaped Mewis duct on the propulsion performance of a 38,000 t bulk cargo ship fitted with a three-blade propeller were studied by Chang et al., (2019) numerically using STAR-CCM+ software. They investigated the effect of various parameters of the duct including the distance of the duct from the propeller, the radius of the trailing edge of the duct and the angle of attack of the inner fins of the duct on the propulsion performance of the ship. They also calculated the axial mean velocity, tangential mean velocity, propeller thrust and torque as well as the efficiency. They observed that after the installation of the duct the efficiency, thrust and torque increased but this caused an increase in the total resistance of the ship. Therefore, they suggested that to achieve the energy saving effect from the duct, there is need to optimize the parameters of the duct.

A Simulation-Based Design Optimization (SBDO) approach for the design of an energy saving device has been explained by Furgas et al., (2020) with the concept of the wake equalizing duct (WED). They varied the geometric parameters of the WED and came up with optimal designs for which they analyzed the performance. They reported that all of the optimized WEDs provided some energy saving even in off-design conditions. The wake flow fields of a ducted propeller have been studied by Xu et al., (2020) for with and without pre-swirl stator by numerical simulations. They analyzed the velocities and pressure fluctuations at various positions from the propeller. They concluded that the pre-swirl stator could improve the near propeller blade velocity as well as the surface pressure distribution near the blade.

c) Contra-rotating propellers (CRP)

Ghassemi (2009) analyzed the hydrodynamic performance of coaxial contra-rotating propellers (CCRP) for large ships (bulk carrier and VLCC) numerically using boundary element method (BEM) and compared the results with experiments. He established that the CCRP system

could raise the propeller efficiency by about 2-3% at the design condition. The characteristics of effective wake for a ship equipped with a CRP system were analyzed by Inukai & Ochi (2009) experimentally and theoretically, as well as by conducting sea trials. They reported an improvement of about 10% in the effective wake by the CRP system as compared to the conventional propeller. A study on the design and performance of the CRP system was conducted by Min et al., (2009) on a full scale 8,600 TEU container ship and they reported that the CRP system could significantly improve the propulsion efficiency as well as fuel consumption.

Inukai (2011) explained the hydrodynamic performance of the IHI Marine United Inc.'s CRP Electric Propulsion System (IHIMU-CEPS), which was designed to improve the fuel consumption of ships. From the results of one vessel, a chemical tanker fitted with this system, the fuel consumption saving of about 20% was reported and this was attributed to the wake gain achieved by the CRP system. Ghassemi & Taherinasab (2013) carried out a numerical study on the hydrodynamic performance of the CRP system for a high-speed vehicle using boundary element method. They analyzed the hydrodynamic coefficients, thrust and torque as well as the pressure distribution and induced velocities between the propellers and behind the aft propeller. Their results show that the CRP system improves the thrust and minimizes the torque. They also pointed out that since the propellers share the load, unlike in a single propeller, the pressure distribution on the blades is more uniform and this lowers the chances of propeller cavitation. Inukai et al., (2014) used a simplified surface panel method known as "Source and Quasi-Continuous vortex lattice Method (SQCM)" for predicting propeller performance by taking into consideration fully wake deformation and reported good agreement of their results with experiment.

The wake evolution of a CRP system was analyzed by Paik et al., (2015) using RANS-based CFD simulations and SPIV flow measurements so as to explain the effect of the CRP system on the flow field. They measured the wake in three transverse stations; one station between the fore and aft propeller, and two stations downstream of the aft propeller, and analyzed the velocity field as well as the axial vorticity. Additionally, they also analyzed the axial vorticity on longitudinal plane around the propeller's shaft. They pointed out that the aft propeller recovers the lost rotational energy of the fore propeller by its opposite direction of rotation which balances the propeller loads in both port and starboard sides.

d) Propeller Boss Cap Fins (PBCFs)

The PBCFs are post-swirl ESDs that are fitted on the propeller boss cap of already existing ships so as to improve their propulsion efficiency by breaking down the hub vortex. Why use the PBCFs? It gives a fuel oil saving of up to 5%, simple to construct and install, it is suitable both for new and existing vessels, and the return on investment period is short (*MOL Tech / MOL Techno-Trade, Ltd.*). Its cost of installation is lower compared to other ESDs since it only requires the modification of the propeller boss cap (Seo et al., 2016).

Nojiri et al., (2011) conducted a study on energy saving effect of PBCFs on four-, five- and six-bladed propellers. They conducted reverse propeller open test (rev POT) experiments and CFD simulations to measure the thrust coefficient, K_T , and torque coefficient, K_Q . Open water efficiency and the velocity distribution around the propeller boss cap were also measured. They reported that K_T increased while K_Q decreased and hence the efficiency increased by about 1.5% for the case with PBCFs. They also explained that the damming effect of the PBCFs prevents the vortex flow from the root of the propeller blade trailing edge from converging into a strong hub vortex.

Kawamura et al., (2013) compared the effect of the PBCFs between model scale and full-scale using commercial CFD software Fluent version 6.3, and explained the causes of the difference. From their results, the energy saving effect of the PBCFs in full-scale was larger than that at model scale. They pointed out that the Reynolds number and the flow condition have major influence on this difference.

Seo et al., (2016) studied the influence of design parameter variations for the PBCFs on global force and wake fields of a propeller and PBCF. They paid attention to the hub vortex dynamics and reported that the PBCFs effectively prevented the generation of hub vortex, and efficiency gains were mainly achieved by the vanishing of the low pressure region behind the propeller boss cap. Also, they noted that the net thrust of the propeller system increased by about 1.6% regardless of advance coefficient, J conditions. Mizzi et al., (2017) conducted a design optimization study of the PBCFs using CFD-based RANS method so as to analyze the impact of the PBCFs on the propeller efficiency. They reported a net efficiency improvement of 1.3% for the optimal case as well as a decrease in the hub vortex.

Kimura et al., (2018) used SPIV measurements and CFD computations to investigate the full scale performance of the PBCFs. They concluded that the strong hub vortex behind the propeller boss as well as the underwater radiation noise disappeared when using the PBCFs. They also used the PBCFs in combination with the rudder-bulb-fin and duct, and observed that the effect of energy saving increased. However, from the study of Sun et al., (2016), in which they studied the influence of the PBCFs on the hydrodynamic performance of rudders, they concluded that the installation of the PBCFs causes an increase in the resistance of the rudders thereby reducing their energy-saving effect. For instance, from their cavitation experiment results at advance ratio, $J=0.8$, the PBCFs increased the propeller efficiency by 1.47%. On the other hand, their numerical results

showed that after installation of the ordinary and twisted rudders the efficiency reduced to 1.08% and 1.16% respectively.

Xu & Wan (2018) investigated the scale effect for the PBCFs at different advance ratios using Improved Delayed Detached Eddy Simulation (IDDES) and sliding mesh technique. They presented their results for the relative change of thrust coefficient, torque coefficient and propulsion efficiency, and observed that the thrust increased a little bit while torque decreased very much. They concluded that the major determinant of propulsion improvement, for the propeller with PBCFs, is the decreasing of torque. They reported a gain in propeller efficiency of 1.18% at model scale and 2.02% at full scale at $J=0.2$ for propeller with PBCFs. They also stated that the low pressure area on the propeller cap is eliminated by the PBCFs hence improving the propeller thrust.

The combined effect of the PBCFs and propeller duct on the propeller efficiency was studied numerically by Majumder et al., (2020). They also did a comparative study with propeller and duct without PBCFs. They realized that the propeller with duct and without PBCFs had a higher propeller efficiency compared to the propeller with PBCFs. They also carried out a detailed flow field analysis at various stations and observed that PBCFs along with the duct significantly reduced the tangential flow velocity and this is evidence of destruction of the hub vortex.

e) Rudders

An energy-saving rudder is a type of ESD that is used downstream of the propeller so as to improve the propulsion efficiency by improving the wake field and attenuating the hub vortex. It can be used alone or in combination with other ESDs. Rudders with a bulb and fins can also gain additional thrust for the ship by utilizing the rotational flow downstream of the propeller. Many

researchers have conducted numerical and experimental studies on the rudder and bulb with fins as an ESD and the relevant ones are captured in this work.

The location of the rudder with respect to the propeller has an influence on a ship's propulsion performance (Reichel, 2009). He experimentally investigated the influence of the rudder location on the propulsive characteristics of a single-screw container ship using six types of rudders at three various locations (59%, 65% and 71% of propeller diameter). He established that the best position for the rudder to achieve the best propulsive efficiency, for all tested ship velocities, is closest to the propeller.

The hydrodynamic characteristics of an X-twisted rudder for a large container ship were numerically and experimentally studied by Ahn et al., (2012). They compared the results of ship performance and cavitation for X-twisted rudder with those for the semi-balanced rudder. They reported that X-twisted rudder improved the ship speed performance and overall maneuverability as well as reduction of cavitation as compared to the semi-balanced rudder.

Kim et al., (2014) numerically studied the performance of three types of twisted rudders; a z-twisted rudder, a z-twisted rudder with a bulb and a z-twisted rudder with bulb and fin, and compared the results with those for the horn-type rudder. They deduced that the z-twisted rudder improved the propulsive efficiency by 2.35% through a reduction in the thrust deduction fraction and an increase in the hull efficiency. The fins on the rudder bulb raised the thrust and effective wake as well and hence raising the propulsive efficiency to 2.95%.

The development of the "Ultimate Rudder" using fiber reinforced plastics has been studied by Okada et al., (2015) and its optimization done using CFD. Two version of the Ultimate Rudder were employed; one with a larger bulb diameter and the other with a smaller bulb diameter. Their

performances were compared with those of the normal rudder and conventional rudder bulb. Their results showed that the Ultimate Rudders improved the self-propulsion factors (1-t, 1-w and efficiency) as compared to the other rudders. The efficiency increased from 4.9 to 5.4% for Ultimate Rudder. From the flow field analysis, the conventional rudder bulb and the Ultimate Rudders reduced the vortex strength at the rear of the propeller as compared to the normal rudder. A study on the scale effects for ESDs on the propulsion efficiency of a ship fitted with a rudder with a bulb and fin has been studied by Hai-Long et al., (2016) using CFD. They validated their results with experimental results. They noted that the energy saving at model scale was about twice that at full scale (model scale energy saving was 4.85% while that at full scale was 2.28%).

The energy saving principles of a “Gate rudder” on a large bulk carrier were explored experimentally and numerically by Sasaki et al., (2016). Their results show that the Gate rudder has a possible energy saving of up to 7-8% and the return on investment is 0.37-0.9 year based on the conventional powering methods. Naing et al., (2016) carried out a viscous flow simulation for KVLCC2 model tanker using a new simple body-force propeller model for with and without rudder conditions. The competency of this method was compared with other body-force models as well as the real propeller computation. They concluded that this model could give results that compare well with other models and that it is competent even though it is simple.

He & Kinnas (2017) carried out a study on the unsteady interaction between the propeller and rudder using a numerical approach based on potential flow method. They used induced velocities to evaluate the interaction between them. They also applied an unsteady scheme as well as the time-averaged scheme so as to predict the rudder performance. They found out that the unsteady scheme predicted smaller lift coefficients than the time-averaged scheme. They attributed this to the wake/rudder interaction and the viscous model that was adopted in the unsteady scheme.

Karim & Naz (2017) studied the flow field around a ship hull together with the self-propulsion factors at various rudder locations. They concluded that the effect of the rudder decreases with an increase in the rudder's longitudinal distance from the propeller.

Liu et al., (2017) compared the energy efficiency performance between a twisted rudder and an ordinary spade rudder in self-propulsion condition by numerical simulations using the naoe-FOAM-SJTU solver. They compared their results with those of experiments, and showed that the twisted rudder increased the hull efficiency by 2.4% through a reduction in the thrust deduction fraction of 25.8% and causing the wake fraction to rise by 1.8%. The delivered power was also reduced by 3.9%.

The characteristics of an Ultimate rudder and normal rudder have been calculated by Tendou et al., (2017) using CFD and their results compared. These included the lift, drag and the steering torque coefficient at the model scale. They realized that the steering torque coefficient of the Ultimate rudder was higher than the one for the normal rudder for steering angles less than 20 degrees. They also observed that the steering torque coefficient was influenced by the clearance between the propeller cap and the rudder bulb. Truong et al., (2017) conducted an EFD and CFD study on the performance of the rudder-bulb-fin (RBF) system for KVLCC2 model tanker in calm water. They carried out an optimization study on the angle of attack (AOA) for the fins to find out the best combination that gives the best energy saving effect. They found out that 0 degree for the port side fin and -1 degrees for the starboard side fin gives the best energy saving effect. They also concluded that the RBF system could reduce the total resistance by about 2.3% compared to the normal rudder.

Su et al., (2020) carried out a numerical and experimental study on a 25m-long ore carrier model to study the performance of the pre-swirl stator and rudder bulb. Numerical simulation was

conducted by Unsteady Reynolds-Averaged Navier Stokes (URANS) method while self-propulsion experiments were conducted at sea. They analyzed the wake field and pressure distribution at stern region in details. They reported an energy saving of 3% and a decrease in the strength of the hub vortex. They also noted that the turbulent kinetic energy before and after the propeller was decreased by the ESDs thereby increasing the propeller's energy utilization rate.

A new type of ESD and maneuvering device, "Gate rudder", and its effects on the ship performance is studied by Tacar et al., (2020) by both experiments and CFD. They conducted model tests for two different scales of models (2m and 5m-long models) of the same 2400GT container ship fitted with a Gate Rudder system (GRS) and a conventional rudder, and compared the results of ship performance. They realized that the GRS considerably reduced the ship's brake power requirements as compared to the conventional rudder. Sasaki et al., (2020) investigated the scale effects on the powering performance of the GRS in order to solve the discrepancies that were noticed in the power-speed data between the subject ship (2400 GT container ship) fitted with GRS and her sister ship fitted with a conventional flap rudder. They proposed scale effect corrections on the drag and lift characteristics of the GRS and this improved the results.

CHAPTER 2: FACILITIES, EQUIPMENT AND EXPERIMENTS

2.1 Facilities and Equipment

2.1.1 Towing Tank

The experiments were conducted at the Osaka University towing tank whose picture is shown in Figure 2-1. The towing tank is 100m long, 7.8m wide and 4.35m deep. It is equipped with a drive carriage which is 7.4m long, 7.8m wide and 6.4m high with a speed range of 0.01 to 3.5m/s which is used for towing the model ship and the SPIV system during experiments. It also has a plunger-type wave generator which is used to generate both regular and irregular waves of up to 500mm wave height and 0.5 to 15m wavelengths. The towing tank is also equipped with a wave dampening beach which is raised during experiment runs and lowered immediately after runs so as to dampen the waves in preparation for the next run. Usually, an interval of about fifteen to thirty minutes is enough to do subsequent runs and this is confirmed by inspecting the water surface visually. Also, the towing tank has a small fixed grid beach at the rear part for the purpose of absorbing waves.

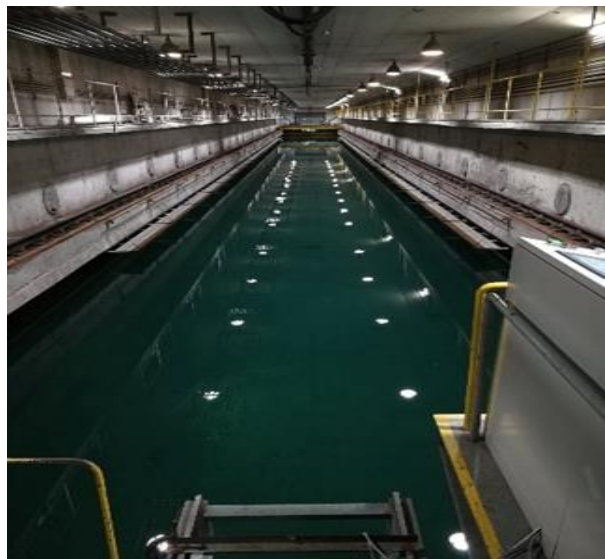


Figure 2-1 Osaka University Towing Tank.

2.1.2 Some of the devices that were used in the experiments

The swing table, shown in Figure 2-2 (a), was used in the experiments for adjustment of the vertical center of gravity (VCG) and the radius of gyration about the y-axis (K_{yy}) of the model ship. The pitch free gimbal (PFG), heaving rod (HR) and the light weight carriage (LWC), as shown in Figure 2-2 (b), were used for the ship to pitch, heave and surge freely.

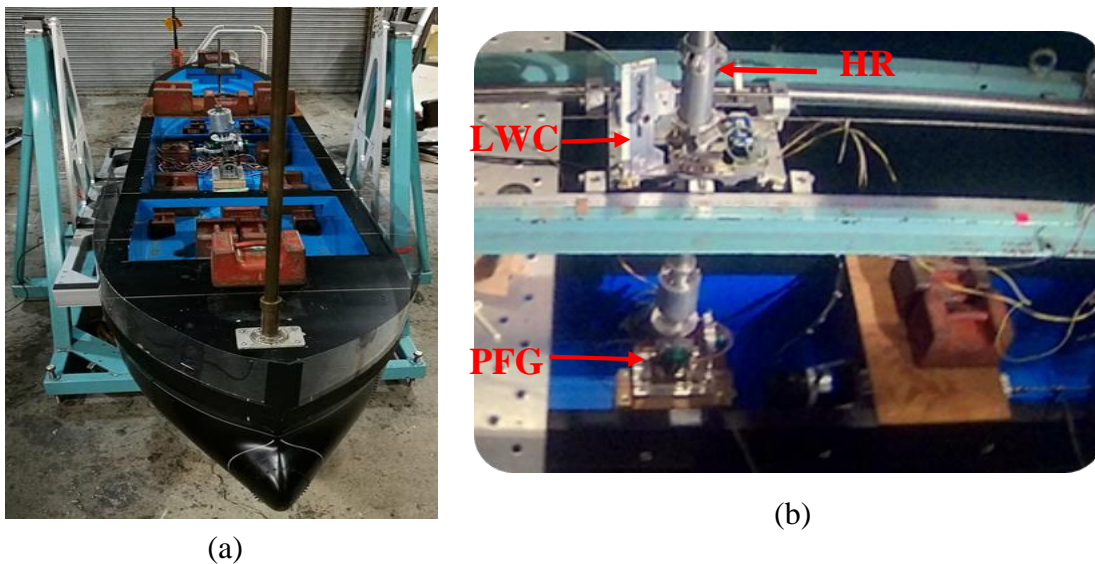


Figure 2-2 (a) Swing table, (b) Pitch free gimbal, heaving rod and light weight carriage.

2.1.3 The SPIV system

The SPIV (Stereo-Particle Image Velocimetry) system that was used for the flow field measurement is as shown in Figure 2-3. It was connected to a computer with Davis (Data acquisition and visualization) software for image acquisition and processing.

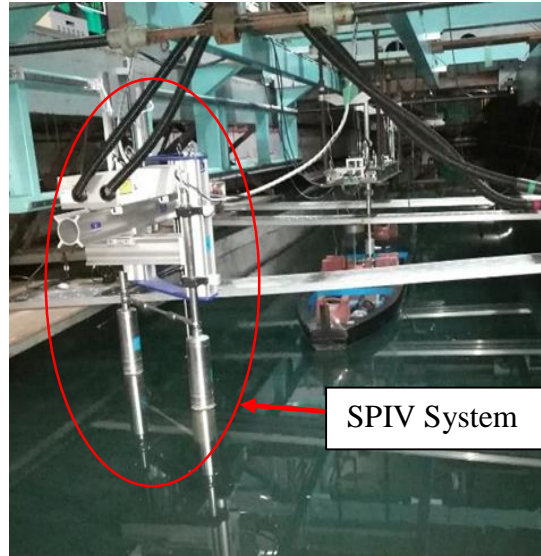


Figure 2-3 The SPIV system.

2.2 The Experiments that were conducted

In this study, the motions and force measurement experiment was done first in which 3 degree of freedom (DOF) motions were measured (heave, pitch and surge) as well as the thrust, torque and resistance in calm water and regular head waves. Then SPIV measurement was done in selected wave conditions as well as in calm water. The experiments are explained in detail as follows:

2.2.1 Motions and Force Measurement Experiment

The experiments for motions and force measurement were done for a fully-loaded, 3.2m KVLCC2 model tanker whose full-scale ship is 320m. A pitch free gimbal and heaving rod were fixed at the CG (center of gravity) of the model ship for pitch and heave free motion, and a yaw guide rod was fitted at the model ship's bow part to constrain it from the yaw motion.

The model ship was towed via a light weight carriage that was connected to the main carriage by a weak spring which allowed the ship to surge freely. An external force F_0 was applied so as to prevent the weak spring from overstretching. In this experiment, the weak spring and the

constant external force were mimicked by a servo-motor, and the force was adjusted by preliminary tests to ensure that the mean surge motion was zero. The incident wave data was collected by a servo-type wave gauge which was mounted upstream of the ship FP. The schematic diagram of the experimental set up is as shown in Figure 2-4 (Matsumoto, 2019).

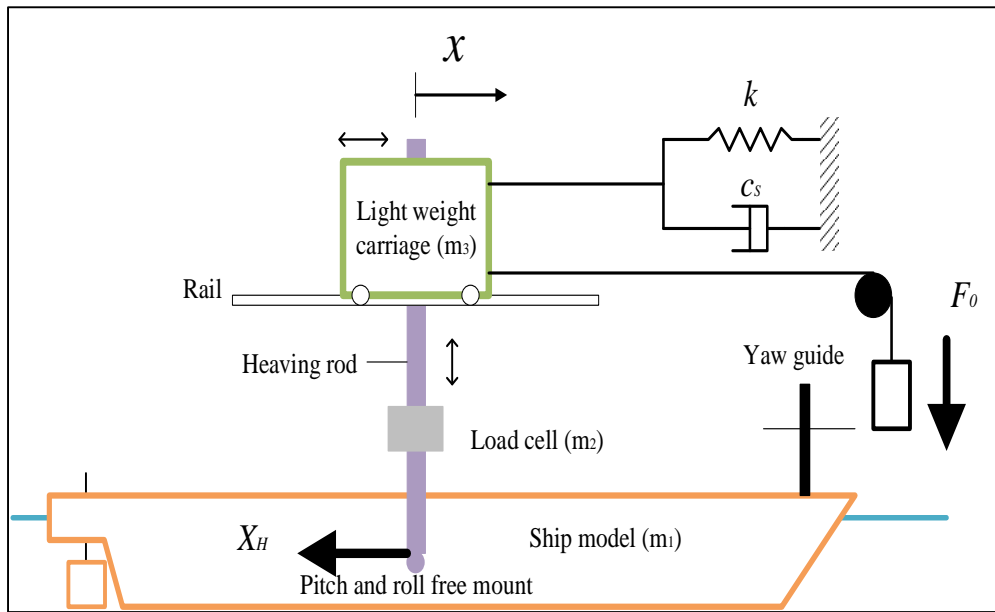


Figure 2-4 Motions and force measurement experimental set up.

2.2.2 Ship Geometry and Particulars

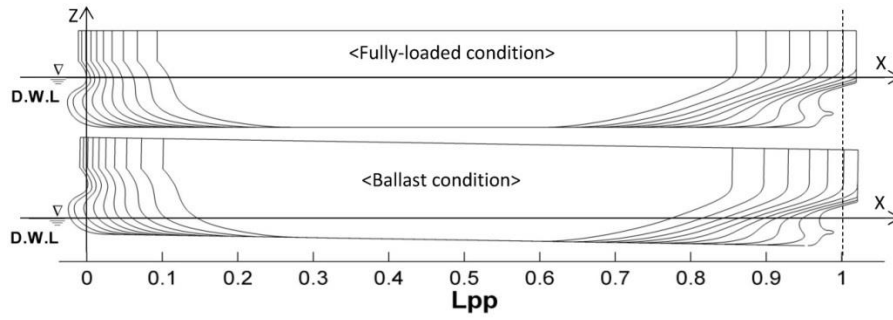
The model ship that was used in this experiment is the KVLCC2 model tanker which was 3.2m long and in fully-loaded condition. Its particulars are as shown in Table 2-1. The body plan and hull form of the ship in fully loaded condition are also shown in Figure 2-5 (Wu, 2013).

Table 2-1 KVLCC2 model Ship particulars.

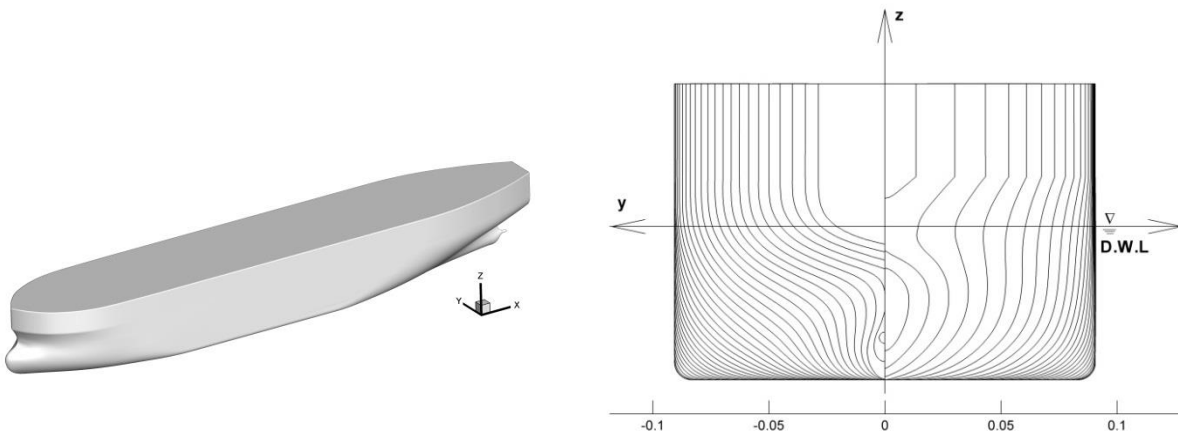
Ship Length between perpendiculars	$L_{pp}(m)$	3.2000
Maximum beam	$B(m)$	0.5800
Depth	$D(m)$	0.3000
Draft	$T(m)$	0.2080
Displacement volume	$\nabla \quad (m^3)$	0.3130
LCB(%)	fwd+	3.4800
Vertical Center of Gravity	$KG(m)$	0.1860
Block coefficient	C_B	0.8098
Moment of Inertia	K_{yy}/L_{pp} K_{zz}/L_{pp}	0.2490

2.2.3 Propeller Particulars

The MOERI propeller model with 4 blades and diameter of 0.0986m was used in the self-propulsion experiments. For the motions and force measurement, only the right-handed propeller was used whereas during SPIV measurement both the right and left hand propellers were used in order to measure the flow field especially in the transverse plane upstream of the propeller where measurement of the flow field in the starboard side was impossible due to the obstruction of the laser sheet and the camera focus by the hull. The propeller models are shown in Figure 2-6.



The side view



A 3-D view

The bow and stern view

Figure 2-5 The KVLCC2 body plan and hull form in fully-loaded condition.



Figure 2-6 MOERI Propeller models.

2.2.4 Coordinate System

The coordinate system that was used in this experiment is as shown in Figure 2-7 with positive x pointing backwards towards the ship stern, positive y and z pointing towards the starboard and upward directions respectively. The origin is at the center of gravity.

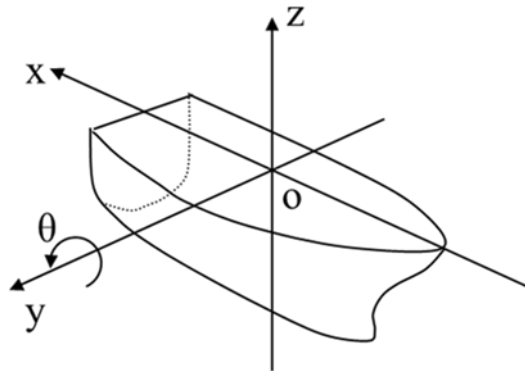


Figure 2-7 The coordinate system.

2.2.5 SPIV Measurement Experiments

The SPIV experiments were done in calm water and selected wavelengths from those done in the motions and force measurement experiment. For the wave amplitude dependency study, the SPIV measurement was done at the after perpendicular (AP) of the ship. The target measurement section was at the propeller plane but there was a lot of laser reflection from the dummy hub and therefore the plane of measurement was shifted to the AP. This laser reflection from the dummy boss could affect the quality of the velocity vectors in the velocity distribution diagrams. Therefore, the measurement at AP could give a good result because from the boundary layer approximation, the flow field at the propeller plane and AP is similar. For the ESDs effect study, the SPIV measurement was done at two transverse planes; one plane was upstream of the propeller and the other downstream of the rudders. The model ship was also free to heave, pitch and surge in this experiment. The phases for the SPIV measurement were set at the wave gauge which was installed

upstream of FP. The wave gauge was equipped with a probe which was controlled by a servomotor, and it moved automatically up and down with the water surface. In this sense the wave elevation data was recorded and sent, as a signal, to the data collecting computer. The same pulse signal was sent to the SPIV system via the programmable timing unit (PTU), which adjusted the delay time, for recording images. The wave encounter period was input into the program code that was run in the computer which was connected to the wave gauge and the PTU, in order to send pulse signals to the SPIV system for recording images at the desired phases. The zero phase for the SPIV measurement was when the zero crossing up of the incident wave occurred at the wave gauge. The recorded wave elevation was not exactly the same as the target wave elevation because of possible vibrations from the wave generator which was mounted on a concrete platform. Some of the details about the SPIV system that was used in this experiment are as discussed below.

a) The SPIV system components.

The SPIV system that was used in this experiment is the LaVision measurement system which consists of two sensor CCD (charge-coupled device) cameras, 135 mJ double-pulsed Nd YAG laser and optic system for light sheet generation, and a computer with Davis (Data Acquisition and Visualization) software for acquisition and processing of images. The lenses were fitted with motors for remote focus and aperture adjustment. Cameras also had motors for automatic adjustment of Scheimpflug angles. The main components of the SPIV system are as shown in Figure 2-8 (LaVision, 2009).

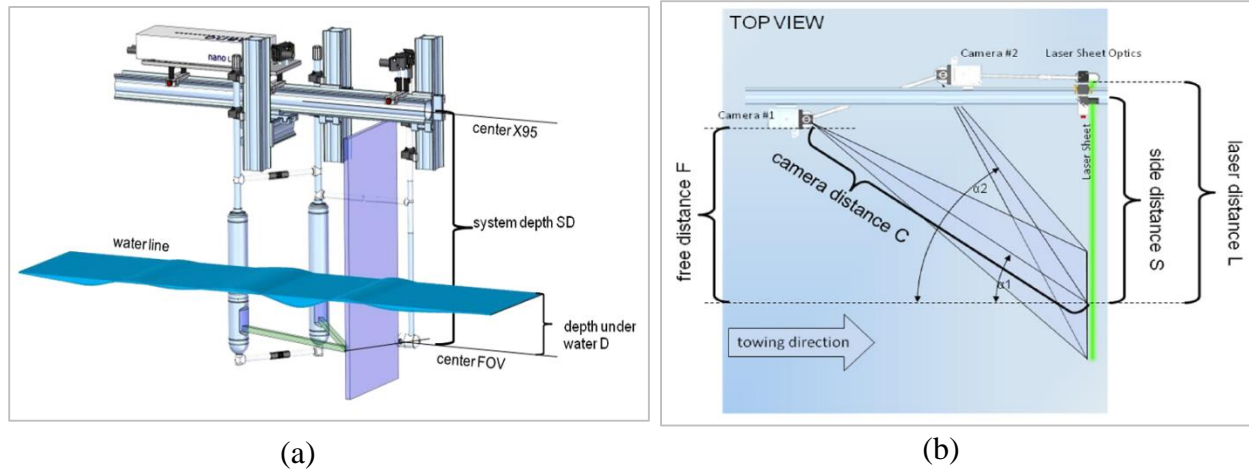


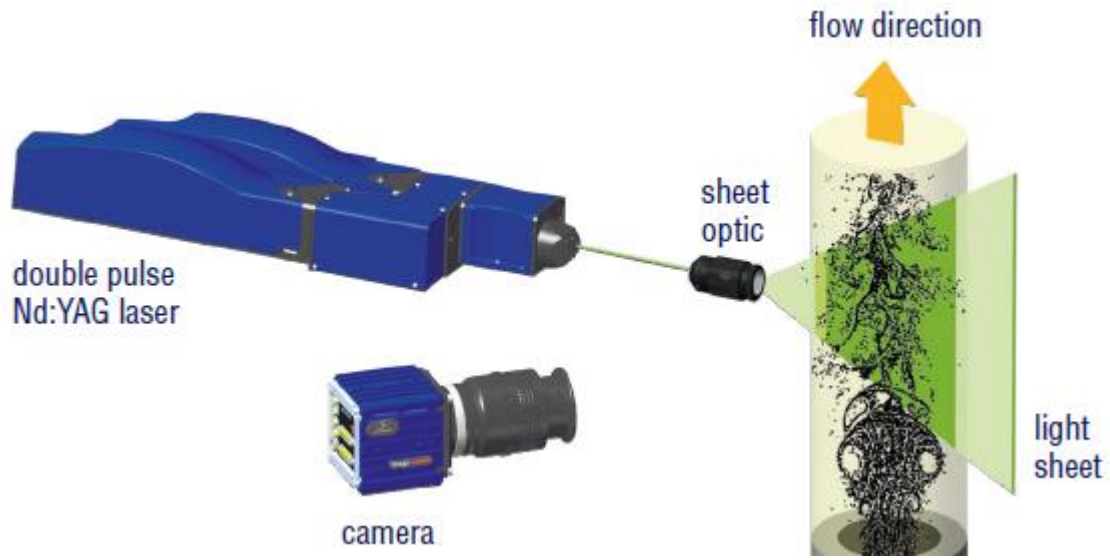
Figure 2-8 The Osaka University SPIV system components.

For calibration of the cameras, the LaVision's type 31 calibration board was used. The board was submerged into the water such that its top surface flushed with the calm water surface. Then the SPIV assembly was moved on the carriage until the front side of the calibration board was in plane with the laser light sheet where the fields of view of the two cameras overlapped. This calibration was done in a step-by-step procedure in the LaVision's computer. Once the calibration was completed, this position of the SPIV system served as the zero point for flow field measurements. However, this vertical position of the SPIV cameras was too deep for measurement of the flow field around the ship's propeller shaft (area of interest). Therefore, the SPIV was moved up so that the field of view was around the position of the shaft, and this movement was done carefully while checking the shaft's position using the live mode option in the LaVision's Davis software in the computer. This new zero point for SPIV was used to capture images for calm water as well as short waves condition ($\lambda/L=0.6$). For long waves ($\lambda/L=1.1$ and 1.6), in which the vertical ship motions were large, this measurement was done in two vertical planes, by adjusting the SPIV system up and down, so as to capture the whole flow field of interest. During the SPIV

measurement experiment, the wave elevation, ship motions (heave, pitch and surge), resistance, as well as thrust and torque were also measured.

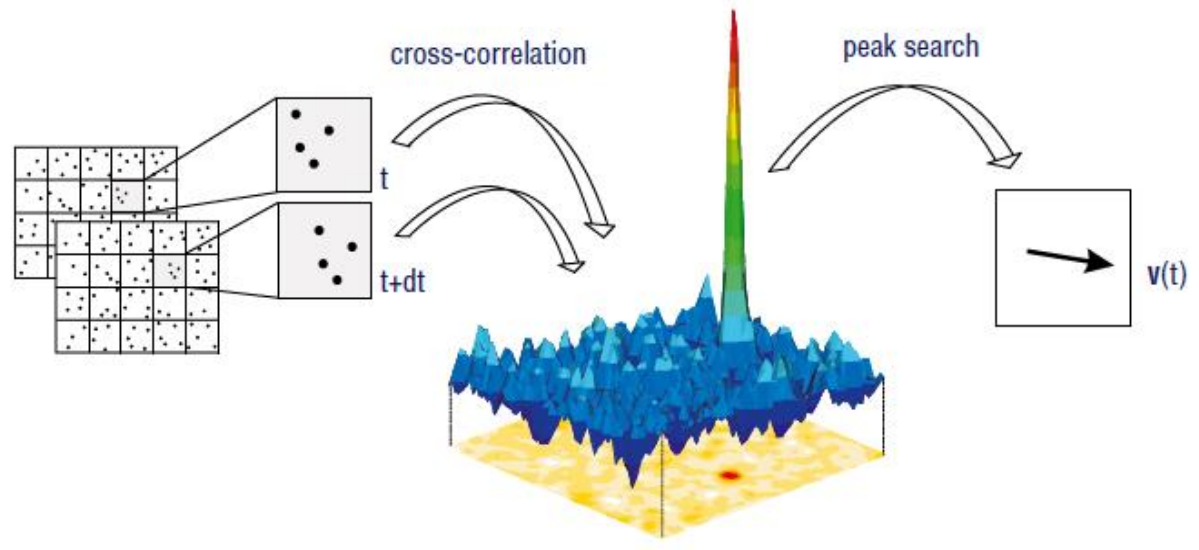
b) The SPIV system working principle.

The working principle of the SPIV system that was used in this experiment is as shown in Figure 2-9 in which the flow is seeded with very small particles that follow the flow. A pulsed laser sheet is fired twice on the area of interest with a short time interval dt and the illuminations are recorded by double-frame high resolution CCD cameras. The CCD cameras have different observation angles to enable them measure the third velocity (out-of-plane) component of the flow in the laser light sheet. The recorded images are then divided into small interrogation windows for cross-correlation purposes. In the time interval dt , the particles of individual interrogation windows would have moved by some displacement ds . This displacement is calculated by a Fast Fourier Transform (FFT)-based cross-correlation of two corresponding interrogation windows in which the location of the highest peak in the correlation plane shows the mean displacement of the tracer particles in that interrogation window. Then the particle velocity is calculated by the ratio ds/dt . Once this is done in all the interrogation windows, a whole instantaneous velocity map is achieved from the displacement vectors as shown in Figure 2-10 (LaVision, FlowMaster).



Source (LaVision, FlowMaster)

Figure 2-9 The SPIV working principle.



Source (LaVision, FlowMaster)

Figure 2-10 The principle of cross-correlation of SPIV system.

c) The SPIV experiment set up.

The SPIV experiment set up is as shown in Figure 2-11 (Wu, 2013). In this experiment the incident wave data was measured at the wave gauge (or wave height meter) which is indicated by the red box in Figure 2-11. At this wave height meter, the phases were set for the SPIV system to record the images. The 0-degree phase is the zero crossing up of the incident wave and the 180-degree phase is at the zero-crossing down of the incident wave at the wave gauge. In the wave amplitude dependency study, the images were recorded at four phases (0, 90, 180 and 270 degrees) for all wavelengths. On the other hand, for the ESDs effect study, a four-pulse program code was used to send signals to the SPIV system to record images at four phases (0, 90, 180 and 270 degrees) for short waves ($\lambda/L=0.6$) whereas for long waves ($\lambda/L=1.1$ and 1.6) a six-pulse program code was used to send signals to the SPIV system to record images at six phases (0, 60, 120, 180, 240 and 300 degrees). The pulse signals were sent to the SPIV system through the programmable timing unit (PTU), which adjusts the delay time, to record images.

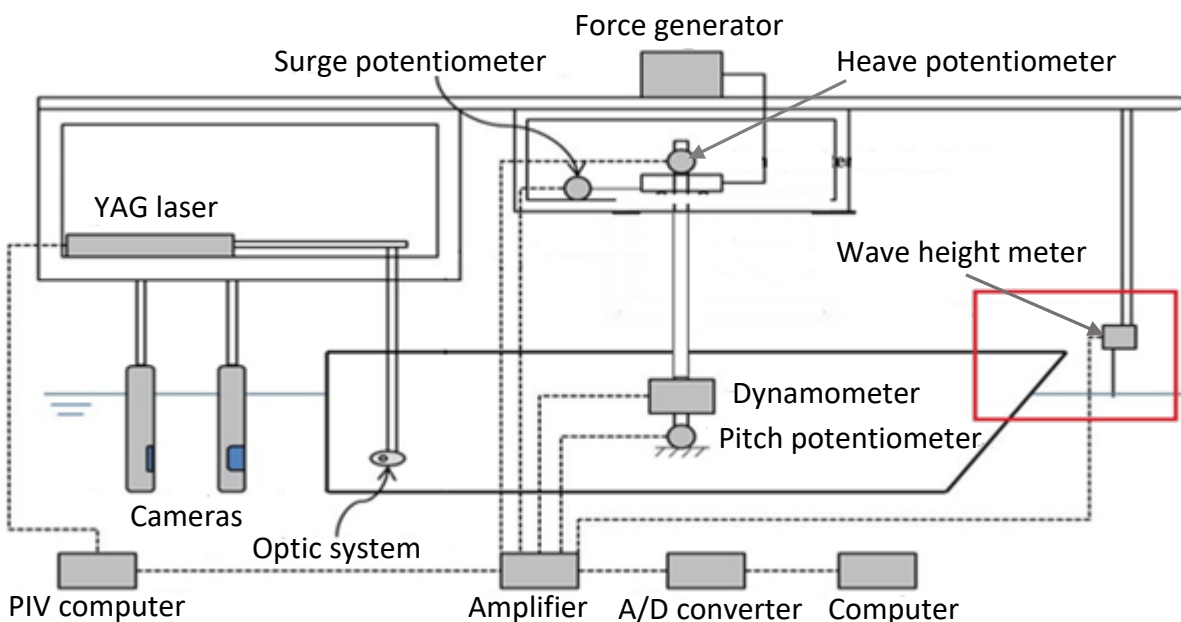


Figure 2-11 The SPIV experiment set up.

An example of synchronizing of phases that was used for SPIV measurement during ESDs effect study is as shown in Figure 2-12. This was used for long wavelengths since it has six pulses per wavelength whereas for shorter wavelengths four pulses were used per wavelength. The pulse signals were sent to the SPIV system at all the desired phases to record the images.

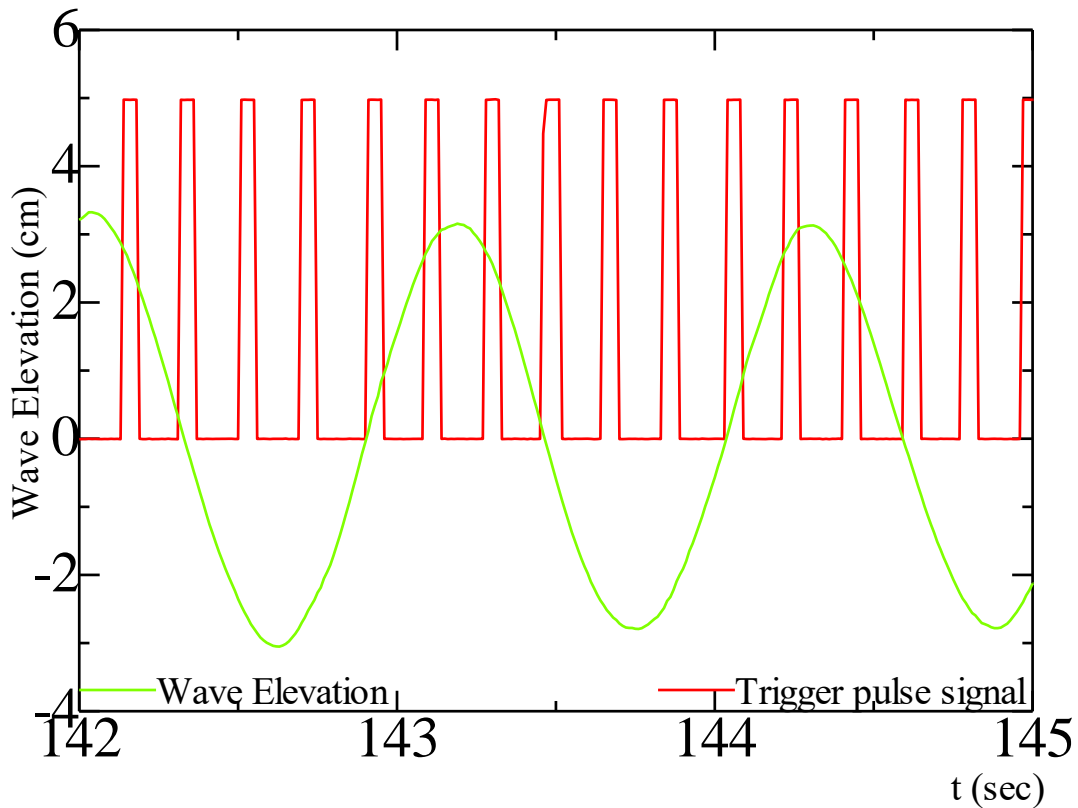


Figure 2-12 SPIV phase synchronization for waves.

2.2.6 Measured Parameters

In both experiments, a number of parameters were measured alongside the flow field and these are; wave elevation, force in the x- direction, heave, pitch and surge motions, as well as thrust and torque. The summary of these parameters, their coordinates and the device that was used for the measurement is as shown in Table 2-2.

Table 2-2 Measured parameters, their coordinates and devices used for measurement.

Parameter	Coordinate	Device Used
Wave Elevation(cm)	Above undisturbed water surface(+)	Servo-type wave gauge
X-Force, F_x (N)	Backward ship movement (+)	Dynamometer
Heave(cm)	Upward ship movement (+)	Heave potentiometer
Pitch(deg)	Pitching bow up (+)	Pitch potentiometer
Surge(cm)	Backward ship movement (+)	Surge potentiometer
Thrust (N)	-	Self-propulsion dynamometer
Torque (Nm)	-	Self-propulsion dynamometer

CHAPTER 3: MOTIONS AND FORCE MEASUREMENT RESULTS

The experiments for motions and force measurement were done both in calm water and regular head waves. The quantities that were measured, as mentioned previously, include the wave elevation, X-force, heave, pitch and surge motions as well as thrust and torque. The heave and pitch motions were free, and surge motion was also free by using a weak spring to compensate the unbalance of the steady force. Therefore, the surge motion due to the wave exciting force as well as the slow surge due to the mass weak spring system were measured. The raw data was obtained in voltage form and was converted into real values by using the calibration values that were obtained before conducting the experiments. The results for motions and forces were analyzed and discussed in detail with respect to the effects of the wave amplitude and the energy saving devices.

3.1 Wave Amplitude Effect

3.1.1 Time histories

From the experimental data, the real physical values were obtained by subtracting the zero point values from the measured values for each channel so as to plot the time histories as shown in the figures below. The original data time histories for both towing and self-propulsion conditions for $\lambda/L= 1.1$, at a wave amplitude, $A= 3\text{cm}$ are shown as examples for the time histories for all wavelengths because they have a similar trend. The time histories for towing condition are as shown in Figure 3-1 whereas those for self-propulsion condition are shown in Figure 3-2 and Figure 3-3.

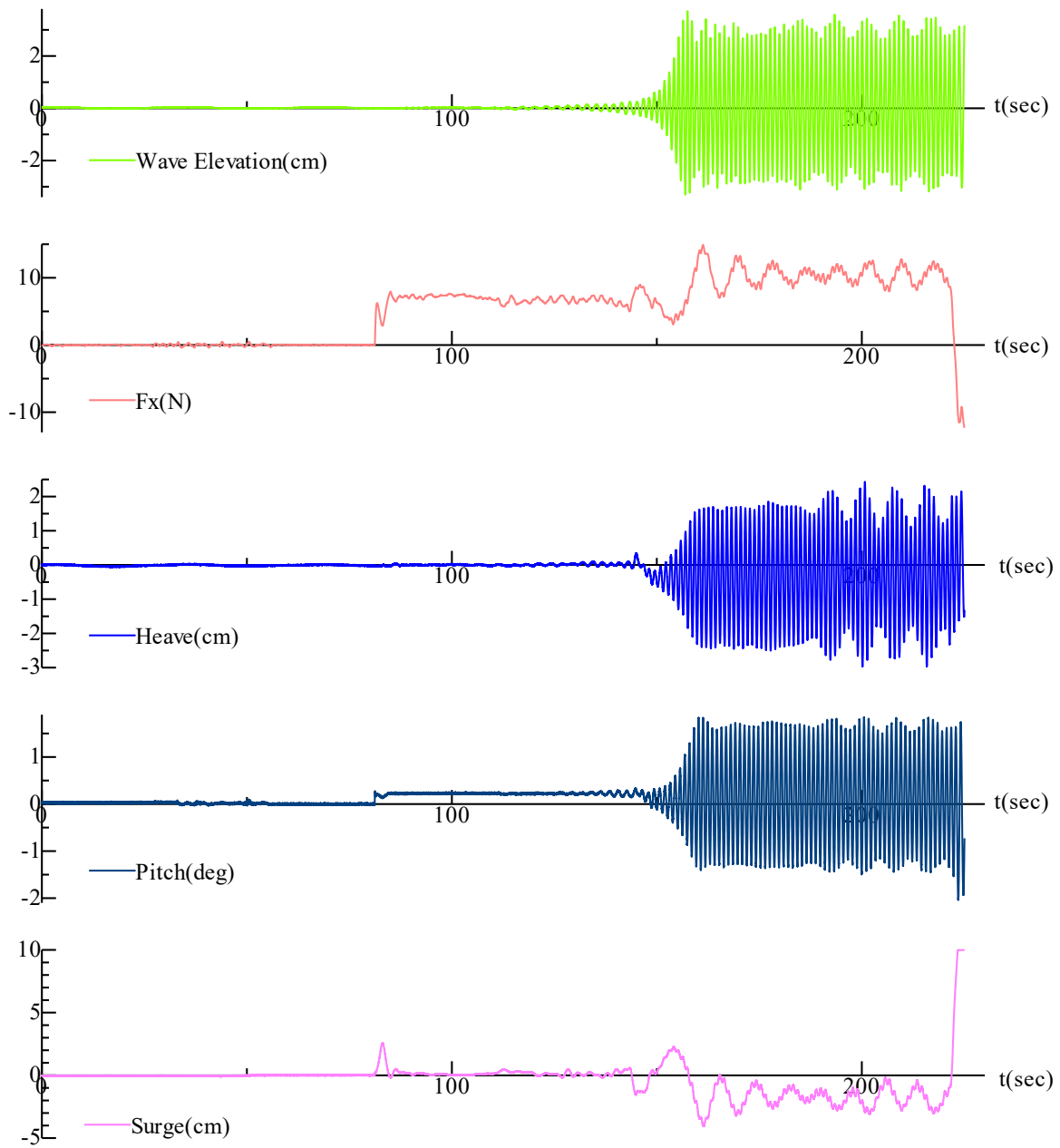


Figure 3-1 Time histories for wave elevation, X-force, heave, pitch and surge for $\lambda/L=1.1$, $A=3\text{cm}$ of a towed KVLCC2 model ship.

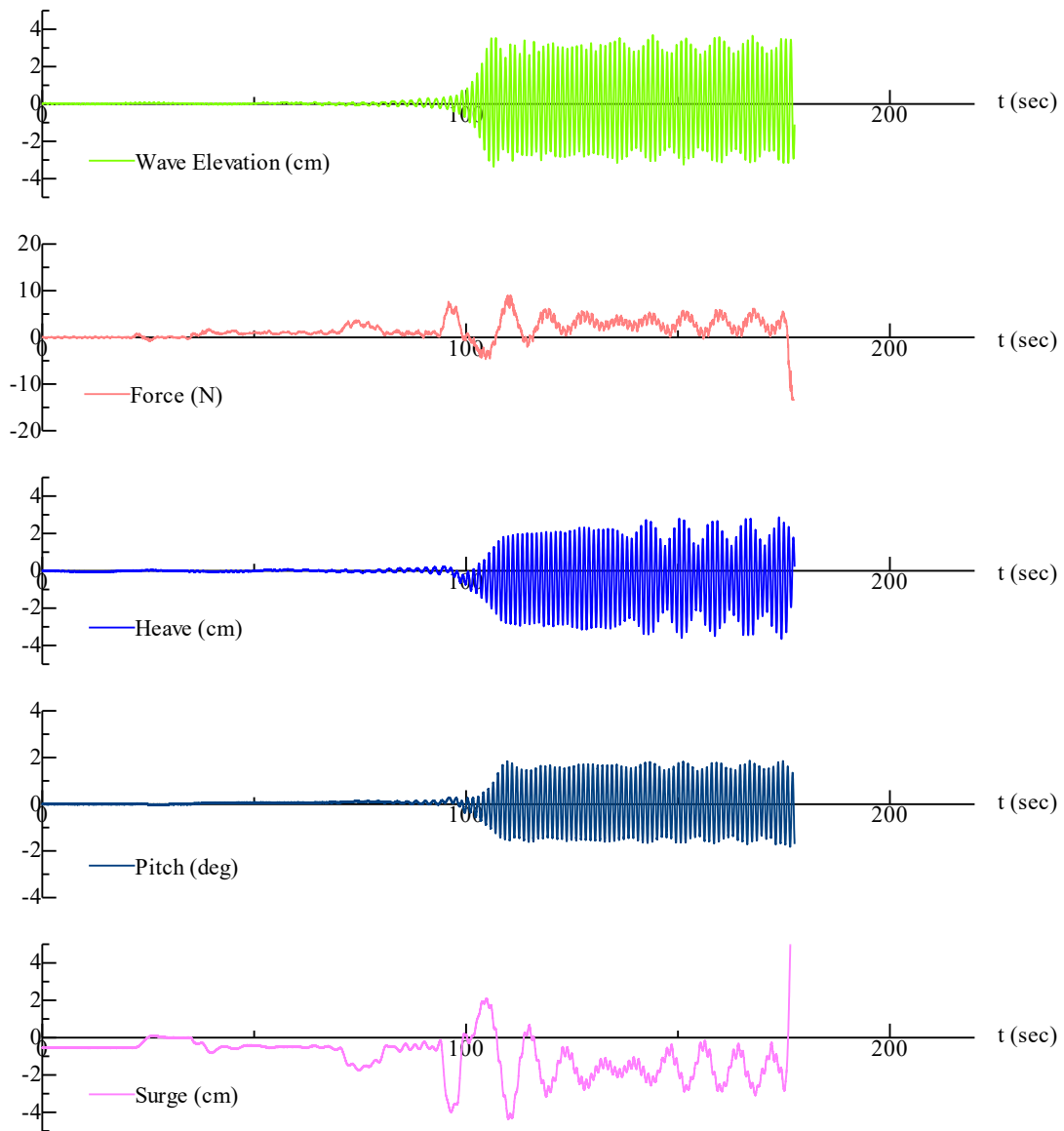


Figure 3-2 Time histories for wave elevation, X-force, heave, pitch and surge for $\lambda/L=1.1$, $A=3\text{cm}$ of a self-propelled KVLCC2 model ship.

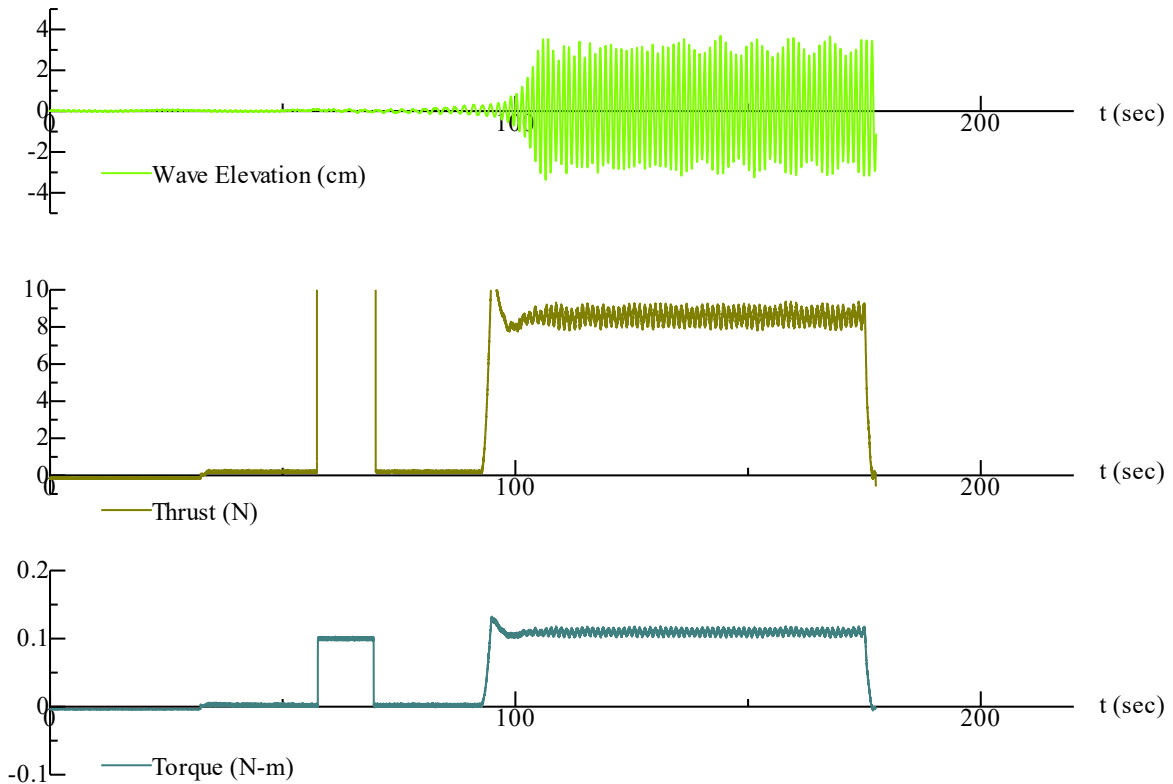


Figure 3-3 Time histories for wave elevation, thrust and torque for $\lambda/L=1.1$, $A=3\text{cm}$ of a self-propelled KVLCC2 model ship.

3.1.2 Thrust, torque and effective wake results

The data for thrust, torque and effective wake was analyzed by Fourier series expansion and reconstructed by ignoring the higher harmonic components than 7th harmonics so as to understand the fluctuation shape in one period. For thrust and torque a lot of noise due to vibration of the connection joints between the motor and the self-propulsion dynamometer was eliminated. It was noted that the 1st, 2nd and 3rd harmonic components are responsible for the thrust and torque oscillations with a quickly increasing slope and a slowly decreasing slope. Therefore, it was concluded that up to 3rd harmonic components are enough to obtain the original thrust and torque shapes.

a) Mean values for forces and self-propulsion factors

The summary of mean values for thrust, torque, effective wake factor and thrust deduction factor are as shown in Table 3-1. From this table, it can clearly be seen that the mean values for thrust decrease slightly as the wave amplitude increases in all wavelength cases. Torque shows some fluctuations but generally the trend is similar to that for thrust. The mean values for effective wake increase slightly as the wave amplitude increases. The increase in the mean values for effective wake indicates an increase in the inflow velocity into the propeller plane, and this is the reason for a slight decrease in thrust and torque mean values. From the values for effective wake factor and thrust deduction factor, the efficiency generally decreases as the wave amplitude increases.

Table 3-1 Mean values for thrust, torque, effective wake and thrust deduction factor.

λ/L	A(cm)	Mean Values			
		Thrust(N)	Torque(N-m)	1-w	1-t
1.1	0.75	8.6285	0.1103	0.6434	0.8446
	1.5	8.5858	0.1096	0.6504	0.8433
	3	8.5809	0.1098	0.6508	0.8437
	4	8.5283	0.1093	0.6589	0.8443
	4.3	8.5235	0.1093	0.6596	0.8459
1.6	0.75	4.4556	0.0585	0.5899	0.8311
	1.5	4.4299	0.0586	0.5951	0.8337
	3	4.3733	0.0581	0.6060	0.8355
	4	4.3324	0.0584	0.6137	0.8378
	4.3	4.3110	0.0581	0.6180	0.8374
2	0.75	4.4403	0.0589	0.5930	0.8331
	1.5	4.4373	0.0593	0.5933	0.8350
	3	4.4080	0.0590	0.5984	0.8383
	4	4.3898	0.0585	0.6011	0.8361
	4.3	4.3657	0.0589	0.6056	0.8394

b) Time histories for thrust, torque and effective wake ($\lambda/L=1.1$)

After reconstructing the data for thrust, torque and effective wake, their time histories for $\lambda/L=1.1$ at different wave amplitudes are as shown in Figure 3-4 to Figure 3-6. The propeller speed, which had been determined by preliminary tests in previous experiments, for this wave condition was 21 revolutions per second (rps). When $t=0$, the wave crest is at the propeller plane.

The thrust and torque time histories are inverse to that of the effective wake as seen from these figures. However, their amplitudes of oscillation increase as the wave amplitude increases. Also, it should be noted that as the wave amplitude increases, the low thrust and torque regions increase downwards resulting in a slight decrease in their mean values. On the other hand, the high effective wake regions increase upwards resulting in a slight increase in its mean values. The wave amplitude values, A , shown on these figures are measured values and not target ones.

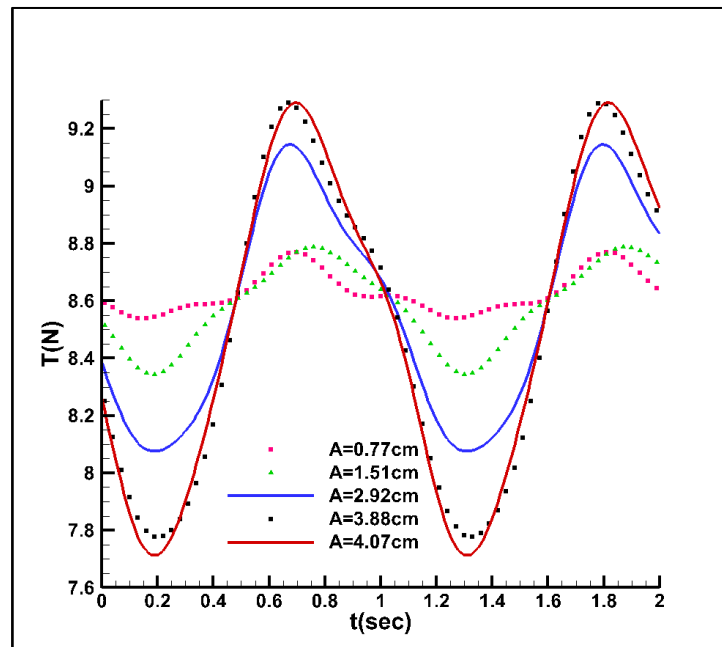


Figure 3-4 Thrust time history for different wave amplitudes at $\lambda/L=1.1$.

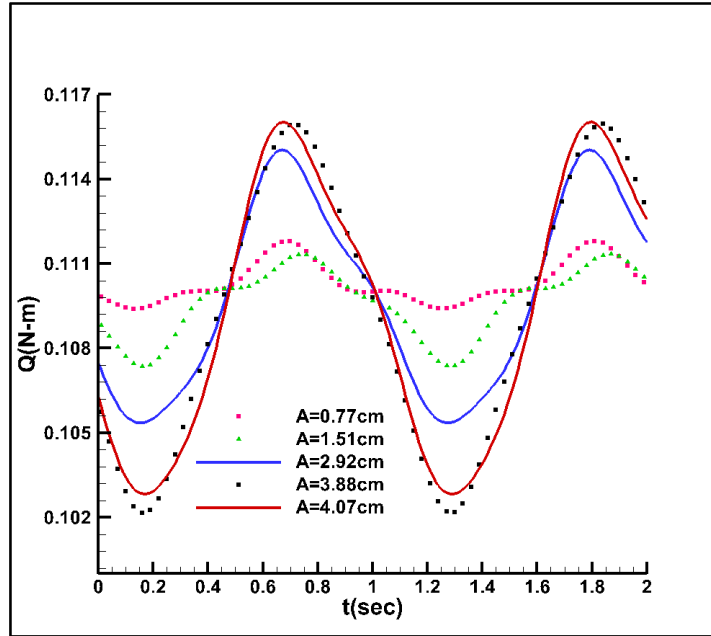


Figure 3-5 Torque time history for different wave amplitudes at $\lambda/L=1.1$.

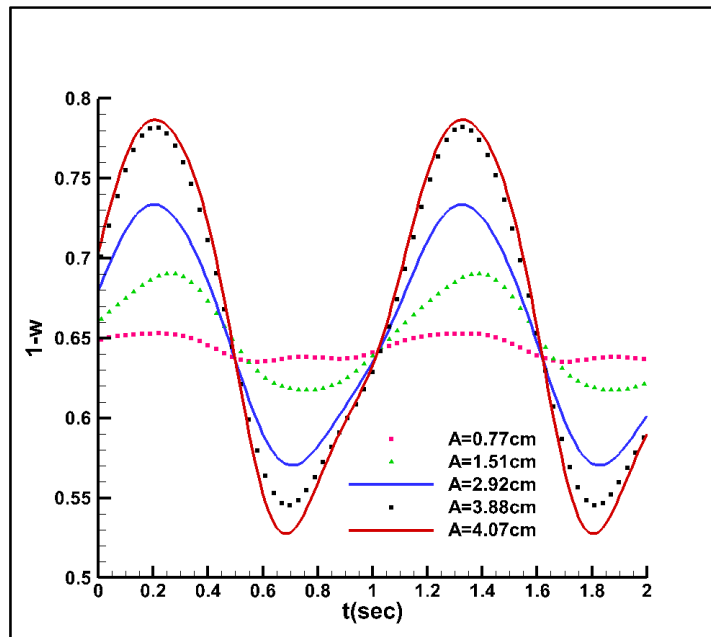


Figure 3-6 Effective wake time history for different wave amplitudes at $\lambda/L=1.1$.

To confirm that up to 3rd harmonic components are enough for thrust and torque fluctuations, a comparison for the 1st, 2nd and 3rd harmonic components was done as shown in

Figure 3-7. The 1st harmonic curve is sinusoidal and is the largest compared to the other curves. The 1st harmonic value is also the largest after the mean value while the 2nd and 3rd harmonic values are about 16% and 10% of the 1st harmonic value respectively. Even though they are small in value, they are very important in determining the thrust and torque fluctuation shapes. Therefore, as the harmonic components increase from 1st to 3rd, the peaks for thrust and torque curves shift towards the left resulting in a shape with a quickly increasing slope and a slowly decreasing slope which is exhibited by thrust and torque time histories.

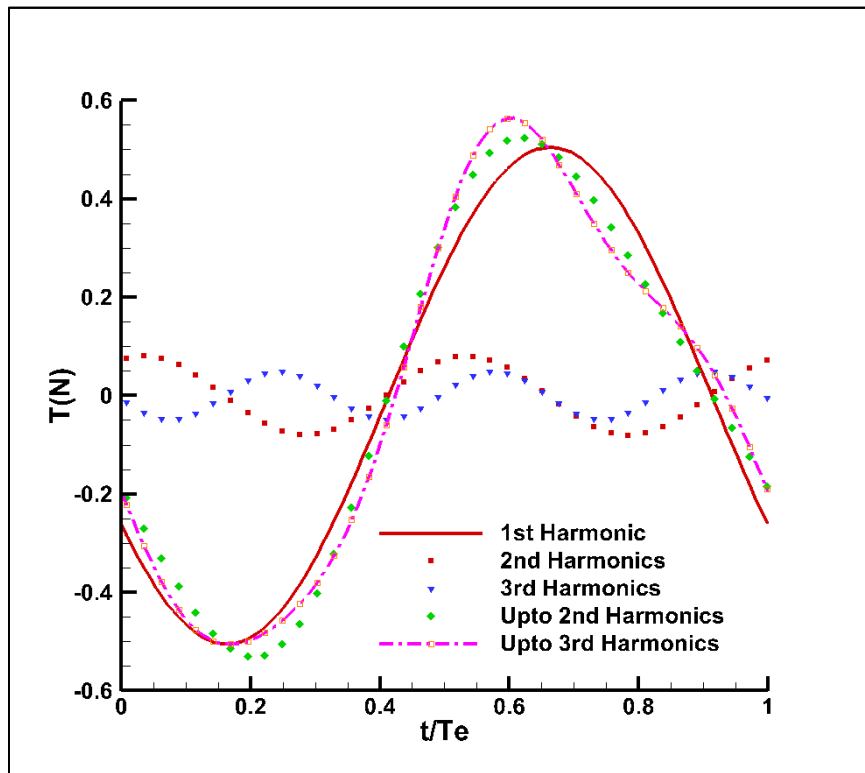


Figure 3-7 Comparison of thrust harmonic components.

c) Time histories for thrust, torque and effective wake ($\lambda/L=1.6$)

The time histories for thrust, torque and effective wake for $\lambda/L=1.6$ have also been plotted as shown in Figure 3-8 ~ Figure 3-10. For these time histories, the wave peak is also at the propeller

plane. The propeller speed, which had been determined by preliminary tests in previous experiments, for this wave condition was 15.89 rps. Also, in this wavelength, the thrust and torque time histories are inverse to that of the effective wake as seen from these figures. Their amplitudes of oscillation increase as the wave amplitude increases. Again, it should be noted that as the wave amplitude increases, the low thrust and torque regions increase downwards resulting in a small decrease in their mean values. On the contrary, the high effective wake regions increase upwards resulting in a slight increase in its mean values.

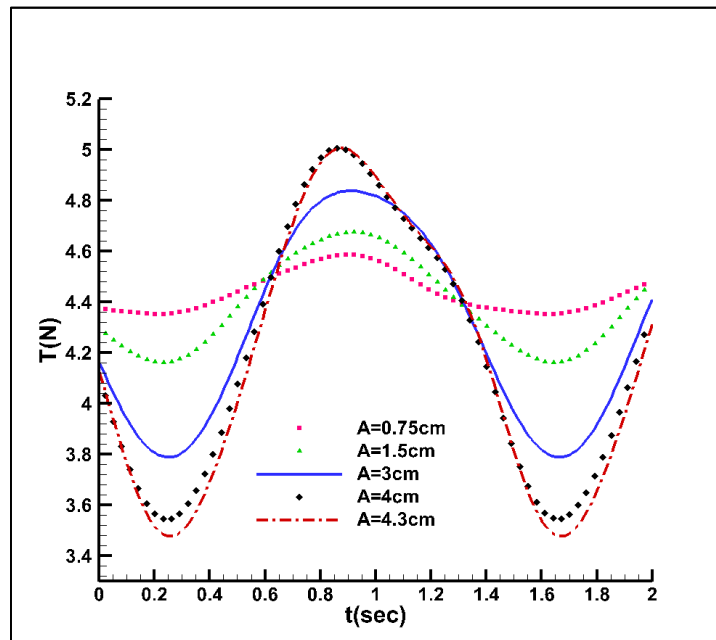


Figure 3-8 Thrust time history for different wave amplitudes at $\lambda/L=1.6$.

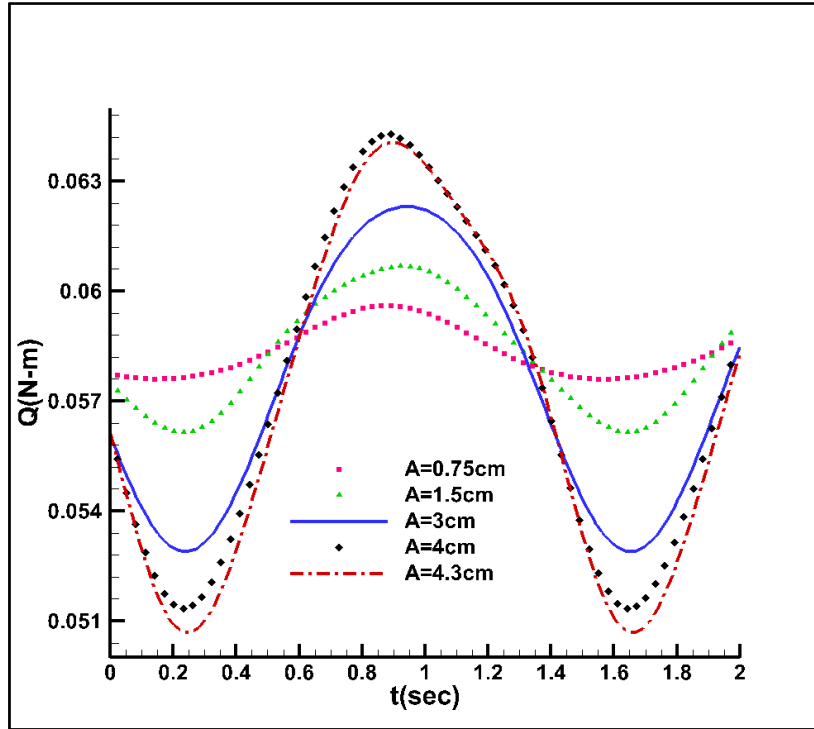


Figure 3-9 Torque time history for different wave amplitudes at $\lambda/L=1.6$.

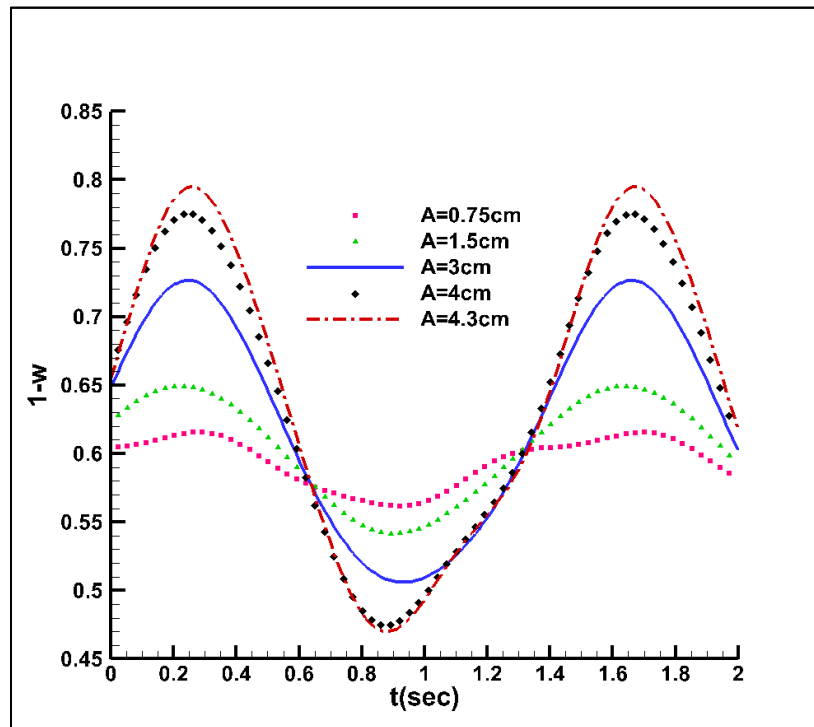


Figure 3-10 Effective wake time history for different wave amplitudes at $\lambda/L=1.6$.

d) Time histories for thrust, torque and effective wake ($\lambda/L=2.0$)

The time histories for thrust, torque and effective wake for $\lambda/L=2.0$ are plotted as shown in Figure 3-11~ Figure 3-13. Also, for these time histories, the wave peak is at the propeller plane. The propeller speed that was used for this wave condition is 15.89 rps. Similarly, in this wavelength, the thrust and torque time histories are inverse to that of the effective wake as seen from these figures. Their amplitudes of oscillation increase as the wave amplitude increases. As in the above wavelengths, as the wave amplitude increases, the low thrust and torque regions increase downwards causing a small decrease in their mean values. Conversely, the high effective wake regions increase upwards occasioning a slight increase in its mean values.

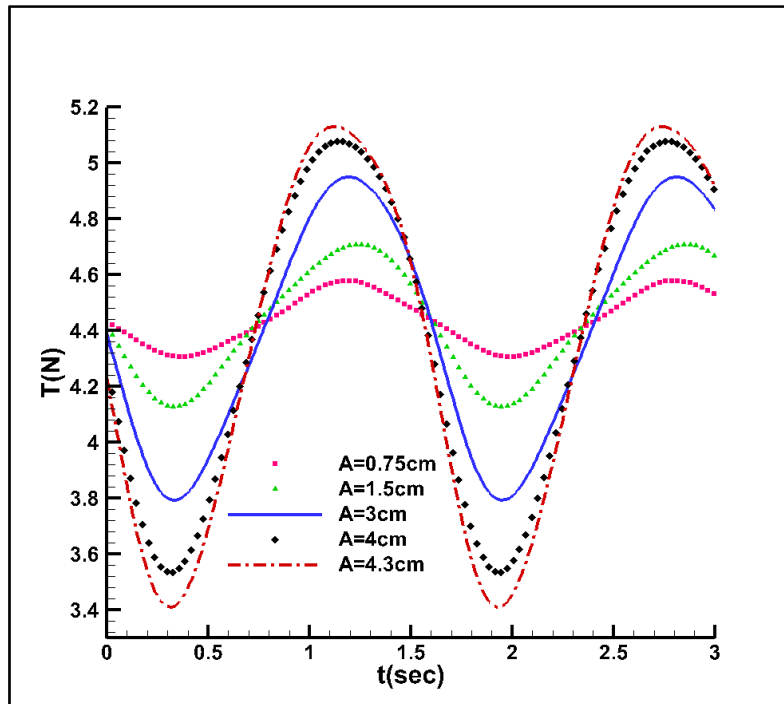


Figure 3-11 Thrust time history for different wave amplitudes at $\lambda/L=2.0$.

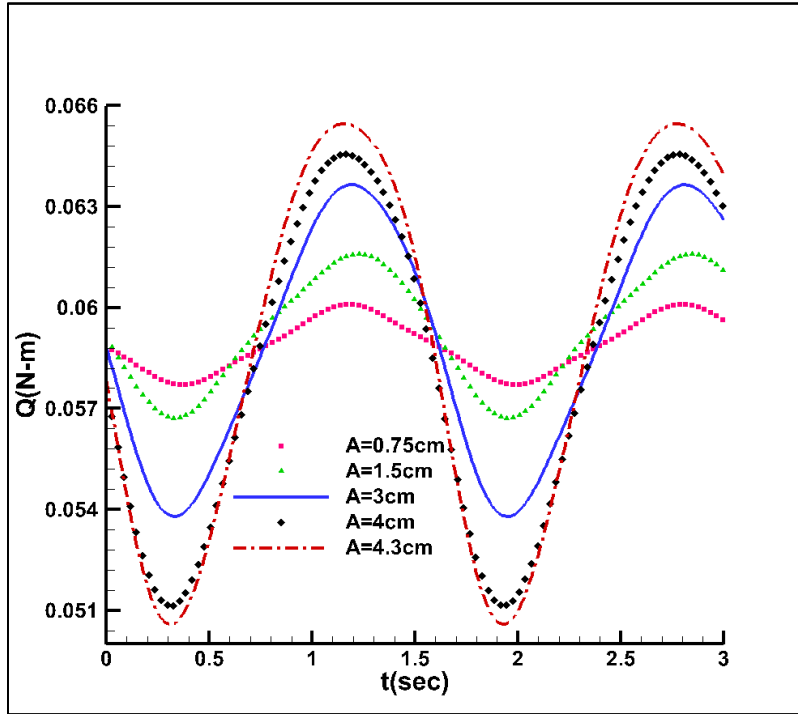


Figure 3-12 Torque time history for different wave amplitudes at $\lambda/L=2.0$.

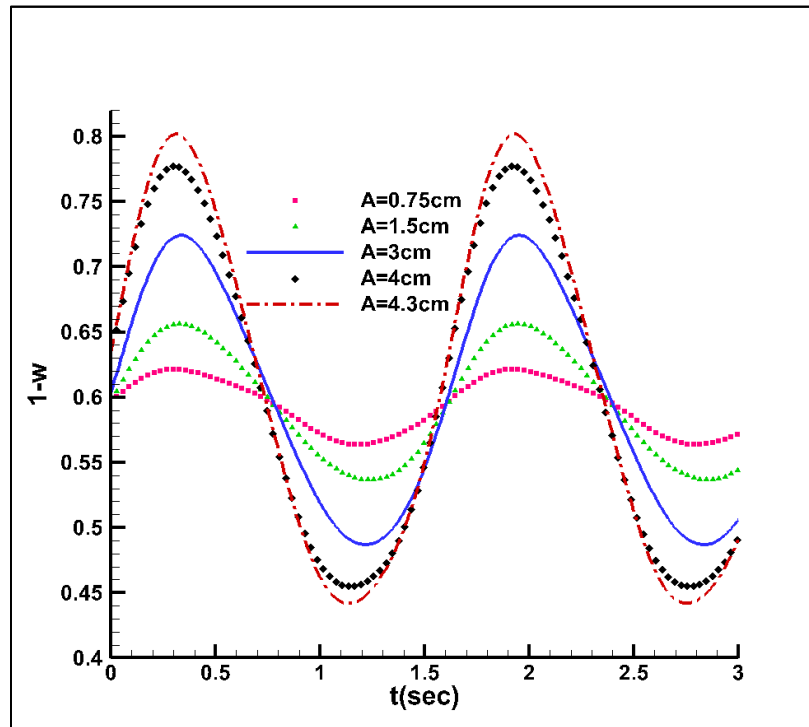


Figure 3-13 Effective wake time history for different wave amplitudes at $\lambda/L=2.0$.

e) **The mean and 1st harmonic values for thrust, torque and effective wake**

The mean and 1st harmonic values for thrust for various wavelengths at different wave amplitudes are shown in Figure 3-14 and Figure 3-15. From these figures, it can be seen that the mean values for thrust decrease slightly as the wave amplitude increases in all wavelengths. The 1st harmonic values increase linearly as the wave amplitude increases in all wavelength conditions.

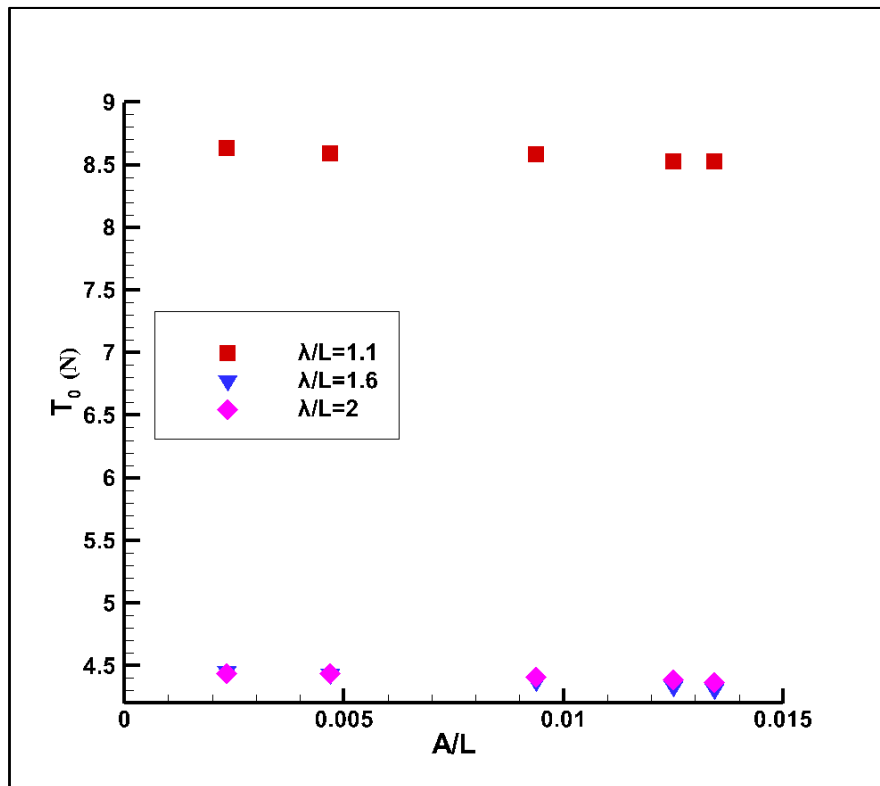


Figure 3-14 Mean values for thrust.

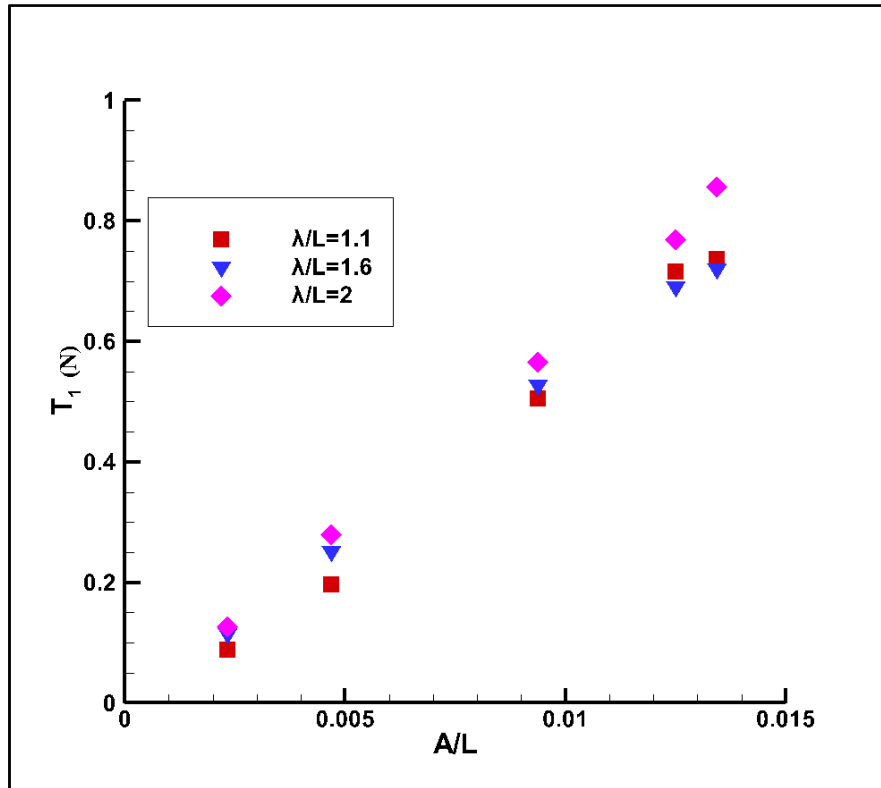


Figure 3-15 1st harmonic values for thrust.

The mean and 1st harmonic values for torque for various wavelengths at different wave amplitudes are shown in Figure 3-16 and Figure 3-17. From these figures, it can be seen that the mean values for torque decrease slightly as the wave amplitude increases in all wavelengths. The 1st harmonic values increase linearly as the wave amplitude increases in all wavelength conditions. Also, the mean and 1st harmonic values for effective wake for various wavelengths at different wave amplitudes are shown in Figure 3-18 and Figure 3-19. It can be seen that the mean values for effective wake increase slightly as the wave amplitude increases in all wavelengths. The 1st harmonic values increase linearly as the wave amplitude increases in all wavelength conditions.

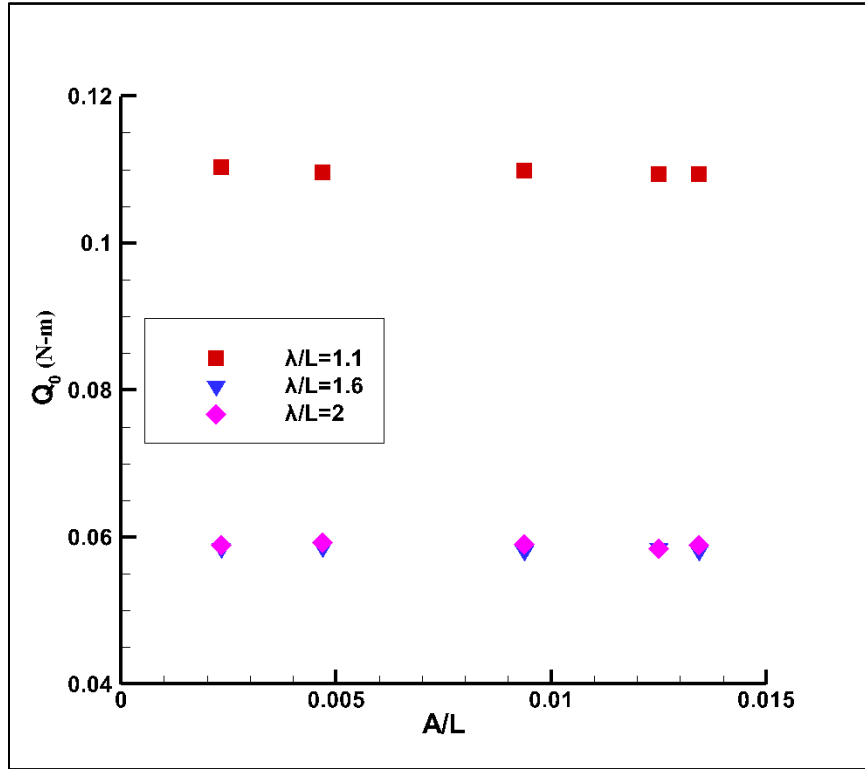


Figure 3-16 Mean values for torque.

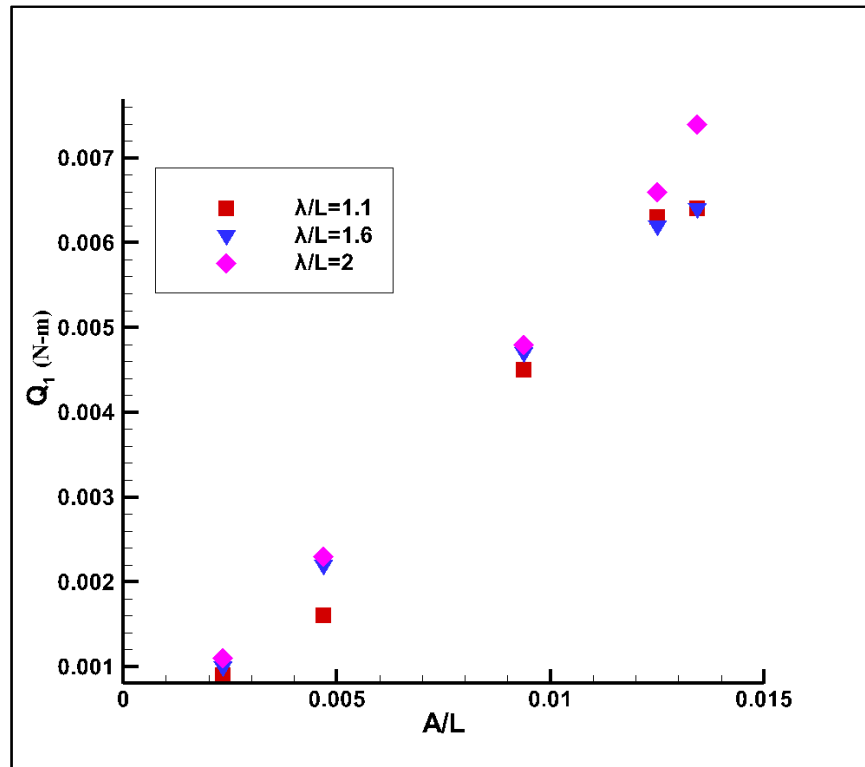


Figure 3-17 1st harmonic values for torque.

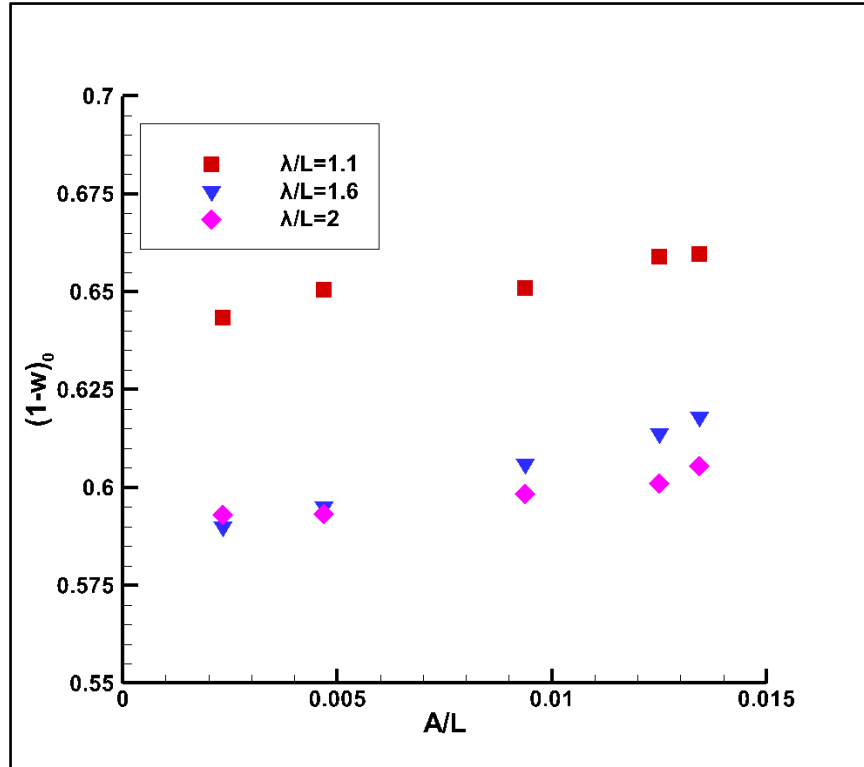


Figure 3-18 Mean values for effective wake.

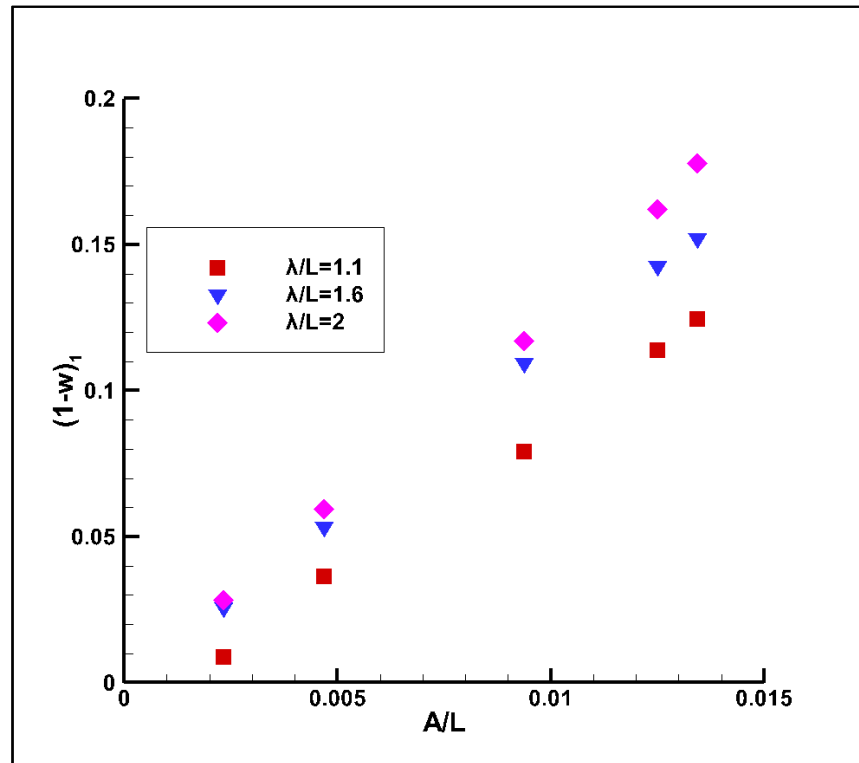


Figure 3-19 1st harmonic values for effective wake.

3.1.3 Motion results

The results for motions were also analyzed by Fourier series expansion and the data reconstructed by ignoring higher than 7th harmonic components. From the results, it was noted that for motion up to 1st harmonic components are enough to obtain the original oscillation shape. The vertical ship motions i.e. heave and pitch motions were analyzed, and their time histories at different wavelengths and wave amplitudes were plotted.

a) Heave Motion

i. Time histories

The time histories for heave motion are as shown in Figure 3-20~Figure 3-22. When $t=0$, the wave crest is at the propeller plane. From these time histories, the amplitudes of oscillation for heave motion increase as the wave amplitude increases and the phase lags are almost similar in all cases.

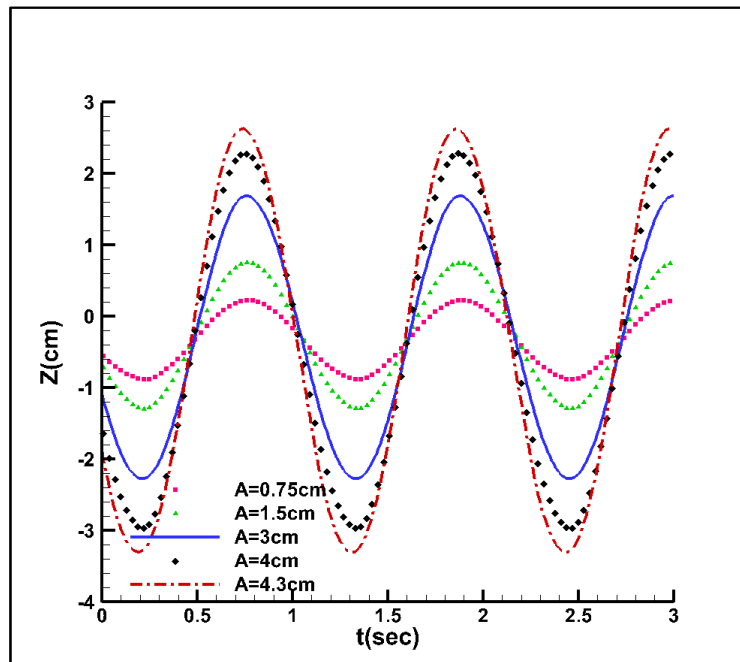


Figure 3-20 Heave motion time history at different wave amplitudes for $\lambda/L=1.1$.

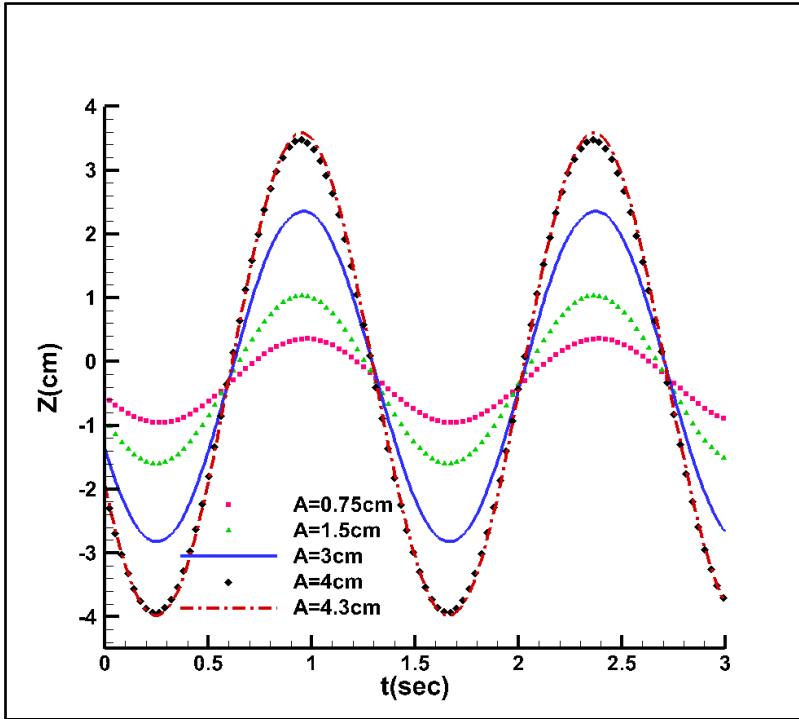


Figure 3-21 Heave motion time history at different wave amplitudes for $\lambda/L=1.6$.

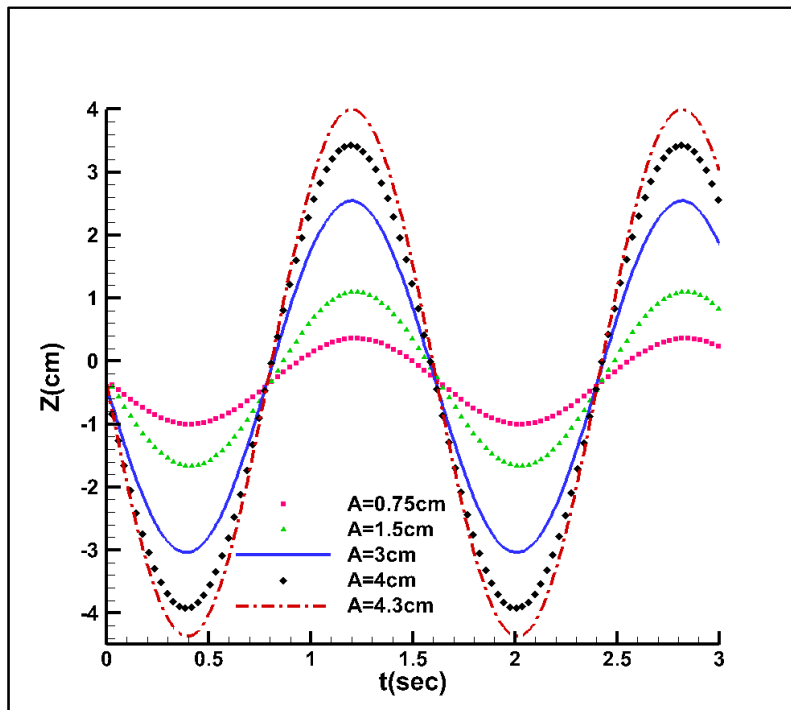


Figure 3-22 Heave motion time history at different wave amplitudes for $\lambda/L=2.0$.

ii. Heave 1st harmonic amplitudes and phases

The 1st harmonic amplitudes for heave motion increase linearly as the wave amplitude increases while the phases are fairly constant as shown in Figure 3-24 and Figure 3-24 respectively. From the figure for amplitudes, it can be seen that for the smallest wave amplitudes, the values are almost similar for all wavelengths. However, as the wave amplitude increases the 1st harmonic amplitudes for $\lambda/L=1.6$ and 2 become larger compared to those for $\lambda/L=1.1$. This is because in larger amplitudes, the heave motion is larger especially for longer waves.

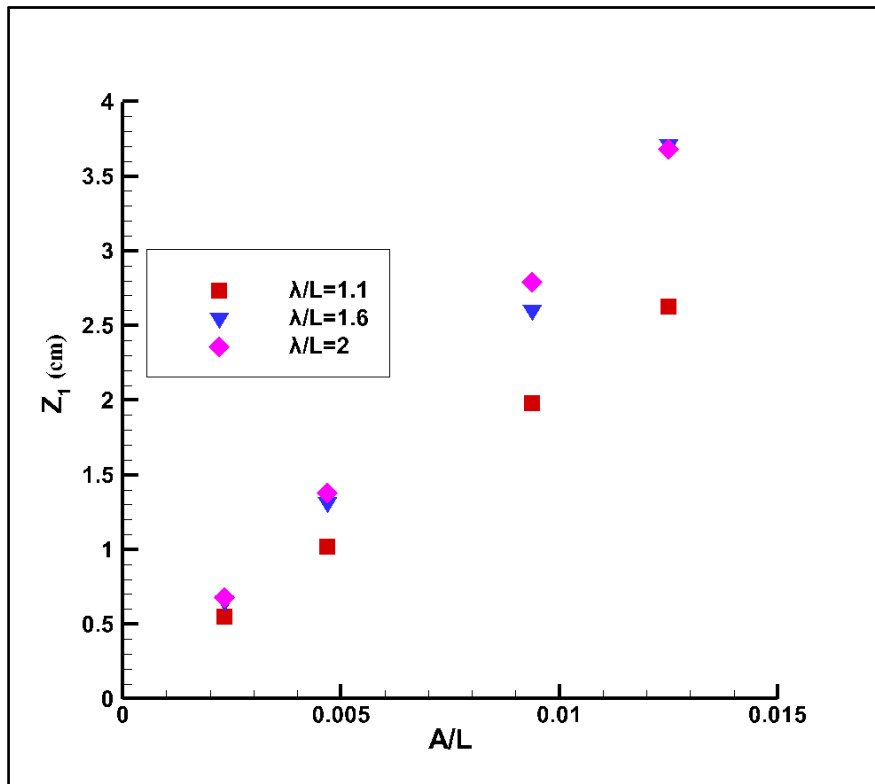


Figure 3-23 1st harmonic amplitudes for Heave motion.

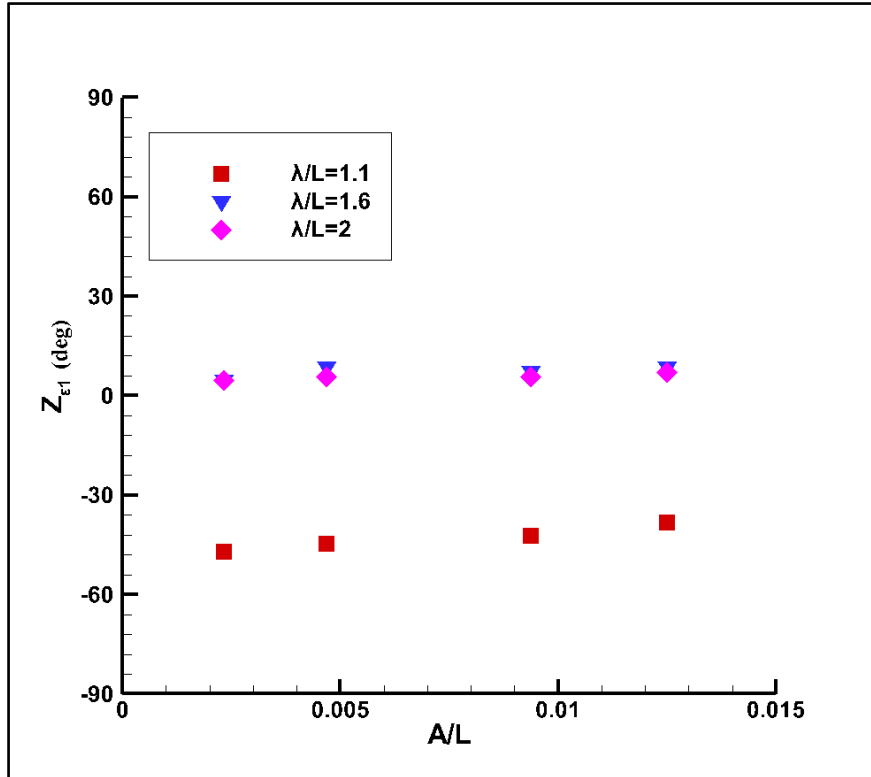


Figure 3-24 1st harmonic phases for Heave motion.

b) Pitch Motion

i. Time histories

The time histories for pitch motion are as shown in Figure 3-25~Figure 3-27. From these time histories, it can be seen that the amplitudes of oscillation for pitch motion increase as the wave amplitude increases and the phase lags are almost similar. Also, when $t=0$ the wave crest is at the propeller plane.

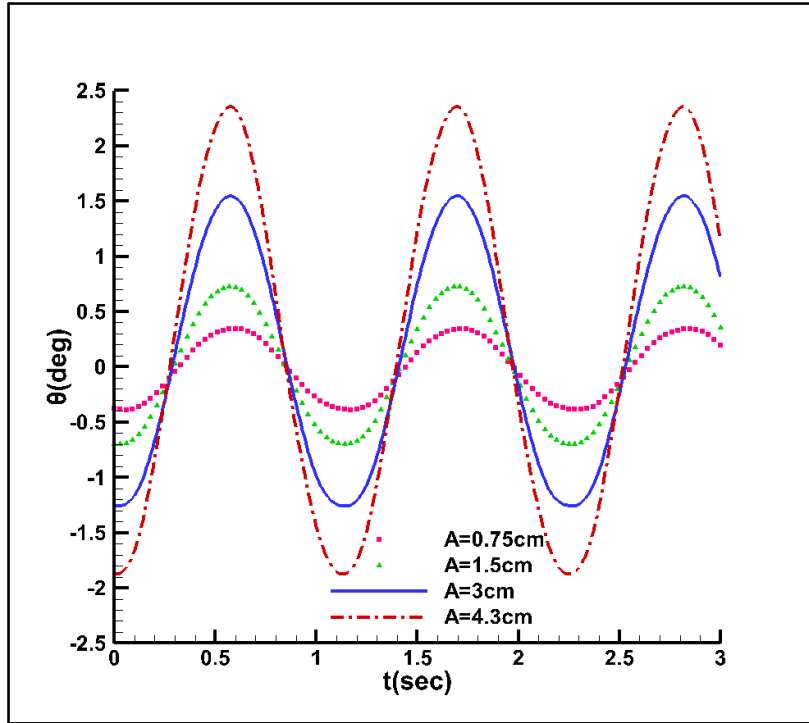


Figure 3-25 Pitch motion time history at different wave amplitudes for $\lambda/L=1.1$.

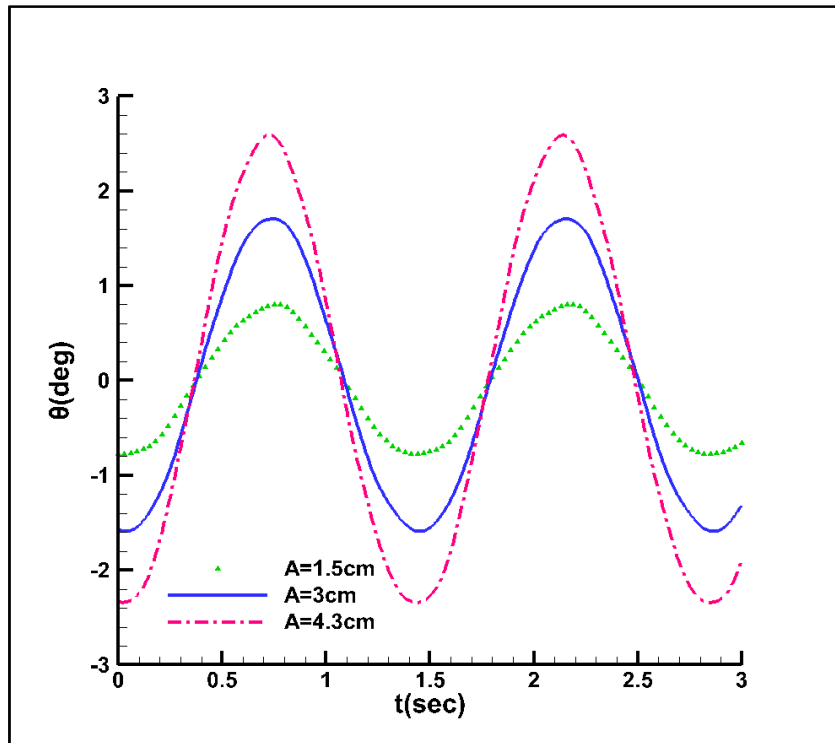


Figure 3-26 Pitch motion time history at different wave amplitudes for $\lambda/L=1.6$.

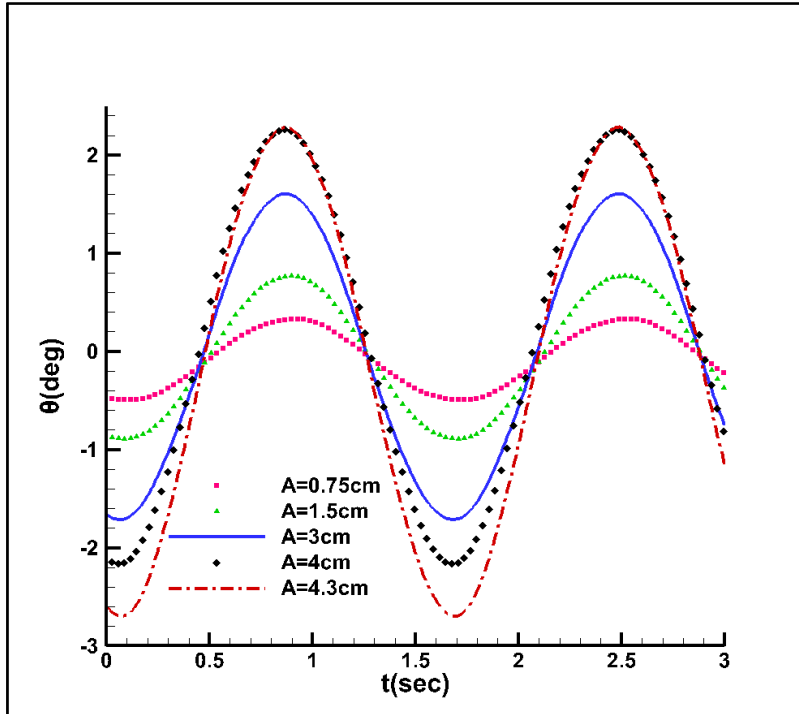


Figure 3-27 Pitch motion time history at different wave amplitudes for $\lambda/L=2.0$.

ii. Pitch 1st harmonic amplitudes and phases

The 1st harmonic amplitudes for pitch motion increase linearly as the wave amplitude increases while the phases are fairly constant as shown in Figure 3-28 and Figure 3-29 respectively.

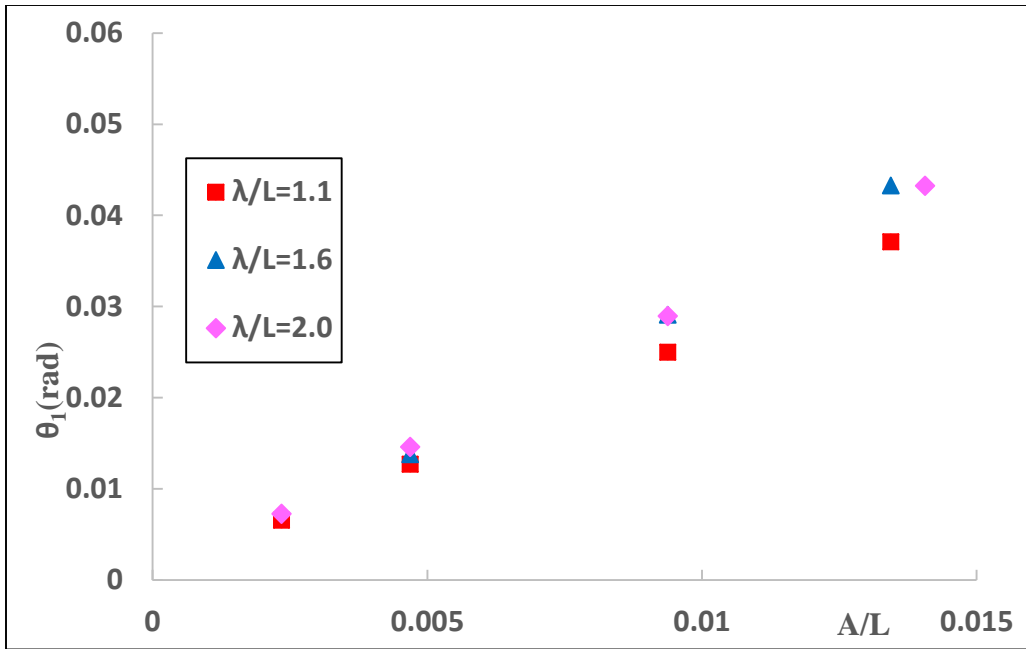


Figure 3-28 1st Harmonic amplitudes for Pitch motion.

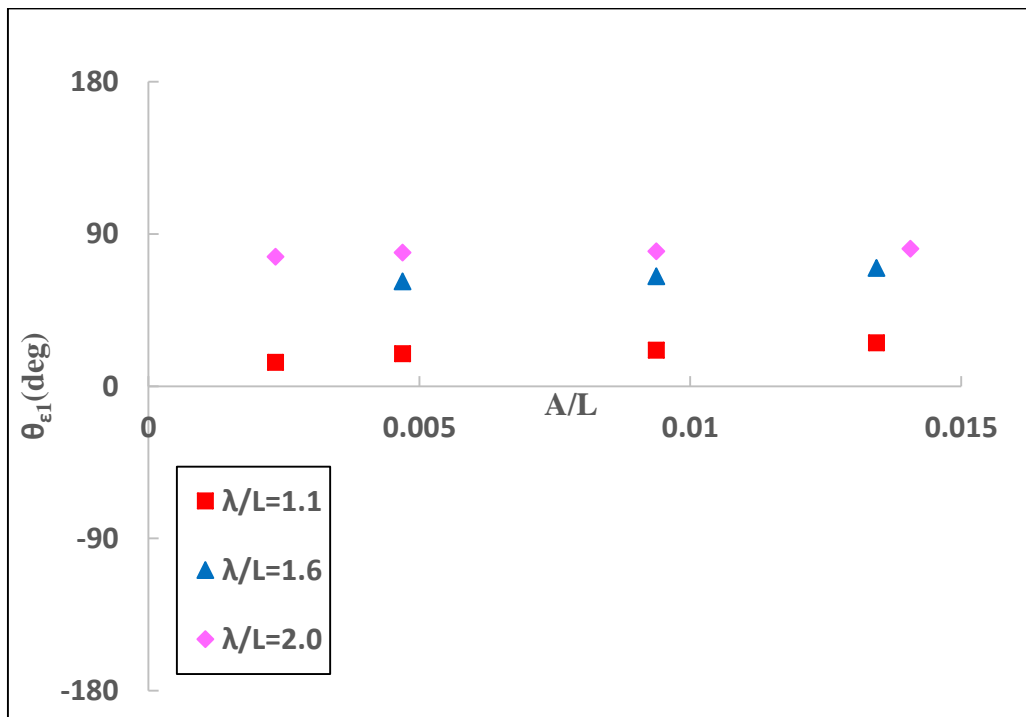


Figure 3-29 1st Harmonic phases for Pitch motion.

3.1.4 Added Resistance results

The added resistance in waves was obtained by subtracting the resistance of the ship in calm water from the mean resistance in waves. The obtained added resistance was plotted versus the square of the wave amplitude as shown in Figure 3-30. It is clearly shown that the added resistance increases linearly with A^2 (directly proportional to A^2) and the increase is tremendous at $\lambda/L=1.1$ because this is where the maximum added resistance is experienced by the ship.

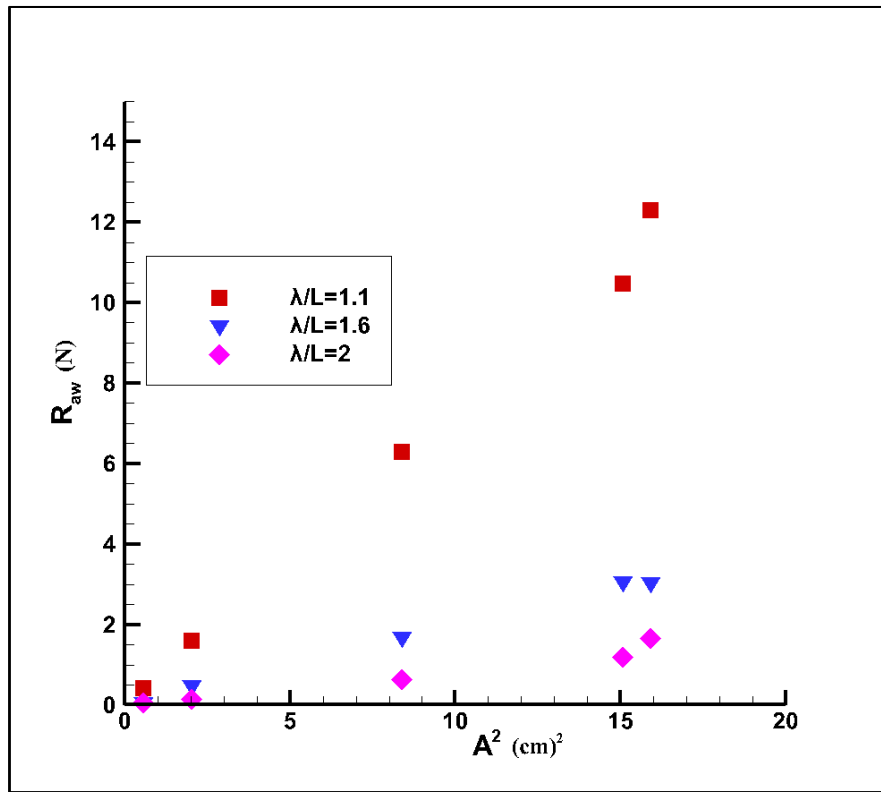


Figure 3-30 Added resistance vs. square of wave amplitude, A^2 at different λ/L .

The change of added resistance coefficient with wave amplitude is as shown in Figure 3-31. From this figure, the added resistance coefficient is fairly constant for all wavelength cases and the highest value is at $\lambda/L=1.1$ due to the maximum added resistance experienced by the ship at

this wavelength. The formula for the added resistance coefficient is as shown in equation (3-1), and from this equation, the added resistance is directly proportional to A^2 .

$$\sigma_{aw} = \frac{R_{aw}}{g\rho A^2 \left(\frac{B^2}{L}\right)} \quad (3-1)$$

Where,

σ_{aw} is the added resistance coefficient, R_{aw} is the added resistance in waves, g is the gravitational acceleration, ρ is the water density, A is the wave amplitude, B is the ship breadth, L is the ship length between the perpendiculars.

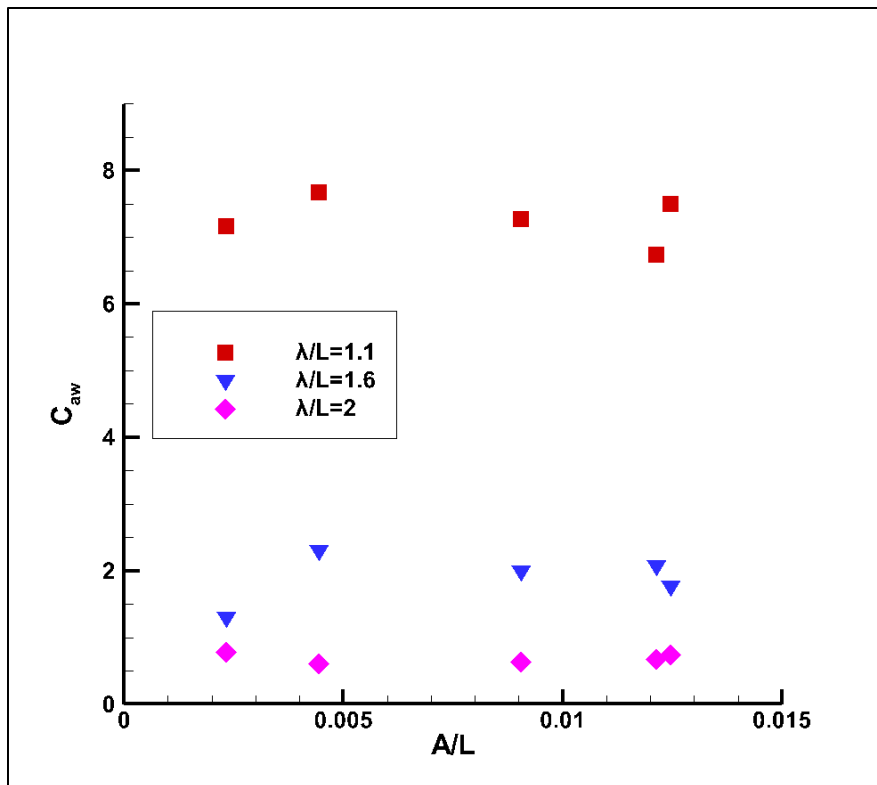


Figure 3-31 The added resistance coefficient vs. A/L at different λ/L .

3.2 ESDs Effect

3.2.1 Time histories

From the experimental data, the real physical values were obtained by subtracting the zero point values from the measured values for each quantity in order to plot their respective time histories. An example of the time histories for wave elevation, X-force, heave, pitch and surge motions is as shown in Figure 3-32, and that for thrust and torque as shown in Figure 3-33. These are used as examples for all time histories for other wave conditions because there is no much difference between them. The propeller speed for this measurement was kept constant at 16.5 rps.

3.2.2 Force measurement results

The results for thrust, torque, resistance under self-propulsion (or F_x), thrust deduction factor, effective wake factor, hull efficiency and delivered horse power from the resistance and self-propulsion experiment are as shown in Table 3-2 (Htay et al., 2021). Thrust, torque and resistance under self-propulsion were calculated using the calibration data. The self-propulsion factors were calculated using equations (3-2)~(3-7).

$$K_T = \frac{T}{\rho n^2 D^4} \quad (3-2)$$

$$K_Q = \frac{Q}{\rho n^2 D^5} \quad (3-3)$$

$$1 - t = \frac{R_T - F_x}{T} \quad (3-4)$$

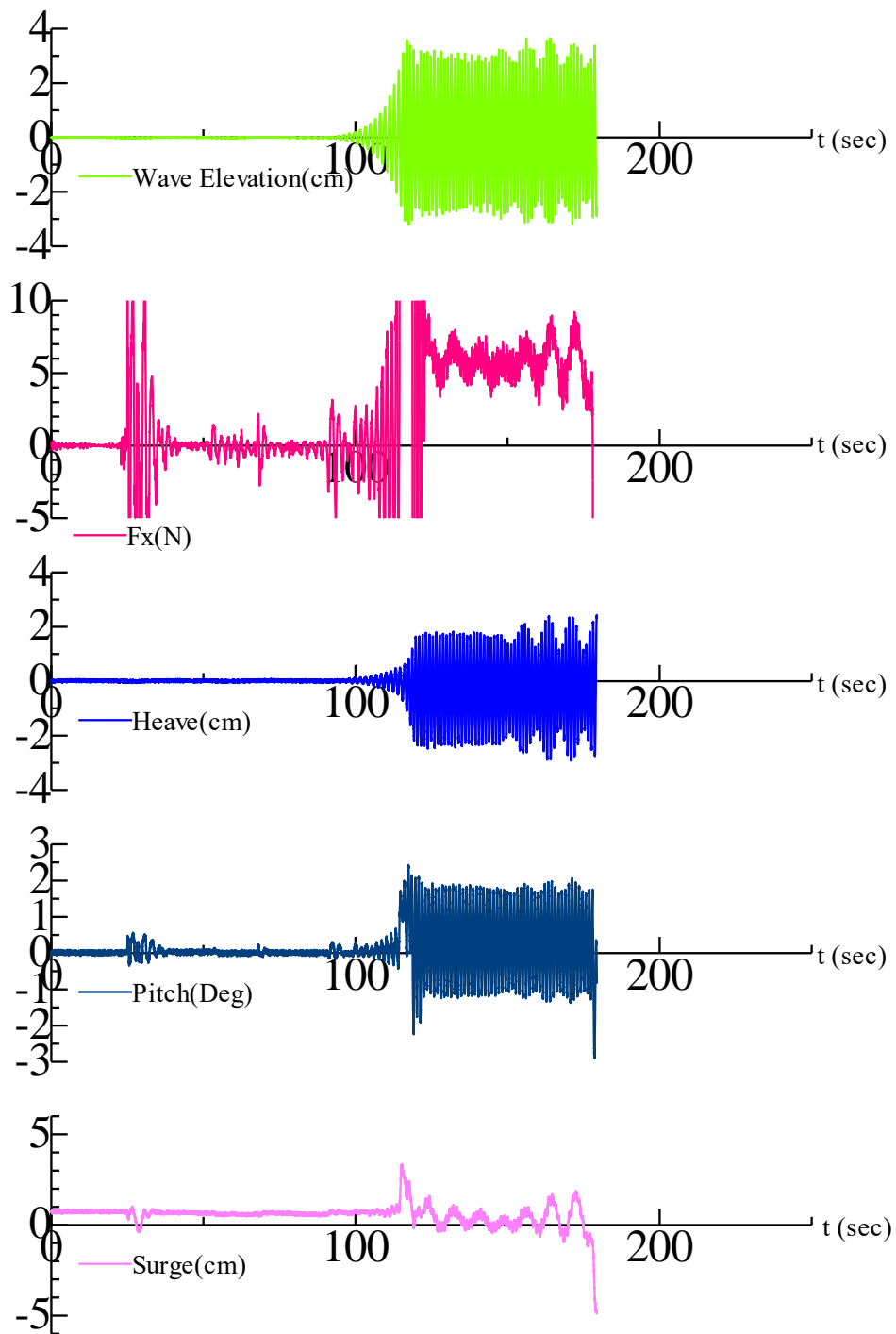


Figure 3-32 The time histories for wave elevation, X-force, heave, pitch and surge motions for $\lambda/L=1.1$ of a self-propelled KVLCC2 model ship.

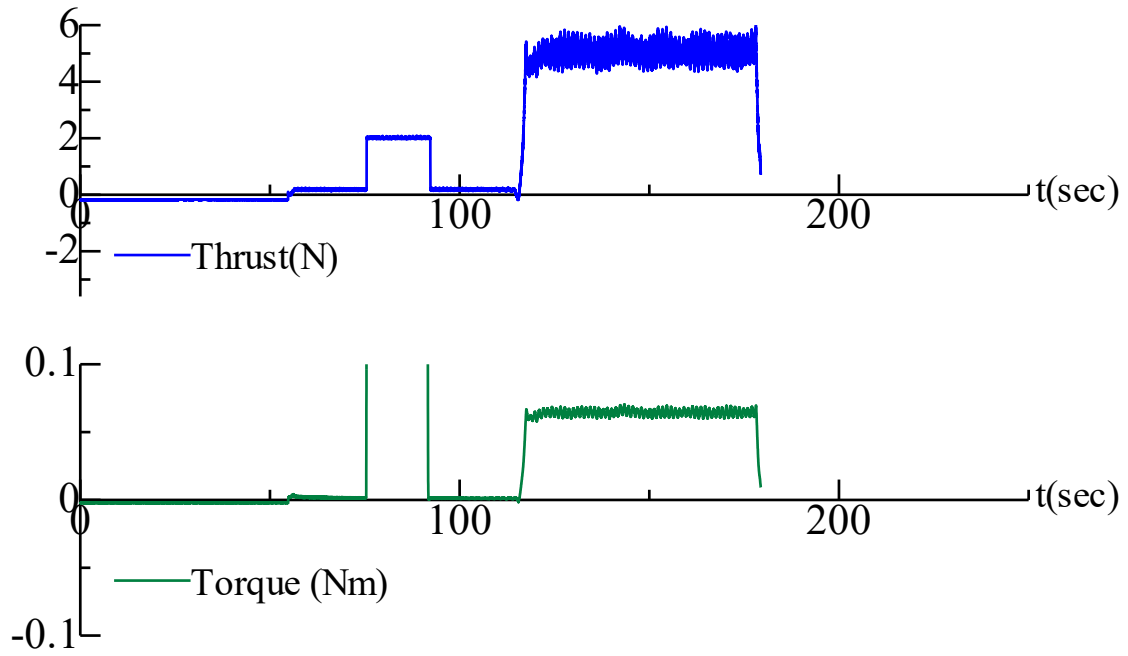


Figure 3-33 The time histories for thrust and torque for $\lambda/L=1.1$ of a self-propelled KVLCC2 model ship.

$$1 - w = \frac{nDJ}{V_s} \quad (3-5)$$

$$\eta_H = \frac{1 - t}{1 - w} \quad (3-6)$$

$$DHP = 2\pi nQ \quad (3-7)$$

Where K_T is the thrust coefficient, K_Q is the torque coefficient, $(1-t)$ is the thrust deduction factor, $(1-w)$ is the effective wake factor, η_H is the hull efficiency, DHP is the delivered horse

power, T is thrust in Newtons, Q is torque in Newton-meter, n is the propeller speed in revolutions per second, D is the propeller diameter, R_T is the resistance without propeller, F_x is the resistance under the self-propulsion condition, J is the advance ratio of the propeller, and V_S is the ship speed.

Table 3-2 The summary of forces and self-propulsion factors.

λ/L	Rudder	T(N)	Q(Nm)	$F_x(N)$ w/p	K_T	1-t	1-w	η_H	DHP(W)
0.6	NR	4.9191	0.0607	2.5096	0.1912	0.8331	0.5419	1.5374	6.2899
	RBF-F	4.9273	0.0641	2.4759	0.1913	0.8386	0.5416	1.5483	6.6540
	RBF-C	4.9540	0.0637	2.4616	0.1923	0.8369	0.5352	1.5637	6.6082
0.85	NR	4.9429	0.0597	3.5054	0.1919	0.8147	0.5375	1.5157	6.1866
	RBF-F	4.9764	0.0641	3.5587	0.1932	0.7985	0.5301	1.5062	6.6488
	RBF-C	4.9789	0.0644	3.4929	0.1933	0.8113	0.5294	1.5323	6.6833
1.1	NR	4.9247	0.0638	6.1933	0.1912	0.8285	0.5423	1.5277	6.6184
	RBF-F	4.9579	0.0639	6.1189	0.1925	0.8379	0.5343	1.5682	6.6302
	RBF-C	4.9730	0.0648	6.2450	0.1931	0.8100	0.5308	1.5259	6.7203
1.35	NR	4.9633	0.0611	4.2175	0.1927	0.8270	0.5327	1.5524	6.3390
	RBF-F	4.9651	0.0626	4.2800	0.1928	0.8141	0.5325	1.5287	6.4951
	RBF-C	4.9996	0.0653	4.2532	0.1941	0.8138	0.5245	1.5515	6.7715
1.6	NR	4.9455	0.0596	1.8031	0.1921	0.8362	0.5368	1.5576	6.1783
	RBF-F	4.9822	0.0627	1.8310	0.1934	0.8244	0.5287	1.5594	6.5029
	RBF-C	4.9853	0.0651	1.7844	0.1935	0.8332	0.5279	1.5783	6.7553

NR is the normal rudder, RBF-F is the rudder with a bulb and full fins on both port and starboard sides whereas the RBF-C is the rudder with a bulb and a full fin on the port side and a cut fin on the starboard side, w/p means with propeller.

From Table 3-2, it can be realized that the values for thrust are higher in the RBFs compared to the normal rudder. For RBFs, the propeller thrust is higher in RBF-C system compared to the RBF-F system in all wave conditions. The average torque is higher in the RBFs compared to the normal rudder in all wavelengths. On the other hand, the effective wake values are higher in the normal rudder condition compared to the RBFs. For the RBFs, the RBF-C system lowers the effective wake more compared to the RBF-F system. Therefore, the rudders with a bulb and fins utilize the rotational flow after the propeller to produce extra thrust for the ship in a more efficient way compared to the normal rudder. The thrust deduction factor is almost similar for all rudders in all wavelength conditions. It can also be seen that the efficiency is improved by RBF systems especially in short waves, and the decrease of efficiency does not occur for all wavelengths.

The data for force and self-propulsion factors was analyzed by Fourier series expansion by equation (3-8) so as to reconstruct it by ignoring harmonic components higher than 7th harmonics in order to understand the fluctuation shape in one period. Then the time histories for various quantities were plotted, and those for thrust and effective wake are as shown in Figure 3-34~Figure 3-39. These time histories are shown for one period for $\lambda/L=0.6, 1.1$ and 1.6 . The horizontal axis represents the non-dimensional time and the vertical axis represents the thrust in Newtons and the effective wake. In these time histories, the wave peak is at the ship's FP.

$$f(t) = a_0 + \sum_{j=1}^n \left\{ a_j \cos\left(j \frac{2\pi t}{T}\right) + b_j \sin\left(j \frac{2\pi t}{T}\right) \right\} \quad (3-8)$$

Where T is the wave encounter period and the coefficients a_0 , a_j and b_j are given by equations (3-9)~(3-11).

$$a_0 = \frac{1}{T} \int_0^T f(t) dt \quad (3-9)$$

$$a_j = \frac{2}{T} \int_0^T f(t) \cos\left(j \frac{2\pi t}{T}\right) dt \quad (3-10)$$

$$b_j = \frac{2}{T} \int_0^T f(t) \sin\left(j \frac{2\pi t}{T}\right) dt \quad (3-11)$$

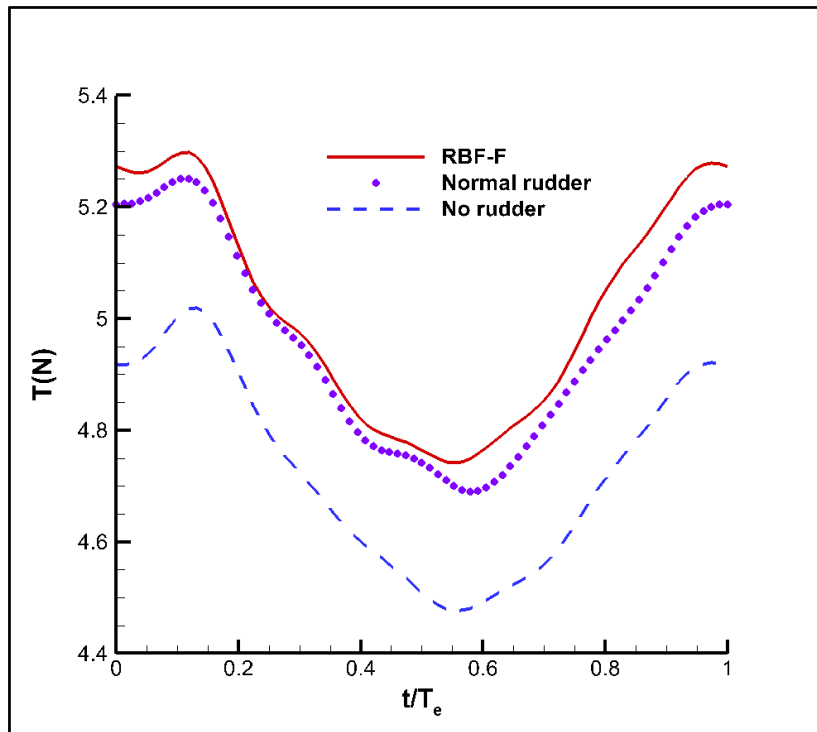


Figure 3-34 Thrust time histories for $\lambda/L=0.6$ for various rudders for one period.

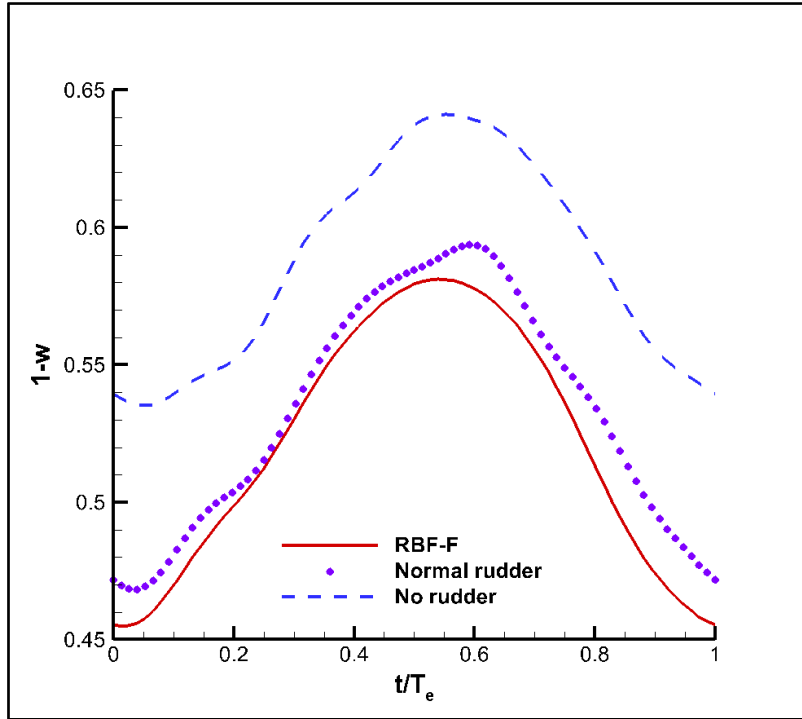


Figure 3-35 Effective wake time histories for $\lambda/L=0.6$ for various rudders for one period.

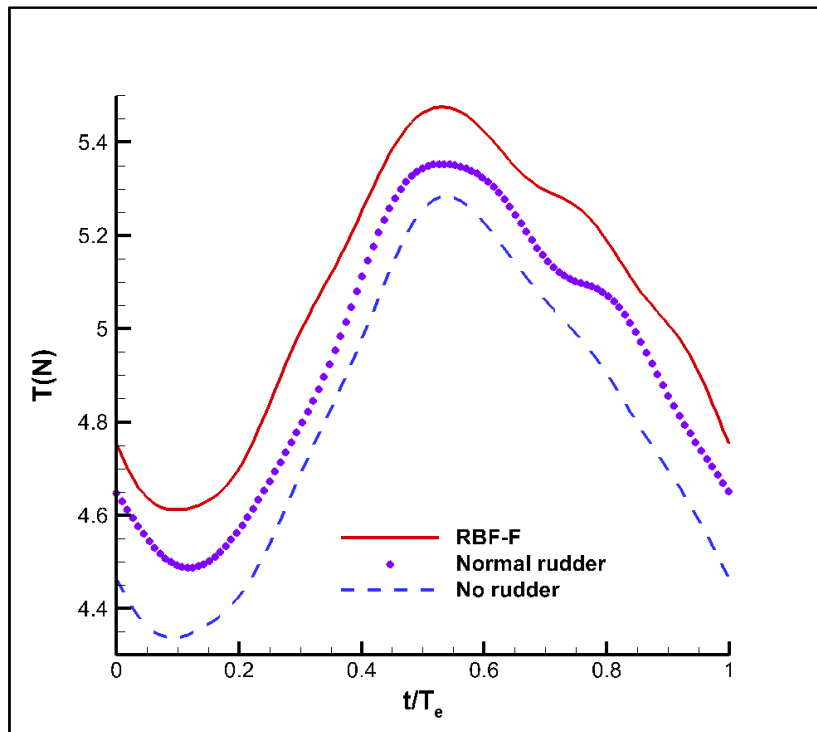


Figure 3-36 Thrust time histories for $\lambda/L=1.1$ for various rudders for one period.

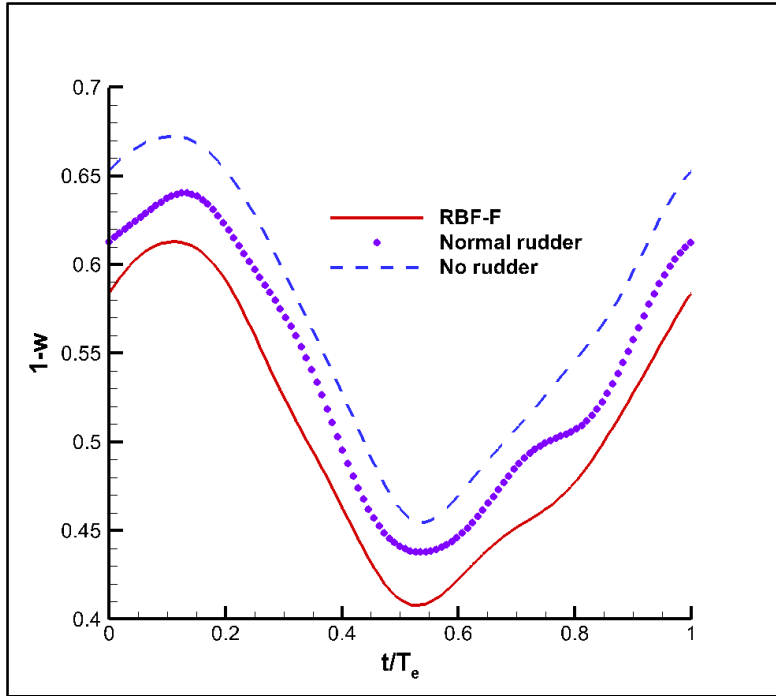


Figure 3-37 Effective wake time histories for $\lambda/L=1.1$ for various rudders for one period.

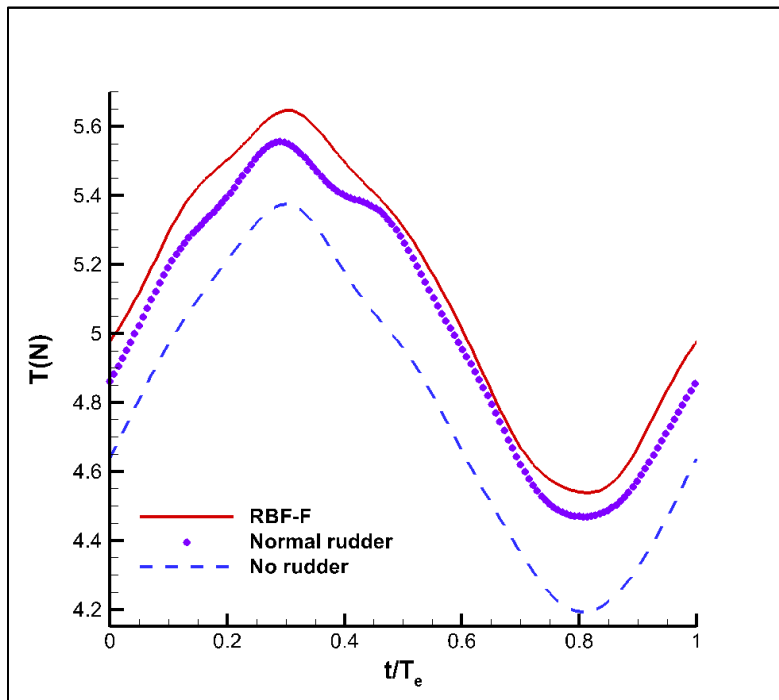


Figure 3-38 Thrust time histories for $\lambda/L=1.6$ for various rudders for one period.

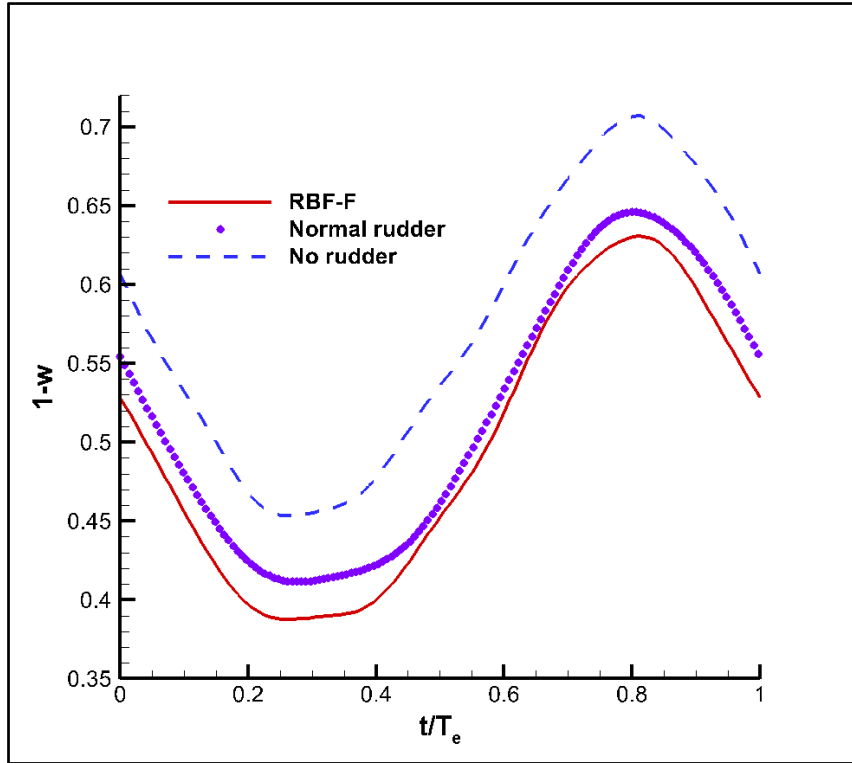


Figure 3-39 Effective wake time histories for $\lambda/L=1.6$ for various rudders for one period.

From Figure 3-34~Figure 3-39, it can be seen that the trends for effective wake time histories are inverse to those of thrust. This was also observed in the study for the wave amplitude effect. For thrust, the curves for the RBF-F system are the highest followed by those for normal rudder and are lowest for without rudder condition. This means that the mean values for thrust are highest for the RBF-F system, followed by the normal rudder and are lowest for without rudder condition as seen in Figure 3-40. The mean and 1st harmonic values for thrust and effective wake are as shown in Figure 3-40~Figure 3-43.

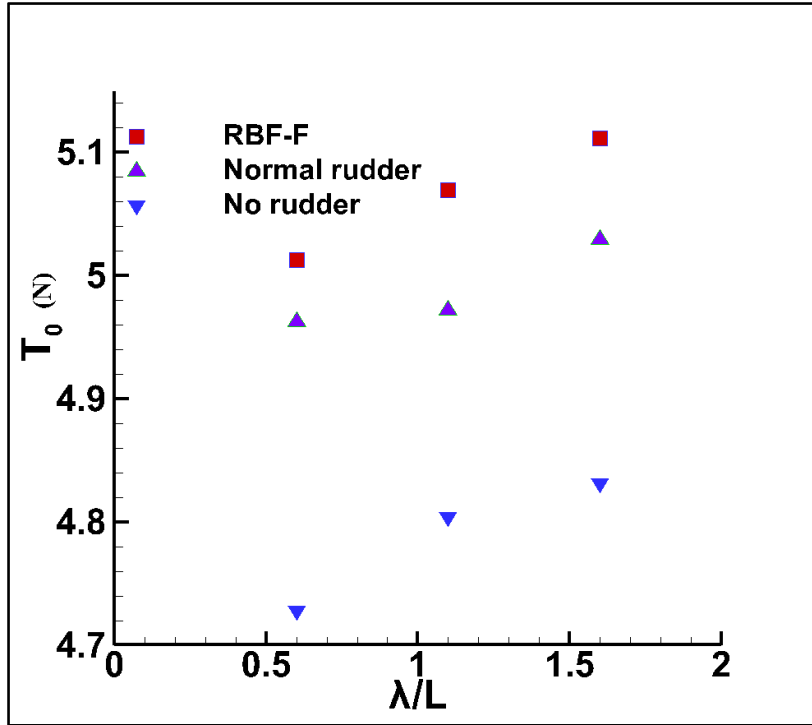


Figure 3-40 Mean thrust values for various rudders at different wavelength conditions.

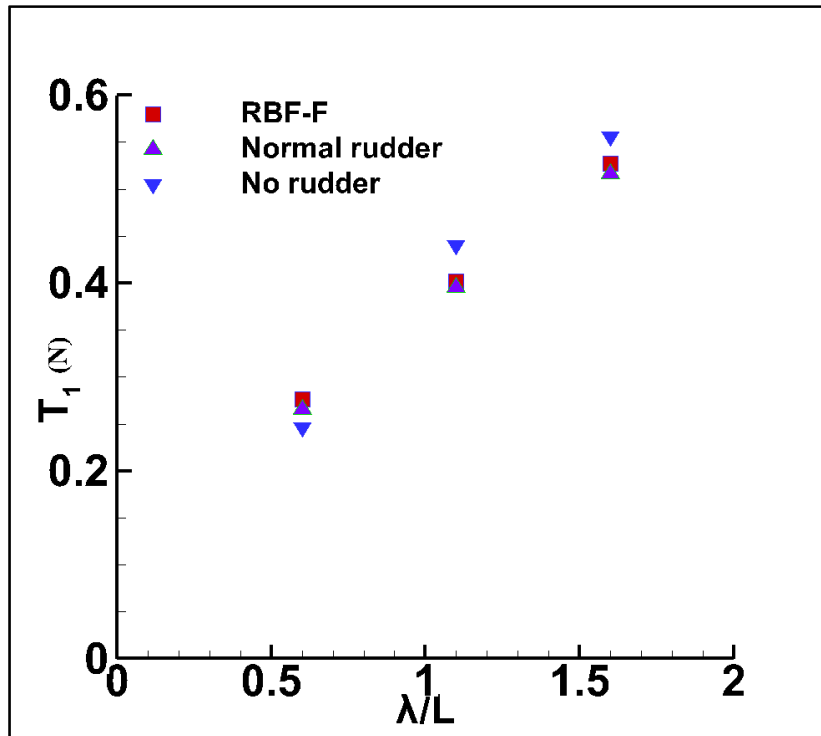


Figure 3-41 1st harmonic thrust values for various rudders at different wavelength conditions.

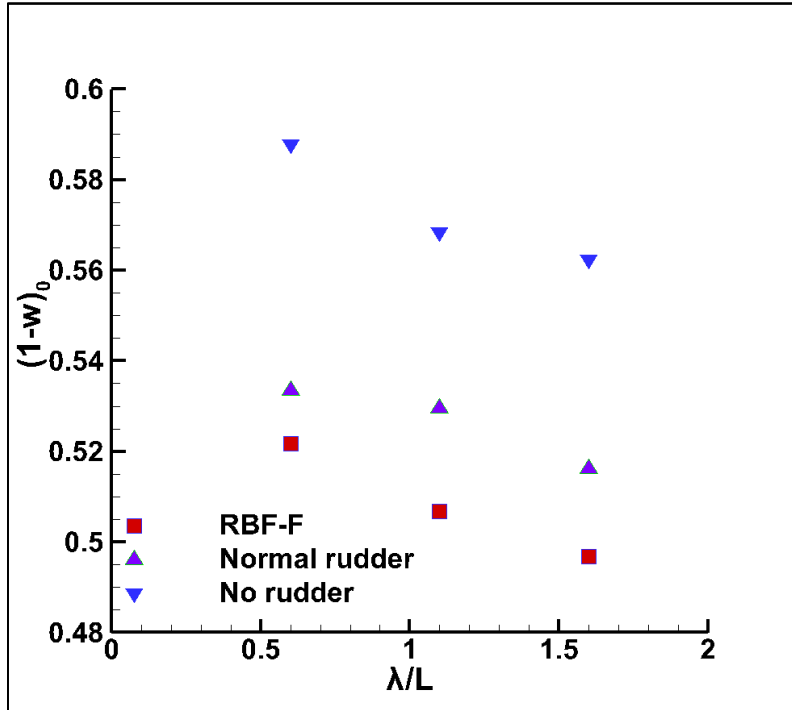


Figure 3-42 Mean effective wake values for various rudders at different wavelength conditions.

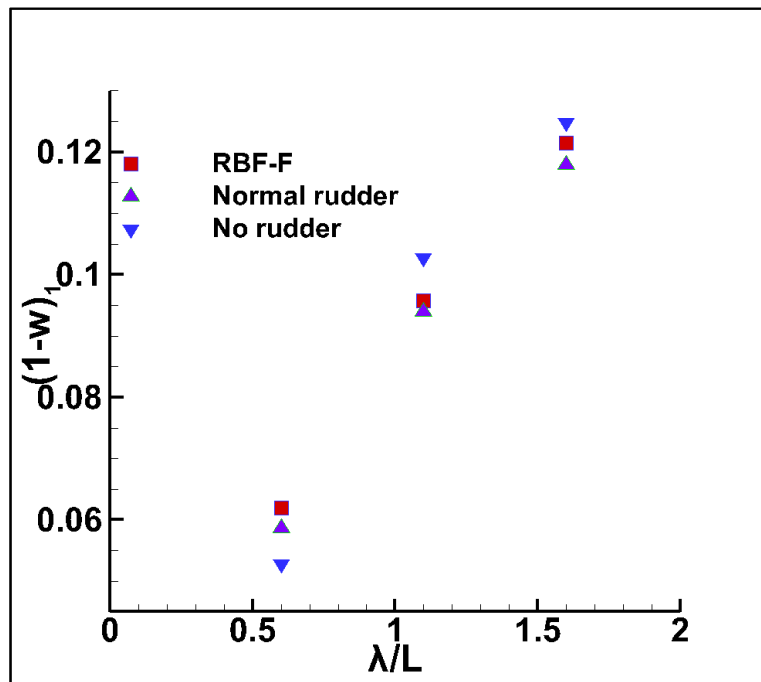


Figure 3-43 1st harmonic effective wake values for various rudders at different wavelength conditions.

From these figures, it can be seen that the mean values for thrust increase slightly as the wavelength increases for both rudder and without rudder conditions. On the other hand, the mean values for effective wake are highest for without rudder, followed by normal rudder and are lowest for the RBF-F system as can be confirmed from Figure 3-42. It can also be seen that the mean values for effective wake decrease slightly as the wavelength increases for both rudder and without rudder conditions. The 1st harmonic values for both thrust and effective wake increase linearly as the wavelength increases for with and without rudder conditions as seen in Figure 3-41 and Figure 3-43.

3.2.3 Motions results

The data for motions was also analyzed by Fourier series expansion so as to reconstruct it by ignoring harmonic components higher than 7th harmonics in order to understand the fluctuation shape in one period. Then, the time histories for the vertical motions (heave and pitch) are plotted as shown in Figure 3-44~Figure 3-46. These time histories are shown for one period for $\lambda/L=0.6$, 1.1 and 1.6. The horizontal axis represents the non-dimensional time and the vertical axis represents the wave elevation at various stations in centimeters, and motions (heave in centimeters and pitch in degrees). The wave peak is at the ship's FP. The 1st harmonic amplitudes and phases for heave and pitch motions are also plotted as shown in Figure 3-47~Figure 3-50.

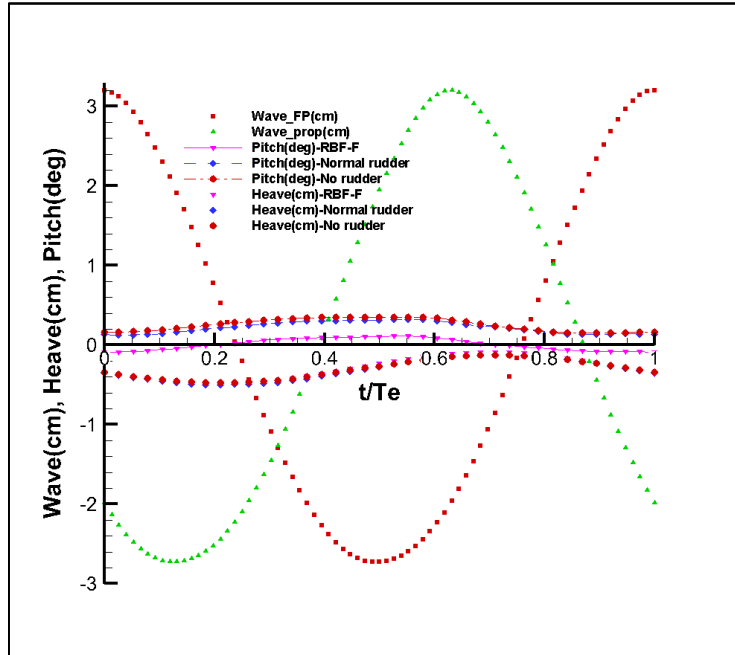


Figure 3-44 Time histories for heave, pitch and wave elevation at different stations for $\lambda/L=0.6$.

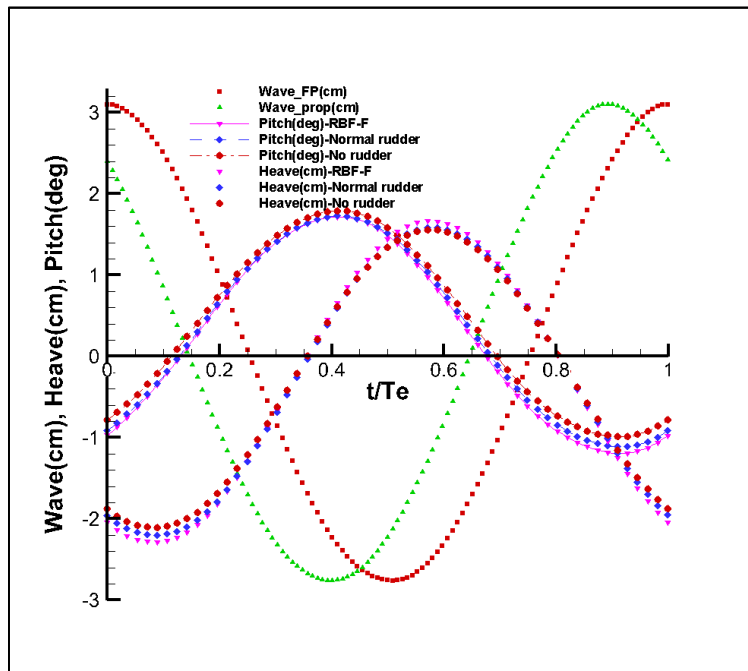


Figure 3-45 Time histories for heave, pitch and wave elevation at different stations for $\lambda/L=1.1$.

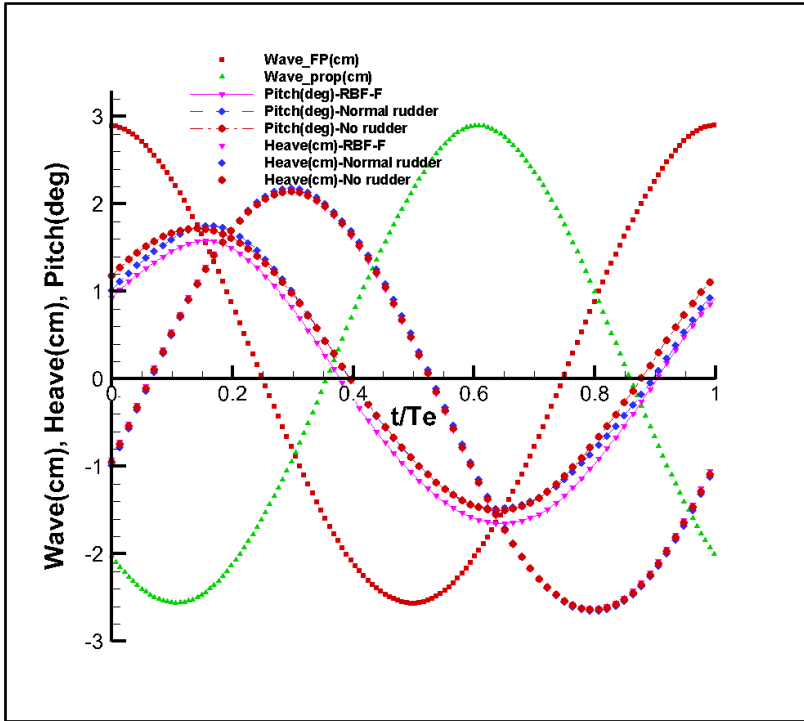


Figure 3-46 Time histories for heave, pitch and wave elevation at different stations for $\lambda/L=1.6$.

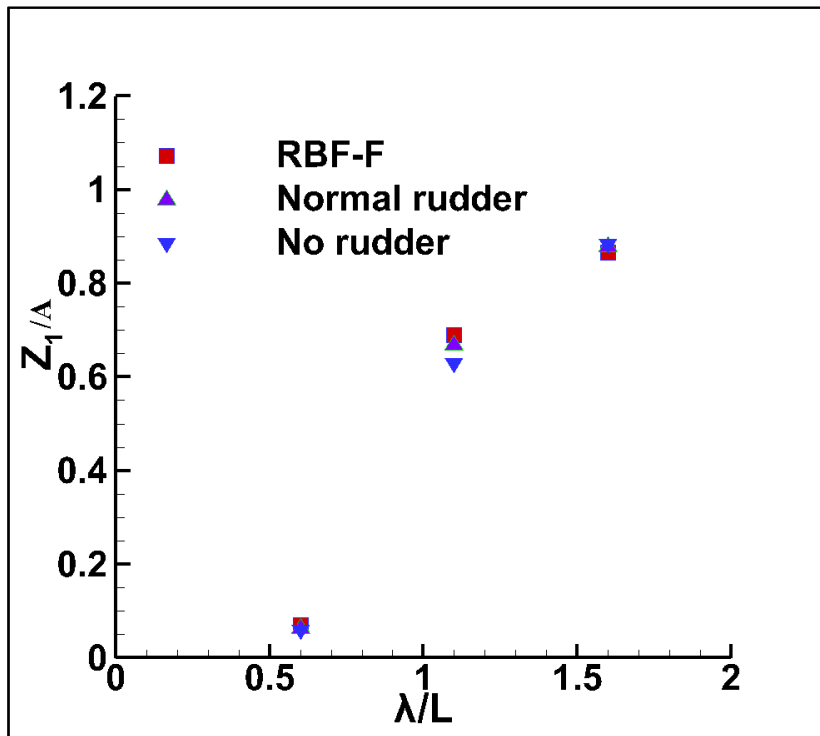


Figure 3-47 1st harmonic RAOs for heave motion for various rudders.

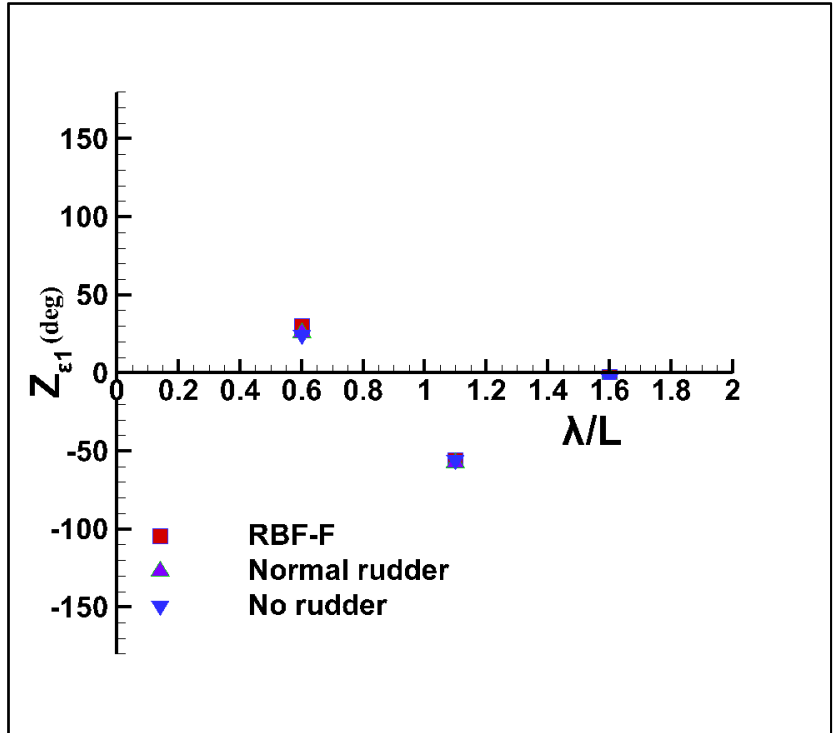


Figure 3-48 1st harmonic phases for heave motion for various rudders.

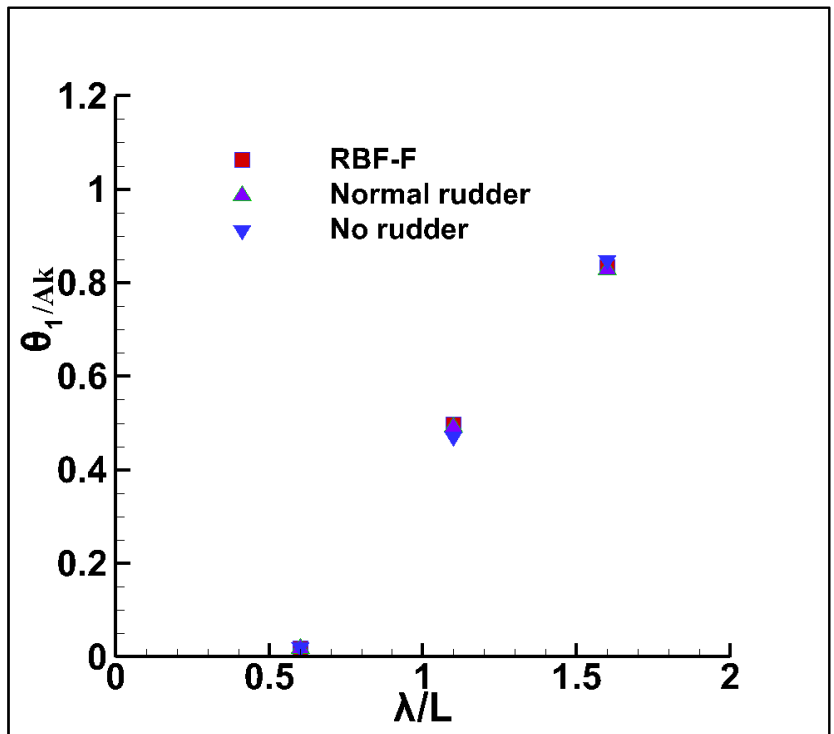


Figure 3-49 1st harmonic RAOs for pitch motion for various rudders.

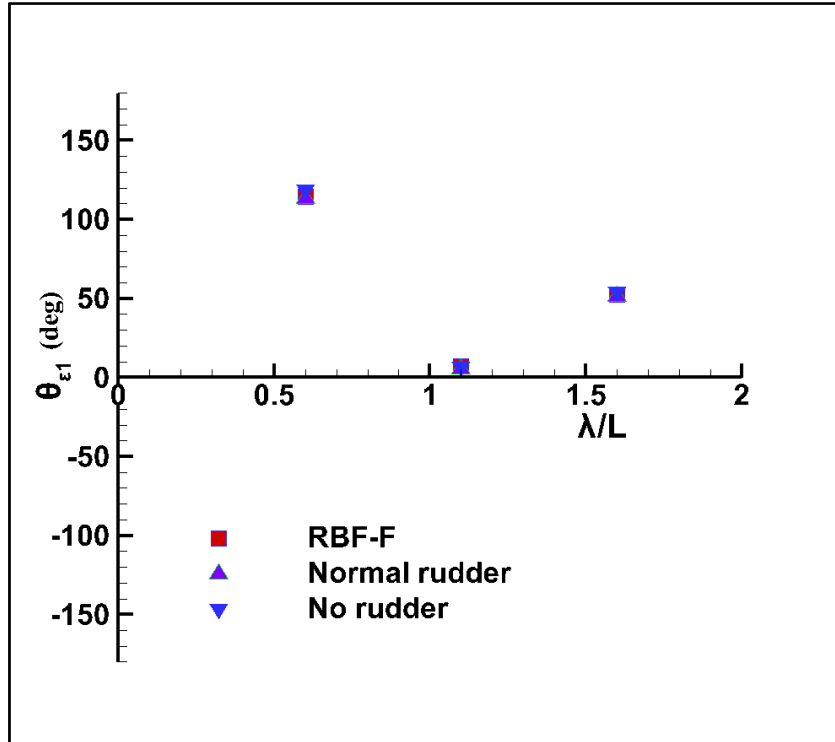


Figure 3-50 1st harmonic phases for pitch motion for various rudders.

From the heave and pitch time histories, it can be seen that the amplitudes of oscillation for the motions are smaller for shorter wavelengths and as the wavelength increases the amplitudes of oscillation increase. From these time histories, there is no significant influence of the rudders on motions. From Figure 3-47, it can also be seen that the 1st harmonic response amplitude operators (RAOs) for heave motion are about 0.06 for shorter wavelengths ($\lambda/L=0.6$) for with and without rudder condition. They increase to about 0.6 for medium wavelength ($\lambda/L=1.1$) and about 0.9 for long wavelength ($\lambda/L=1.6$) for both rudder and without rudder conditions. The increase is linear as the wavelength increases. From Figure 3-48, it can be seen that the 1st harmonic phases for heave motion are around 30 degrees for shorter waves and they decrease to about -60 degrees for ($\lambda/L=1.1$) from where they increase to about 0 degrees for longer waves ($\lambda/L=1.6$) for both

rudder and without rudder conditions. This shows that in long waves the ship just moves up and down with the waves.

From Figure 3-49 it can be seen that the 1st harmonic RAOs for pitch motion are around zero for shorter wavelength ($\lambda/L=0.6$) and increase linearly to about 0.85 in long waves ($\lambda/L=1.6$) for both rudder and without rudder conditions. From Figure 3-50, the 1st harmonic phases for shorter waves are around 115 degrees and decrease drastically to about 0 degrees for medium wavelength ($\lambda/L=1.1$) and thereafter increase to about 55 degrees for longer waves ($\lambda/L=1.6$) for all rudder cases. The 1st harmonic phase lags for heave and pitch motions were obtained from the difference between the phases for motions and the wave at the heaving rod (the ship's center of gravity). From these figures, it is also observed that for both heave and pitch motions there is no major difference among the 1st harmonic values for with and without rudder condition.

CHAPTER 4: SPIV MEASUREMENT RESULTS

4.1 Wave Amplitude Effect

4.1.1 Velocity field result for calm water

The velocity field result for calm water without propeller condition is as shown in Figure 4-1. The axial velocity, u and the cross flow velocities (v and w) are non-dimensionalized by the ship's forward speed, V_s . The y and z axes are non-dimensionalized by the ship's length between the perpendiculars, L . The bilge vortices can be seen above the dummy hub rotating clockwise at the port side and counter clockwise at the starboard side within the propeller radius. About 230 images were collected and averaged to get the velocity distribution diagram for calm water condition. For the measurement of the flow field in calm water, internal signals were used for the SPIV system to record the images.

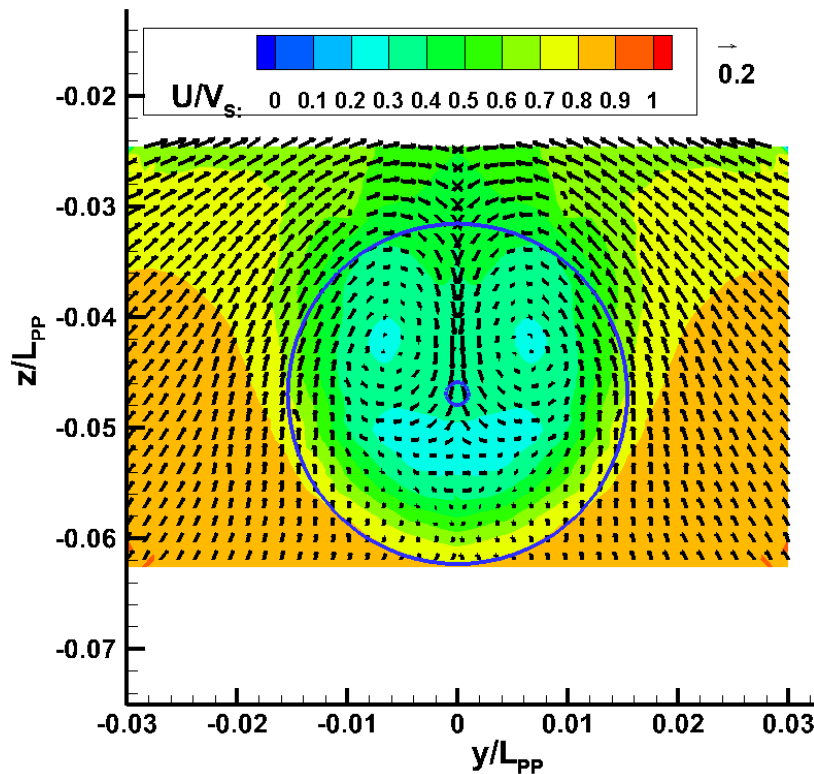


Figure 4-1 Velocity distribution for calm water condition.

4.1.2 Velocity field results for waves

a) Results for $\lambda/L=1.1$

The phase averaged nominal wake fields at the ship AP for different wave amplitudes at $\lambda/L=1.1$, are as shown in Figure 4-2~Figure 4-5. For the smallest wave amplitude ($A=0.75\text{cm}$), the SPIV measurement was done at one vertical plane but for larger wave amplitudes i.e. $A= 1.5, 3$ and 4.3cm , the SPIV measurement was done at two vertical planes. For example, at $A=4.3\text{cm}$, one vertical plane was where the SPIV system was lowered by 50mm from the zero-point position and the other position was where it was raised by 50mm from the zero-point position. These two vertical measurement planes had an overlap for continuity in capturing the whole flow field of interest. The average number of images collected per phase was 180 so as to obtain a sufficient number of images for the velocity field analysis. In order to visualize clearly the vertical relative motion between the propeller disk and the low velocity region, the propeller disk and its center under the undisturbed calm water surface are drawn on the figures. The distance of the propeller center under the undisturbed calm water surface and its diameter are non-dimensionalized by the ship's length between the perpendiculars (L) and they are; $z/L=-0.04688$ and $d/L=0.03081$.

From the velocity field figures, the vertical relative motion between the propeller disk and the low velocity region can clearly be seen. The bilge vortices, in the middle layer of the wake, can be seen moving relative to the vertical stern motion. Sometimes the bilge vortices move outside the propeller radius especially when the ship stern is moving down (phase 90 degree) and when the ship stern is moving up (phase 270 degree) in larger wave amplitudes. As the wave amplitude increases, this relative motion increases and high velocity flow enters the propeller disk from the bottom. These phenomena certainly have an influence on the thrust fluctuations.

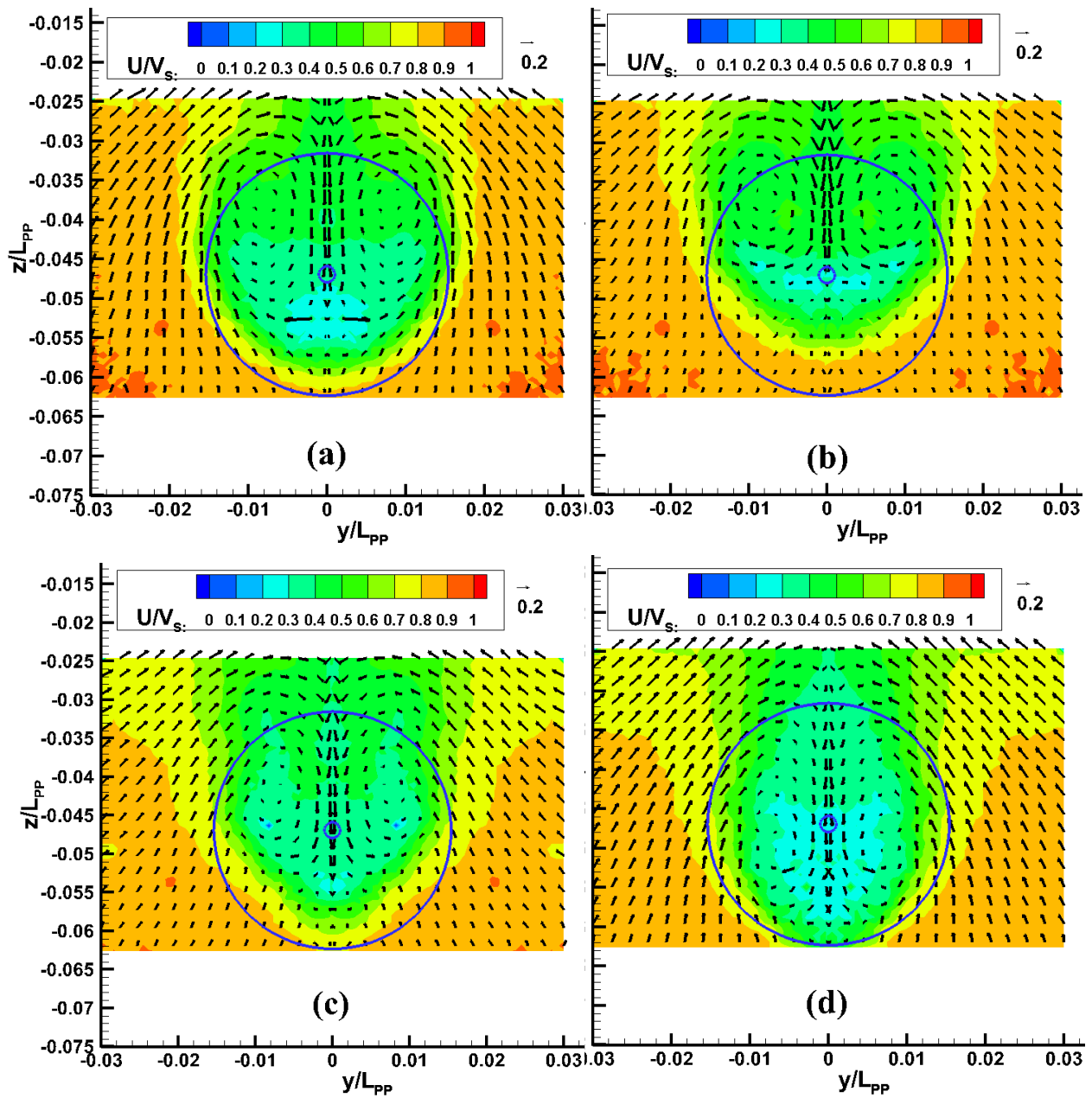


Figure 4-2 Phase-averaged velocity distribution at AP for $\lambda/L=1.1$, $A=0.75\text{cm}$; (a) 0° , (b) 90° (c) 180° and (d) 270° .

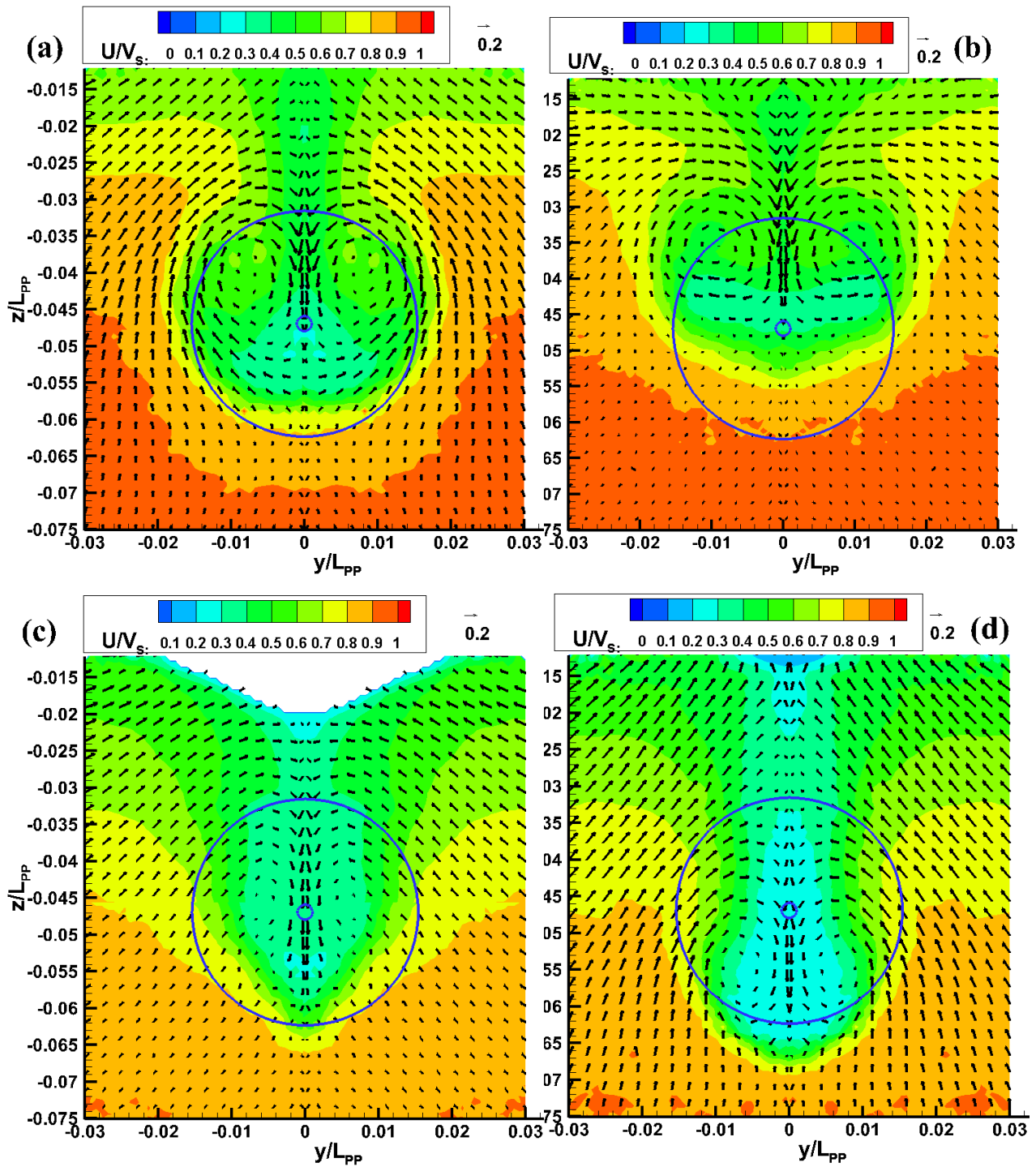


Figure 4-3 Phase-averaged velocity distribution at AP for $\lambda/L=1.1$, $A=1.5\text{cm}$; (a) 0° , (b) 90° (c) 180° and (d) 270° .

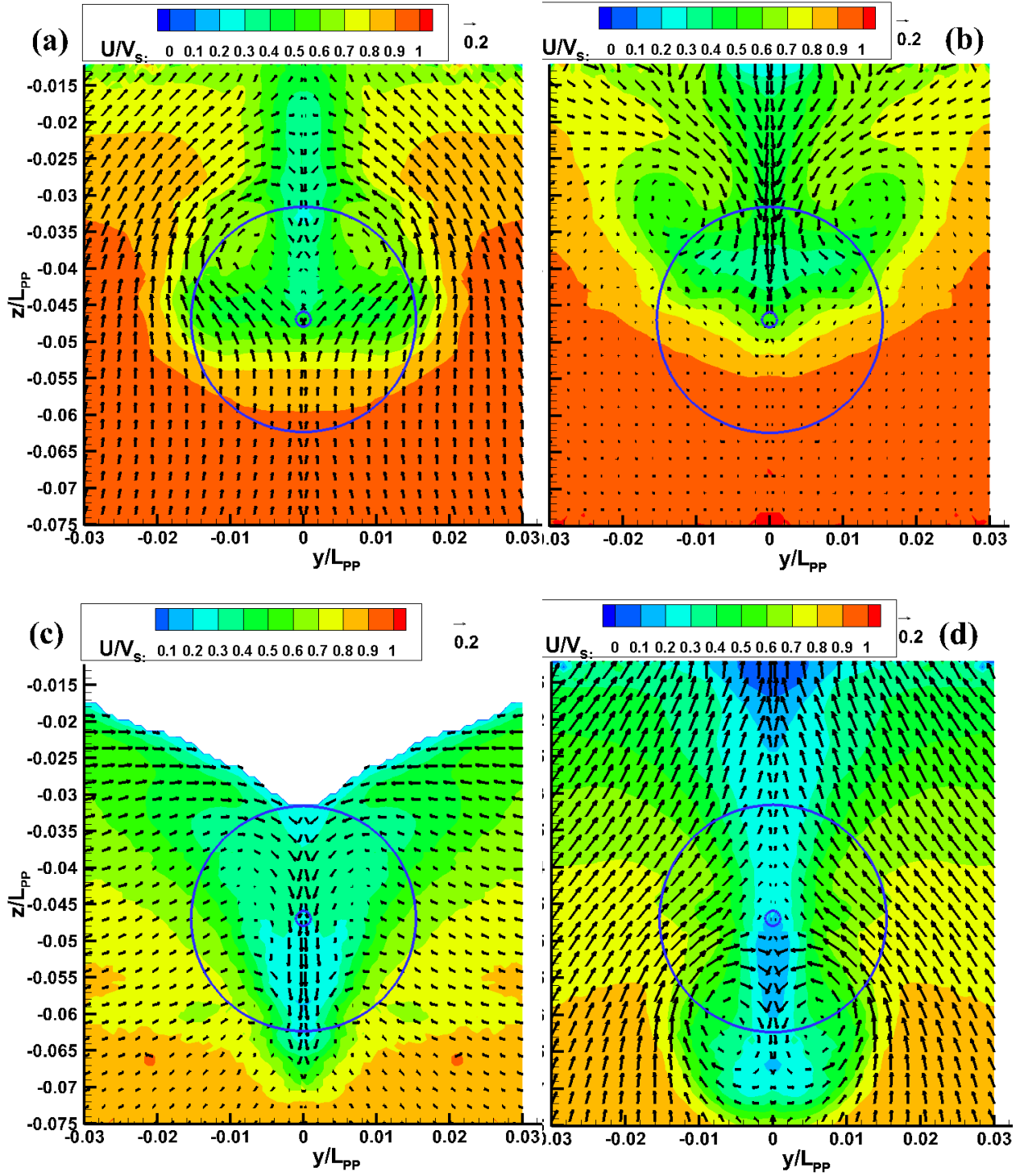


Figure 4-4 Phase-averaged velocity distribution at AP for $\lambda/L=1.1$, $A=3\text{cm}$; (a) 0° , (b) 90° (c) 180° and (d) 270° .

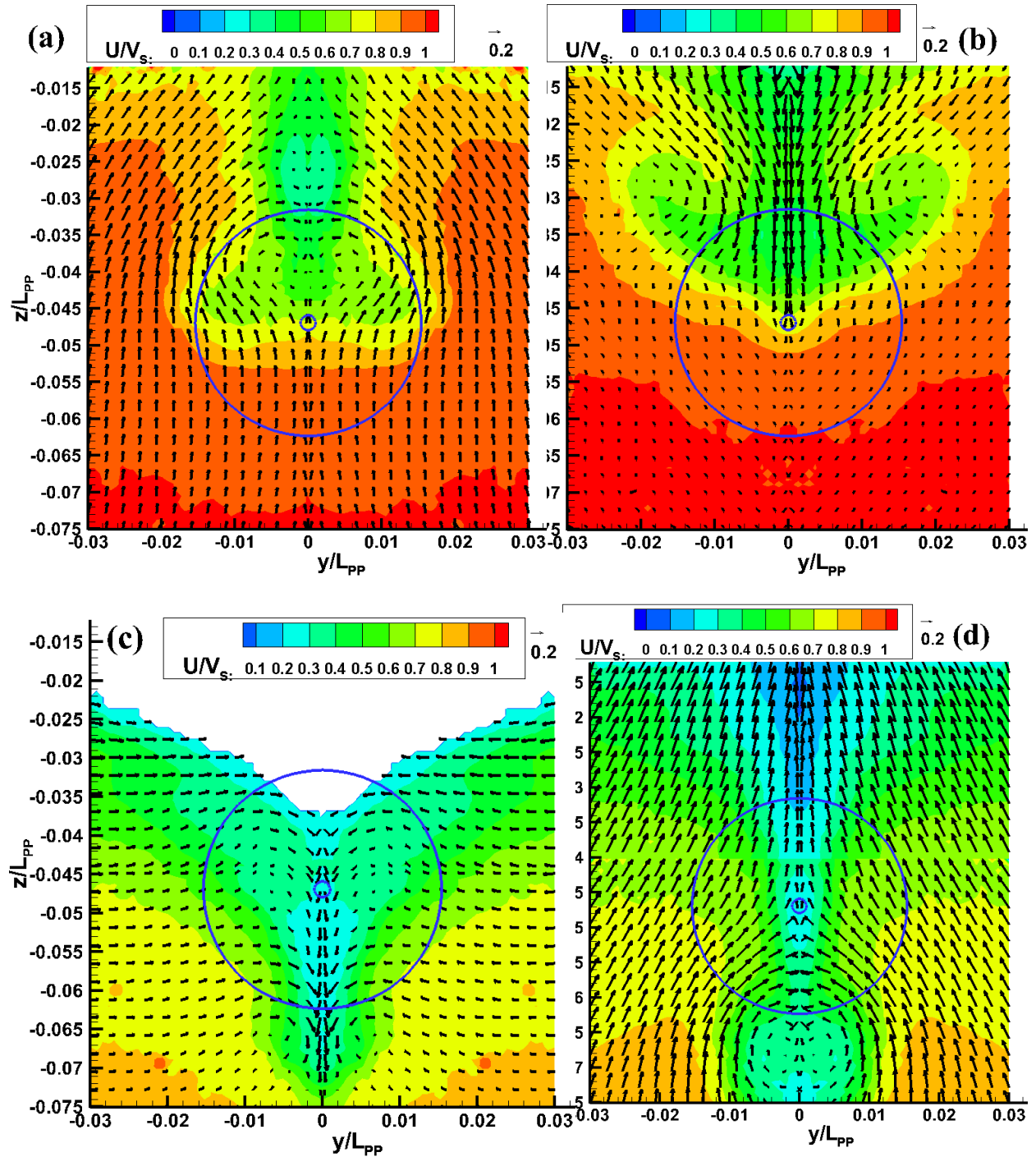


Figure 4-5 Phase-averaged velocity distribution at AP for $\lambda/L=1.1$, $A=4.3\text{cm}$; (a) 0° , (b) 90° (c) 180° and (d) 270° .

From the phase-averaged velocity distribution figures for $\lambda/L=1.1$, the inflow velocity into the propeller disk is highest at phase 90 when the ship stern is moving down and lowest at phase 270 when the ship stern is moving up. Figure 4-6 and Figure 4-7 show the thrust fluctuation, wave elevation at various stations and phases where the flow field measurement was done in one period. Looking at the thrust fluctuation trend at the shown phases, it can be concluded that the inflow into the propeller influences the propeller thrust. Moreover, since the inflow into the propeller changes with the wave amplitude, the propeller thrust will certainly be influenced. It should be noted that in these figures, the wave peak is at the propeller plane.

From the thrust time history in Figure 4-7, the lowest thrust region is at phase 90 degree where the inflow velocity into the propeller is highest and the highest thrust region is at phase 270 degree where the inflow velocity into the propeller is the lowest. This can be confirmed from Figure 4-6 in which the thrust fluctuation for a wave amplitude, $A=3\text{cm}$ has been used as an example. The true mean value for thrust is not zero as indicated in this figure, but the mean value has been subtracted intentionally from thrust time history values so as to understand how thrust changes with the wave at the propeller plane by directly placing the thrust curve against the waves' curves. As the wave amplitude increases, the lowest thrust region increases downwards causing a slight decrease in the mean thrust as shown by the horizontal dotted lines in Figure 4-7 and as discussed in the section above for thrust, torque and effective wake results. The wave amplitude values shown on this figure are measured values and not target ones.

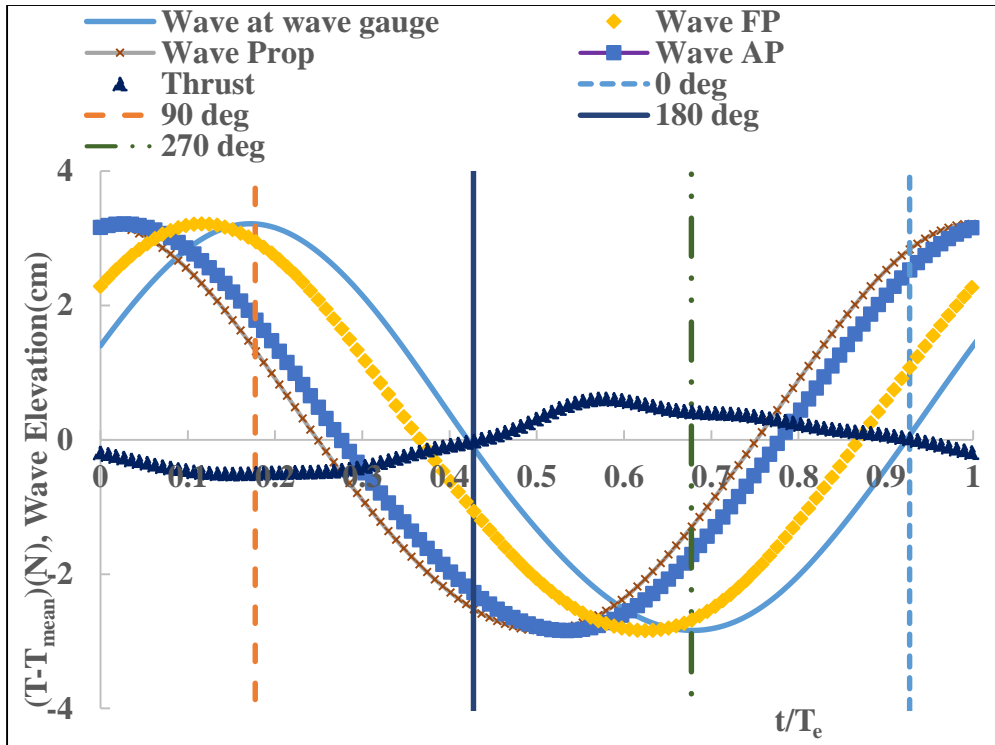


Figure 4-6 Thrust fluctuation and wave elevation for one period at $\lambda/L=1.1$, $A=3\text{cm}$.

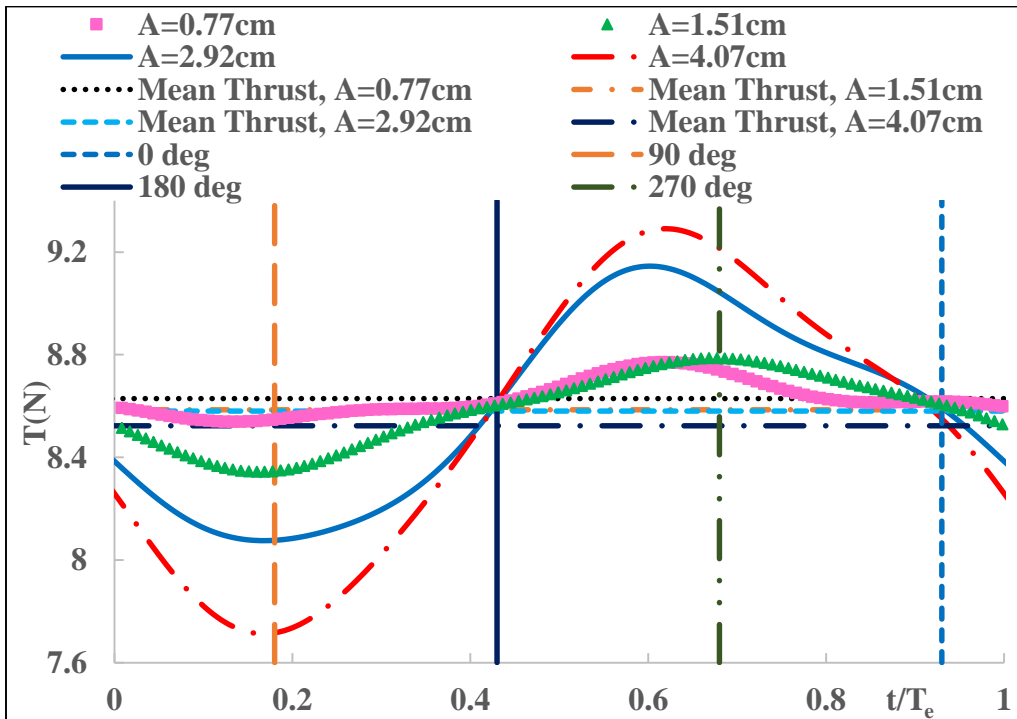


Figure 4-7 Thrust time history with its mean values for $\lambda/L=1.1$, at different wave amplitudes.

b) Result for $\lambda/L=1.6$

The phase averaged nominal wake fields at the ship AP for different wave amplitudes at $\lambda/L=1.6$, are as shown in Figure 4-8~Figure 4-10. For the wave amplitude ($A=1.5\text{cm}$), the SPIV measurement was done at one vertical plane but for larger wave amplitudes i.e. $A= 3$ and 4.3cm the SPIV measurement was done at two vertical planes where the SPIV system was raised and lowered by 40mm and 50mm from the zero-point position respectively. The average number of images collected per phase was 180 so as to obtain sufficient number of images for the velocity field analysis. In order to visualize clearly the vertical relative motion between the propeller disk and the low velocity region, the propeller disk and its center under the undisturbed calm water surface are also drawn on the figures.

From the phase-averaged velocity field figures, the vertical relative motion between the propeller disk and the low velocity region can clearly be seen. The bilge vortices, in the middle layer of the wake, can be seen moving relative to the vertical ship stern motion, and sometimes they even move outside the propeller radius. This occurs especially in larger wave amplitudes. As the wave amplitude increases, this relative motion increases and high velocity flow enters the propeller disk from the bottom. These phenomena definitely have an influence on the thrust fluctuations.

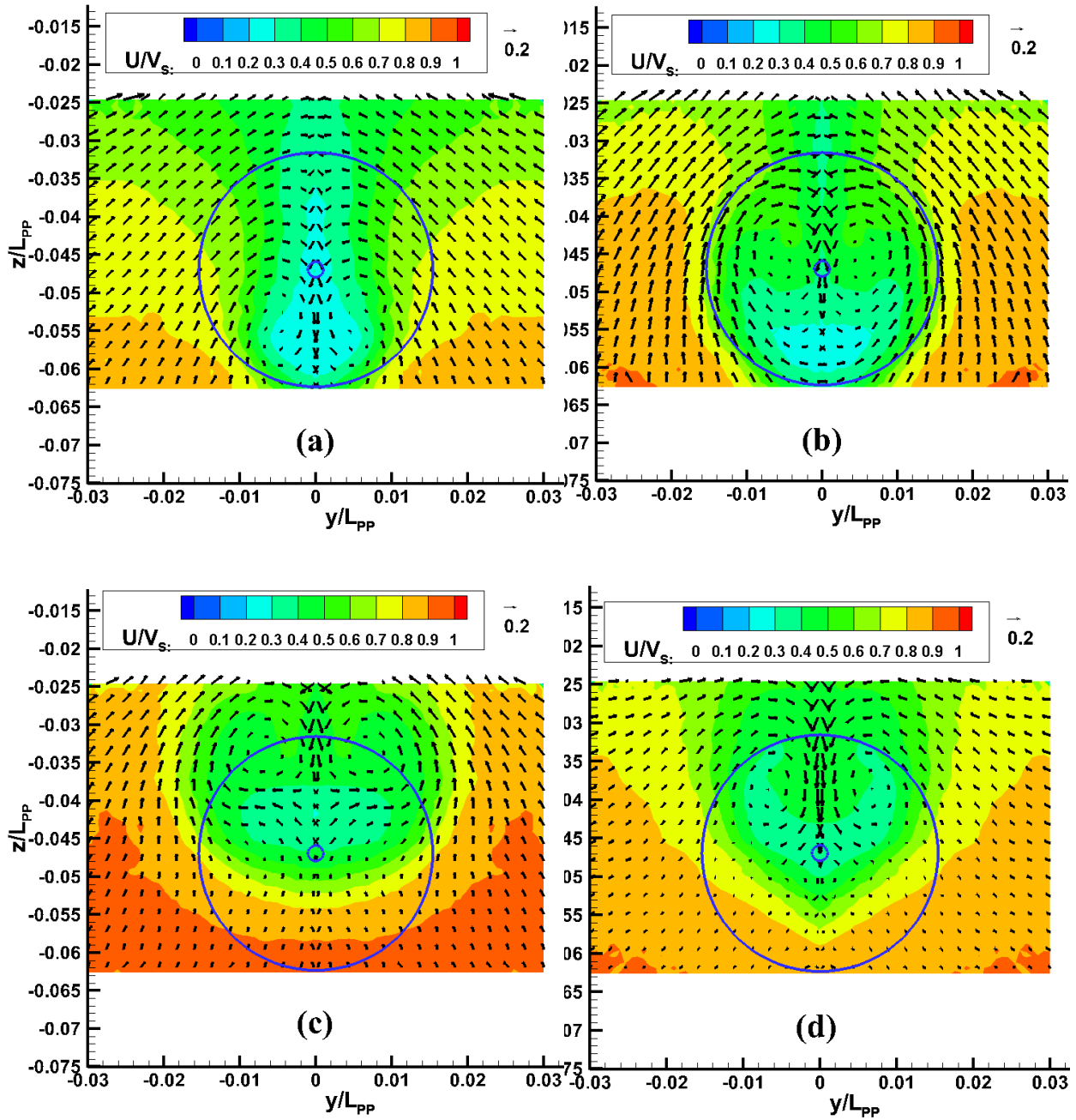


Figure 4-8 Phase-averaged velocity distribution at AP for $\lambda/L=1.6$, $A=1.5\text{cm}$; (a) 0° , (b) 90° (c) 180° and (d) 270° .

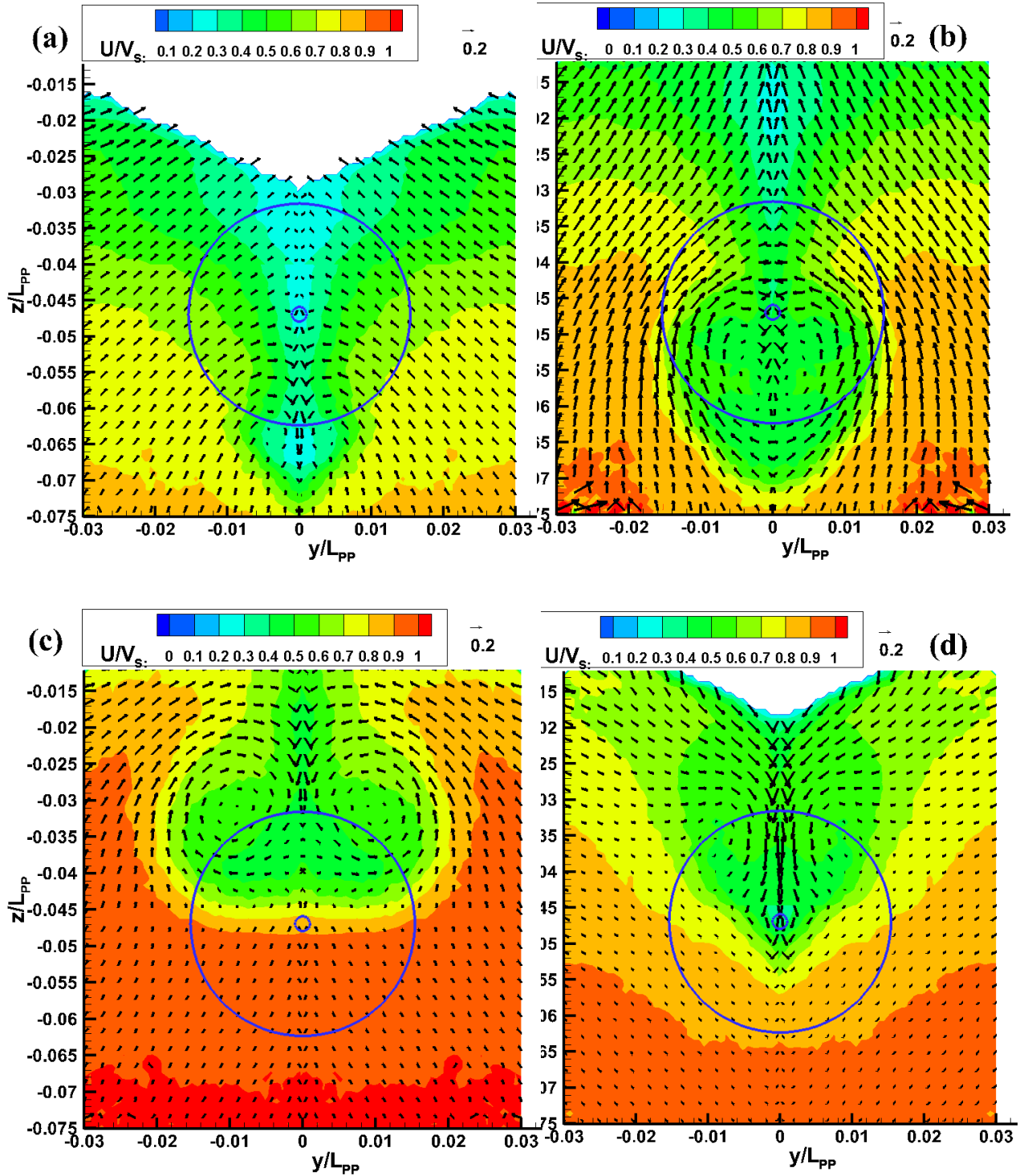


Figure 4-9 Phase-averaged velocity distribution at AP for $\lambda/L=1.6$, $A=3.0\text{cm}$; (a) 0° , (b) 90° (c) 180° and (d) 270° .

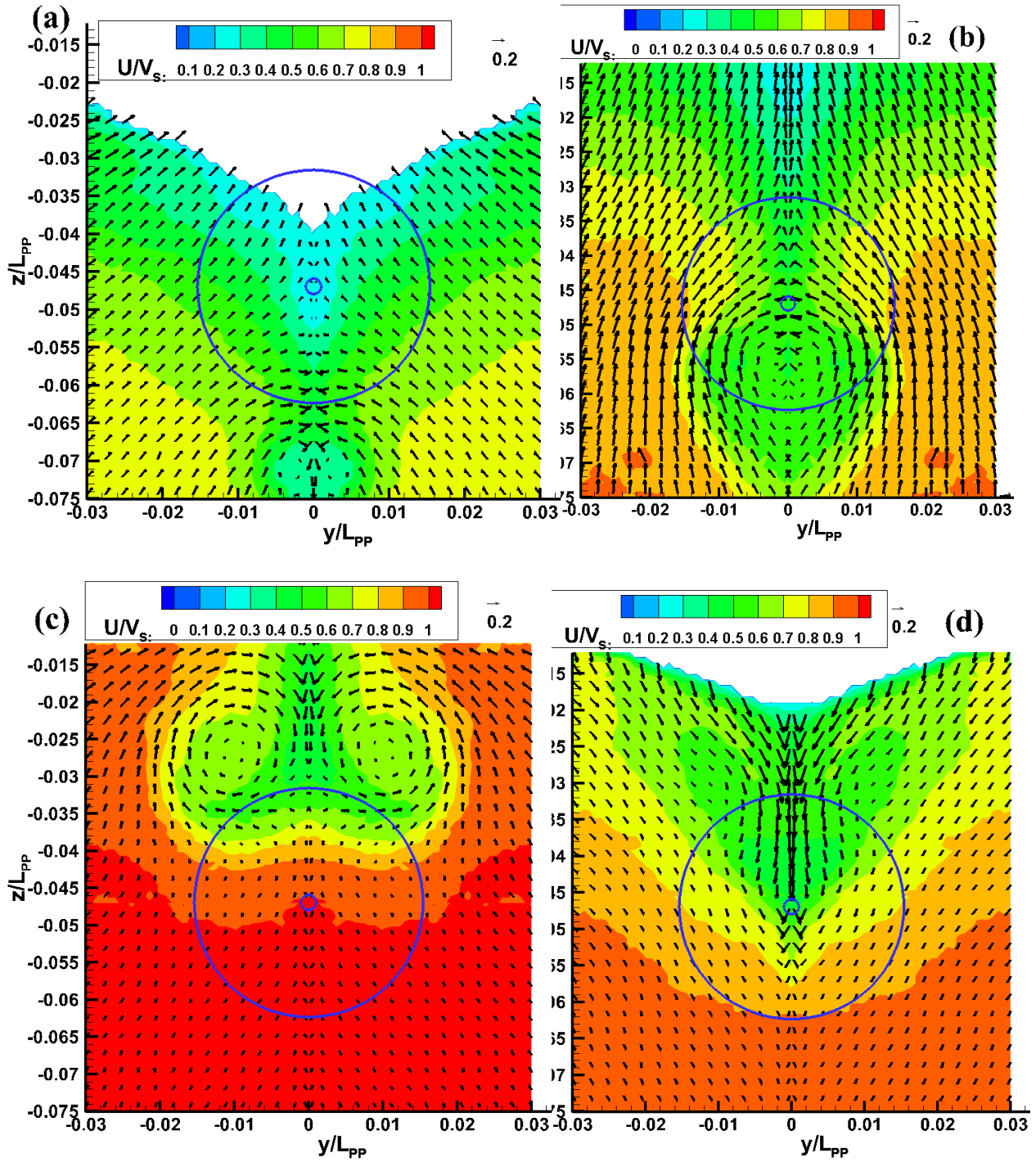


Figure 4-10 Phase-averaged velocity distribution at AP for $\lambda/L=1.6$, $A=4.3\text{cm}$; (a) 0° , (b) 90° (c) 180° and (d) 270° .

From the phase-averaged velocity distribution figures for $\lambda/L=1.6$, the inflow velocity into the propeller disk is highest at phase 270 degree when the ship stern is moving down and lowest at phase 90 degree when the ship stern is moving up. Figure 4-11 and Figure 4-12 show the thrust fluctuations, wave elevation at various stations and phases where the flow field measurement was done in one period. Observing the thrust fluctuation trend at the shown phases, it can be established that the inflow into the propeller influences the propeller thrust. Furthermore, since the inflow into the propeller changes with the wave amplitude, the propeller thrust will undoubtedly be influenced as well. In these figures, the wave peak is at the propeller plane.

From the thrust time history in Figure 4-12, the lowest thrust region is at phase 270 degree where the inflow velocity into the propeller is highest and the highest thrust region is at phase 90 degree where the inflow velocity into the propeller is the lowest. This can be confirmed from Figure 4-11 in which the thrust fluctuation for a wave amplitude, $A=3\text{cm}$ has been used as an example. The true mean value for thrust is not zero as indicated in this figure, but the mean value has been subtracted intentionally from the thrust time history values so as to understand how thrust changes with the wave at the propeller plane by directly placing the thrust curve against the waves' curves.

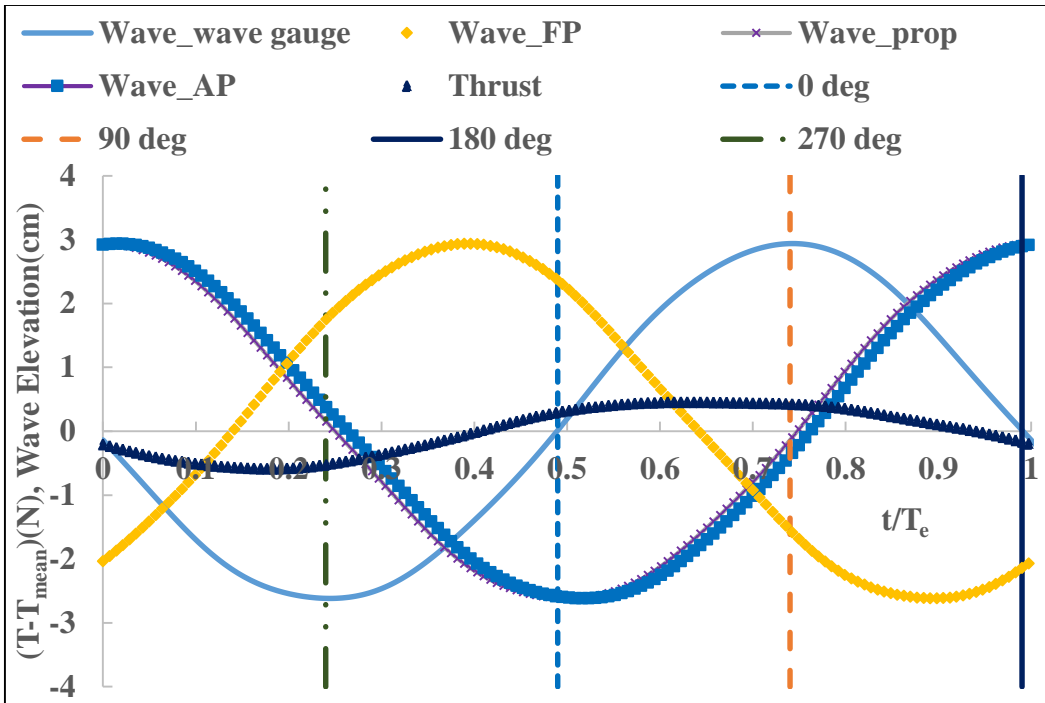


Figure 4-11 Thrust fluctuation and wave elevation for one period at $\lambda/L=1.6$, $A=3\text{cm}$.

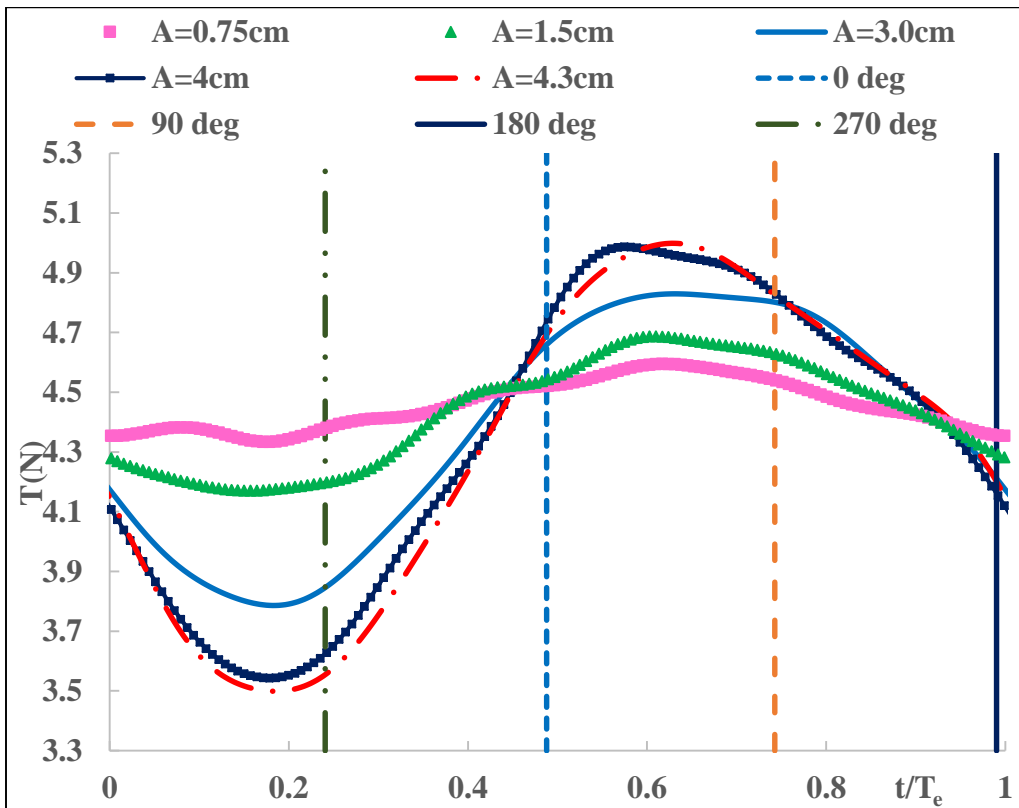


Figure 4-12 Thrust time history for $\lambda/L=1.6$, at different wave amplitudes.

4.2 ESDs Effect

For the ESDs effect study, the SPIV measurement was conducted in selected wavelengths ($\lambda/L=0.6, 1.1$ and 1.6) as mentioned previously at two transverse planes. One plane was 10 cm ($x/L=0.9688$) upstream of AP in order to analyze the flow before entering the propeller and the other plane was 8cm ($x/L=1.025$) downstream of AP so as to analyze the flow after the propeller and rudder. In this way, the effect of the rudders on the flow field around the stern region of the model ship could be explained. The two transverse planes are as shown in Figure 4-13 (Matsuura, 2021). Two types of rudder were used during the SPIV measurement; a conventional rudder (or normal rudder) without appendages on both sides and a rudder with a bulb and full fins (RBF-F system) of zero angle of attack (AOA) on both the port and starboard sides, and are as shown in Figure 4-15 (Htay et al., 2020). For the right-hand propeller's RBF-F system, the port side fin had a camber line on the upper side so as to obtain a forward force from the upward flow that was generated by the rotation of the propeller. Conversely, the starboard side fin had a camber line on the lower side so as to generate a forward force from the downward flow on the starboard side. The RBF-F system, for the right-handed propeller, that was used is as shown in Figure 4-14 (Matsuura, 2021) and Figure 4-15. For section $x/L=0.9688$, where the SPIV measurement on the starboard side was not possible because of obstruction of the laser sheet and camera focus by the hull, a counterclockwise rotating propeller was used, and in that case a RBF-F system with opposite port and starboard side camber lines was used.

The velocity field results were phase averaged for four phases (0, 90, 180 and 270 degrees) for shorter waves ($\lambda/L=0.6$) and six phases (0, 60, 120, 180, 240 and 300 degrees) for long waves ($\lambda/L=1.1$ and 1.6) in order to investigate how the velocity field changes in one encounter period for various rudders and without rudder conditions.

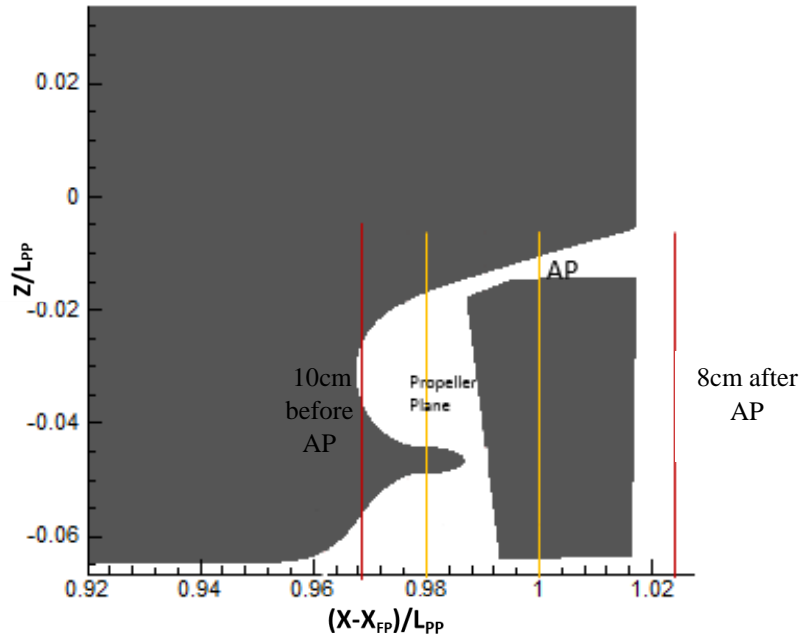


Figure 4-13 SPIV Measurement transverse planes.

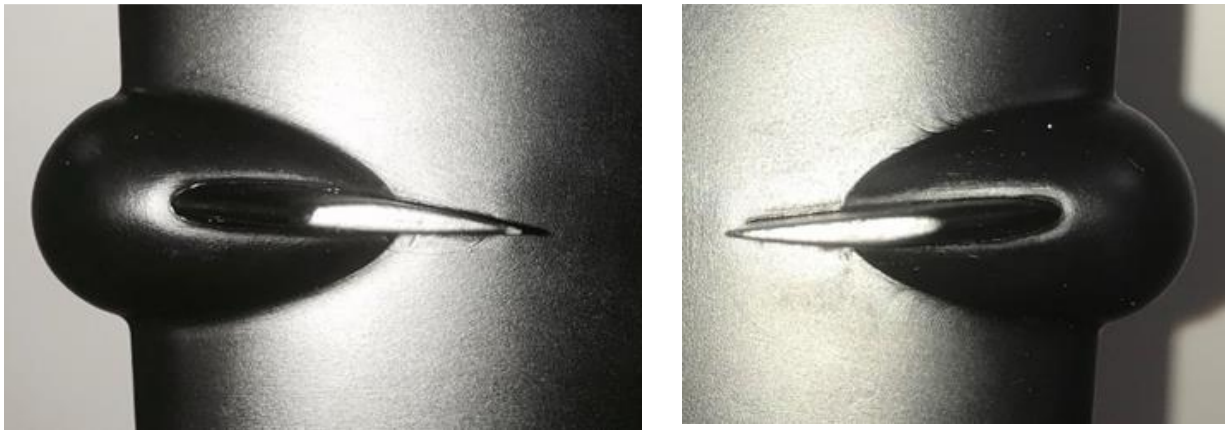


Figure 4-14 The RBF-F system's port and starboard sides fins.

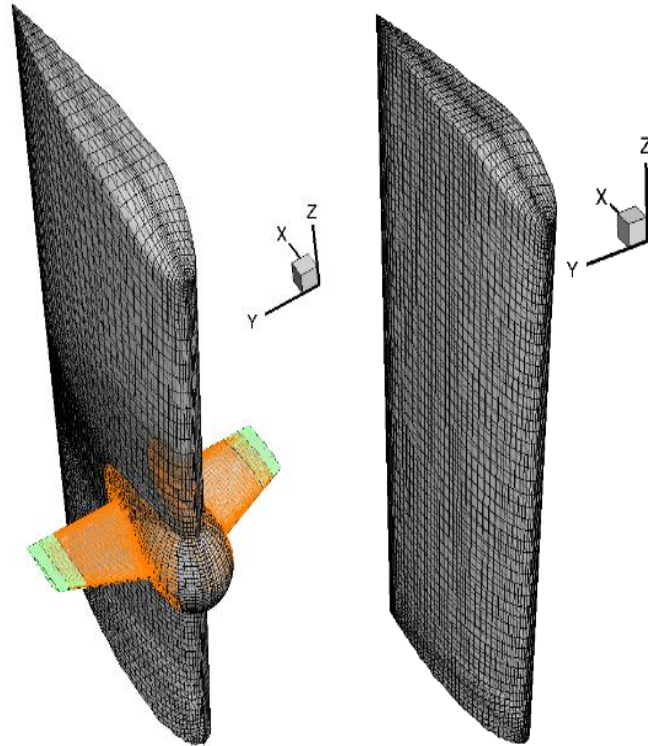


Figure 4-15 The RBF-F system and the normal rudder.

4.2.1 Velocity field result for calm water

Before the SPIV measurement was conducted in waves, it was done in calm water for validation purposes with the CFD result. The velocity field results for calm water for with and without rudder conditions at section $x/L=1.025$ at a propeller speed of 16.5 revolutions per second (rps) are as shown in Figure 4-16. The y and z axes are non-dimensionalized by the ship's length between the perpendiculars (L) and the axial velocity u as well as the cross flow velocities (v and w) are non-dimensionalized by the ship's forward speed, V_S . The number of images collected for calm water condition were about 200 images.

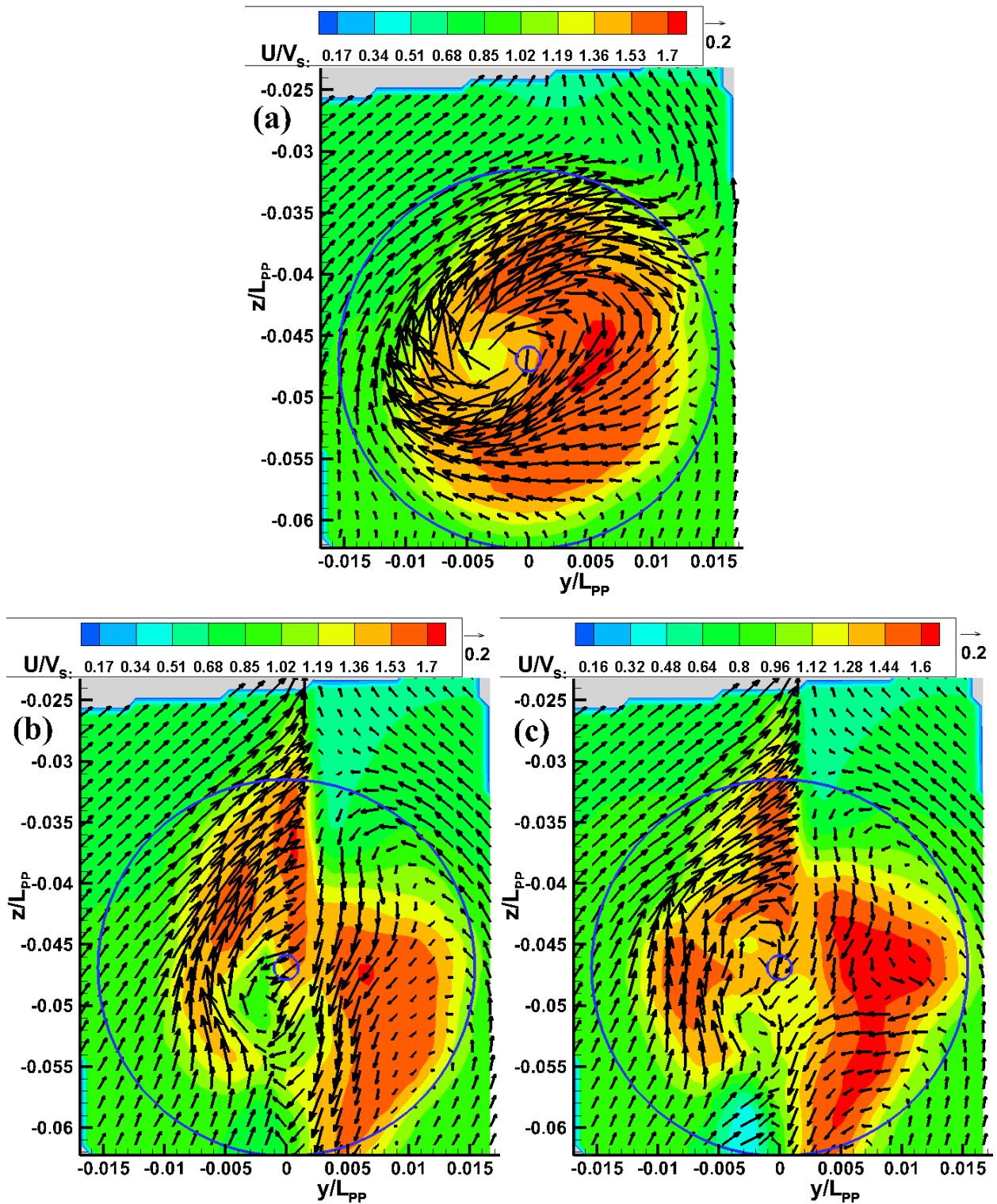


Figure 4-16 Phase averaged velocity distribution for calm water (a) without rudder, (b) normal rudder, (c) RBF-F system.

From these figures, the flow field is clearly captured for with and without rudder conditions. The high speed axial velocity contour is within the propeller radius since there are no vertical ship motions. At this section of measurement, ($x/L=1.025$), the nature of rotation of the right-handed propeller can clearly be seen since the cross flow velocity vectors (v/V_s , w/V_s) are twisted towards the starboard side. The propeller accelerates the flow downstream to 1.7 times the ship's forward speed for without rudder and normal rudder condition but in the RBF-F system it is 1.6 times the ship's forward speed. It can also be seen that the high speed axial velocity contours and the velocity at the core of the hub vortex are very different for with and without rudder conditions. The normal rudder and the RBF-F system deform the shape of the propeller slipstream into a twisted contour whose part on the port side is higher and lower on the starboard side for both rudders. However, the axial velocity contour has an almost round and smooth shape for the normal rudder but this shape is bulged out into a concave shape at the position corresponding to the bulb and fins for the RBF-F system. This makes the shape of the high speed axial velocity contour to be a bit larger for the RBF-F system compared to that for the normal rudder. The hub vortex in the propeller slipstream is shifted to the left (port side of the center line $Y=0$) in the upward stern flow for rudder and without rudder conditions. It can also be noted that the velocity at the core of the hub vortex is highest for without rudder condition but it is attenuated by using the rudders. When considering the rudder condition only, the velocity at the core of the hub vortex is lower for the RBF-F system as compared to the normal rudder condition.

4.2.2 Velocity field results for waves

The SPIV measurement in waves was done at two transverse planes; upstream of the propeller and downstream of the rudders as mentioned previously. The results were phase averaged at four phases for shorter waves ($\lambda/L=0.6$) as shown by the vertical lines in Figure 4-17. For long

wavelengths ($\lambda/L=1.1$ and 1.6), the velocity fields were phase averaged at six phases as shown in Figure 4-18 and Figure 4-19. The wave elevation and heave motion are in cm, pitch motion is in degrees and thrust in Newtons. The horizontal axis represents non-dimensional time. As mentioned in the previous sections, the phases for SPIV measurement were set at the wave gauge and therefore, the wave elevation at the wave gauge was used as a reference to show the phases in these figures. The wave peak is at the forward perpendicular (FP) of the model ship. The number of images collected was about 150 for shorter waves and 117 for longer waves per phase.

a) Velocity field upstream of the propeller

The phase averaged velocity fields for $\lambda/L=0.6$ for normal rudder and RBF-F system at transverse plane $x/L=0.9688$ at a propeller speed of 16.5 revolutions per second (rps) are as shown in Figure 4-20~Figure 4-23.

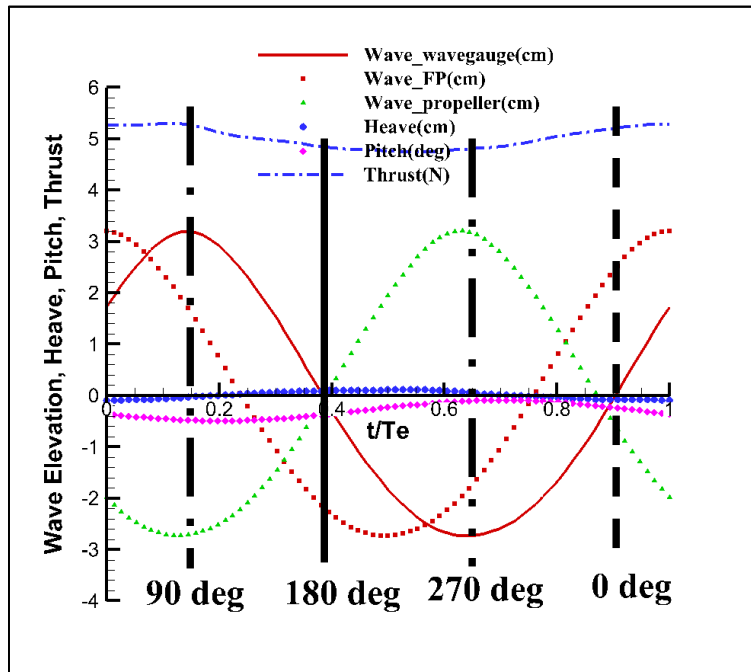


Figure 4-17 Wave elevation at various stations, motions, thrust and phases for SPIV measurement for $\lambda/L=0.6$.

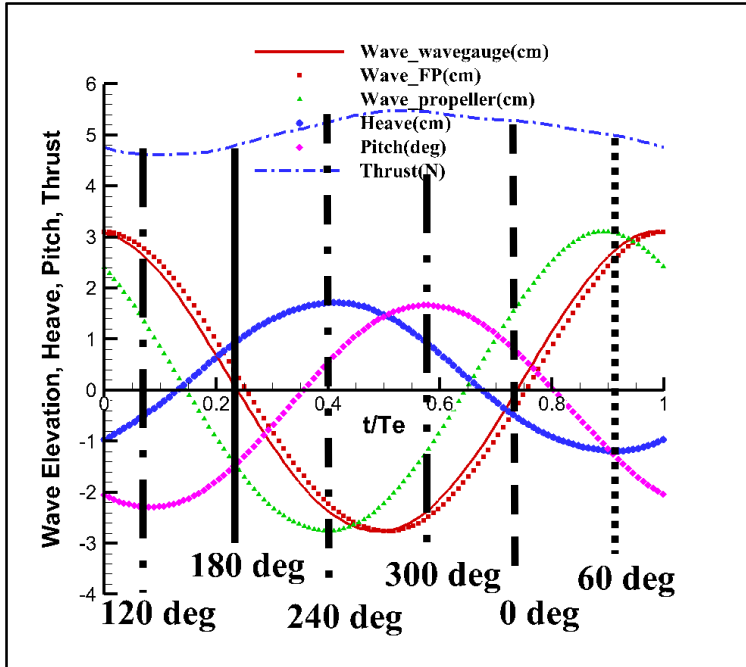


Figure 4-18 Wave elevation at various stations, motions, thrust and phases for SPIV measurement for $\lambda/L=1.1$.

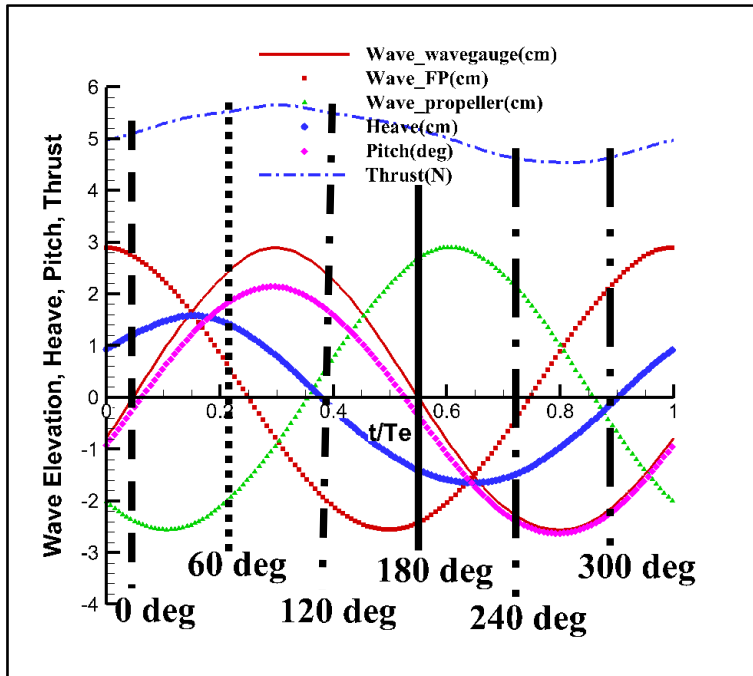


Figure 4-19 Wave elevation at various stations, motions, thrust and phases for SPIV measurement for $\lambda/L=1.6$.

The y and z axes are non-dimensionalized by the ship's length between the perpendiculars (L) and the axial velocity, u as well as the cross flow velocities (v, w) are non-dimensionalized by the ship's forward speed, V_s . In these figures, (a) shows the velocity fields for normal rudder condition without the propeller, whereas those for normal rudder and RBF-F system with the propeller are shown in (b) and (c) respectively. Also, the velocity field result for normal rudder condition without the propeller was subtracted from that for normal rudder with the propeller so as to know the influence of the propeller on the flow field upstream of the propeller as shown in (d). Given that $\lambda/L=0.6$ is a shorter wavelength, the ship's vertical motions are relatively small and this can clearly be seen from the velocity distribution diagrams as the wake does not move very much vertically relative to the propeller disk.

From the velocity field results for the normal rudder and RBF-F system, it can be seen that there is no significant difference between them. The boundary layer thickness is changing almost in a similar trend in one period for both rudder conditions and this is due to the change in the wave pressure field and the external flow. It can also be seen that the velocity is a little bit higher in the starboard side due to higher loading in the starboard side by the cross-sectional flow. The influence of the propeller on the flow field is clearly seen when the difference between the results for the normal rudder condition with and without the propeller is taken. It can be seen that the part of the flow field that is accelerated by the propeller moves in the same way as the boundary layer. The suction by the propeller becomes stronger at the bottom of the hull when the ship stern is moving up (270 degree), and it is dispersed and weakened when the ship stern is moving down (90 degree). Also, it is confirmed that the propeller suction becomes a little bit stronger in the starboard side.

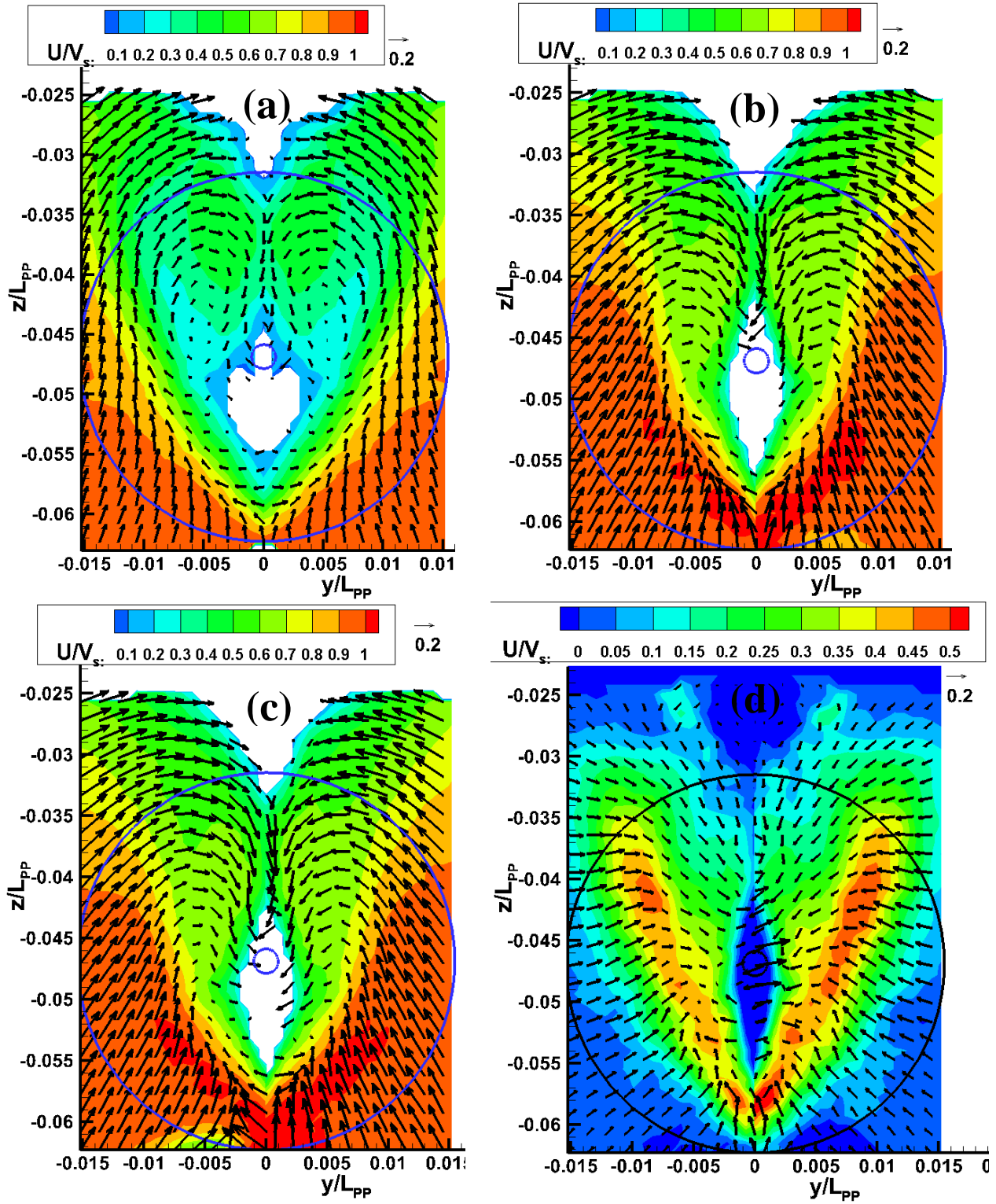


Figure 4-20 Phase averaged velocity distribution for (0°) for $\lambda/L=0.6$; (a) with normal rudder, no propeller, (b) normal rudder, (c) RBF-F system and (d)=(b)-(a).

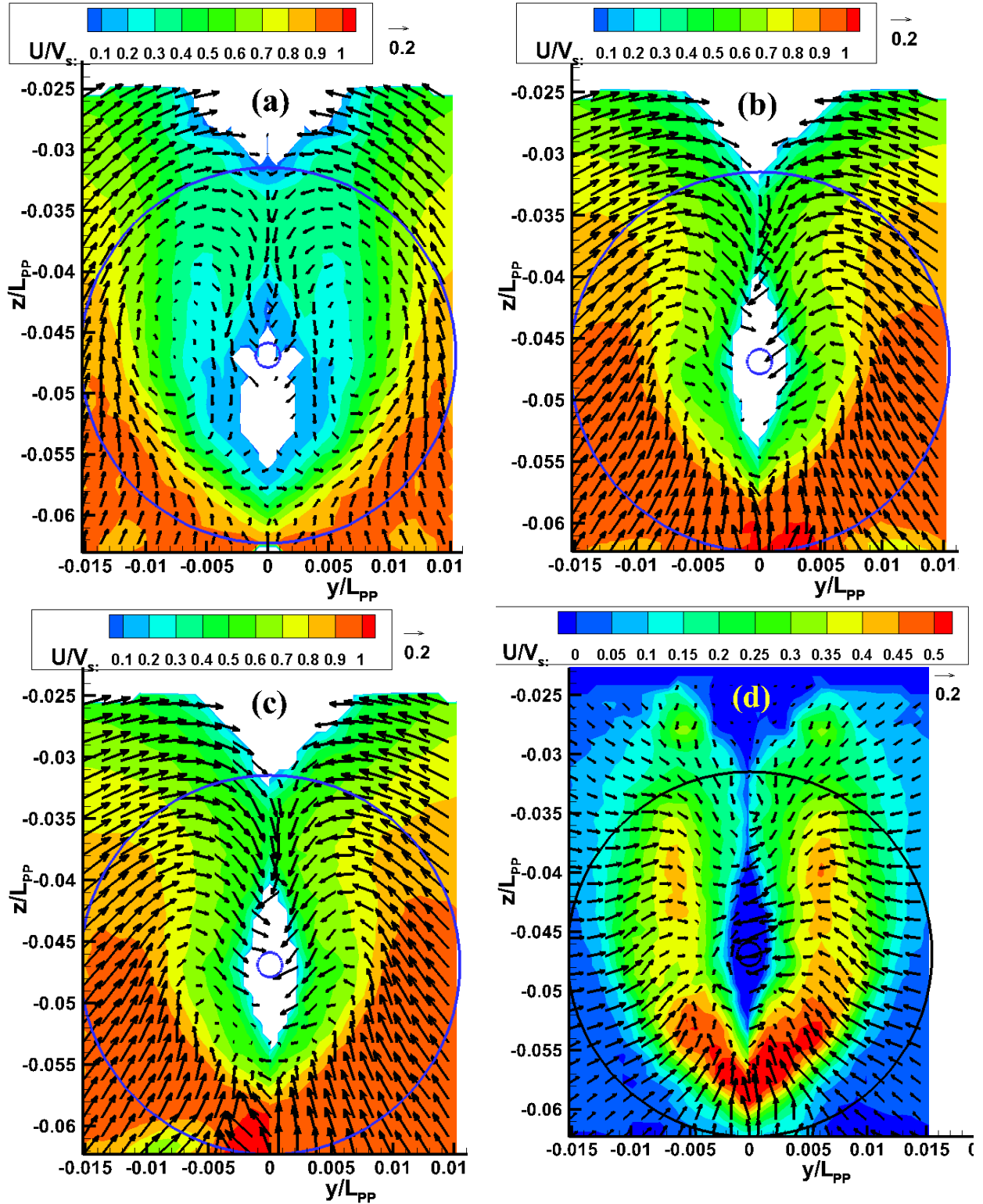


Figure 4-21 Phase averaged velocity distribution for (90°) for $\lambda/L=0.6$; (a) with normal rudder, no propeller, (b) normal rudder, (c) RBF-F system and (d)=(b)-(a).

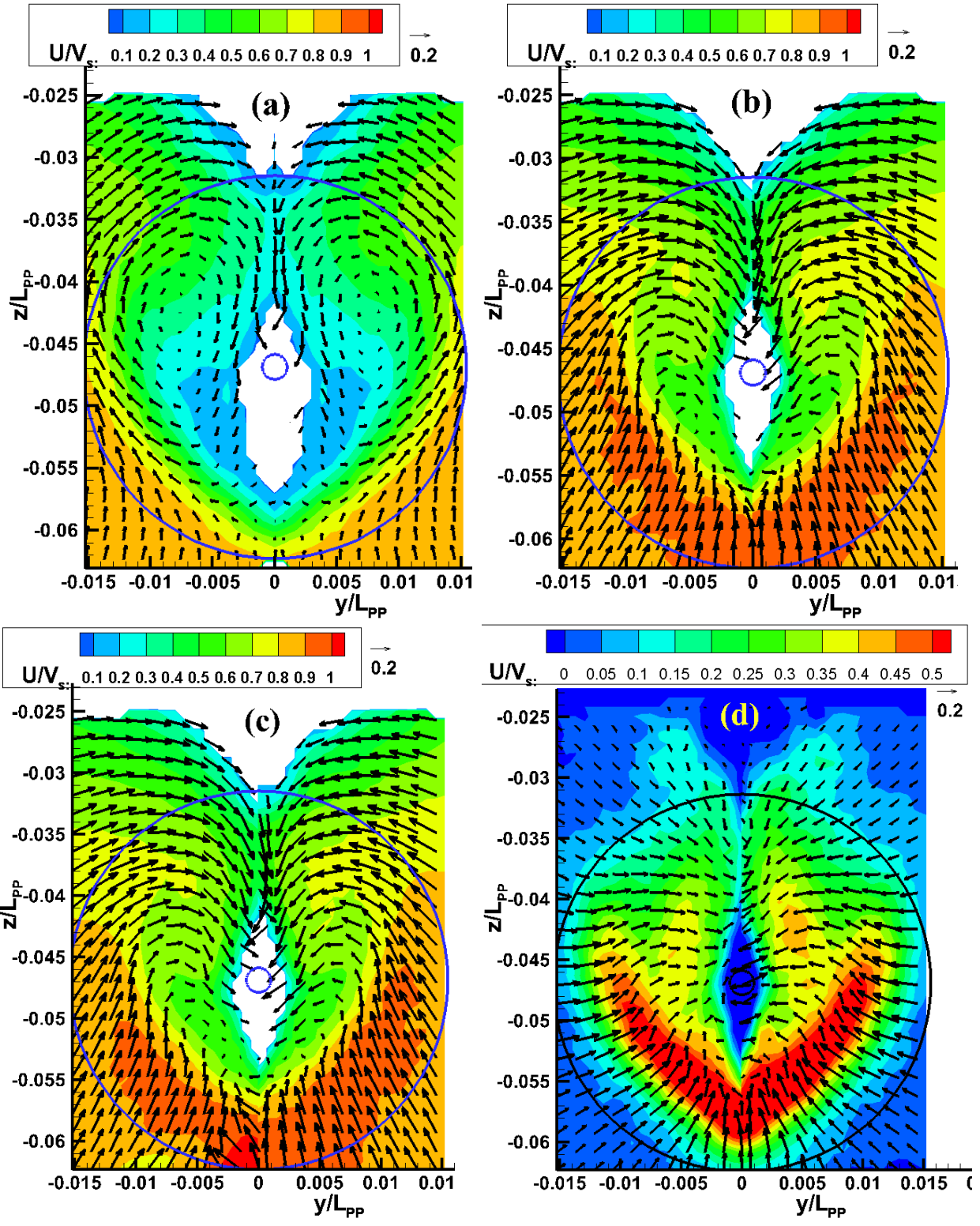


Figure 4-22 Phase averaged velocity distribution for (180°) for $\lambda/L=0.6$; (a) with normal rudder, no propeller, (b) normal rudder, (c) RBF-F system and (d)=(b)-(a).

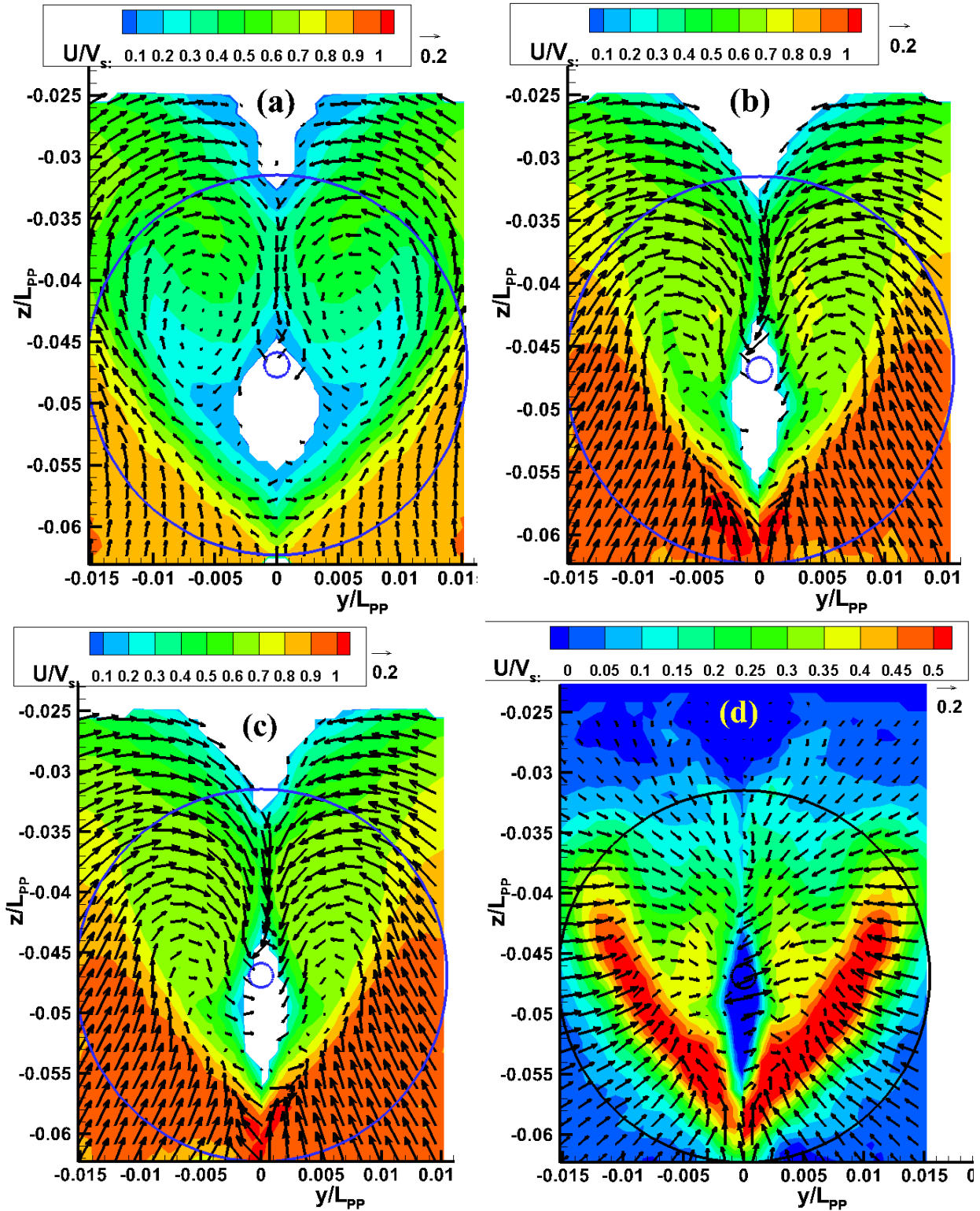


Figure 4-23 Phase averaged velocity distribution for (270°) for $\lambda/L=0.6$; (a) with normal rudder, no propeller, (b) normal rudder, (c) RBF-F system and (d)=(b)-(a).

The phase averaged velocity fields for $\lambda/L=1.1$ for normal rudder and RBF-F system at cross-section $x/L=0.9688$ at a propeller speed of 16.5 rps are shown in Figure 4-24~Figure 4-29. The y and z axes are non-dimensionalized by the ship's length between the perpendiculars (L) and the axial velocity, u as well as the cross flow velocities (v, w) are non-dimensionalized by the ship's forward speed, V_s . In these figures, (a) shows the velocity fields for normal rudder condition without the propeller, whereas those for normal rudder and RBF-F system with the propeller are shown in (b) and (c) respectively. Similarly, the velocity field result for normal rudder condition without the propeller was subtracted from that for normal rudder with the propeller so as to see the influence of the propeller on the flow field upstream of the propeller as shown in (d). Since $\lambda/L=1.1$ is a longer wavelength, the ship's vertical motions are relatively large compared to those for $\lambda/L=0.6$, and this can clearly be seen from the velocity distribution diagrams as the wake moves very much vertically relative to the propeller disk.

From the velocity field results it can be seen that there is no major difference between the results for the normal rudder and the RBF-F system. The boundary layer thickness is changing more or less in a similar trend in one period for both rudder conditions. Moreover, the influence of the propeller on the flow field is clearly seen from the difference between the results for the normal rudder condition with and without the propeller. It can be seen that the part of the flow field that is accelerated by the propeller moves in the same way as the boundary layer. The suction by the propeller becomes stronger at the bottom of the hull when the ship stern is moving up (phases 240 and 300 degrees), and it is dispersed and weakened when the ship stern is moving down (phases 60 and 120 degrees). Also, it can be seen that the suction by the propeller is a little bit weak on the port side of the RBF-F system than that of the normal rudder.

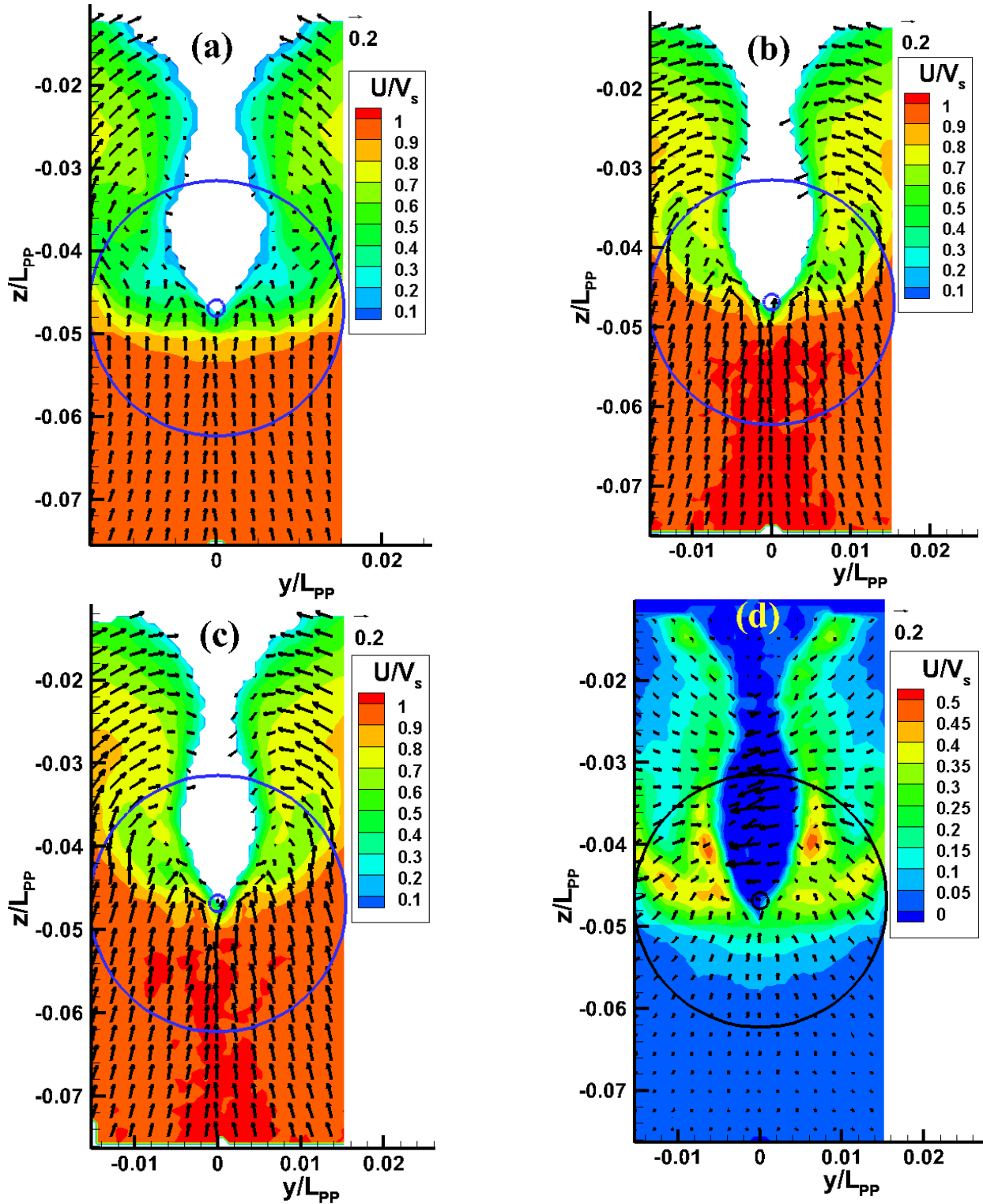


Figure 4-24 Phase averaged velocity distribution for (0°) for $\lambda/L=1.1$; (a) with normal rudder, no propeller, (b) normal rudder, (c) RBF-F system and (d)=(b)-(a).

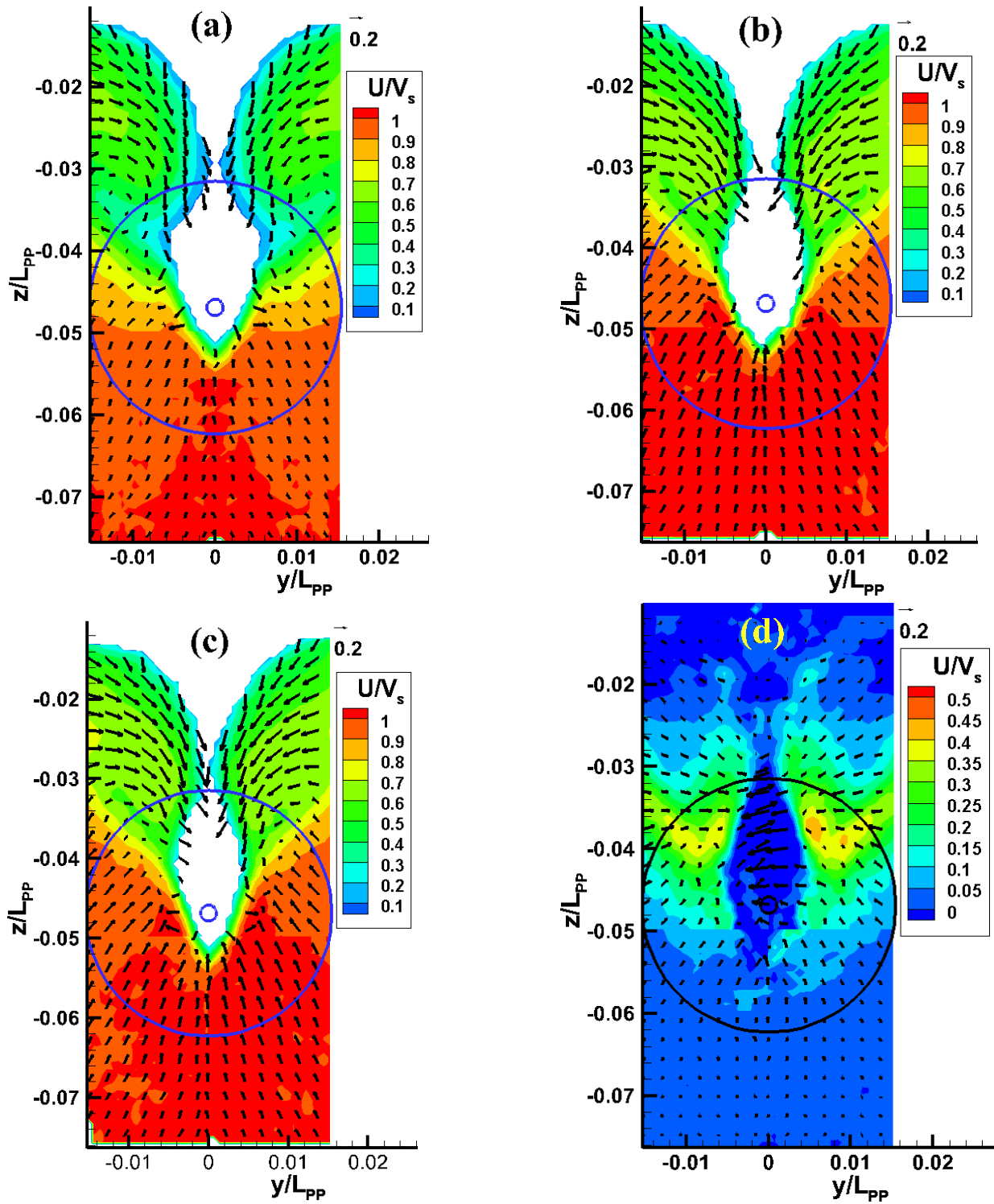


Figure 4-25 Phase averaged velocity distribution for (60°) for $\lambda/L=1.1$; (a) with normal rudder, no propeller, (b) normal rudder, (c) RBF-F system and (d)=(b)-(a).

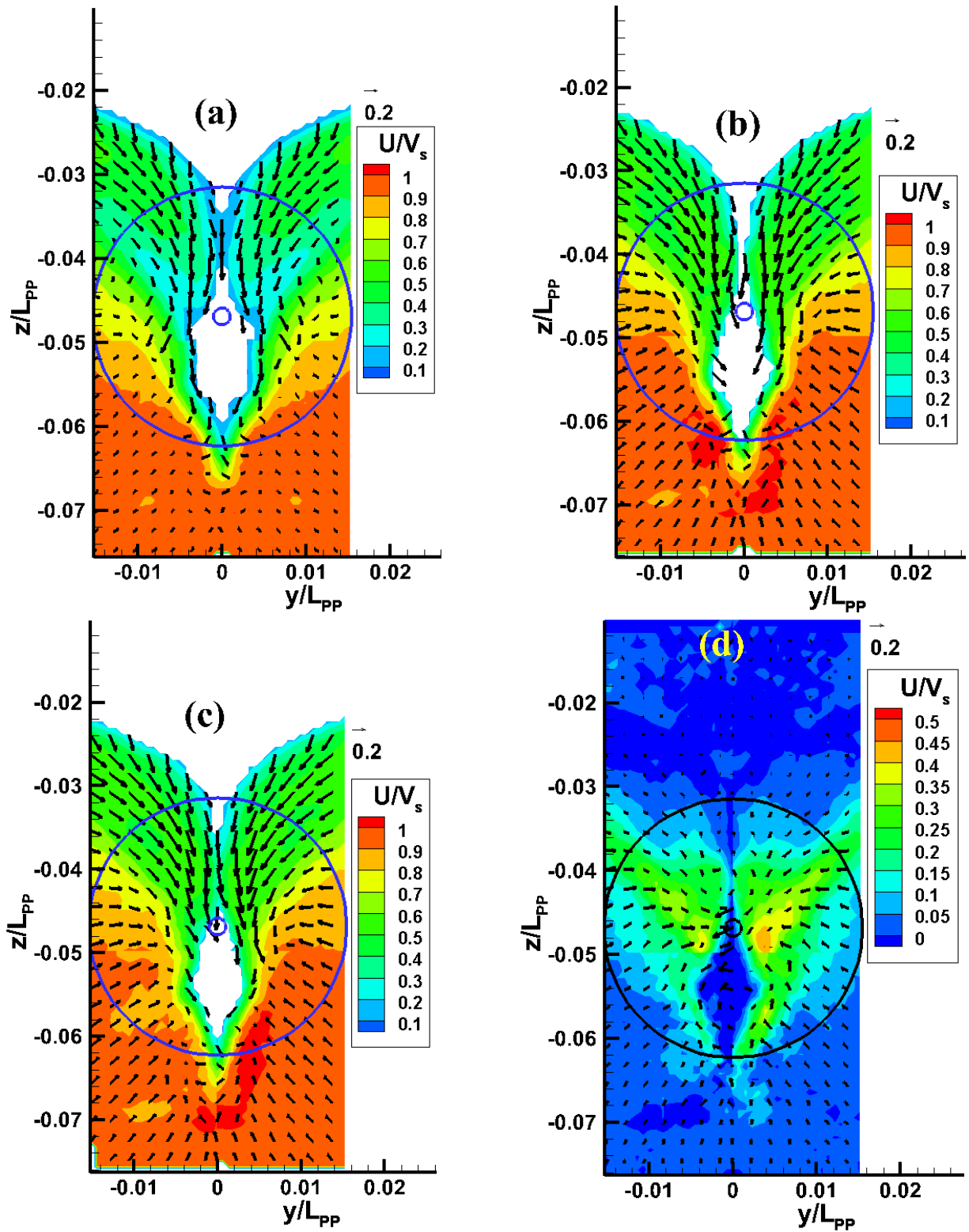


Figure 4-26 Phase averaged velocity distribution for (120°) for $\lambda/L=1.1$; (a) with normal rudder, no propeller, (b) normal rudder, (c) RBF-F system and (d)=(b)-(a).

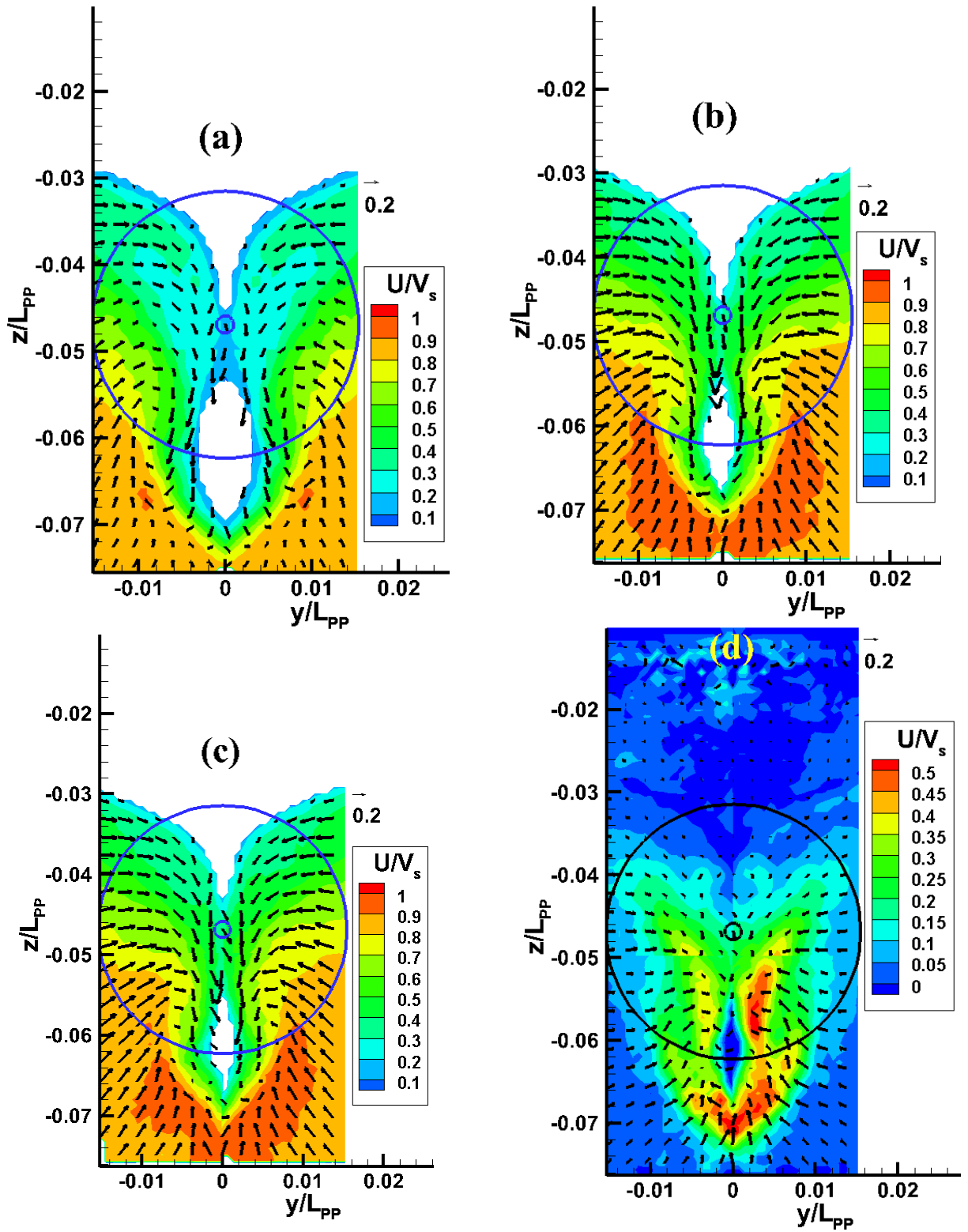


Figure 4-27 Phase averaged velocity distribution for (180°) for $\lambda/L=1.1$; (a) with normal rudder, no propeller, (b) normal rudder, (c) RBF-F system and (d)=(b)-(a).

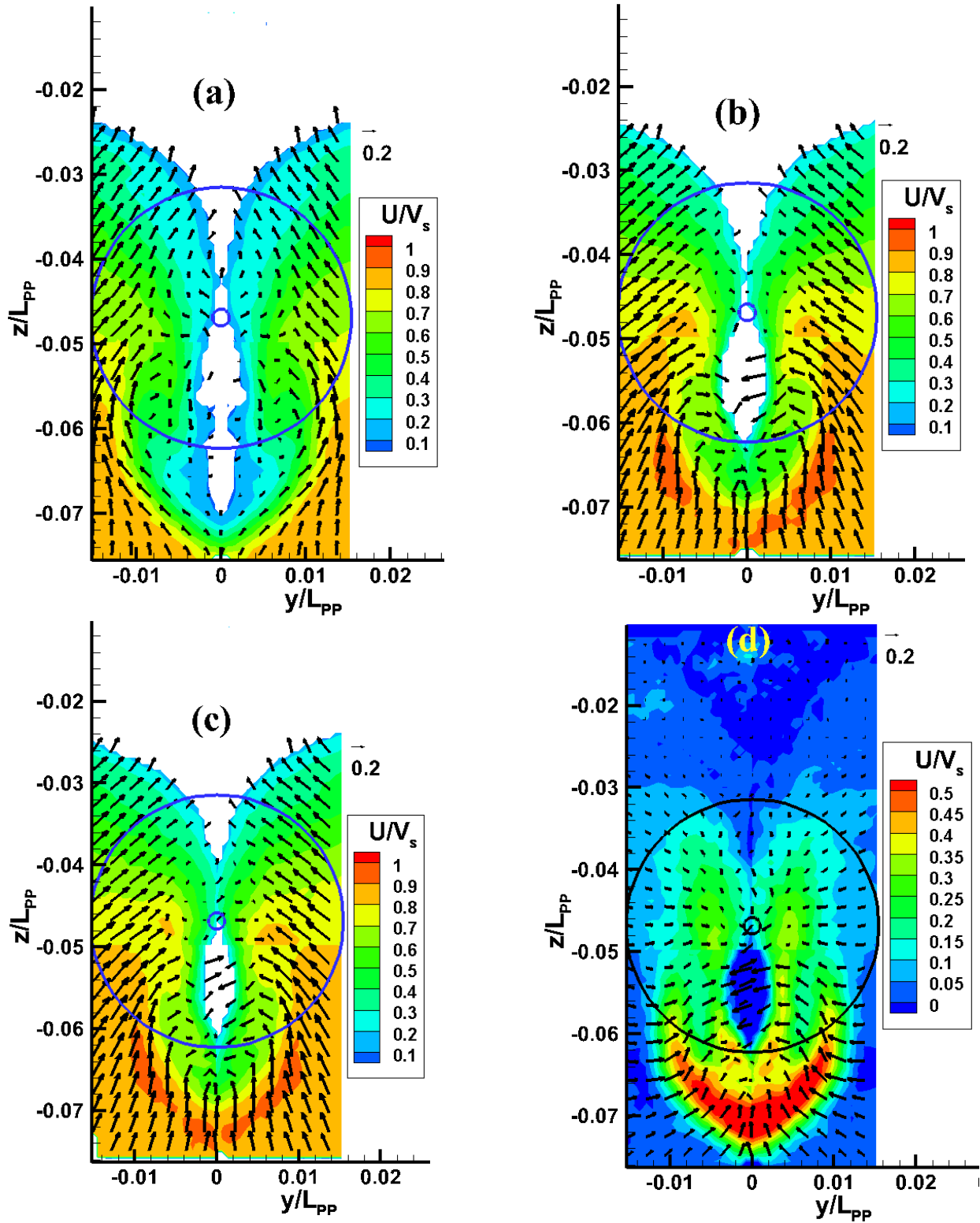


Figure 4-28 Phase averaged velocity distribution for (240°) for $\lambda/L=1.1$; (a) with normal rudder, no propeller, (b) normal rudder, (c) RBF-F system and (d)=(b)-(a).

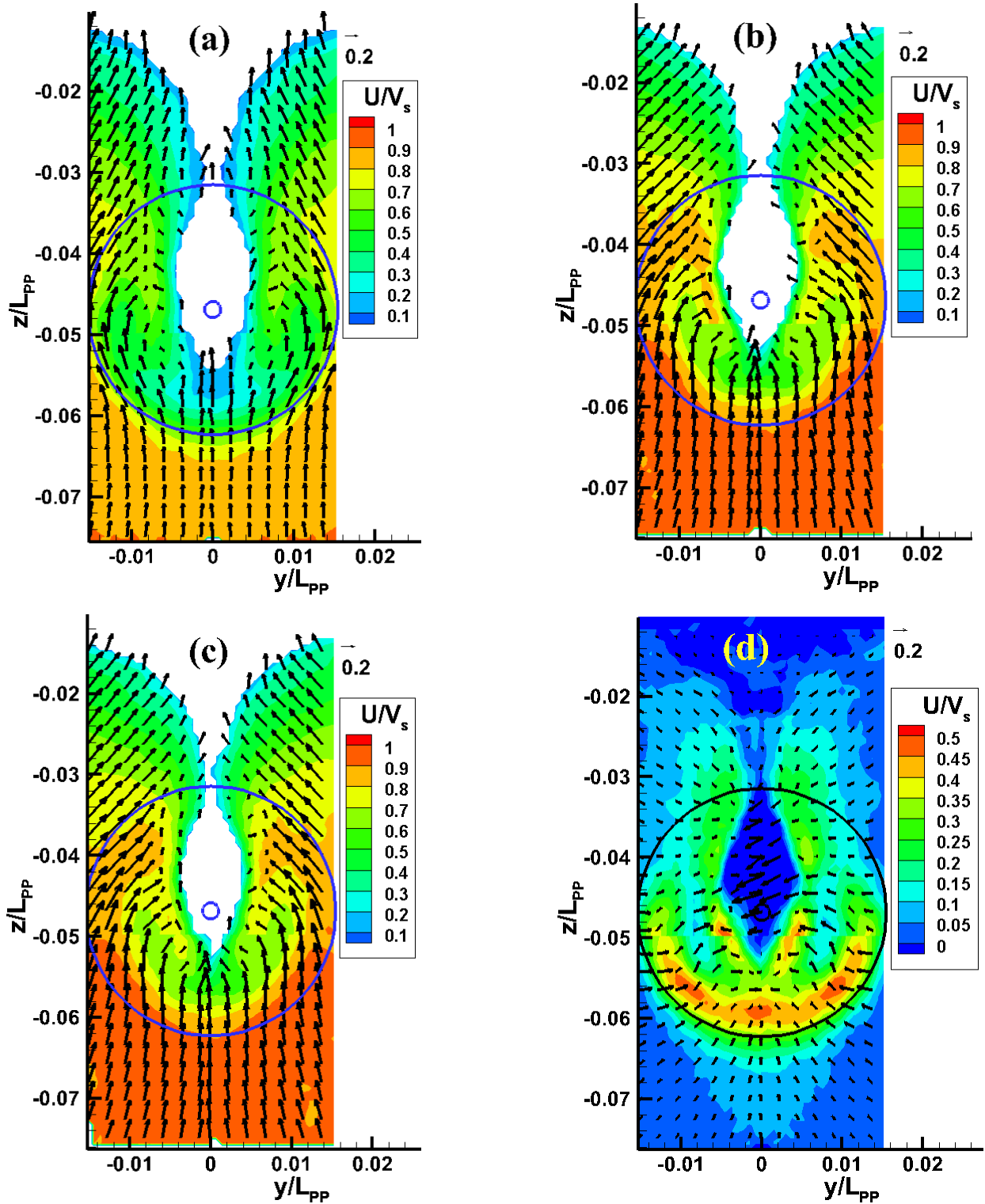


Figure 4-29 Phase averaged velocity distribution for (300°) for $\lambda/L=1.1$; (a) with normal rudder, no propeller, (b) normal rudder, (c) RBF-F system and (d)=(b)-(a).

The phase averaged velocity fields for $\lambda/L=1.6$ for normal rudder and RBF-F system at cross-section $x/L=0.9688$ at a propeller speed of 16.5 rps are shown in Figure 4-30~Figure 4-35. The y and z axes are non-dimensionalized by the ship's length between the perpendiculars (L) and the axial velocity, u as well as the cross flow velocities (v, w) are non-dimensionalized by the ship's forward speed, V_s . In these figures, (a) shows the velocity fields for normal rudder condition without the propeller, whereas those for normal rudder and RBF-F system with the propeller are shown in (b) and (c) respectively. Besides, the velocity field result for normal rudder condition without the propeller was subtracted from that for normal rudder with the propeller so as to understand the influence of the propeller on the flow field upstream of the propeller as shown in (d). As $\lambda/L=1.6$ is a longer wavelength, the ship's vertical motions are relatively large compared to those for $\lambda/L=0.6$ and 1.1, and this can clearly be seen from the velocity distribution diagrams since the wake moves very much vertically relative to the propeller disk.

The velocity field results show that there is no considerable difference between the results for the normal rudder and RBF-F system since the boundary layer thickness is changing nearly in a similar tendency in one period for both rudder conditions. Moreover, the influence of the propeller on the flow field is clearly seen from the difference between the results for the normal rudder condition with and without the propeller. It can be seen that the part of the flow field that is accelerated by the propeller moves in a similar manner as the boundary layer. The suction by the propeller becomes stronger at the bottom of the hull when the ship stern is moving up (phases 60 and 120 degrees), and it is dispersed and attenuated when the ship stern is moving down (phases 240 and 300 degrees).

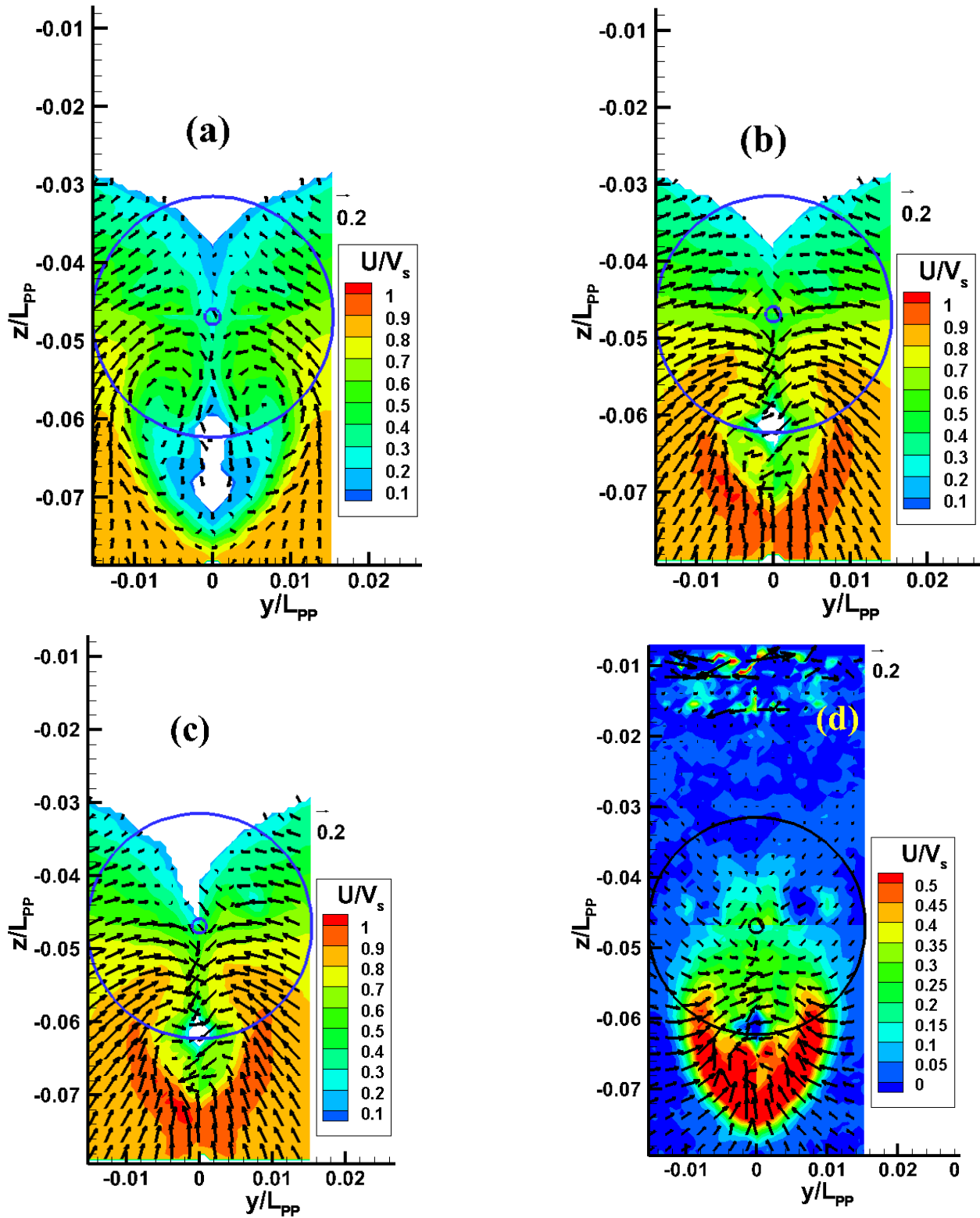


Figure 4-30 Phase averaged velocity distribution for (0°) for $\lambda/L=1.6$; (a) with normal rudder, no propeller, (b) normal rudder, (c) RBF-F system and (d)=(b)-(a).

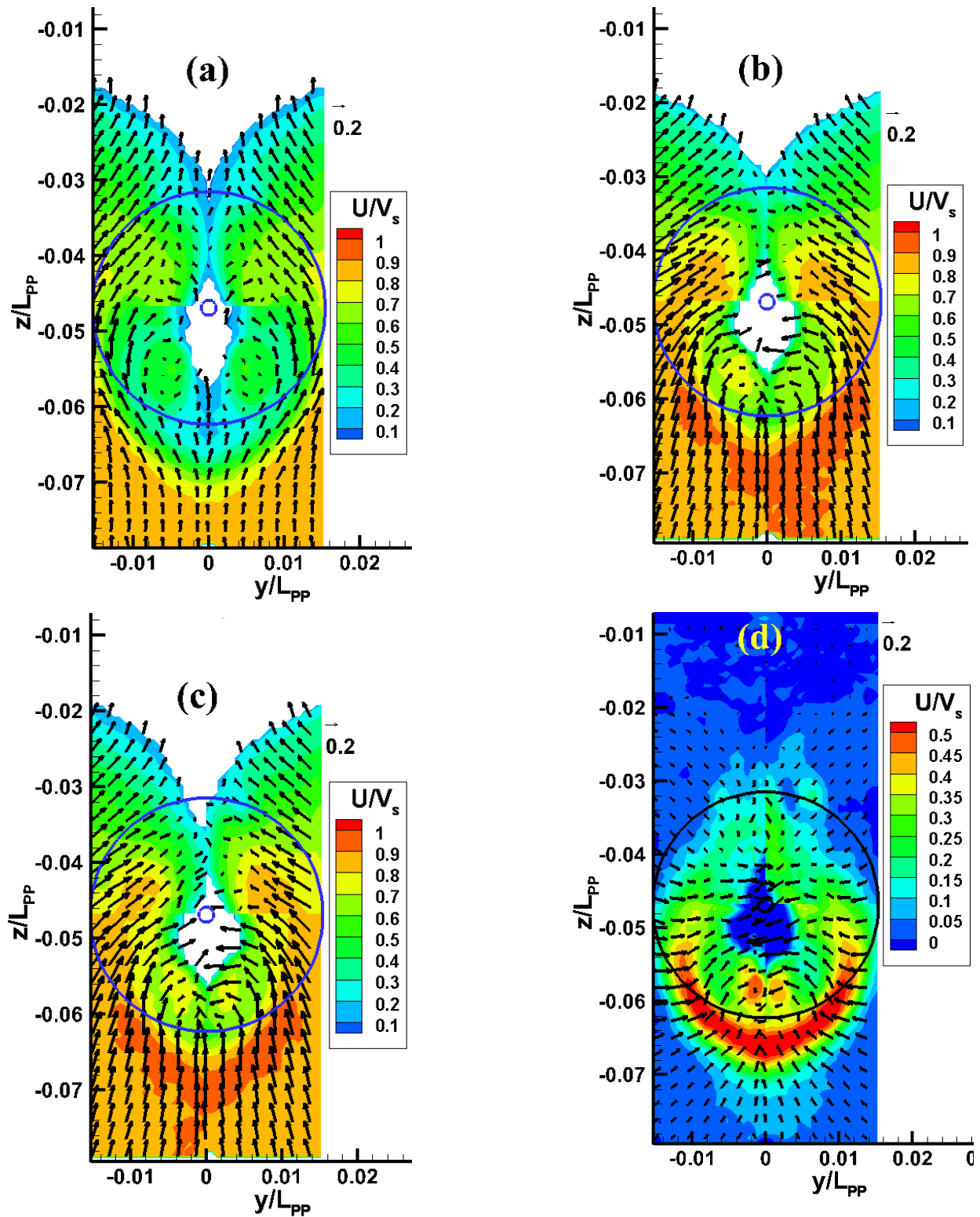


Figure 4-31 Phase averaged velocity distribution for (60°) for $\lambda/L=1.6$; (a) with normal rudder, no propeller, (b) normal rudder, (c) RBF-F system and (d)=(b)-(a).

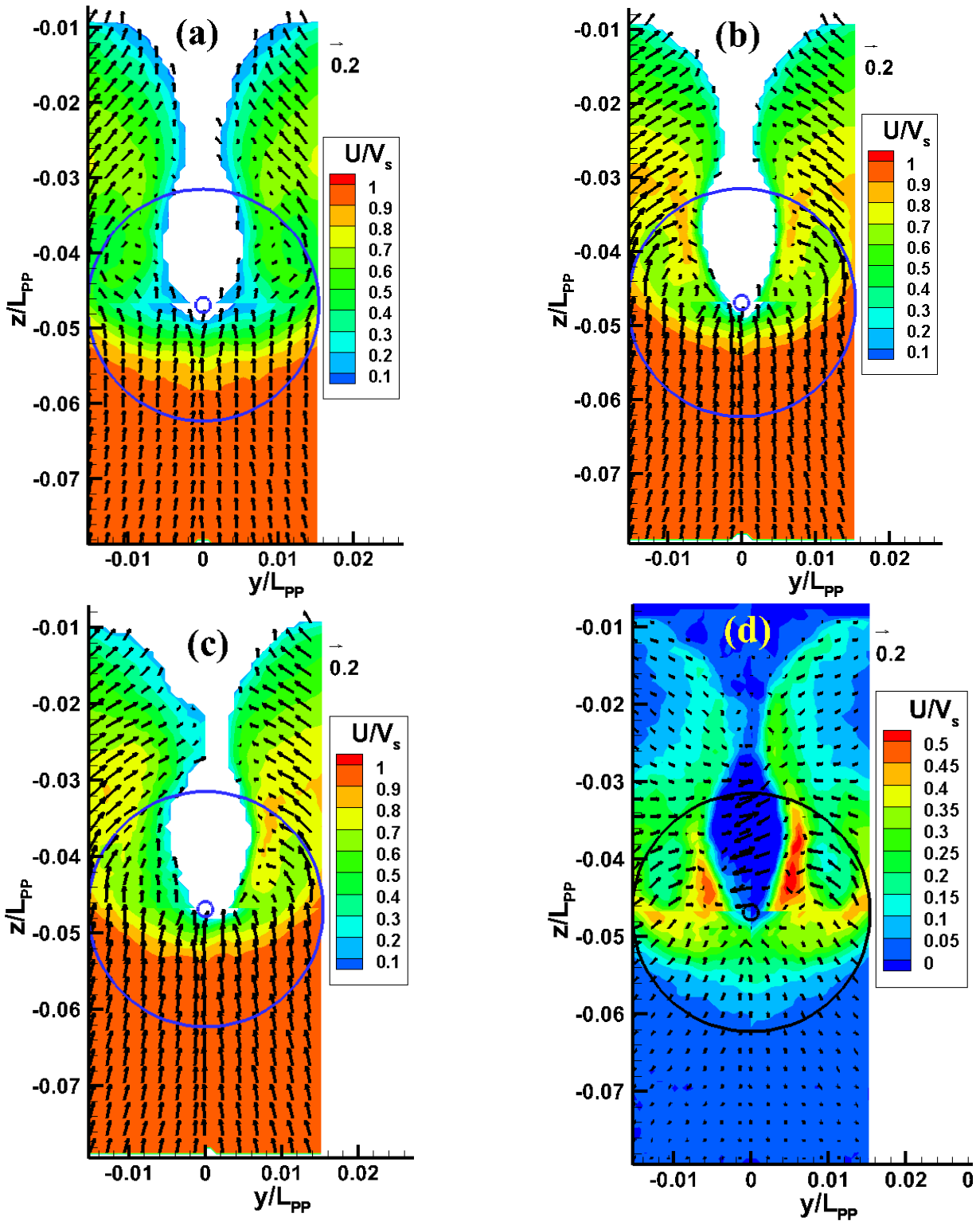


Figure 4-32 Phase averaged velocity distribution for (120°) for $\lambda/L=1.6$; (a) with normal rudder, no propeller, (b) normal rudder, (c) RBF-F system and (d)=(b)-(a).

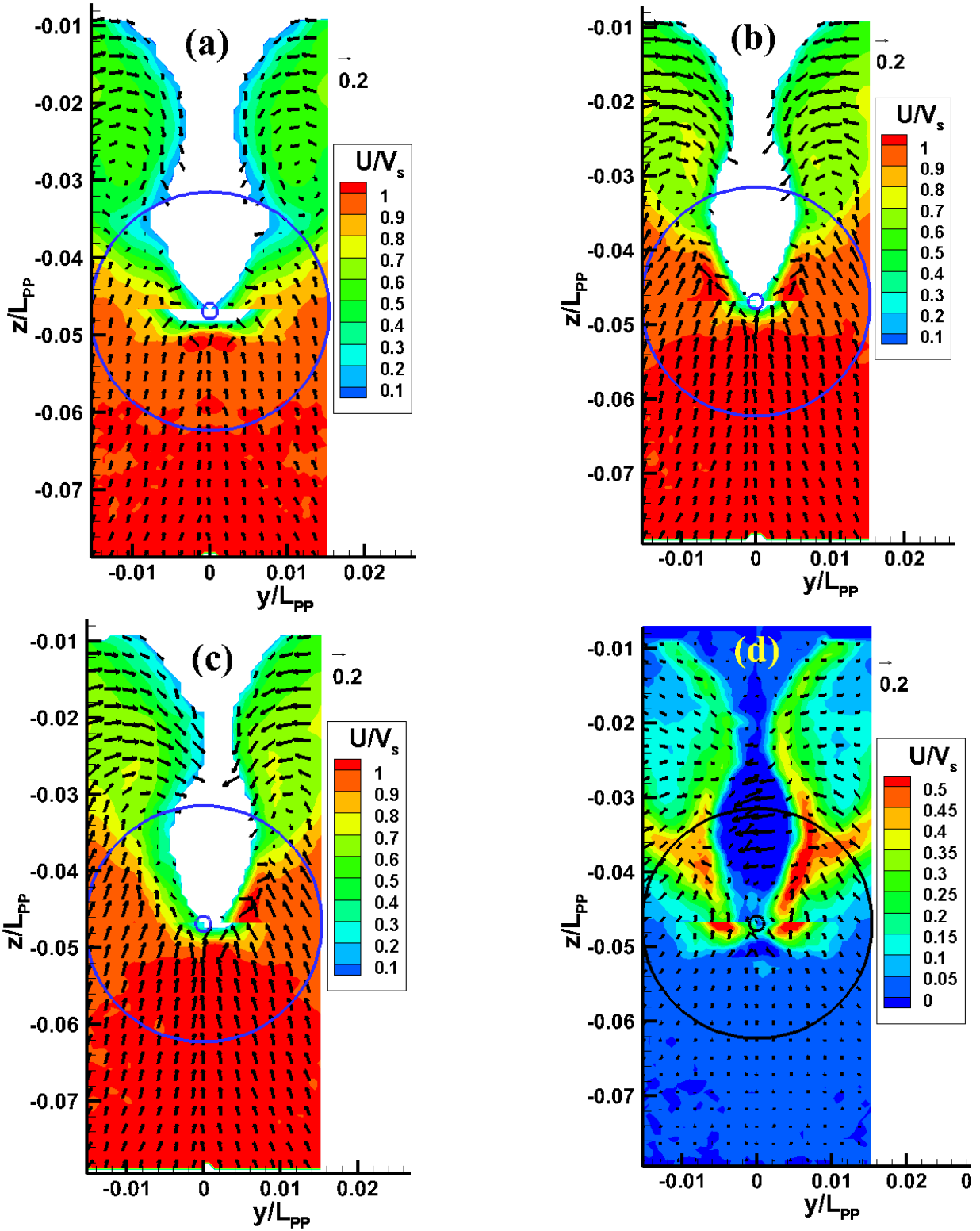


Figure 4-33 Phase averaged velocity distribution for (180°) for $\lambda/L=1.6$; (a) with normal rudder, no propeller, (b) normal rudder, (c) RBF-F system and (d)=(b)-(a).

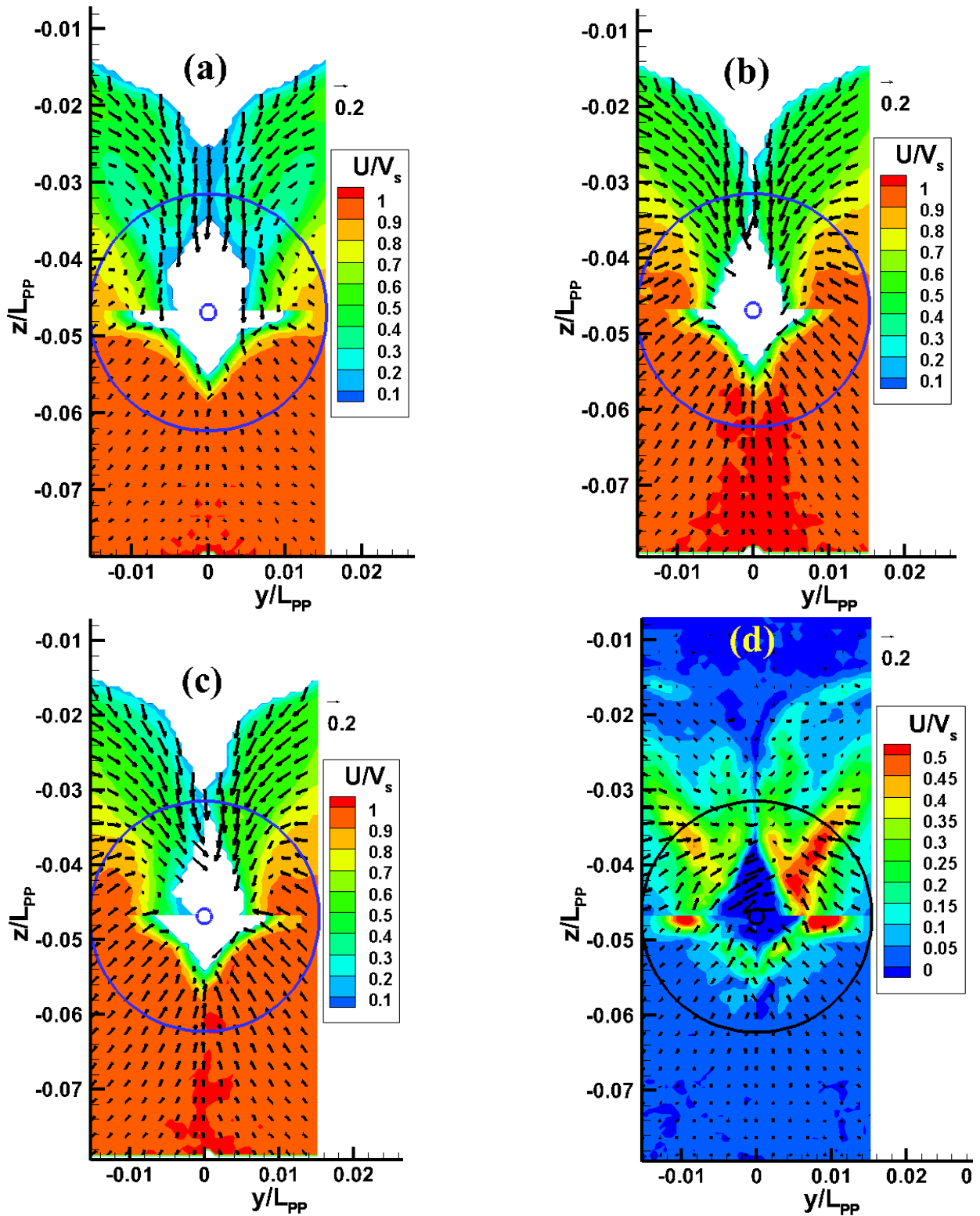


Figure 4-34 Phase averaged velocity distribution for (240°) for $\lambda/L=1.6$; (a) with normal rudder, no propeller, (b) normal rudder, (c) RBF-F system and (d)=(b)-(a).

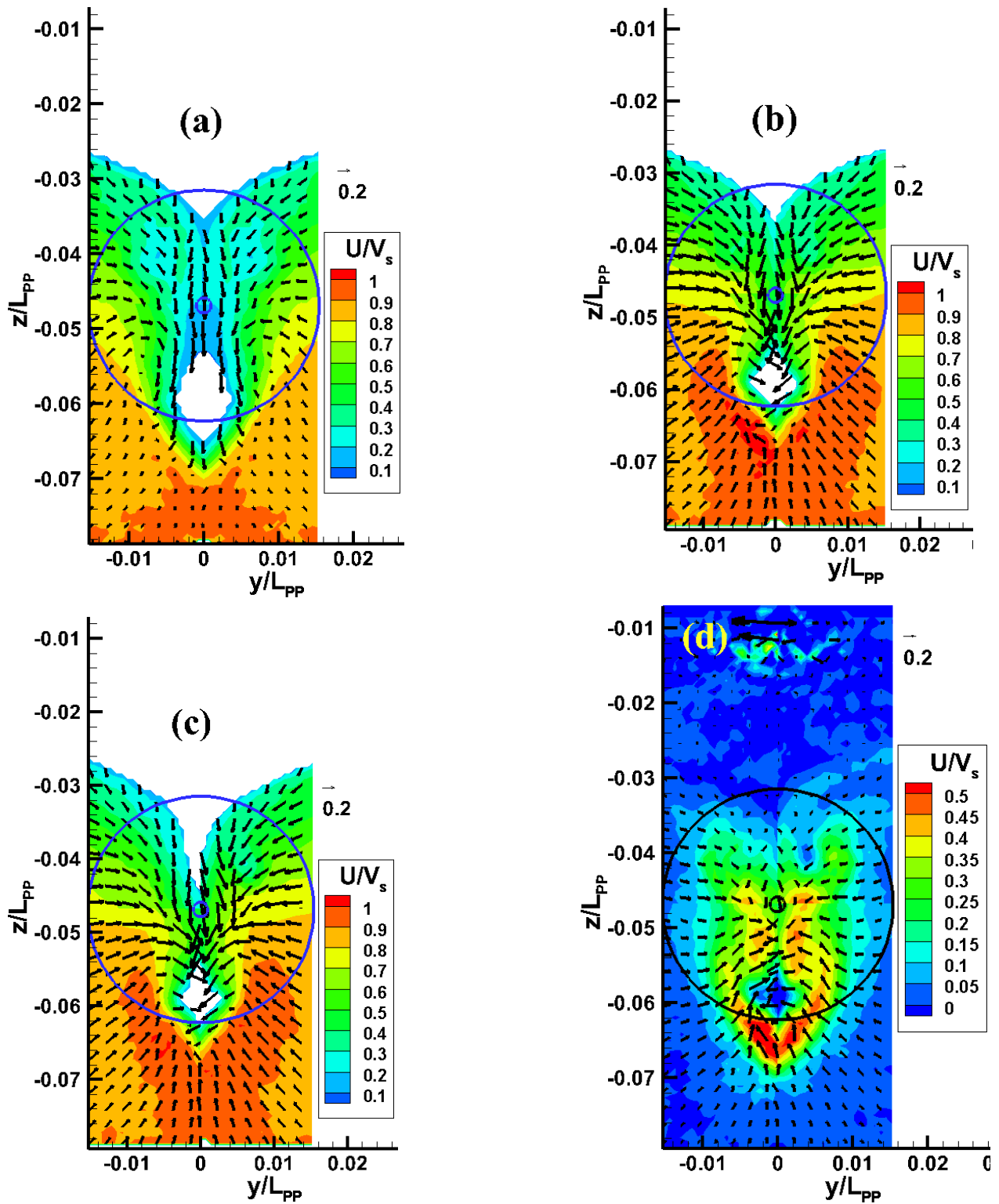


Figure 4-35 Phase averaged velocity distribution for (300°) for $\lambda/L=1.6$; (a) with normal rudder, no propeller, (b) normal rudder, (c) RBF-F system and (d)=(b)-(a).

b) Velocity field downstream of the rudders

The phase averaged velocity field results for $\lambda/L=0.6$ for with and without rudder conditions at cross-section $x/L=1.025$ at a propeller speed of 16.5 rps are as shown in Figure 4-36~Figure 4-39. The y and z axes are non-dimensionalized by the ship's length between the perpendiculars (L) and the axial velocity, u as well as the cross flow velocities (v and w) are non-dimensionalized by the ship's forward speed, V_s . As seen from these figures, the high speed axial velocity contour as well as the cross flow velocity vectors are clearly captured for with and without rudder conditions. Given that $\lambda/L=0.6$ is a shorter wavelength, the ship's vertical motions are relatively small and this can clearly be seen from the velocity distribution diagrams since the high speed axial velocity contours are generally within the propeller disk radius. At this cross-section, the nature of rotation of the right-handed propeller can clearly be seen because the cross flow vectors (v/V_s , w/V_s) are twisted towards the starboard side. The propeller accelerates the flow downstream to 1.6 times the ship's forward speed in all cases.

The high speed axial velocity contours and the velocity at the core of the hub vortex are also very different between the rudders themselves as well as between the rudders and without rudder condition. The normal rudder and the RBF-F system deform the shape of the high speed axial velocity contour into a twisted contour whose part on the port side is higher and lower on the starboard side. However, the axial velocity contour has an almost round and smooth shape for the normal rudder but this shape is bulged out into a concave at the position corresponding to the bulb and fins for the RBF-F system. This makes the shape of the high speed axial velocity contour to be a little bit larger for the RBF-F system as compared to that of the normal rudder. Therefore, it is observed that the bulb and fins in the RBF-F system have a direct effect on the velocity distribution in this section, downstream of the propeller, unlike in the section upstream of the

propeller. Also, it can be seen that the velocity is higher on the right side of both rudders. It is thought that this is the reason why the suction by the propeller was stronger on the starboard side in the comparison between the result for with and without propeller of the normal rudder at the upstream section from the propeller. The hub vortex in the propeller slipstream is shifted to the left of the center line ($Y=0$) into the port side's upward flow for both rudder and without rudder condition. The velocity at the core of the hub vortex is attenuated by using rudders. The RBF-F system reduces this velocity a little bit more compared to the normal rudder.

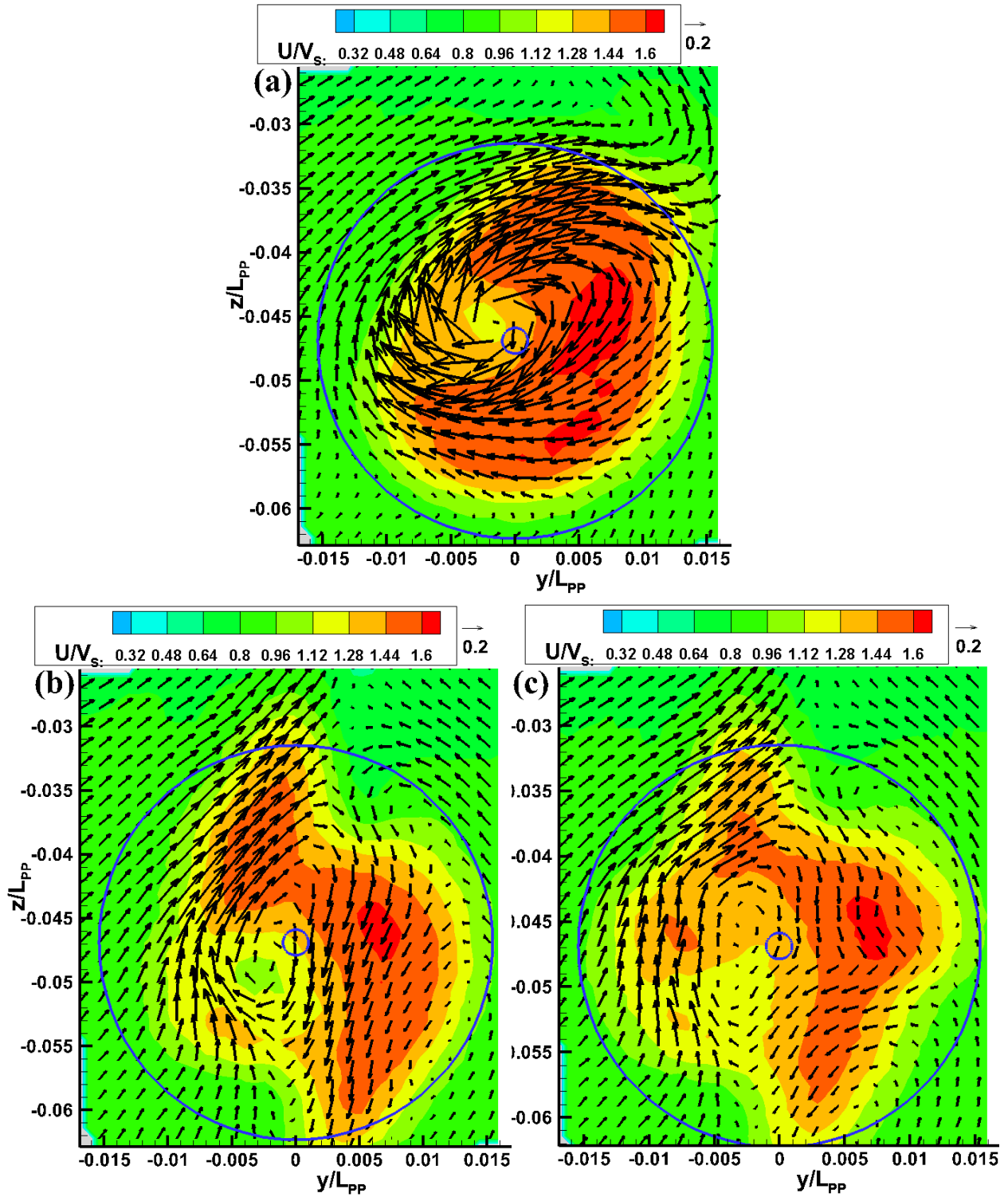


Figure 4-36 Phase averaged velocity distribution for (0°) for $\lambda/L=0.6$, for (a) without rudder, (b) normal rudder and (c) RBF-F system.

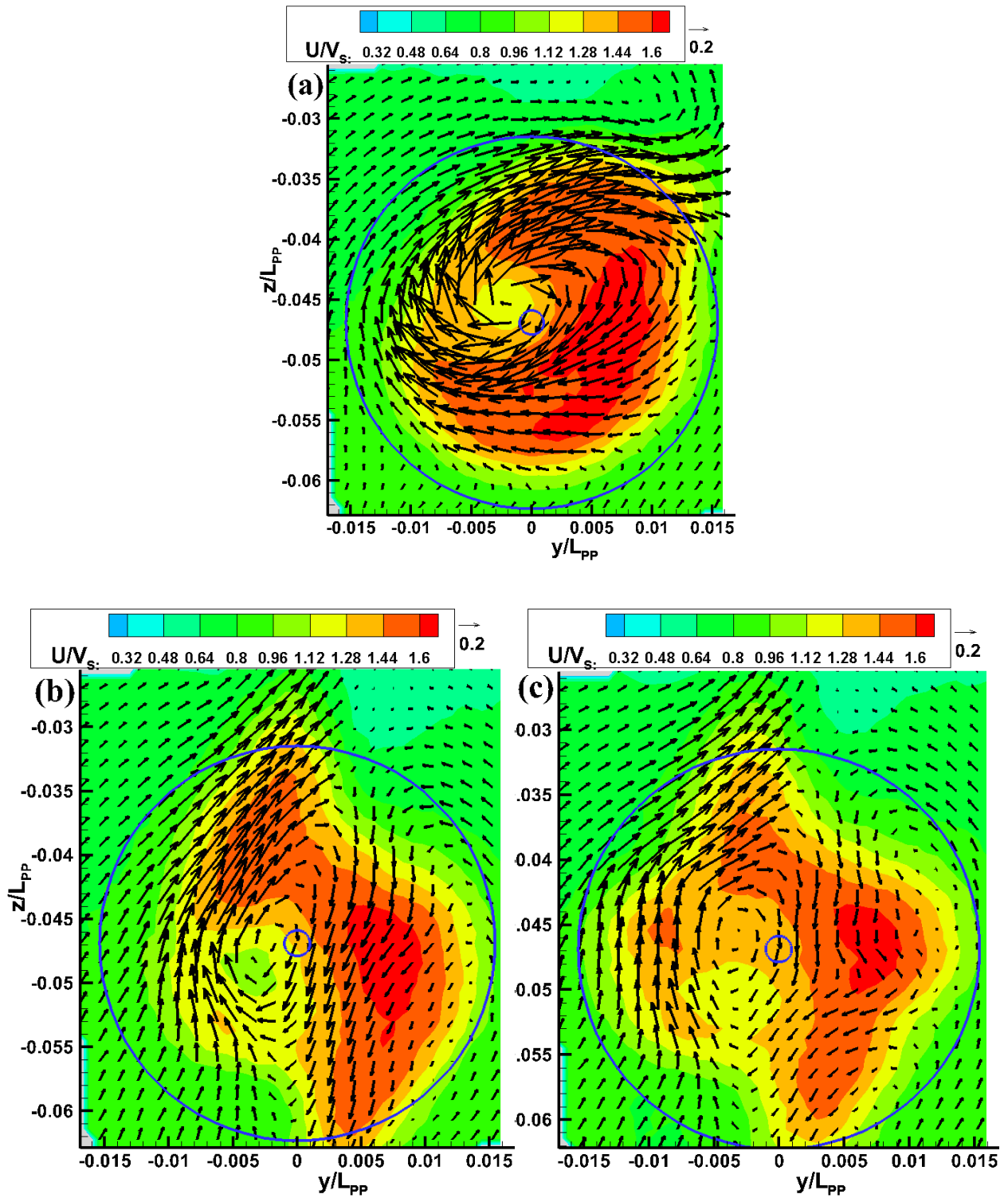


Figure 4-37 Phase averaged velocity distribution for (90°) for $\lambda/L=0.6$, for (a) without rudder, (b) normal rudder and (c) RBF-F system.

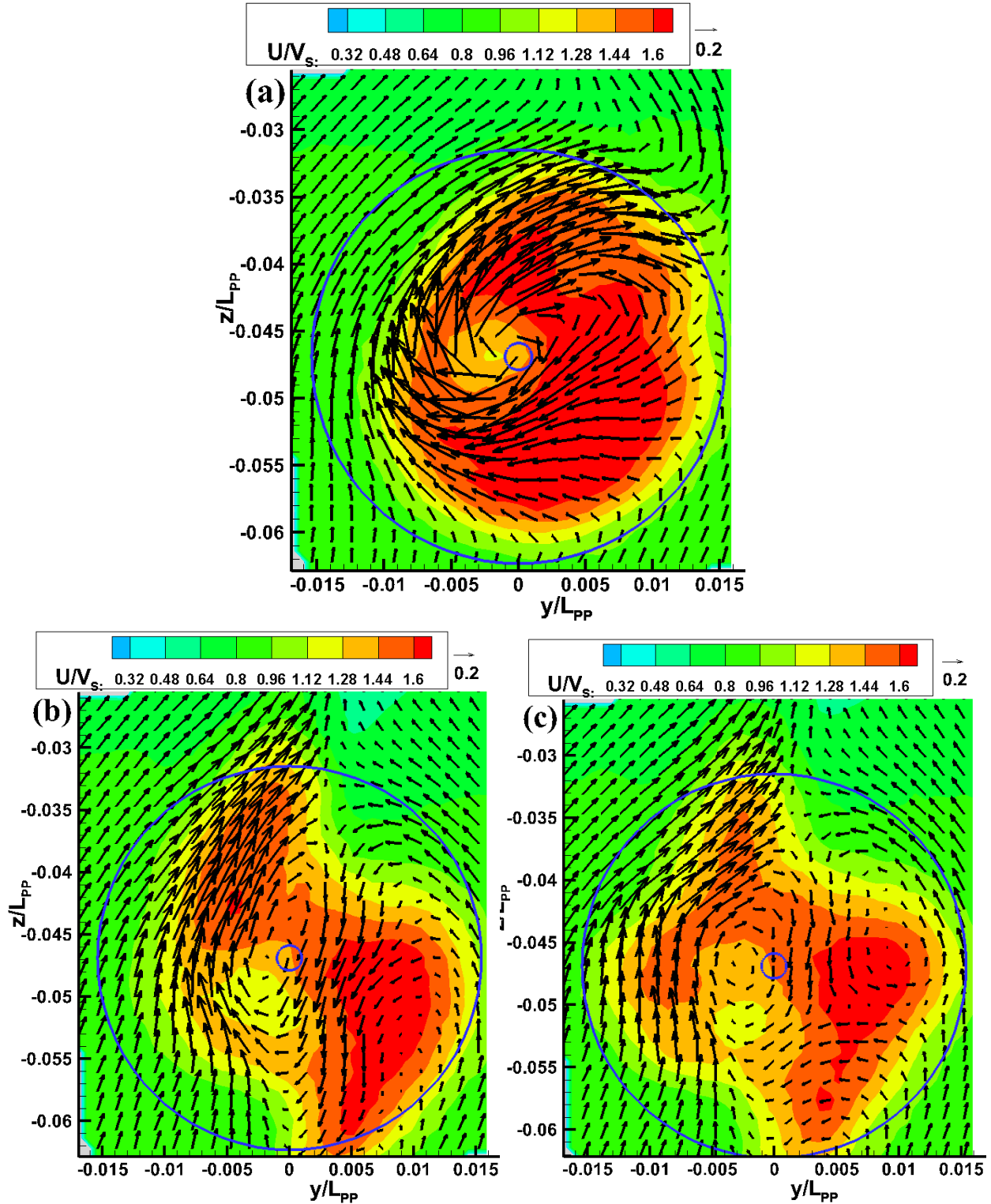


Figure 4-38 Phase averaged velocity distribution for (180°) for $\lambda/L=0.6$, for (a) without rudder, (b) normal rudder and (c) RBF-F system.

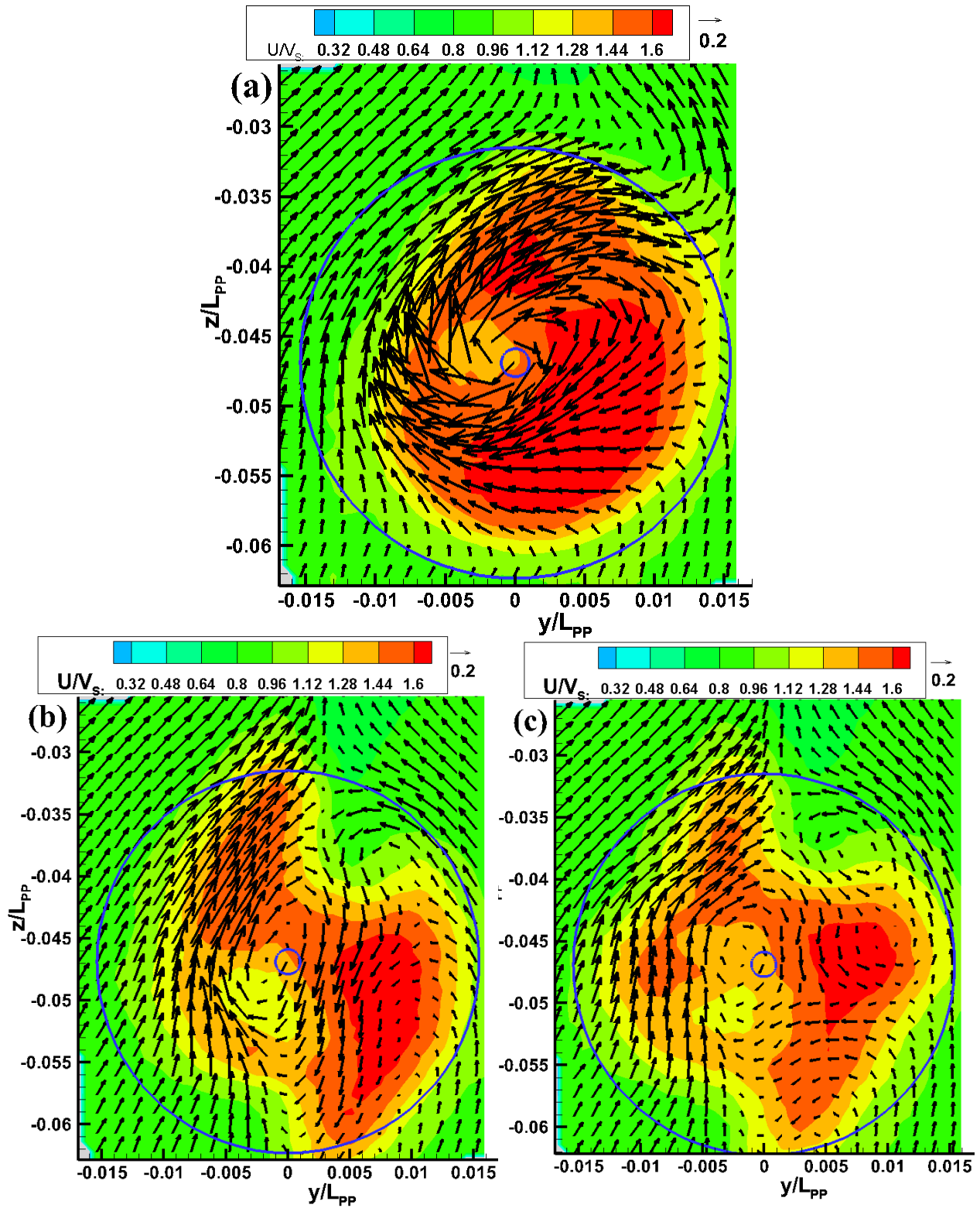


Figure 4-39 Phase averaged velocity distribution for (270°) for $\lambda/L=0.6$, for (a) without rudder, (b) normal rudder and (c) RBF-F system.

The phase averaged velocity field results for $\lambda/L=1.1$ for with and without rudder conditions at cross-section $x/L=1.025$ at a propeller speed of 16.5 rps are shown in Figure 4-40~Figure 4-45. The y and z axes are non-dimensionalized by the ship's length between the perpendiculars (L) and the axial velocity, u as well as the cross flow velocities (v and w) are non-dimensionalized by the ship's forward speed, V_s . From these figures, the vertical position of the high speed axial velocity contour changes very much within one encounter period, unlike in shorter wavelength ($\lambda/L=0.6$). This implies that in longer waves the vertical ship motions are larger. In order to visualize clearly the vertical relative motion between the high speed axial velocity contour and the propeller disk, the propeller disk and its center under the undisturbed calm water surface are drawn on the figures. The distance of the propeller center under the undisturbed calm water surface and its diameter are non-dimensionalized by the ship's length between the perpendiculars (L) and they are; $z/L=-0.04688$ and $d/L=0.03081$. Like in calm water and $\lambda/L=0.6$ wave condition, the nature of rotation of the right-handed propeller can clearly be seen since the cross flow velocity vectors are twisted towards the starboard side. The propeller accelerates the flow downstream to about 1.6 times the ship's forward speed in almost all phases for with and without rudder conditions.

In this wave condition, the high speed axial velocity contours and the velocity at the core of the hub vortex are also very different between the rudders themselves as well as between the rudders and without rudder conditions. The normal rudder and the RBF-F system distort the shape of the high speed axial velocity contour into a twisted contour whose part is higher on the port side and lower on the starboard side of the rudders. However, the high speed axial velocity contour has a nearly round and smooth shape for the normal rudder but this shape is bulged out into a concave shape at the position corresponding to the bulb and fins for the RBF-F system. This results in the

shape of the axial velocity contour to be a little bit larger for the RBF-F system compared to the normal rudder. The shape of the high speed axial velocity contour is almost round for without rudder condition when the ship stern is moving down and when it is at the bottom most position (phases 60, 120 and 180 degrees). It changes into an oval-like shape when the ship stern is moving up and when it is at the top most position (phases 240, 300 and 0 degrees). Also, it can be seen that the upper left part of the high speed axial velocity contour is slower in the RBF-F system compared to the normal rudder especially when the ship stern is going down. Moreover, when the ship stern is moving down the high speed axial velocity contour has a regular shape for both normal rudder and RBF-F system but it changes into an irregular shape when the ship stern is moving up. This irregular shape of the high speed axial velocity contour, when the ship stern is moving up, implies that the propeller thrust is higher in these respective phases as seen in Figure 4-18.

The hub vortex in the propeller slipstream is shifted to the left side (port side of the center line, $Y=0$) in the upward stern flow for both rudder and without rudder conditions. The velocity at the core of the hub vortex is highest for without rudder condition but it is weakened by using rudders. For the rudder conditions, the velocity at the core of the hub vortex is lower for the RBF-F system as compared to the normal rudder condition. This indicates that the RBF-F system weakens the hub vortex strength and may reduce the resistance due to the vortex, and hence improve the propulsive performance of the ship as compared to the normal rudder. Also, from the velocity field figures another counter-clockwise rotating vortex is seen at around $y/L=0.008$, $z/L=-0.038$ for phase 60 degree, and $y/L=0.008$, $z/L=-0.046$ for phase 120 degree for with and without rudder condition. It occupies a position above that for the hub vortex but in the downward flow in the starboard side, and it is due to the downward movement of the ship stern.

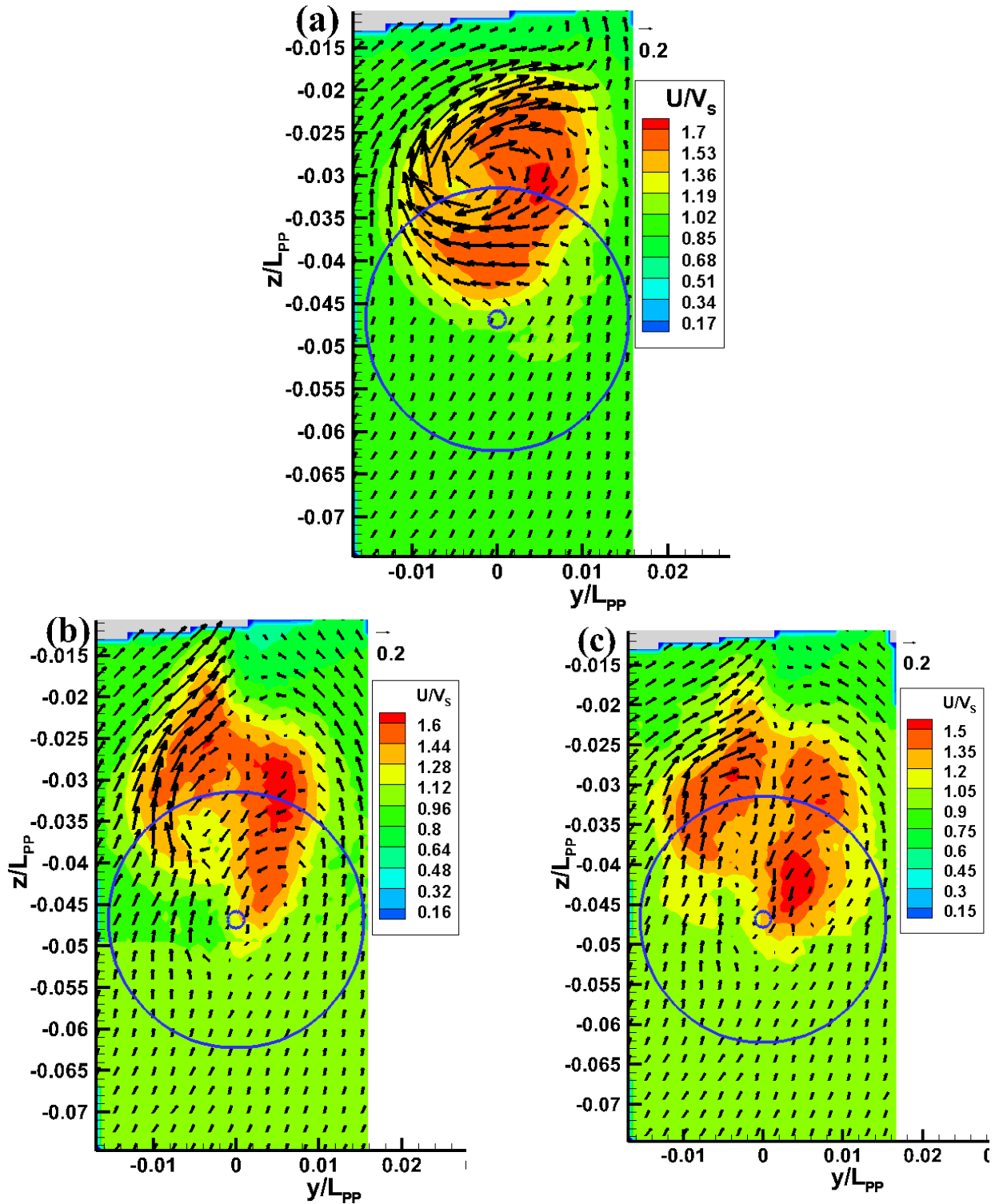


Figure 4-40 Phase averaged velocity distribution for (0°) for $\lambda/L=1.1$; (a) without rudder, (b) normal rudder and (c) RBF-F system.

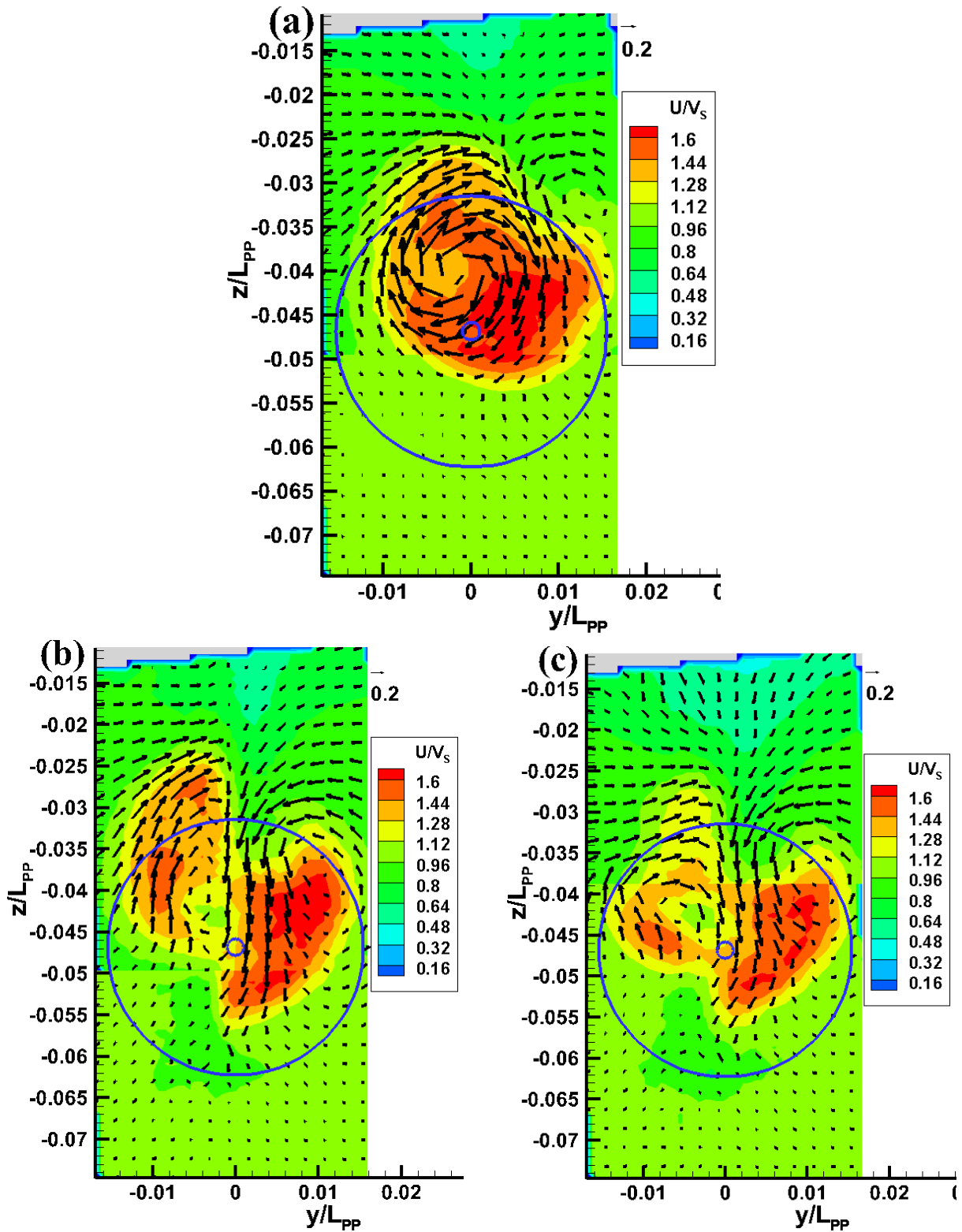


Figure 4-41 Phase averaged velocity distribution for (60°) for $\lambda/L=1.1$; (a) without rudder, (b) normal rudder and (c) RBF-F system.

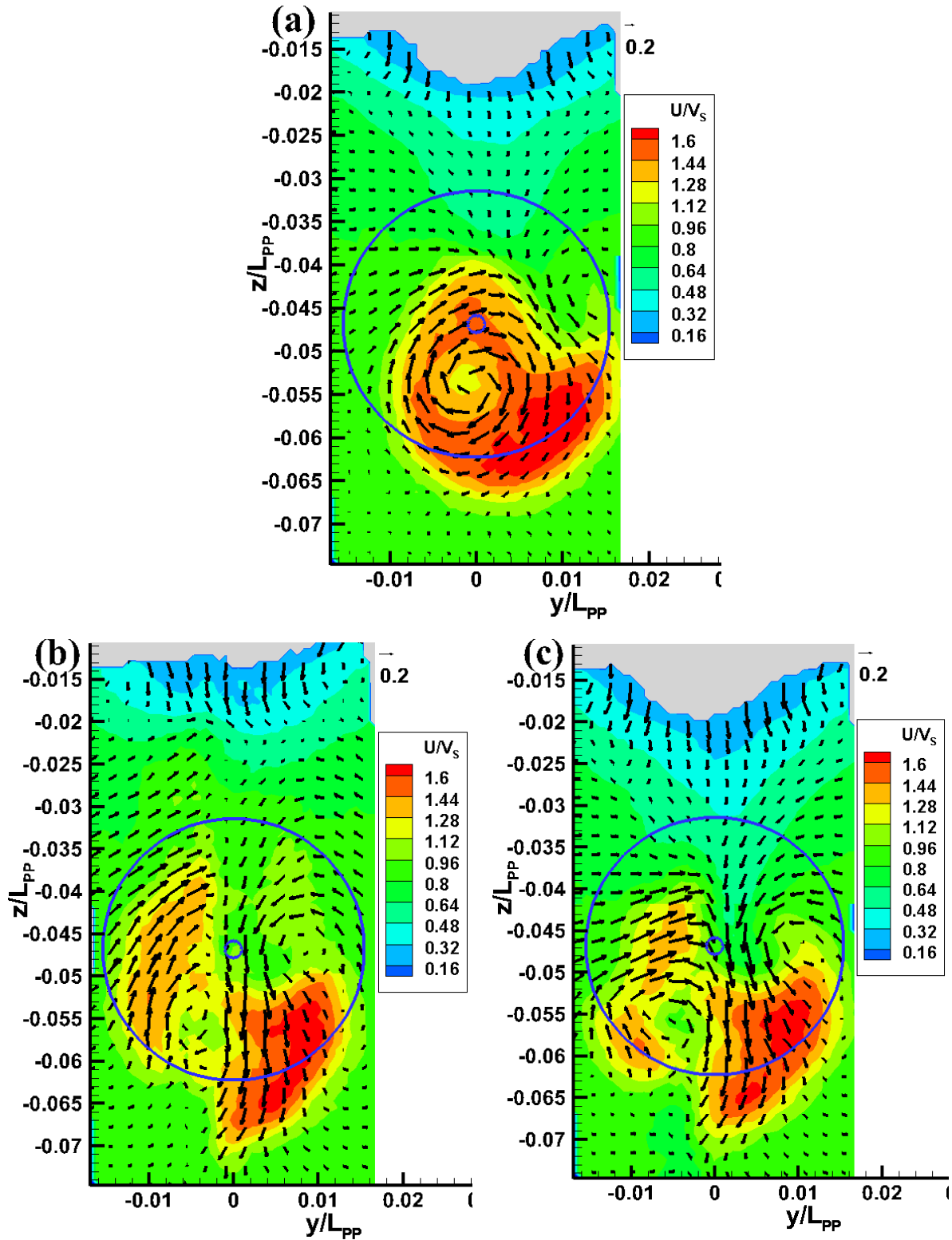


Figure 4-42 Phase averaged velocity distribution for (120°) for $\lambda/L=1.1$; (a) without rudder, (b) normal rudder and (c) RBF-F system.

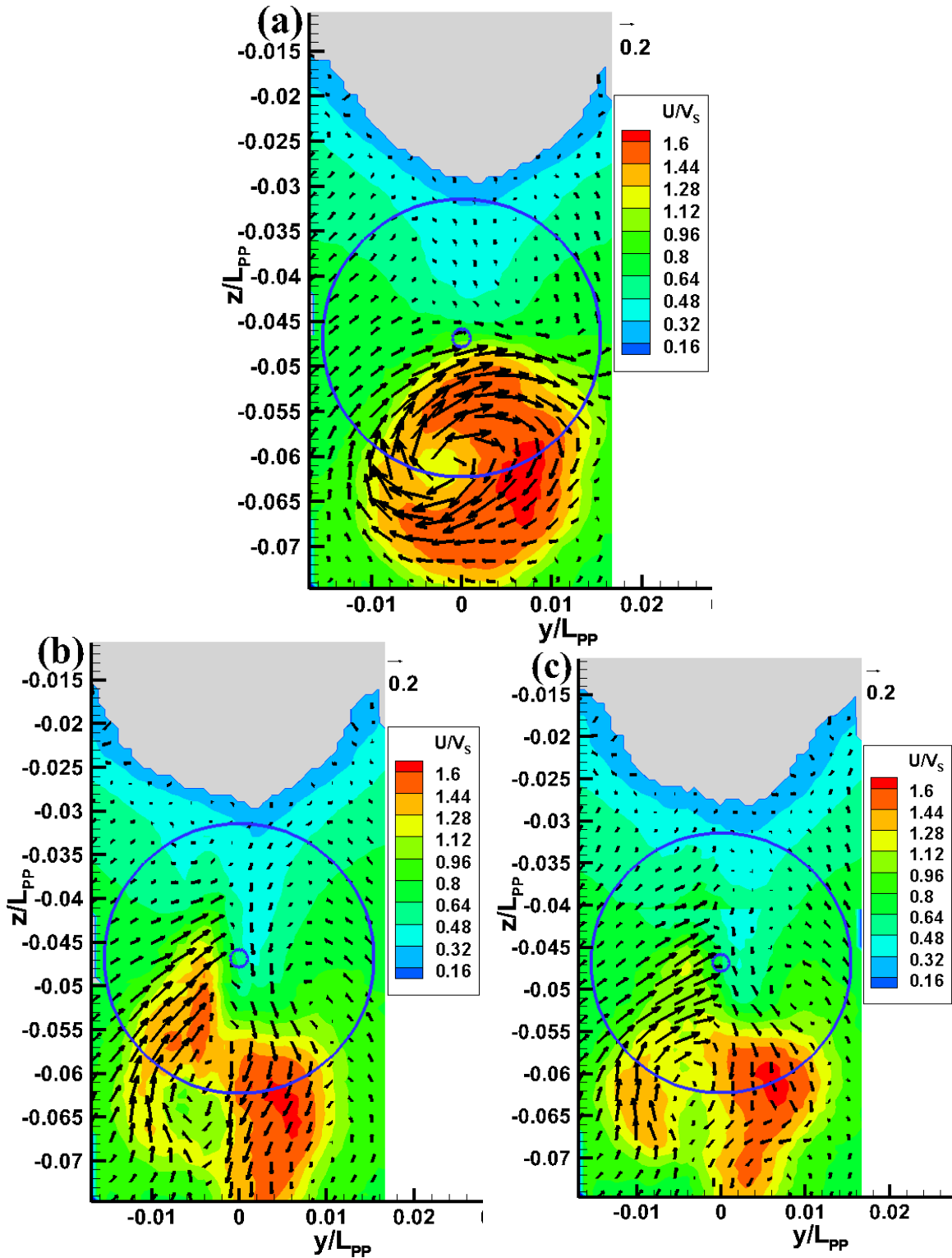


Figure 4-43 Phase averaged velocity distribution for (180°) for $\lambda/L=1.1$; (a) without rudder, (b) normal rudder and (c) RBF-F system.

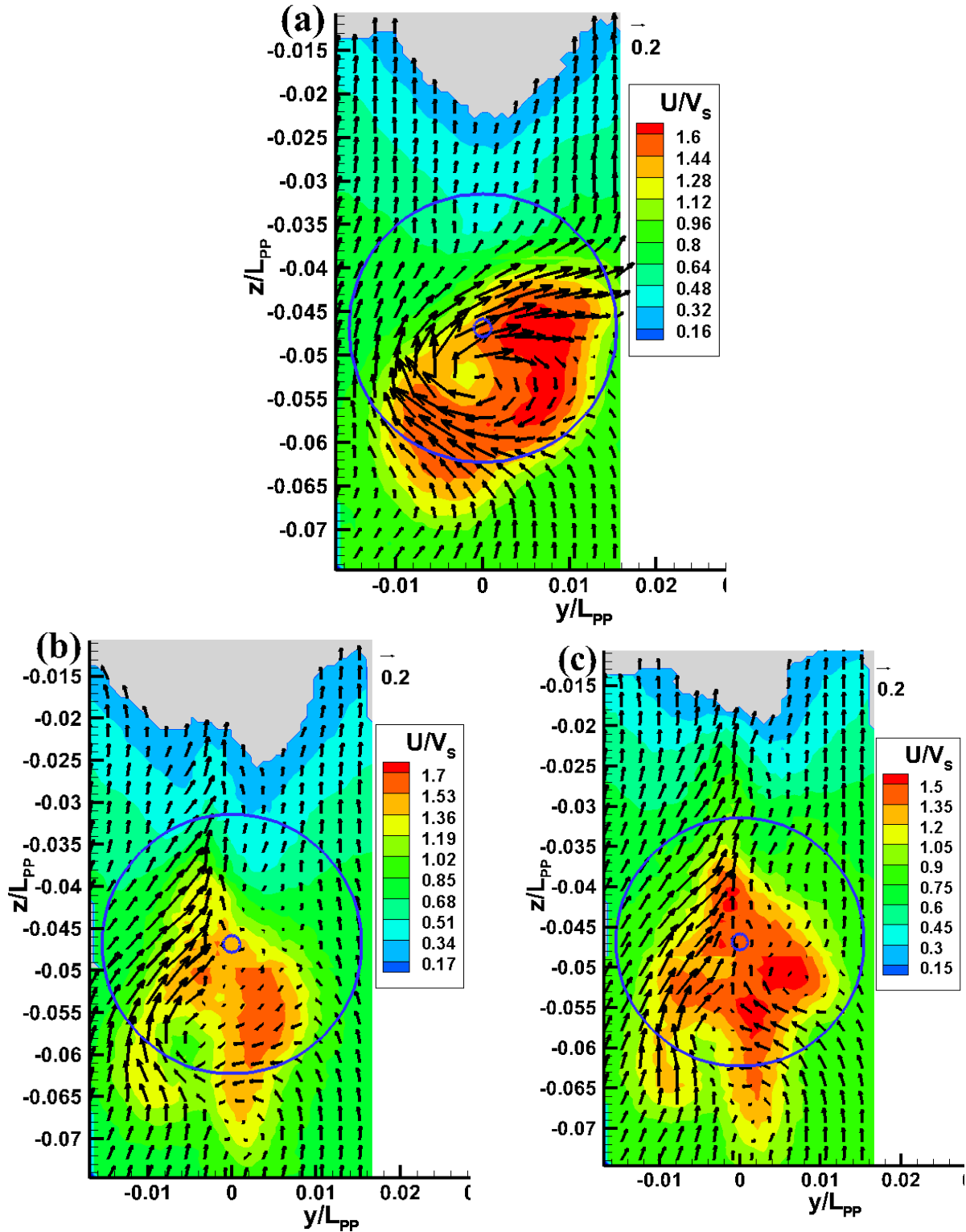


Figure 4-44 Phase averaged velocity distribution for (240°) for $\lambda/L=1.1$; (a) without rudder, (b) normal rudder and (c) RBF-F system.

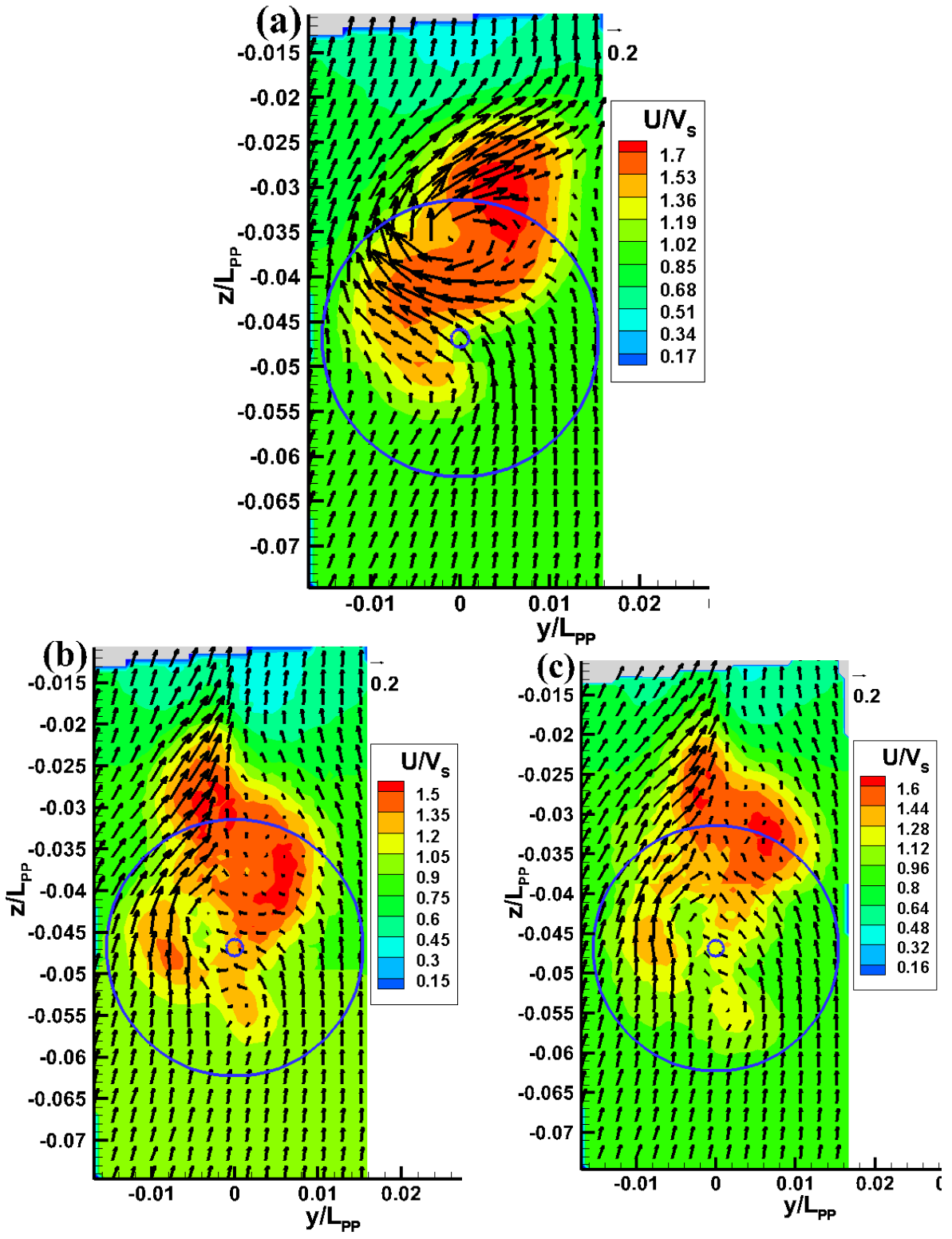


Figure 4-45 Phase averaged velocity distribution for (300°) for $\lambda/L=1.1$; (a) without rudder, (b) normal rudder and (c) RBF-F system.

The phase averaged velocity field results for $\lambda/L=1.6$ for with and without rudder conditions at cross-section $x/L=1.025$ at a propeller speed of 16.5 rps are shown in Figure 4-46~Figure 4-51. The y and z axes are non-dimensionalized by the ship's length between the perpendiculars (L) and the axial velocity, u as well as the cross flow velocities (v and w) are non-dimensionalized by the ship's forward speed, V_s . From these figures, it can clearly be seen that the high speed axial velocity contour and the cross flow vectors (v/V_s , w/V_s) are also clearly captured for both rudder and without rudder conditions. Like in the medium wavelength ($\lambda/L=1.1$), the vertical position of the high speed axial velocity contour changes very much within one encounter period. This implies that in this wavelength the vertical ship motions are larger compared to the other wavelengths. To visualize clearly the vertical motion of the high speed axial velocity contour, the propeller disk and its center under the undisturbed calm water surface are also drawn on the figures. The distance of the propeller center under the undisturbed calm water surface and its diameter are similar to those indicated in $\lambda/L=0.6$ and 1.1. Like in calm water and the aforementioned wave conditions, the nature of rotation of the right-handed propeller can clearly be seen since the cross flow velocity vectors are twisted towards the starboard side. The propeller accelerates the flow downstream to about 1.6 times the ship's forward speed in almost all phases for with and without rudder conditions.

The high speed axial velocity contours and the velocity at the core of the hub vortex are also very different between the rudders themselves as well as between the rudders and without rudder conditions. The normal rudder and RBF-F system deform the shape of the high speed axial velocity contour into a twisted contour whose part is higher on the port side and lower on the starboard side of the rudders. However, the high speed axial velocity contour has a more or less round and smooth shape for the normal rudder but this shape is bulged out into a concave shape at

the position corresponding to the bulb and fins for the RBF-F system. This makes the shape of the high speed axial velocity contour to be a little bit larger for the RBF-F system compared to the normal rudder. The shape of the high speed axial velocity contour is almost round for without rudder condition when the ship stern is moving down and when it is at the bottom most position (phases 240, 300 and 0 degrees). It changes into an oval-like shape when the ship stern is moving up and when it is at the top most position (phases 60, 120 and 180 degrees). Also, when the ship stern is moving down the high speed axial velocity contour has a regular shape for both normal rudder and RBF-F system but it changes into an irregular shape when the ship stern is moving up. Similarly, this irregular shape of the high speed axial velocity contour means that the propeller thrust is higher at the phases when the ship stern is moving up compared to the phases when the ship stern is moving down as seen in Figure 4-19.

The hub vortex in the propeller slipstream is also shifted to the left side of the center line, $Y=0$ (port side) in the upward stern flow for both with and without rudder conditions. The velocity at the core of the hub vortex is highest for without rudder condition but it is diminished by using rudders. The RBF-F system weakens the hub vortex more compared to the normal rudder, and in this way it may reduce the resistance due to the vortex and hence improve the propulsive performance of the ship as compared to the normal rudder. Also, another counter-clockwise rotating vortex is seen at around $y/L=0.01$, $z/L=-0.032$ for phase 240 degree, and $y/L=0.01$, $z/L=-0.042$ for phase 300 degree for with and without rudder condition. These vortices occupy a position which is above that of the hub vortex but in the downward flow in the starboard side, and it is due to the downward movement of the ship stern.

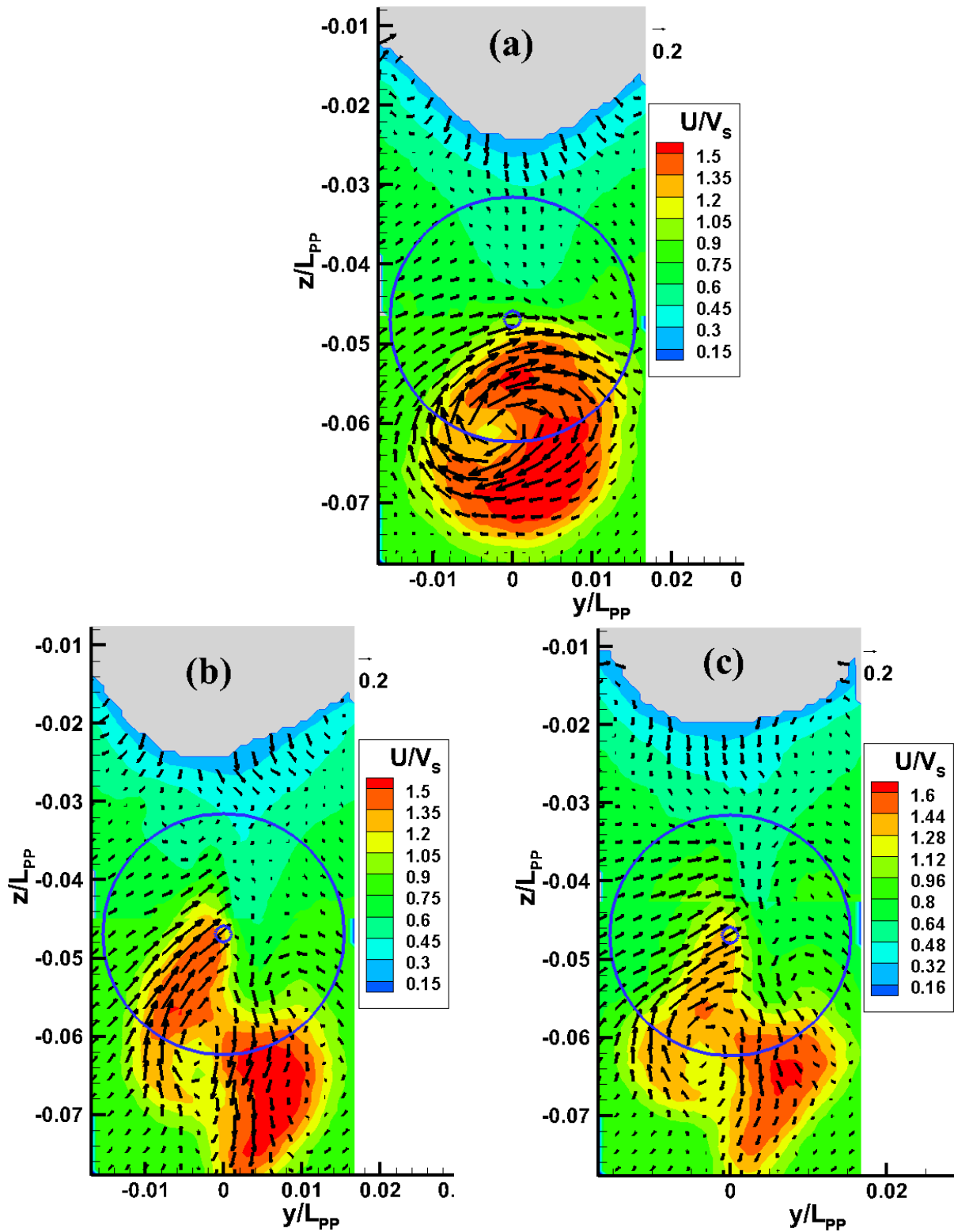


Figure 4-46 Phase averaged velocity distribution for (0°) for $\lambda/L=1.6$; (a) without rudder, (b) normal rudder and (c) RBF-F system.

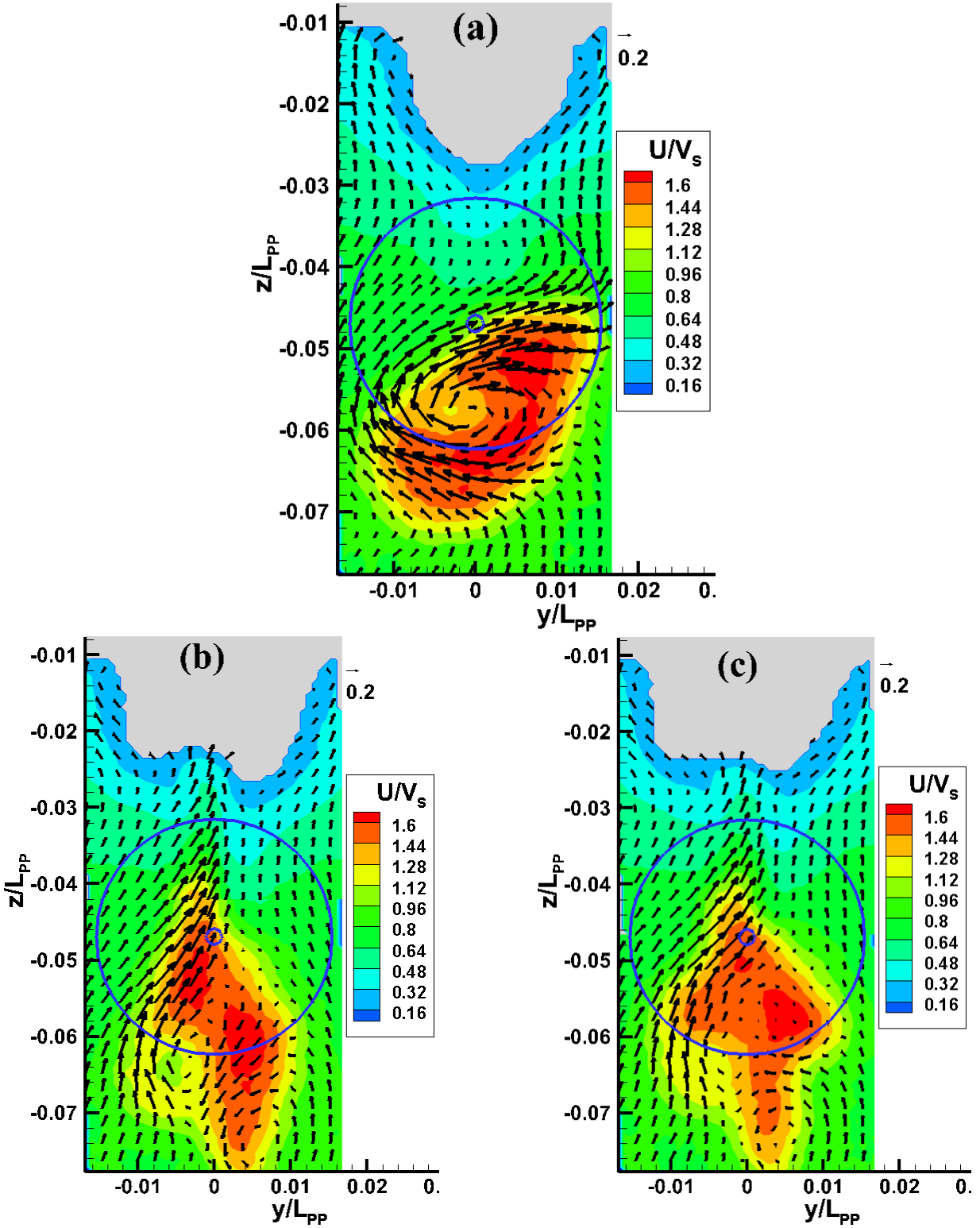


Figure 4-47 Phase averaged velocity distribution for (60°) for $\lambda/L=1.6$; (a) without rudder, (b) normal rudder and (c) RBF-F system.

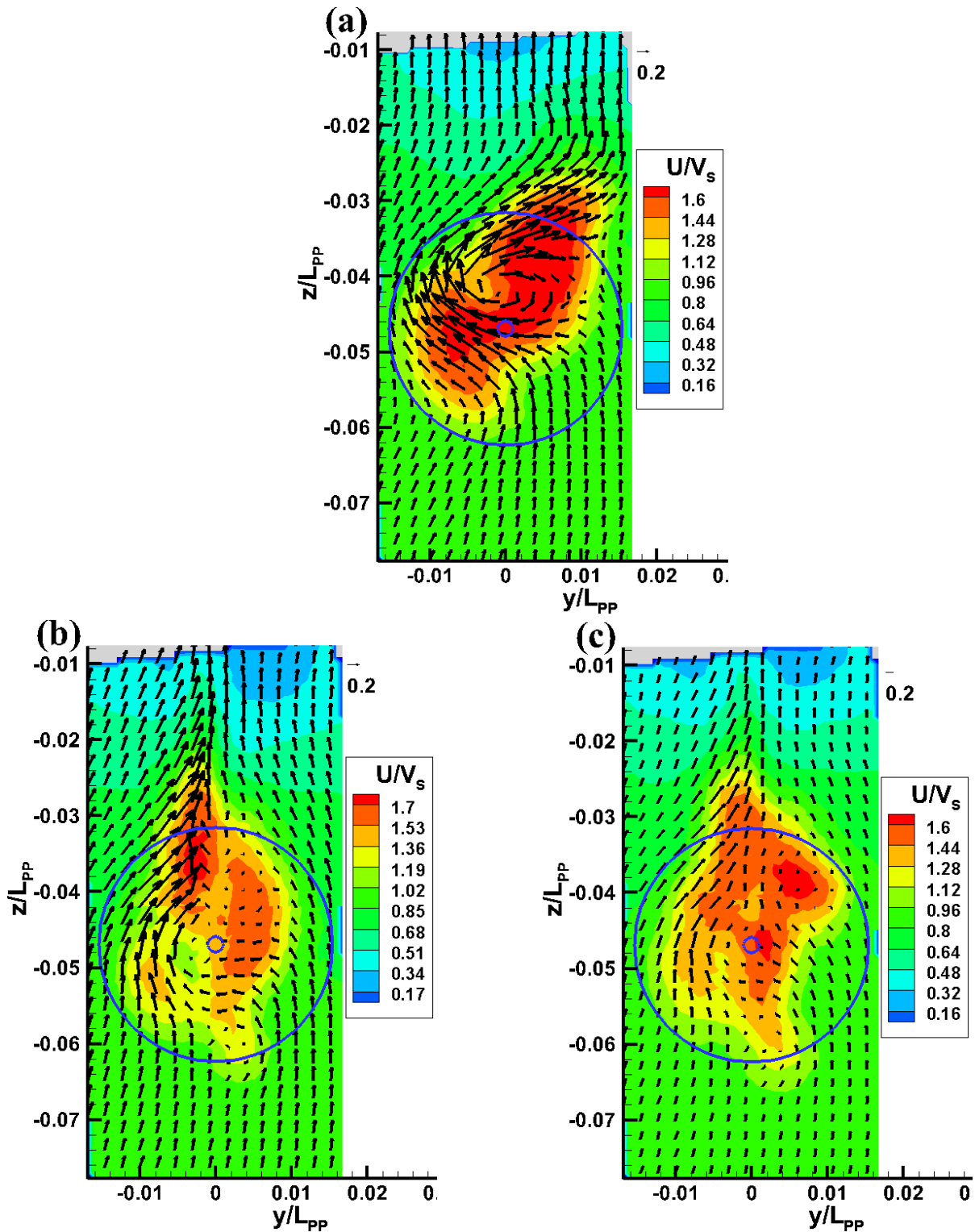


Figure 4-48 Phase averaged velocity distribution for (120°) for $\lambda/L=1.6$; (a) without rudder, (b) normal rudder and (c) RBF-F system.

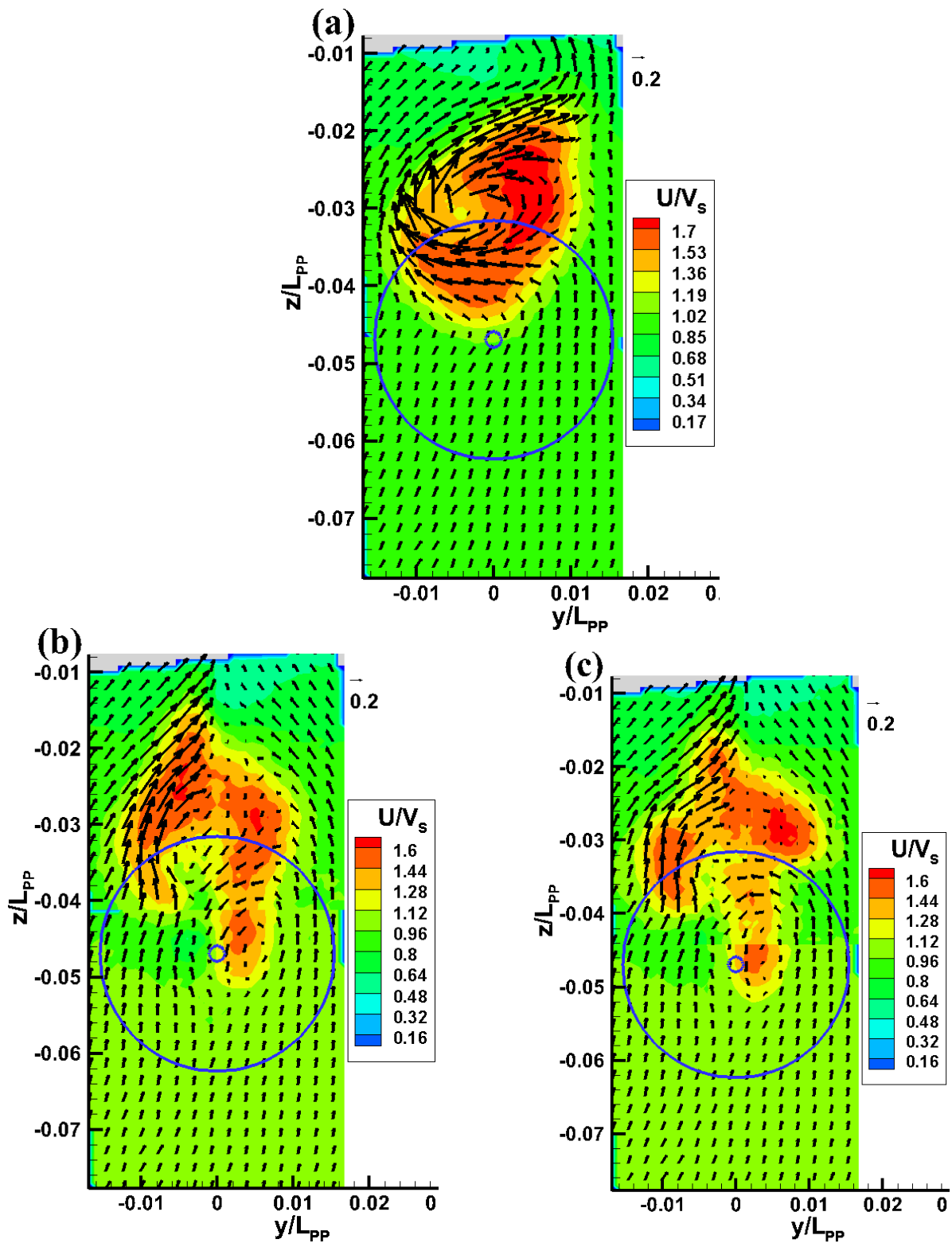


Figure 4-49 Phase averaged velocity distribution for (180°) for $\lambda/L=1.6$; (a) without rudder, (b) normal rudder and (c) RBF-F system.

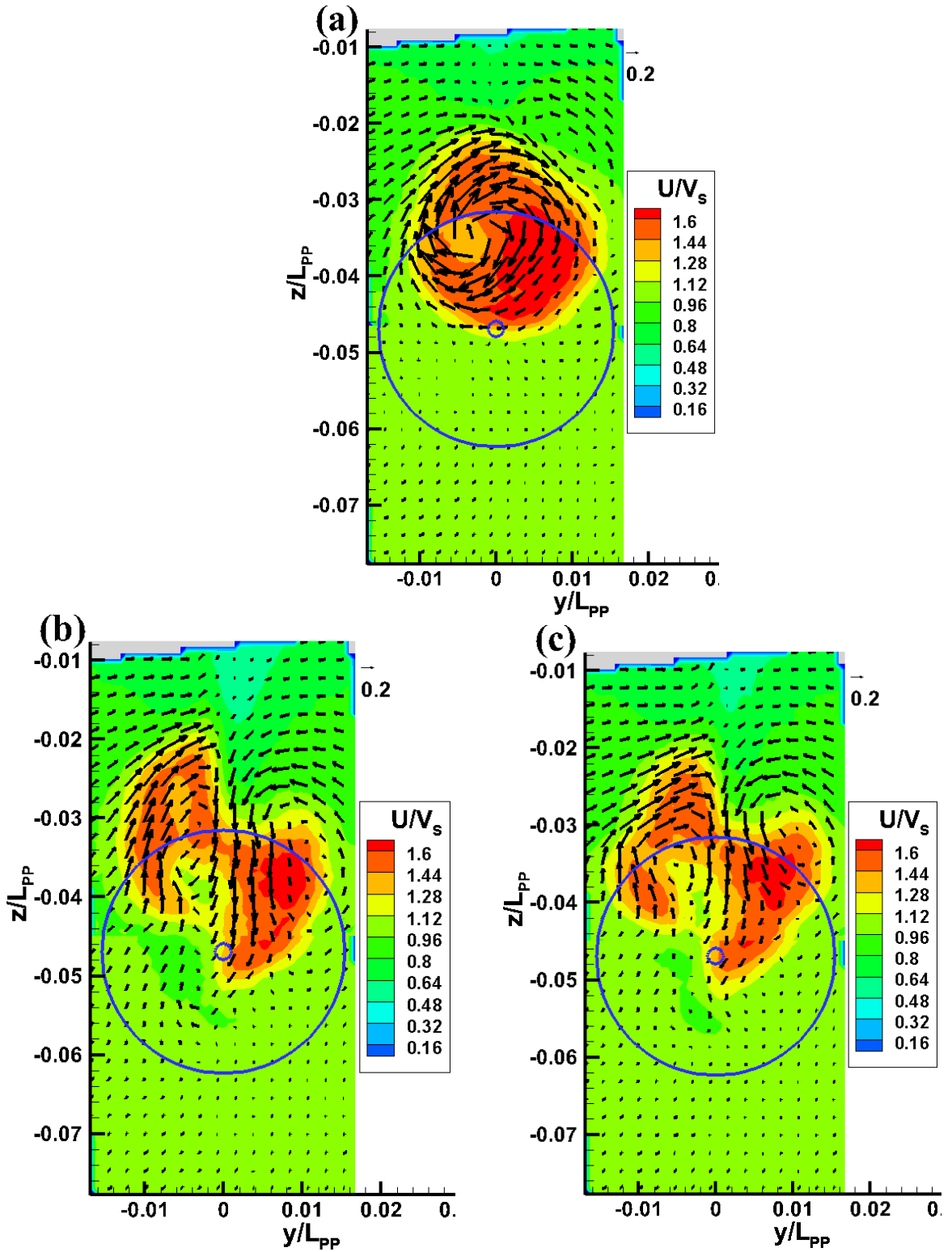


Figure 4-50 Phase averaged velocity distribution for (240°) for $\lambda/L=1.6$; (a) without rudder, (b) normal rudder and (c) RBF-F system.

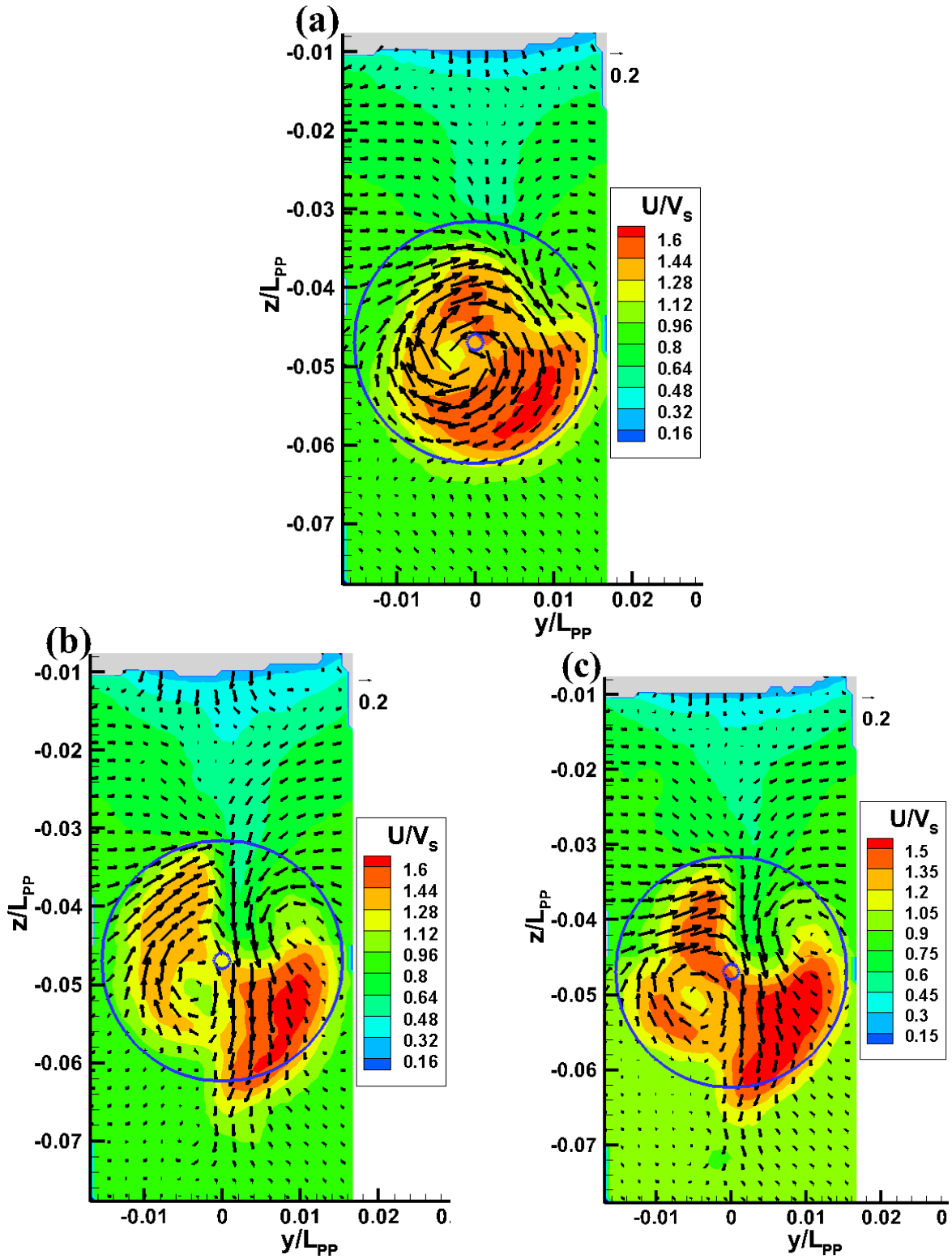


Figure 4-51 Phase averaged velocity distribution for (300°) for $\lambda/L=1.6$; (a) without rudder, (b) normal rudder and (c) RBF-F system.

CHAPTER 5: CONCLUSIONS AND FUTURE WORKS

5.1 CONCLUSIONS

a) Wave amplitude effect

The wave amplitude dependency for thrust, torque, towing force and 3DOF motions were investigated for KVLCC2 tanker model in long, regular head waves at design $Fr=0.142$. From the results of Fourier analysis of the motions and forces, it was noted that for motions up to 1st harmonic components are enough to obtain the original motion trend while for thrust and torque up to 3rd harmonic components are enough.

From the motions and force measurement results, by increasing the wave amplitude, the mean values for thrust and torque decrease slightly whereas those for effective wake increase slightly. The 1st harmonic values for thrust, torque and effective wake increase linearly as the wave amplitude increases. For motions, the 1st harmonic amplitudes increase linearly while phases are fairly constant as the wave amplitude increases. The added resistance increases linearly with the square of the wave amplitude whereas the added resistance coefficient is fairly constant as the wave amplitude increases.

The flow field around the ship stern was also measured by the SPIV system and its change with the wave amplitude investigated. Moreover, the velocity distribution at the stern was analyzed and discussed with respect to the thrust fluctuation in waves even though the velocity field was measured for without propeller condition. The vertical relative motion between the propeller disk and the low velocity region, due to bilge vortices, was observed. As the wave amplitude increases this relative motion increases and high velocity flow enters the propeller plane from the bottom.

This phenomenon certainly influences the propeller performance. Since the time averaged inflow velocity increases as the wave amplitude increases, the efficiency decreases for long waves.

Therefore, it is imperative to analyze the viscous inflow velocity into the propeller since it is very important in the study to improve the propulsive performance, including the engine characteristics, for a ship in waves as a measure to reduce GHG emissions from the shipping industry.

b) ESDs effect

In this study, the effect of various energy-saving rudders on the flow field around the stern of KVLCC2 model tanker as well as on motions and forces was investigated. From the results, there was no significant difference between the vertical ship motions for with and without rudder conditions. Therefore, the rudders did not have much effect on motions. However, on the forces, the rudders had a significant effect. For instance, the values for thrust for the RBF systems were higher compared to those for the normal rudder in all wavelength conditions. On the other hand, the effective wake values were higher for normal rudder compared to the RBF systems in all wavelengths. Also, efficiency improvement by RBF system was observed in short waves, and a decrease in efficiency was not observed in all wavelengths. However, it doesn't give any large energy saving effect in waves. The thrust deduction factor is almost similar for all rudders in all wavelength conditions.

Regarding the flow field, the effect of the normal rudder and the RBF-F system on the flow field around the stern region of KVLCC2 model tanker was also investigated and discussed. The measurement was done at two transverse plane; one plane was upstream of the propeller and the other one was downstream of the rudders. From the results for the velocity field of upstream of the

propeller, it was observed that there was no major difference between the results for both rudders. The only effect on the flow at this plane was from the propeller suction. However, at the plane downstream of the rudders there was a significant difference between the velocity field results for both rudders. These differences have been discussed in detail in the section for results. In a nutshell, it was observed that the normal rudder and RBF-F system deform the shape of the high speed axial velocity contour into a twisted contour whose part is higher on the port side and lower on the starboard side. However, for the normal rudder the shape of the high speed axial velocity contour is almost round and smooth but this shape is bulged out into a concave shape at the position corresponding to the bulb and fins for the RBF-F system. Also, the hub vortex shifts to the left side of the center plane ($Y=0$) in the upward stern flow for both rudder and without rudder condition. The RBF-F system is able to weaken the hub vortex strength in the propeller slipstream more compared to the normal rudder because of its bulb and fins. Therefore, the RBF-F system has a higher energy saving capability than the normal rudder.

5.2 FUTURE WORKS

To conduct SPIV measurement for the same model ship using a similar RBF system but with a cut fin on the starboard side, and various RBF systems with some angles of attack. Also, to conduct a similar study using another type of ship such as the high-speed KRISO Container Ship (KCS). Furthermore, it is proposed to conduct similar experiments in waves using other ESDs such as a duct, Propeller Boss Cap Fins (PBCFs) etc.

REFERENCES

- Ahn, K., Choi, G. H., Son, D. I., & Rhee, K. P. (2012). Hydrodynamic Characteristics of X-Twisted rudder for Large Container Carriers. *International Journal of Naval Architecture and Ocean Engineering*, 4(3), 322-334. <https://doi.org/10.3744/JNAOE.2012.4.3.322>
- Carlton, J. (2012). Marine Propellers and Propulsion. In *Marine Propellers and Propulsion*, 321-330. <https://doi.org/10.1016/C2010-0-68327-1>
- Çelik, F. (2007). A Numerical Study for Effectiveness of a Wake Equalizing Duct. *Ocean Engineering*, 34(16), 2138–2145. <https://doi.org/10.1016/j.oceaneng.2007.04.006>
- Chang, X., Sun, S., Zhi, Y., & Yuan, Y. (2019). Investigation of the Effects of a Fan-Shaped Mewis Duct before a Propeller on Propulsion Performance. *Journal of Marine Science and Technology (Japan)*, 24(1), 46-59. <https://doi.org/10.1007/s00773-018-0530-x>
- Dang, J., Dong, G., & Chen, H. (2012). An Exploratory Study on the Working Principles of Energy Saving Devices (ESDs) - PIV, CFD Investigations and ESD Design Guidelines. *Proceedings of the 34th International Conference on Offshore Mechanics and Arctic Engineering - OMAE*, 5. <https://doi.org/10.1115/OMAE2012-83053>
- Furcas, F., Vernengo, G., Villa, D., & Gaggero, S. (2020). Design of Wake Equalizing Ducts using RANSE-based SBDO. *Applied Ocean Research*, 97. <https://doi.org/10.1016/j.apor.2020.102087>
- Ghassemi, H. (2009). Hydrodynamic Performance of Coaxial Contra-Rotating Propeller (CCRP) for large ships. *Polish Maritime Research*, 16(1). [https://doi.org/10.2478/v10012-008-0006-](https://doi.org/10.2478/v10012-008-0006-8)

- Ghassemi, H., & Taherinasab, M. (2013). Numerical Calculations of the Hydrodynamic Performance of the Contra-Rotating Propeller (CRP) for High Speed Vehicle. *Polish Maritime Research*, 20(2). <https://doi.org/10.2478/pomr-2013-0012>
- Guiard, T., Leonard, S., & Mewis, F. (2013). The Becker Mewis Duct ®-Challenges in Full-Scale Design and new Developments for Fast Ships. *3rd International Symposium on Marine Propulsors smp'13*, Tasmania, Australia, 11A.2.
- Hai-Long, S., Obwogi, E. O., & Yu-Min, S. (2016). Scale Effects for Rudder Bulb and Rudder Thrust Fin on Propulsive Efficiency based on Computational Fluid Dynamics. *Ocean Engineering*, 117, 199-209. <https://doi.org/10.1016/j.oceaneng.2016.03.046>
- He, L., & Kinnas, S. A. (2017). Numerical Simulation of Unsteady Propeller/Rudder Interaction. *International Journal of Naval Architecture and Ocean Engineering*, 9(6), 677-692. <https://doi.org/10.1016/j.ijnaoe.2017.02.004>
- Hossain, Md. A., Wu, P-C., Shibano, Y., & Toda, Y. (2018). Forces, Ship Motions and Velocity Wake Field for KRISO Container Ship Model in Regular Head Waves. *28th International Ocean and Polar Engineering Conference*, Sapporo, Japan.
- Htay, N. W., Magari, A., & Toda, Y. (2021). A Study on the Performance of Rudder Bulb Fins System of KVLCC2 in Regular Head Waves. *Proceedings of the 31st International Ocean and Polar Engineering Conference*, Rhodes, Greece, 2643-2650.
- Htay, N. W., Truong, T. Q., & Toda, Y. (2020). A CFD based Comparison Study of Conventional Rudder and Rudder with Bulb-Fins System of KVLCC2 in Waves. *Proceedings of the 30th International Ocean and Polar Engineering Conference*, Shanghai, China, ISOPE, 3377-3384.

- IMO (2020). Fourth Greenhouse Gas Study 2020. Retrieved April 20, 2021 from <https://www.imo.org/en/OurWork/Environment/Pages/Fourth-IMO-Greenhouse-Gas-Study-2020.aspx>.
- Inukai, Y. (2011). Development of Electric Propulsion Vessels with Contra-Rotating Propeller. *Journal of The Japan Institute of Marine Engineering*, 46(3), 26-32. <https://doi.org/10.5988/jime.46.313>
- Inukai, Y., Kaneko, T., Nagaya, S., & Ochi, F. (2017). Energy-Saving Principle of the IHIMU Semicircular Duct and Its Application to the Flow Field around Full Scale Ships. *IHI Engineering Review*, 44(1), 17-22.
- Inukai, Y., Kanemaru, T., & Ando, J. (2014). Prediction of Steady Performance of Contra-Rotating Propellers Including Wake Alignment. *Journal of the Japan Society of Naval Architects and Ocean Engineers*, 19(0). <https://doi.org/10.2534/jjasnaoe.19.31>
- Inukai, Y., & Ochi, F. (2009). A study on the Characteristics of Self-propulsion Factors for a Ship Equipped with Contra-Rotating Propeller. In *SMP '09*, Trondheim, Norway, MB1-3.
- Jang, J., Choi, S. H., Ahn, S. M., Kim, B., & Seo, J. S. (2014). Experimental Investigation of Frictional Resistance Reduction with Air Layer on the Hull Bottom of a Ship. *International Journal of Naval Architecture and Ocean Engineering*, 6(2), 363-379. <https://doi.org/10.2478/IJNAOE-2013-0185>
- Karim, M. M., & Naz, N. (2017). Computation of Flow Field around Ship Hull including Self Propulsion Characteristics at Varying Rudder Positions. *Procedia Engineering*, 194, 96-103. <https://doi.org/10.1016/j.proeng.2017.08.122>

- Kawakita, C., Sato, S., & Okimoto, T. (2015).) Application of Simulation to Mitsubishi Air Lubrication System. *Mitsubishi Heavy Industries Technical Review*, (Vol. 52, Issue 1), 50-56.
- Kawakita, C., Takashima, R., & Sato, K. (2012).) CFD on Cavitation around Marine Propellers with Energy-Saving Devices. *Mitsubishi Heavy Industries Technical Review*, (Vol. 49, Issue 1), 63-67
- Kawamura, T., Ouchi, K., & Takeuchi, S. (2013). Model and Full Scale CFD Analysis of Propeller Boss Cap Fins (PBCF), *Third International Symposium on Marine Propulsors smp'13*, Tasmania, Australia, 486-493.
- Kim, H. (2014). Phase-Averaged SPIV Wake Field Measurement for KVLCC2 Propeller Plane in Waves. *Doctoral Thesis*, Osaka University, Japan. <https://doi.org/10.18910/50513>
- Kim, J. H., Choi, J. E., Choi, B. J., & Chung, S. H. (2014). Twisted Rudder for Reducing Fuel-oil Consumption. *International Journal of Naval Architecture and Ocean Engineering*, 6(3), 715-722. <https://doi.org/10.2478/IJNAOE-2013-0207>
- Kim, J. H., Choi, J. E., Choi, B. J., Chung, S. H., & Seo, H. W. (2015). Development of Energy-Saving Devices for a Full Slow-speed Ship Through Improving Propulsion Performance. *International Journal of Naval Architecture and Ocean Engineering*, 7, 390-398.
- Kim, M., Hizir, O., Turan, O., & Incecik, A. (2017). Numerical Studies on Added Resistance and Motions of KVLCC2 in Head Seas for Various Ship Speeds. *Ocean Engineering*, 140, 466–476. <https://doi.org/10.1016/j.oceaneng.2017.06.019>
- Kimura, K., Ando, S., Ono, S., Tanaka, Y., & Takeuchi, S. (2018). Investigation on Full Scale

- Performance of the Propeller Boss Cap Fins (PBCF). In *Full Scale Ship Performance*.
- LaVision (2009). “System Design Specification Underwater PIV for Osaka University,” p 1-13.
- LaVision: FlowMaster Advanced PIV/PTV Systems for Quantitative Flow Field Analysis
- LaVision: Product-Manual, “Flow Master Getting Started” Item-number(s): 1105011-4
- Liu, C., Wang, J., & Wan, D. (2017). The Numerical Investigation on Hydrodynamic Performance of Twisted Rudder during Self-propulsion. *ICCM2017*, Guilin, Guangxi, China, 934-943.
- Majumder, P., Avanapu, D. K., & Maity, S. (2020). Numerical Investigation to Observe Combined Effect of Propeller Boss Cap Fin (PBCF) and Propeller Duct to Improve Propeller Efficiency. *Journal of Marine Science and Technology (Japan)*. <https://doi.org/10.1007/s00773-020-00775-w>
- Martinas, G. (2015). Cavitation of a Propeller and Influence of an Wake Equalizing Duct. *TransNav, the International Journal on Marine Navigation and Safety of Sea Transportation*, 9(2), 235-241. <https://doi.org/10.12716/1001.09.02.11>
- Matsumoto, A. (2019). Added Resistance/ Powering and Motion Measurements of KRISO Container Ship in Regular Head Waves. *Master's Thesis*, Osaka University, Japan. (In Japanese)
- Matsuura, H. (2021). SPIV Measurement of Stern Flow Field in Waves around KVLCC2 with Energy-Saving Rudders. *Master's Thesis*, Osaka University, Japan. (In Japanese)
- Mewis, F., & Guiard, T. (2011). Mewis Duct® – New Developments , Solutions and Conclusions. *Second International Symposium on Marine Propulsors smp'11, Hamburg, Germany*.
- Min, K. S., Chang, B. J., & Seo, H. W. (2009). Study on the Contra-Rotating Propeller System

- Design and Full-Scale Performance Prediction Method. *International Journal of Naval Architecture and Ocean Engineering*, 1(1). <https://doi.org/10.3744/JNAOE.2009.1.1.029>
- Mizzi, K., Demirel, Y. K., Banks, C., Turan, O., Kaklis, P., & Atlar, M. (2017). Design Optimisation of Propeller Boss Cap Fins for Enhanced Propeller Performance. *Applied Ocean Research*, 62, 210-222. <https://doi.org/10.1016/j.apor.2016.12.006>
- MOL Tech / MOL Techno-Trade, Ltd. Retrieved May 30, 2021, from <https://www.motech.co.jp/en/>
- Nakamura, S., Hosoda, S., & Inoue, M. (1975). Propulsive Performance of a Container Ship in Waves (4th report). *Journal of Kansai Society of Naval Architects of Japan*, No. 159, 29-39.
- Naing Win, Y., Wu, P.-C., Akamatsu, K., Okawa, H., Stern, F., & Toda, Y. (2016). RANS Simulation of KVLCC2 using Simple Body-Force Propeller Model With Rudder and Without Rudder. *Journal of the Japan Society of Naval Architects and Ocean Engineers*, 23(0). <https://doi.org/10.2534/jjasnaoe.23.1>
- Nojiri, T., Ishii, N., & Kai, H. (2011). Energy Saving Technology of PBCF (Propeller Boss Cap Fins) and its Evolution. *Journal of The Japan Institute of Marine Engineering Marine Engineering*, 46(3), 63-71. <https://doi.org/10.5988/jime.46.350>
- Nowruzi, H., & Najafi, A. (2019). An experimental and CFD study on the effects of different pre-swirl ducts on propulsion performance of series 60 ship. *Ocean Engineering*, 173, 491-509. <https://doi.org/10.1016/j.oceaneng.2019.01.007>
- Ohashi, K., Sakamoto, N., & Hino, T. (2013). Numerical Simulation of Flows around KVLCC2 Hull Form with Ship Motions in Regular Waves. *International Conference on Computational*

Methods in Marine Engineering (MARINE), Hamburg, Germany, 794-805.

Okada, Y., Kawasaki, M., Katayama, K., Okazaki, A., Fukuda, K., & Okazaki, M. (2015). The Development of “Ultimate Rudder” for EEDI. *MARINE 2015 - Computational Methods in Marine Engineering VI*, Rome, Italy, 605-612.

Paik, K. J., Hwang, S., Jung, J., Lee, T., Lee, Y. Y., Ahn, H., & Van, S. H. (2015). Investigation on the Wake Evolution of Contra-Rotating Propeller using RANS Computation and SPIV Measurement. *International Journal of Naval Architecture and Ocean Engineering*, 7(3), 595-609. <https://doi.org/10.1515/ijnaoe-2015-0042>

Park, S., Oh, G., Hyung Rhee, S., Koo, B. Y., & Lee, H. (2015). Full Scale Wake Prediction of an Energy Saving Device by using Computational Fluid Dynamics. *Ocean Engineering*, 101, 254-263. <https://doi.org/10.1016/j.oceaneng.2015.04.005>

Reichel, M. (2009). Influence of Rudder Location on Propulsive Characteristics of a Single Screw Container Ship, *1st International Symposium on Marine Propulsors, smp'09*, Trondheim, Norway.

Sadat-Hosseini, H., Wu, P. C., Carrica, P. M., Kim, H., Toda, Y., & Stern, F. (2013). CFD Verification and Validation of Added Resistance and Motions of KVLCC2 With Fixed and Free Surge in Short and Long Head Waves. *Ocean Engineering*, 59, 240–273. <https://doi.org/10.1016/j.oceaneng.2012.12.016>

Saettone, S., Regener, P. B., & Andersen, P. (2016). Pre-Swirl Stator and Propeller Design for Varying Operating Conditions. *PRADS 2016 - Proceedings of the 13th International Symposium on Practical Design of Ships and Other Floating Structures*.

- Sasaki, N., Atlar, M., & Kuribayashi, S. (2016). Advantages of Twin Rudder System with Asymmetric Wing Section aside a Propeller. *Journal of Marine Science and Technology*, 21(2), 297-308. <https://doi.org/10.1007/s00773-015-0352-z>
- Sasaki, N., Kuribayashi, S., Fukazawa, M., & Atlar, M. (2020). Towards a Realistic Estimation of the Powering Performance of a Ship with a Gate Rudder System. *Journal of Marine Science and Engineering*, 8(1). <https://doi.org/10.3390/JMSE8010043>
- Seo, J., Lee, S. J., Han, B., & Rhee, S. H. (2016). Influence of Design Parameter Variations for Propeller-Boss-Cap-Fins on Hub Vortex Reduction. *Journal of Ship Research*, 60(4), 203-218. <https://doi.org/10.5957/JOSR.60.4.160003>
- Shin, H. J., Lee, J. S., Lee, K. H., Han, M. R., Hur, E. B., & Shin, S. C. (2013). Numerical and Experimental Investigation of Conventional and Un-Conventional Pre-Swirl Duct for VLCC. *International Journal of Naval Architecture and Ocean Engineering*, 5(3), 414-430. <https://doi.org/10.3744/JNAOE.2013.5.3.414>
- Su, Y. min, Lin, J. feng, Zhao, D. gang, Guo, C. yu, & Guo, H. (2020). Influence of a Pre-Swirl Stator and Rudder Bulb System on the Propulsion Performance of a Large-scale Ship Model. *Ocean Engineering*, 218. <https://doi.org/10.1016/j.oceaneng.2020.108189>
- Sun, Y., Su, Y., Wang, X., & Hu, H. (2016). Experimental and Numerical Analyses of the Hydrodynamic Performance of Propeller Boss Cap Fins in a Propeller-Rudder System. *Engineering Applications of Computational Fluid Mechanics*, 10(1), 145-159. <https://doi.org/10.1080/19942060.2015.1121838>
- Tacar, Z., Sasaki, N., Atlar, M., & Korkut, E. (2020). An Investigation into Effects of Gate Rudder® System on Ship Performance as a Novel Energy-Saving and Manoeuvring Device.

Ocean Engineering, 218. <https://doi.org/10.1016/j.oceaneng.2020.108250>

Tendou, Y., Okada, Y., Kajihama, T., Kajino, T., Katayama, K., Okazaki, M., & Fukuda, K. (2017).

Study on the Rudder Characteristics of Ultimate Rudder by Numerical Calculation. *7th International Conference on Computational Methods in Marine Engineering, MARINE 2017*, Nantes, France, 932-937.

Tokgoz, E., Wu, P.-C., Okawa, H., Tamaki, K., & Toda, Y. (2015). Computation and SPIV

Measurement of the Flow Field around Self-Propelled Ship in Waves Using Body-Force Model. *Proceedings of the Japan Society of Naval Architects and Ocean Engineers*, 20, 255-258.

Truong, T. Q., Wu, P. C., Aoyagi, K., Koike, K., Akiyama, Y., & Toda, Y. (2017). The EFD and

CFD Study of Rudder-Bulb-Fin System in Ship and Propeller Wake Field of KVLCC2 Tanker in Calm Water. *Proceedings of the International Offshore and Polar Engineering Conference*, San Francisco, USA, ISOPE, 823-830.

Tsukada, Y., Hinatsu, M., & Hasegawa, J. (1997). Measurement of Unsteady Ship Wakes in

Waves. *Journal of Kansai Society of Naval Architects of Japan*, 228, 15-20.

Wu, P.C. (2013). A CFD Study on Added Resistance, Motions and Phase Averaged Wake Fields

of Full Form Ship Model in Head Waves. *Doctoral Thesis*, Osaka University, Japan. <https://doi.org/10.18910/26191>

Wu, P.-C., Sadat-Hosseini, H., Toda, Y., Okawa, H., Kim, H., Akamatsu, K., & Stern, F. (2014).

Added Resistance and Nominal Wake in Waves of KVLCC2 Model Ship in Ballast Condition. *Proceedings of the 30th Symposium on Naval Hydrodynamics*, Hobart, Tasmania, Australia.

<https://www.researchgate.net/publication/287216134>

Xu, J., Hao, Z., Wang, Y., Ren, W., & Liu, G. (2020). Effect of Pre-Swirl Stator on Wake Flow of an Ducted Propeller. *Journal of Physics: Conference Series*, 1570(1).
<https://doi.org/10.1088/1742-6596/1570/1/012040>

Xu, L., & Wan, D. (2018). Numerical Investigation of Scale Effect for Propeller Boss Cap Fins. *Proceedings of the 28th International Offshore and Polar Engineering Conference*, 805-811.

LIST OF PUBLICATIONS

Conference Papers

Mwangi, B. O., Matsuura, H., and Toda, Y. (2021). The effect of Energy Saving Devices (ESDs) on the Flow Field around the Stern of KVLCC2 Model Tanker. *Proceedings of 31st International Ocean and Polar Engineering Conference*, Rhodes, Greece, ISOPE, 2651-2658.

Mwangi, B. O., Nango, H., and Toda, Y. (2019). SPIV Measurement for a Self-propelled Ship in Regular Head Waves with Different Amplitudes. *Proceedings of 11th International Workshop on Ship and Marine Hydrodynamics*, Hamburg, Germany, Paper 041.

Mwangi, B. O., Nango, H., and Toda, Y. (2019). SPIV Measurement for a Self-propelled Ship in Regular Head Waves with Different Amplitudes. *Proceedings of the Japan Society of Naval Architects and Ocean Engineers Conference*, Nagasaki, Japan, vol. 28, p.405-409.

CURRICULUM VITAE

EDUCATION

2018 - To date: Doctoral Course, Naval Architecture and Ocean Engineering

Osaka University- Suita City, Japan

Advisor: Prof. Yasuyuki Toda

Areas of research: Experimental Fluid Dynamics (EFD), Ship Hydrodynamics, Energy Saving Devices (ESDs).

Topic: "SPIV Flow Field Measurement around the Stern of a Self-propelled KVLCC2 Model Ship in Regular Head Waves"

2016 - 2018: Master of Engineering, Naval Architecture and Ocean Engineering

Osaka University- Suita City, Japan

Advisor: Prof. Yasuyuki Toda

2008 - 2012: Bachelor of Science, Mechanical Engineering

Jomo Kenyatta University of Agriculture and Technology- Kenya